Emergent constraints on soil carbon feedbacks under climate change

Submitted by
Rebecca May Varney
to the University of Exeter as a thesis for the degree of
Doctor of Philosophy in Mathematics,
June 2022

I certify that all material in this thesis which is not my own work has been identified and that any material that has previously been submitted and approved for the award of a degree by this or any other University has been acknowledged.

Signed: ..R. Varney.....

Abstract

Global soils are the largest terrestrial store of carbon, and are sensitive to changes in the Earth's climate system due to anthropogenic emissions of CO_2. Predicted changes in soil carbon by Earth System Models (ESMs) represent the greatest uncertainty in quantifying future projections of land carbon storage under climate change. Reducing this uncertainty is vital to achieve accurate future projections of global climate change and to successfully mitigate against its effects. The Coupled-Model Intercomparison Project phase 6 (CMIP6) includes the latest ESMs, as used within the latest Intergovernmental Panel on Climate Change 6^{th} Assessment Report (IPCC AR6). Model development since the previous CMIP generation (CMIP5) has aimed to improve the representation of soil carbon related processes within ESMs, and reduce the uncertainty associated with predicted soil carbon change. On top of model development, additional methods such as emergent constraints suggest promise to constrain future uncertainties associated with soil carbon under climate change. The aim of this thesis is to evaluate and analyse soil carbon in CMIP6 ESMs to help quantify future soil carbon changes, and to attempt to reduce uncertainty in future soil carbon projections.

Although some improvements are found in CMIP6 compared to CMIP5, significant uncertainties still remain, especially in the below ground processes that determine the effective soil carbon turnover time (Varney et al., 2022). The uncertainty in projected soil carbon stocks is found to be result of counteracting terms due to increasing Net Primary Productivity (NPP), and reductions in soil carbon turnover time (τ_s), as well as a significant non-linearity between NPP and τ_s. In the research presented in this thesis, a novel spatial emergent constraint is developed to constrain the subsequent changes in soil carbon due to reductions in τ_s under global warming (Varney et al., 2020). Comparison to the more standard breakdown of carbon storage changes into linear terms representing the response to changes in CO_2 and global temperature, reveals that there are significant reductions in τ_s under increasing CO_2, even in the absence of climate change. This effect is traced to 'false priming', which is especially prevalent in the CMIP6 models, and acts to reduce the spread in projected soil carbon changes in CMIP6 compared to CMIP5. These findings suggest some promising avenues for future research.

Acknowledgements

This thesis was funded by the European Research Council 'Emergent Constraints on Climate-Land feedbacks in the Earth System (ECCLES)' project, grant agreement number 742472.

I would like to acknowledge the World Climate Research Programme's Working Group on Coupled Modelling, who are responsible for CMIP, and I would like to thank the climate modelling groups for producing and making their model output available to enable research such as the research presented in this thesis.

On a more personal note, I would like to thank my supervisors Peter Cox and Sarah Chadburn for making my PhD experience better than I could have hoped for. Despite a pandemic, they have both made the experience very enjoyable and I am very thankful for their continuous support, insight and patience throughout. I would also like to thank everyone in Exeter Climate Systems for making Exeter such a friendly environment to do a PhD, with a special thanks to my 901 office! Additionally, thank you to Eleanor Burke at the Met Office for always being on hand to help when needed.

Outside of the office, I am lucky to have many people in my life who have helped me along the way. I am grateful to Megan who I have shared my entire University life with and can safely say I wouldn't have been able to do it without her. Thank you to Marianne and Laura for helping me become a better and happier version of myself over the last 3 years. Also, thank you to my cheerleaders from afar: Emily, Lauren and Hannah, for always being there.

A special thank you to Shuna for being my best friend for so many years and to Simon for being my rock and for always knowing how to make me smile. I would also like to thank my family for always being there for me come what may. My mum for being my number one supporter and for helping me to believe in myself, my number one nanny, my dad, sister, brother and little Splashy.

Finally, I would like to thank my Pa to whom I dedicate this thesis. Without him I would not be where I am today, and I know he would be very proud.

Contents

List of Figures

List of Tables

Associated Papers

Varney, R. M., Chadburn, S. E., Burke, E. J., and Cox, P. M. (2022). Evaluation of soil carbon simulation in cmip6 earth system models. *Biogeosciences*, 19(19):4671–4704

Varney, R. M., Chadburn, S. E., Friedlingstein, P., Burke, E. J., Koven, C. D., Hugelius, G., and Cox, P. M. (2020). A spatial emergent constraint on the sensitivity of soil carbon turnover to global warming. *Nature communications*, 11(1):1–8

Acronyms, Abbreviations & Symbols

IPCC	Intergovernmental Panel for Climate Change
ESM	Earth System Model
CMIP	Coupled Model Intercomparison Project
SSP	Shared Socioeconomic Pathway
RCP	Representative Concentration Pathway
C4MIP	Coupled Climate-Carbon Cycle Model Intercomparison Project
BGC	Biogeochemically coupled 1% CO_2 simulation
RAD	Radiatively coupled 1% CO_2 simulation
NEP, $\boldsymbol{F_L}$	Net Ecosystem Productivity
NPP, $\boldsymbol{\Pi_N}$	Net Primary Productivity
$\boldsymbol{C_s}$	Soil carbon
$\boldsymbol{C_v}$	Vegetation carbon
$\boldsymbol{C_L}$	Land carbon
$\boldsymbol{R_h}$	Heterotrophic respiration
$\boldsymbol{\tau_s}$	Soil carbon turnover time
$\boldsymbol{\beta}$	Carbon-concentration feedback parameter
$\boldsymbol{\gamma}$	Carbon-climate feedback parameter

Chapter 1

Introduction

Abstract

This introductory chapter describes the rationale and background for the thesis. The terrestrial carbon cycle is explained, with a particular emphasis on the importance of uncertainties in the response of soil carbon to 21$^{\mathrm{st}}$ century climate change. The concept of Emergent Constraints is also described, which is a promising approach to reduce these uncertainties and is used within the thesis.

1.1 The terrestrial carbon cycle

Since the start of the industrial revolution, anthropogenic emissions have resulted in a significant increase in atmospheric CO_2 concentrations. This increased CO_2 concentration has resulted in increased global temperatures due to an enhanced greenhouse effect, which in turn results in further changes to the Earth's climate system (IPCC, 2021b; Arias et al., 2021; Stocker et al., 2013). The Summary for Policymakers contained within the Intergovernmental Panel for Climate Change 5$^{\mathrm{th}}$ Assessment Report (IPCC AR5; IPCC (2013)) states that global warming will result in long-lasting changes to all components of the climate system, which will cause severe and irreversible impacts for both people and ecosystems on Earth. Limiting and quantifying future atmospheric CO_2 concentrations and understanding the subsequent changes to the Earth system, is therefore vital for reducing and mitigating against future climate change.

The terrestrial carbon cycle is an important component of the climate system and is fundamental to understanding future climate change projections. In the current climate, the land surface is known to absorb approximately a third of anthropogenic emissions of CO_2 (Friedlingstein et al., 2020, 2019; Le Quéré et al., 2018), so provides a vital store of carbon. However, it is known that the carbon cycle is sensitive to changes in climate and therefore understanding how

it will respond to future climate change is important for overall climate projections (Canadell et al., 2021; Ciais et al., 2013). Coupled climate-carbon models known as Earth System Models (ESMs), incorporate atmospheric and terrestrial processes to predict how the physical climate system and carbon cycle interact to determine the response of the climate system to anthropogenic emissions of CO_2 (Bradford et al., 2016). The response of the terrestrial carbon cycle presents one of the greatest sources of uncertainty in future climate predictions (Friedlingstein et al., 2014; Arora et al., 2013). Identifying and quantifying the causes of this uncertainty is therefore crucial.

The terrestrial carbon cycle describes how carbon is exchanged and stored within the Earth's biosphere, as shown in Figure 1.1 (taken from Ciais et al. (2013)), where carbon is stored in pools and transferred via fluxes. Anthropogenic fossil fuel burning and land-use change is altering the balance between the Earth's carbon pools and fluxes of CO_2 to and from the land surface. These changes to the fluxes further affect the concentration of CO_2 in the atmosphere, subsequently influencing how the overall climate system will respond to anthropogenic emissions (Wenzel et al., 2014; Arora et al., 2013; Hansen and Takahashi, 1984). This response depends on feedbacks associated with the carbon cycle under the perturbation from an increased CO_2 concentration as well as the subsequent changes in climate, and is the cause of much of the associated importance and uncertainty of the carbon cycle.

Friedlingstein et al. (2003, 2006) defines the feedbacks of the carbon cycle to climate change through two parameters to help quantify the overall magnitude, these are known as the carbon-concentration (β) and carbon-climate (γ) feedbacks. The future change in land carbon storage (ΔC_L) is linearly approximated as the contribution from both increased CO_2 concentrations (ΔCO_2) and global warming (ΔT), as shown by Equation 1.1. This linear feedback approach is commonly used in model analysis studies which aim to understand the temporal evolution of the land carbon sink (Arora et al., 2020, 2013).

$$\Delta C_L = \beta_L \Delta CO_2 + \gamma_L \Delta T \tag{1.1}$$

The land carbon-concentration feedback (β_L) represents the response of the carbon cycle to an increased atmospheric CO_2 concentration, and is defined as a direct biogeochemical response describing the ability of the land surface to absorb CO_2 from the atmosphere. On a decadal timescale, the land surface is known to absorb approximately a third of anthropogenic emissions of CO_2 (Friedling-

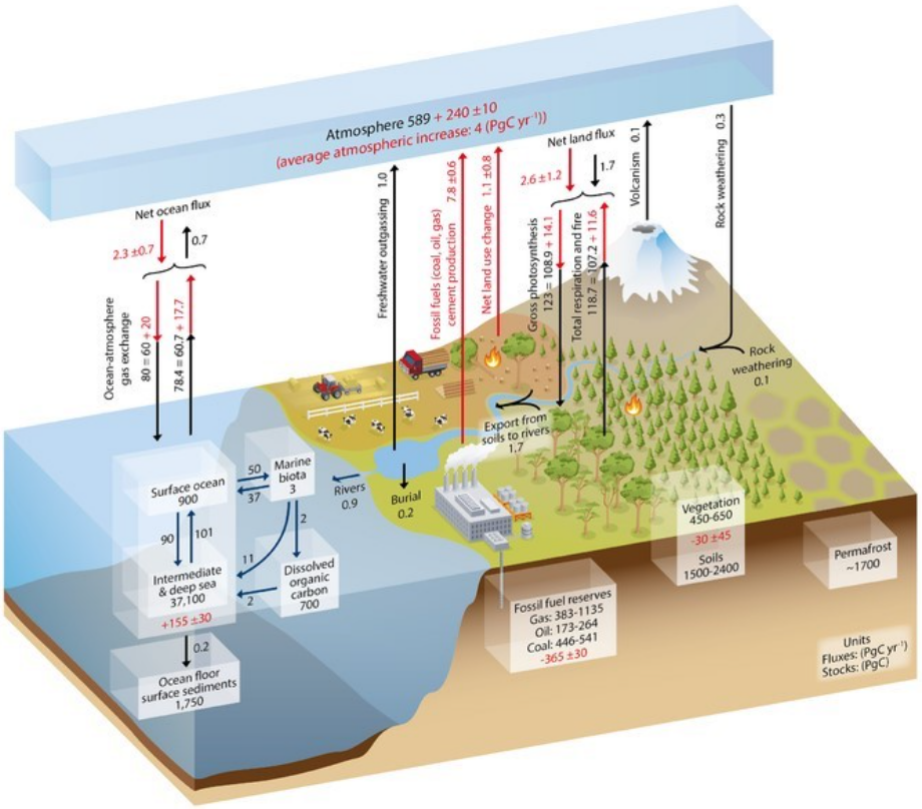

Figure 1.1: Schematic of the carbon cycle taken from the IPCC AR5 Chapter 6, 'Carbon and Other Biogeochemical Cycles', Ciais et al. (2013). The diagram shows global carbon pools in units of PgC and carbon fluxes in units of PgC yr^{-1}.

stein et al., 2020, 2019; Le Quéré et al., 2018), which is a result of plants taking in CO_2 during photosynthesis (seen in Figure 1.1). The carbon-concentration feedback refers to an in increased productivity from plants under climate change due to the increased concentration of CO_2 in the atmosphere (Schimel et al., 2015; Woodward et al., 1998). This results in more CO_2 being removed from the atmosphere. Conversely, the land carbon-climate feedback (γ_L) represents the response of the carbon cycle to the subsequent changes in climate; for example, increased global temperatures and regional precipitation changes. Unlike the carbon-concentration feedback, the subsequent response of the carbon cycle to climate changes has counteracting impacts. For example, increased temperatures can increase microbial respiration within the soil, which would result in more carbon being released into the atmosphere (Crowther et al., 2016; Davidson and Janssens, 2006). However, increased temperatures in northern latitudes could also result in the northward expansion of boreal forests (Pugh et al., 2018; Krankina et al., 1997), which may increase forest productivity and terrestrial carbon storage in these regions.

Carbon cycle feedbacks are therefore both positive, which results in a further increase to the atmospheric CO_2 concentration and enhances climate change,

and negative, where increased absorption of carbon by the land negates the anthropogenic release of CO_2 into the atmosphere. The uncertainty comes from whether the overall feedback of the carbon cycle to climate change will result in a positive or negative feedback, and whether the overall change in land carbon storage (ΔC_L) will increase or decrease. This is due to the challenges presented when quantifying the two complex and counteracting feedbacks (Arora et al., 2020; Friedlingstein et al., 2014; Arora et al., 2013; Gregory et al., 2009). Understanding and quantifying these feedbacks is critical for calculating an accurate global carbon budget, which is required if Paris agreement targets are to be met (Friedlingstein et al., 2020; Ballantyne et al., 2015). Therefore, reducing the uncertainty in carbon cycle projections is required to inform global and national climate policies (Tian et al., 2015).

Within the terrestrial carbon cycle, the feedback from global soils presents one of the greatest uncertainties in determining the overall response of land carbon storage to CO_2-induced climate change (Bradford et al., 2016; Nishina et al., 2015; Todd-Brown et al., 2014). Global soils represent the largest store of terrestrial carbon in the Earth's climate system, with a magnitude of two to three times the amount of carbon contained within the atmosphere (Canadell et al., 2021; Ciais et al., 2013; Post et al., 1982). A large proportion of soil carbon stocks are found in the northern latitudes, where much of the carbon stored in these soil is held within permafrost (Jackson et al., 2017; Jobbágy and Jackson, 2000). This can be seen in Figure 1.1, where the IPCC diagram estimates an additional 1700 PgC within permafrost. This is on top of the estimated 1500-2400 PgC found in non-frozen soils globally.

The carbon fluxes between the soil and atmosphere are sensitive to changes in climate, which will result in soil carbon driven feedbacks to climate change. The large quantities of carbon present in global soils indicate that a relatively small release of this carbon into the atmosphere could result in a significant positive feedback to climate change (Bradford et al., 2016). Additionally, permafrost is known to be particularly sensitive to climate change, and permafrost thaw under climate change has the potential to release significant amounts of carbon into the atmosphere over a short period of time with increased warming (Hugelius et al., 2020; Burke et al., 2017; Schuur et al., 2015; Zimov et al., 2006), representing a significant feedback within the climate system.

The overall effect of climate change on soil carbon is not very well understood and constrained due to competing soil carbon feedbacks (Todd-Brown et al., 2014). Consequently, there exists high uncertainty in the magnitude of future soil carbon

change, and the potential release of carbon from the soil. Quantifying this feedback is of particular significance as potential carbon release from soils implies the possibility of the terrestrial carbon sink becoming a carbon source during the 21$^{\mathrm{st}}$ century, which would accelerate climate change (Crowther et al., 2016; Cox et al., 2000).

1.2 The soil carbon response to climate change

Both observational and model based studies have aimed to quantify and predict the response of soil carbon to future changes in the Earth system (Crowther et al., 2016; Nishina et al., 2015; Todd-Brown et al., 2014; Knorr et al., 2005), however these studies typically highlight the magnitude of the uncertainty surrounding future soil carbon change (Van Gestel et al., 2018; Gregory et al., 2009). For example, Todd-Brown et al. (2014) found projections amongst CMIP5 ESMs of future changes in soil carbon stocks ranged from a loss of 72 PgC to a gain of 253 PgC by the end of the 21$^{\mathrm{st}}$ century. The majority of this uncertainty is due to counteracting effects of CO_2-induced climate change on soil carbon storage, such as soil carbon driven carbon-concentration and carbon-climate feedbacks (Medlyn et al., 2000).

One way to isolate the sources of this uncertainty is to investigate the individual processes that influence soil carbon stocks. Without climate change, the uptake of carbon by soils is in a long-term balance with carbon losses, keeping the overall amount of carbon stored in the soil in a steady state. The net change in soil carbon stocks under climate change will be determined by changes in both input and output fluxes of carbon to and from the soil, and therefore is dependent on the sensitivity of these fluxes to changes in climate and CO_2. The main input into the soil is known as litterfall and refers to the dead organic material, mainly from vegetation, that falls to the land surface and adds organic carbon to the soil (SOC). The main output flux is known as heterotrophic respiration (R_h), which refers to the breakdown of this organic carbon by microbes within the soil.

The main causes of future soil carbon uncertainty is understanding and quantifying how the input flux of carbon, the output flux of carbon, and how long carbon resides in the soil will change under climate change (Todd-Brown et al., 2014). The underlying processes which control these responses determine the subsequent soil carbon carbon-concentration and carbon-climate feedbacks, and the overall response of soil carbon to climate change.

1.2.1 The response of carbon input to the soil

The primary input of carbon to the soil is from vegetation, and therefore soil carbon is influenced by the response of vegetation to CO_2-induced climate change. The uptake of carbon by vegetation is generally expected to increase with increased atmospheric CO_2 concentrations (Anav et al., 2013), where this increased vegetation productivity is known as the CO_2 fertilisation effect (Schimel et al., 2015; Woodward et al., 1998; Cao and Woodward, 1998). This effect controls the direct carbon-concentration feedback which leads to increased photosynthesis under increased atmospheric CO_2 concentrations and can be quantified using Net Primary Productivity (NPP, Π_N), defined as the net rate of accumulation of carbon by vegetation arising from photosynthesis minus the loss from plant respiratory fluxes. The CO_2 fertilisation effect has been seen in both models studies (Todd-Brown et al., 2014; Matthews et al., 2005) and empirical experiments, such as in Free-Air CO_2 Enrichment (FACE) experiments (De Kauwe et al., 2016; Piao et al., 2013).

Despite this qualitative agreement, the magnitude of CO_2 fertilisation is greatly debated. Todd-Brown et al. (2014) found projected increases of global NPP in CMIP5 ESMs to be between 11% and 59% over the 21$^{\text{st}}$ century. One key cause of uncertainty has been the neglect of nutrient limitations (primarily nitrogen and phosphorus) in models up to the CMIP5 model generation. Nutrient availability is expected to constrain the increase in NPP with CO_2, resulting in a likely reduction in the projected land carbon sink (Wieder et al., 2015b; Zaehle et al., 2010; Thornton et al., 2009). Wieder et al. (2015b) found that the nutrients required for the projected increases in NPP exceeds the estimated nutrient supply, which suggests unrealistically high projected productivity increases. They suggested that solely accounting for nitrogen limitation would lower the expected end of century change in NPP by 19%. Additionally, FACE field experiments have shown that the NPP increase drops after 5 years of sustained CO_2 increase, which is likely due to nitrogen availability limitations on CO_2 fertilisation (Norby et al., 2010).

On top of the direct feedback from increased atmospheric CO_2, there are additional indirect responses affecting the potential input of carbon to the soil. The response of NPP to changes in climate is spatially variable, where Nishina et al. (2015) states that the dominant source of uncertainty for changes in NPP varies along climatic gradients. For example, the rate of atmospheric temperature increase is greatest in the northern latitudes (Soong et al., 2020; Serreze and Barry, 2011), where the increased temperatures seen in these regions can result in an increased length of the growing season enabling more plant growth and increasing annual NPP (Forkel et al., 2016; Graven et al., 2013; Reichstein et al.,

2013; Peñuelas and Filella, 2001). Additionally, the increased temperatures in the northern latitudes could result in the northward expansion of boreal forests, which would also increase NPP in these regions as a result of increased forest productivity (Pugh et al., 2018; Krankina et al., 1997).

Conversely, future changes to precipitation patterns could reduce NPP in specific regions. This is particularly relevant in tropical regions, where climate change induced drought could limit the projected NPP increase (Phillips et al., 2009; Betts et al., 2004). Green et al. (2019) state the significance of soil moisture for potential land carbon uptake, where a reduction in soil moisture can induce vegetation mortality through water stress and increased fire frequency. The reduction in NPP due to moisture limitations are not found to be negated by the converse increases in soil moisture in other regions; for example, extreme increases in soil moisture can result in the formation of bogs, which also results in a NPP reduction. Long-term changes to soil moisture can also result in the transition of an ecosystem to a different vegetation type; for example, a transition of a forest to a grassland after forest dieback (McDowell and Allen, 2015; Cox et al., 2004), which would have a long-term affect on the input of litter to the soil.

Uncertainties surrounding the magnitude of the CO_2 fertilisation effect and future climate impacts leads to uncertainty in the response of soil carbon to climate change. Additionally, human-induced disturbance can also affect the litterfall carbon and therefore store of carbon in the soil (Nyawira et al., 2017; Anav et al., 2013), where Brovkin et al. (2013) found that land-use change within CMIP5 ESMs resulted in a reduced land carbon storage of 25 to 205 PgC, when compared to simulations with no land-use change. Changes in terrestrial disturbance, such as increased fire frequency under climate change, will also affect the vegetation litter under climate change and future soil carbon storage (Davidson and Janssens, 2006). The fraction of litter carbon that will end up within long-term soil carbon stocks is also debated (Van Groenigen et al., 2014; Todd-Brown et al., 2014). The allocation of carbon into soil carbon pools is uncertain, and whether this will change under increased litter input is an additional complication (Schmidt et al., 2011). The potential of increased soil carbon storage has been suggested by empirical studies, where increases have been seen in surface soil carbon (Lichter et al., 2008; Jastrow et al., 2005). Though the same increases have not been seen in deeper soils, suggesting the possibility of increased carbon only entering faster, short-term turnover pools. The sequestration of carbon in soils has more recently been discussed as a climate mitigation tool (Bossio et al., 2020; Amundson and Biardeau, 2018), however this is subject to similar uncertainties and it requires a greater understanding of the long-term storage of soil carbon

and pool allocation.

1.2.2 The response of carbon output from the soil

To investigate the sensitivity of carbon output from global soils under climate change, studies involve either a direct focus on soil or heterotrophic respiration, or a focus on the carbon turnover in the soil (τ_s). The term soil respiration is often used as a collective term to include below-ground plant respiration from roots together with the microbially-induced heterotrophic respiration (Davidson and Janssens, 2006). Soil carbon turnover time represents the time it takes for carbon to be transferred from the atmosphere into the soil and back to the atmosphere, and can be defined as the ratio of soil carbon stocks to the carbon output flux (Koven et al., 2017; Carvalhais et al., 2014). Therefore, a change to the carbon output flux alone will have an effect on the carbon turnover time (Jones et al., 2005), and can also be used to investigate the release of carbon from soils under climate change.

The main control of carbon output from the soil is from the process of microbial decomposition of carbon stored, however this is known to be controlled by multiple processes (Schmidt et al., 2011; Davidson and Janssens, 2006). Microbial decomposition is fundamentally a chemical reaction, so is naturally dependent on temperature (Davidson and Janssens, 2006), implying that a change in temperature can drive a change in the rate of release of CO_2 from the soil to the atmosphere. Increased global temperatures allow microbes contained within the soil to be more active, which increases the rate at which they can decompose carbon in the soil and increases the output of carbon via heterotrophic respiration (Crowther et al., 2019). Therefore, an increased rate of respiration in the soil is expected with global warming and has been evaluated in many experimental studies investigating the sensitivity of decomposition to temperature (Hartley and Ineson, 2008; Sanderman et al., 2003; Dalias et al., 2001; Holland et al., 2000; Kätterer et al., 1998; Lloyd and Taylor, 1994; Jenkinson and Ayanaba, 1977).

Further evidence for temperature being a dominant control on soil carbon dynamics can be seen from investigating spatial turnover times of soil carbon on Earth. Trumbore et al. (1996) investigated soil carbon at various experimental sites at differing altitudes and found that slower turnover times are found in colder regions compared with faster turnover times in warmer regions. Additionally, soil is known to be spatially heterogeneous and the magnitude of carbon stored within soils varies significantly across the globe (Koven et al., 2017). The northern latitudes are associated with cold temperatures and large soil carbon stocks, with long turnover times of up to thousands of years (Jackson et al., 2017). However,

the tropical regions are associated with warmer temperature and lower soil carbon stocks, with fast turnover times of only a few years. One limitation in experiments involving turnover times of soil carbon is often the relatively short experimental timescales compared with longer soil carbon pools, which limits the understanding of the soil carbon response in these regions (Davidson and Janssens, 2006).

Furthermore, the amount of moisture in the soil has a control on decomposition rates and is also critical to determine the response of heterotrophic respiration to changes in climate. The impact of soil moisture on decomposition has been shown to vary between ESM projections and is a subject of ongoing debate. Todd-Brown et al. (2014) deduced that soil moisture is not a primary driver of changes in soil carbon decomposition at a global scale in CMIP5 ESMs, whereas Exbrayat et al. (2013a) deduced that future changes in ESMs are sensitive and dependent on the choice of moisture function. This is likely to be due to more uncertain regional changes. The impact of soil moisture changes on regional soil carbon is associated with increased uncertainty due to uncertainties in predictions of regional moisture changes, which are less well known compared to temperature changes (Falloon et al., 2011). The sensitivity to moisture may also be dependent on temperature, where models and observations are found to differ in regions with the most extreme temperature and moisture values (Sierra et al., 2015).

This uncertainty is reflected in both empirical and modelling studies aiming to quantify increased soil carbon loss under climate change. Disagreement is found in the magnitude of increased heterotrophic respiration under climate change amongst ESMs, where Todd-Brown et al. (2014) found that the percentage increase seen in modelled heterotrophic respiration ranges from 16.9% to 58.3% by the end of the 21$^{\text{st}}$ century in CMIP5 ESMs, which relates to significant differences in the changes to soil carbon stocks. Empirical studies such as Crowther et al. (2016) have attempted to quantify the carbon loss from global soils under global warming. This was done by assessing data from 49 field experiments, where an empirical relationship dependent on initial soil carbon stocks was derived and extrapolated to predict the loss of carbon. A carbon loss of 30 ± 30 PgC to 203 ± 161 PgC from the top 10cm of soil under one degree of global warming was estimated, where the result was found to be dependant on the timescale of the response. However, Van Gestel et al. (2018) stated a limiting factor of this study is the number of field experiments within northern latitude regions, where an under representation of the northern latitudes could lead to an under estimation of the loss of carbon from soils due to the significant magnitudes of soil carbon found in these regions (Jackson et al., 2017; Schädel et al., 2016; Schuur et al., 2015).

More recent insights into soil carbon cycling suggest that there are additional, complex processes influencing soil decomposition that are yet to be fully understood (Schmidt et al., 2011), which adds to the uncertainty in the extent and timescale of future soil carbon change (Bradford et al., 2016; Cramer et al., 2001). The rate of decomposition is dependent on chemical, biological and environmental conditions, which vary between different ecosystems on Earth. This results in multiple processes which directly and indirectly control decomposition rates (Davidson and Janssens, 2006; Schmidt et al., 2011). Soils vary both geographically and with depth, and contain thousands of different carbon compounds. Similarly to in plants, microbial decomposition requires minerals such as nitrogen. Depending on the ratio of carbon to nitrogen within the soil, microbes can either immobilise nitrogen by taking inorganic nitrogen from litter, or mineralise nitrogen by decomposing organic nitrogen within the soil. Soil warming could accelerate nutrient mineralisation due to increased microbial activity resulting in the breakdown of plant litter, which could result in a liberation of nitrogen and alleviate the nutrient limitation in plants (Todd-Brown et al., 2014; Bai et al., 2013; Peng et al., 2011; Zaehle et al., 2010; Thornton et al., 2009; Dalias et al., 2001; Rustad et al., 2001). Additionally, soil micro-organisms represent diverse biological communities, which are known to have varying impacts on carbon cycling within the soil (Crowther et al., 2019). Associated processes such as priming, have been suggested by empirical evidence showing an accelerated rate of decomposition due to increased plant carbon inputs to the soil under elevated CO_2 (Georgiou et al., 2015; Bader et al., 2013). Moreover, the complex process of aggregate formation, could stabilise carbon stored within soils and result in a reduced rate of decomposition (Todd-Brown et al., 2014; Six et al., 2002).

1.3 Mathematical modelling of soil carbon

The fate of soil carbon stocks under climate change is associated with uncertainty due to effects from multiple complex and interacting processes which must be considered and quantified. Despite this, soil carbon has historically been modelled using first-order biogeochemical models, which greatly simplify these complicated processes (Manzoni et al., 2009). Figure 1.2 presents a schematic of the terrestrial carbon cycle processes included in an ESM, taken from Bonan (2008), where the transfer of carbon from the atmosphere and to the land surface is illustrated.

A change in soil carbon (dC_s/dt) is determined by the difference between the input from vegetation (litterfall, Λ) and the output heterotrophic respiration (R_h), as

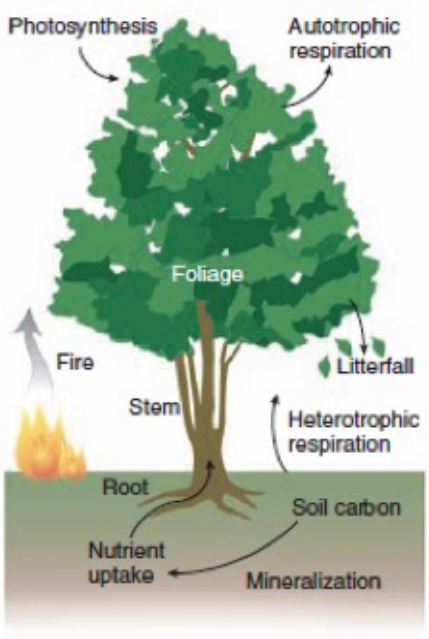

Figure 1.2: A screenshot taken from Figure 2 in Bonan (2008). The schematic shows the biosphere and atmosphere interactions involved in the carbon cycle which are simulated within ESMs.

shown by Equation 1.2.

$$\frac{dC_s}{dt} = \Lambda - R_h \tag{1.2}$$

Biogeochemical models aim to quantify R_h, the respired CO_2 from the soil to the atmosphere, and its response to climate change. Within first-order linear biogeochemical models, the respiration rate (R_h) is often mathematically defined in the form of Equation 1.3, where i represents different carbon pools. $R_{h,i}$ is dependent on the decay rate (k_i), the function defining the sensitivity of decomposition to soil moisture ($f_W(\theta_s)$), the function defining the sensitivity of decomposition to soil temperature ($f_T(T_s)$), and depends linearly on the mass of soil carbon in the pool ($C_{s,i}$). Within models, the different defined carbon pools will then have different k values which control the rate of decomposition of that pool, depending on a defined resistance to decomposition.

$$R_{h,i} = k_i \cdot f_W(\theta_s) \cdot f_T(T_s) \cdot C_{s,i} \tag{1.3}$$

The function representing the temperature sensitivity of soil respiration ($f_T(T_s)$) is often modelled using an exponential dependence of specific respiration rate on temperature, such as a Q_{10} or Arrhenius relationship, where both relationships are based on empirical data in the absence of an effect due to soil moisture (Todd-

Brown et al., 2013; Kätterer et al., 1998; Lloyd and Taylor, 1994). These relationships are widely used as a measure of the temperature sensitivity of chemical or biological processes, such as decomposition within soil (Mundim et al., 2020; Davidson and Janssens, 2006). The modelled q_{10} factors within ESMs have been found to be consistent with the observed distribution found in the literature, which suggest values between 1.4 and 2.2 (Todd-Brown et al., 2018; Mahecha et al., 2010; Davidson and Janssens, 2006). Examples of the modelled behaviour of the sensitivity of decomposition to temperature is shown in Figure 1.3(b), which is taken from Exbrayat et al. (2013a). Figure 1.3(b) compares the temperature functions for respiration used in three models: CASA-CNP (Wang et al., 2011, 2010), K1995 (Kirschbaum, 1995), and PnET (Aber et al., 1997). Exponential relationships are seen between temperature and decomposition in the models CASA-CNP and PnET, however a limit to the increase in decomposition is seen in the K1995 model at 37°C, where the decomposition rate decreases above some optimal temperature (Exbrayat et al., 2013a).

Similarly, the sensitivity to moisture ($f_W(\theta_s)$) is typically modelled using a first-order process which relates the rate of decay to the quantity of soil carbon (Exbrayat et al., 2013a; Todd-Brown et al., 2013). The effect of moisture on soil decomposition dynamics is often assumed to be a linear relationship, where soil respiration is linearly related to water content up until a certain moisture content is reached (Cook and Orchard, 2008; Orchard and Cook, 1983). Figure 1.3(a) (again taken from Exbrayat et al. (2013a)) compares the representation of the sensitivity of decomposition to soil moisture in three models: CASA-CNP (Wang et al., 2011, 2010), SOILN (Jansson and Berg, 1985) and TRIFFID (Cox, 2001). The three models show a similar pattern, where decomposition in the soil is shown to increase with moisture up until a volumetric soil moisture concentration of approximately $\theta = 0.6$, above which the rate of decomposition then decreases. However, the shape of the function is shown to differ between the models.

Biogeochemical models represent carbon in both the litter and soil using separate 'carbon pools', which are used to represent differing sensitivities to decomposition, and then the overall rate of R_h is dependent on the decomposition rates of these individual pools (Exbrayat et al., 2013a; Clark et al., 2011). Giardina and Ryan (2000) presented evidence from laboratory experiments showing that soil decomposition does not depend on temperature, however since this study it has been argued that the results are based on the assumption of a single homogeneous soil carbon pool (Knorr et al., 2005; Davidson et al., 2000), which is not comparable with the real world. Simple models which consider multiple soil carbon pools with different intrinsic turnover rates have been shown to recreate

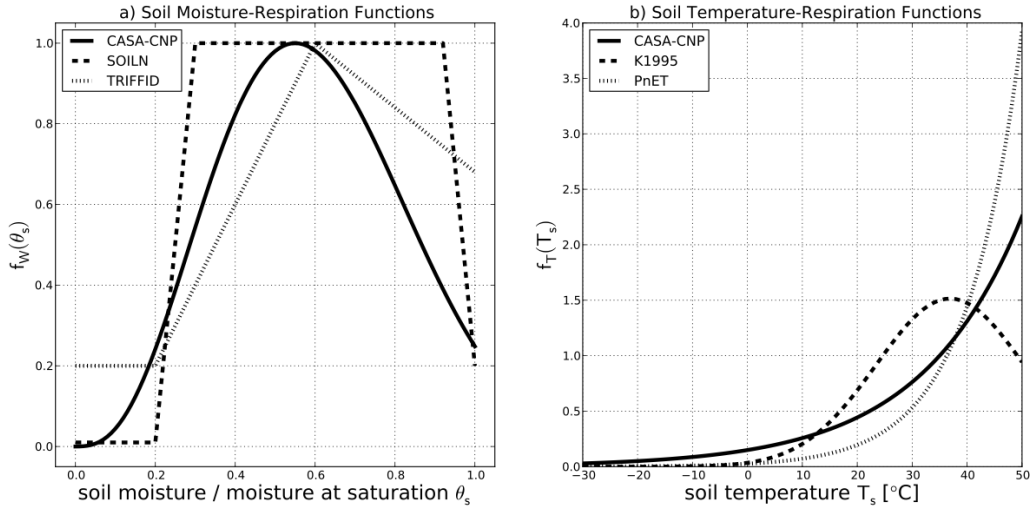

Figure 1.3: Taken from Exbrayat et al. (2013a), where different functions for the sensitivity of decomposition within the soil to temperature ($f_T(T_s)$) and moisture ($f_W(\theta_s)$) are plotted using the Carnegie–Ames–Stanford Approach with a Carbon–Nitrogen–Phosphorus (CASA-CNP) model (Wang et al., 2010) coupled with the Community Atmosphere Biosphere Land Exchange (CABLE) land surface model (Wang et al., 2011).

results seen in experimental data, where rapid depletion of labile carbon stocks is seen and negligible depletion of non-labile soil carbon within the experimental timescales (Knorr et al., 2005). This has identified the importance of the representation of differing turnover times in models (Hartley and Ineson, 2008), which has been shown to be especially significant for slow carbon pools (Jones et al., 2005).

Since early decomposition models, the allocation into different carbon pools has often been dependent on the molecular structure of the litter. Early examples of soil carbon models are the grass and agroecosystems dynamic model (CENTURY; Parton et al. (1988)) and the Rothamsted carbon model (ROTH-C; Jenkinson et al. (1991)). Updated variants of these models are still widely used to represent soil carbon decomposition in modern ESMs (Arora et al., 2020; Todd-Brown et al., 2018). Both models allocate litter into two distinct pools which represent carbon readily available for decomposition and carbon which is more resistant: (1) liable (metabolic in CENTURY and DPM in ROTH-C) and (2) resistant (structural in CENTURY and RPM in ROTH-C). However, in the CENTURY model allocation is based on the chemical composition of the litter, where it is dependent on the lignin-to-nitrogen ratio (Parton et al., 1988), whereas in the ROTH-C model allocation is based on specified ratios which depend on the vegetation type within biomes (Jenkinson et al., 1991; Clark et al., 2011). Soil organic carbon (SOC) is then also stored within multiple carbon pools, similarly based on the long-term stability of the carbon. For example, the CENTURY model has 3 pools with in-

creasing turnover times; i.e. fast, medium, and slow (Parton et al., 1988). The rate of decomposition in ESMs is also often dependent on a clay content fraction, which is known to be an important determinant of the stability of SOC (Wei et al., 2014; Wiltshire et al., 2021). The clay content in models is often used as a proxy for the influence of mineral stabilisation on carbon within the soil (Todd-Brown et al., 2014; Schmidt et al., 2011; Six et al., 2002).

In more recent years, new insights into the way soil carbon exists in the real world suggests this differs from the way soil carbon has been historically modelled. Despite the importance of the chemical composition of litter in predicting future soil carbon stocks, without more realistic representation of the environmental and biological processes controlling the soil within ecosystems, the long-term stability of soil carbon in the future will continue to be uncertain (Schmidt et al., 2011). These more recent insights into additional processes which control decomposition have now brought into question this simplified view of modelling soil carbon. Biogeochemical models use molecular structure of the litter to determine the rate of decomposition, as this controls the allocation of carbon into soil carbon pools. However, despite this being likely to be a more valid assumption for an initial decomposition rate, it is now thought that additional factors affect the long-term decomposition rate (Schmidt et al., 2011). Schmidt et al. (2011) identify the importance of additional processes controlling soil decomposition rates and highlight the need to include these processes within future generations of soil carbon models. The different types of litter are discussed and how the derivation of the litter influences the long-term storage in the soil; for example, litter derived from roots is more resistant to decomposition than the above-ground input from leaves.

Additionally, the link between ecosystem dynamics and micro-organisms has been a recent focus for soil carbon models (Chadburn et al., 2020; Walker et al., 2018; Wieder et al., 2015a), where the direct role of microbes on decomposition has historically been ignored within land surface modelling. It was thought that due to the long turnover times of soil carbon, with one of the longest time scales in the terrestrial carbon cycle (up to thousands of years), compared to very short turnovers of microbes within the soil (time frame of days), the affect of microbial communities would not be significant on the long-term soil carbon response (Blyth et al., 2021). Additionally, due to the nature of microbial communities varying geographically, for example differing communities in tropical regions and high latitudes, environmental conditions have been used as a proxy within modelling for variations in soil microbial communities (Crowther et al., 2019). However, new insights suggest climate can influence soil carbon cycling through changes in both metabolic activity and community structure (Wieder et al., 2015a; Schmidt et al.,

2011). Xenakis and Williams (2014) compare decomposition rates using two model structures: one with standard first-order kinetics and one which includes functional microbial activity, where differing responses were found to warming and increased carbon input from litter. More recent studies have focused on improving the representation of microbial dynamics by including this effect in future generations of soil carbon models (Wieder et al., 2013; Conant et al., 2011; Neill and Gignoux, 2006; Pendall et al., 2004), however progress needs to be made on the inclusion into ESMs. This would also lead to the representation of missing processes, such as biological priming, which is not currently explicitly represented (Koven et al., 2015).

In more recent years, progress has been made on the inclusion of interactive nitrogen on soil carbon cycling within models, where this is now commonly represented in CMIP6 ESMs (Davies-Barnard et al., 2020). The availability of nitrogen is necessary for soil carbon to be decomposed, and within a biogeochemical model the simulation of interactive nitrogen allows the amount of nitrogen present to change by flowing between soil pools, as with soil carbon, opposed to being a set fraction. For example, in the UK land surface model JULES-CN, which includes a coupled terrestrial carbon–nitrogen scheme, nitrogen (N) has four pools, two equivalent to the litter pools and two equivalent to the SOC pools following the structure of the ROTH-C model (Jenkinson et al., 1991; Wiltshire et al., 2021). Nitrogen is transferred from the litter pools to the SOC pools by immobilisation of inorganic nitrogen to organic nitrogen, and then is released from the soil from mineralisation of organic nitrogen to inorganic, which then makes it available for plant uptake (see Figure 1.2).

$$R_{h,i} = k_i \cdot f_W(\theta_s) \cdot f_T(T_s) \cdot C_{s,i} \cdot f_N \tag{1.4}$$

To include a limitation of nitrogen content on respiration, an additional function (f_N) is used to modify the decomposition rate ($R_{h,i}$). The function f_N is dependent on the ratio of the nitrogen available in the soil to the nitrogen required by microbes for decomposition. This additional function controlling decomposition rates is shown by Equation 1.4, compared to Equation 1.3 with no nutrient limitations. Therefore, if decomposition is nitrogen limited within models, it represents an insufficient quantity of nitrogen available for microbes to decompose the litter to SOC (Wiltshire et al., 2021). Additional processes, such as interactive nitrogen, are required to be represented within biogeochemical models to reduce the long-term uncertainty in soil carbon stability under climate change.

1.4 New generation of Earth System Models

Reducing the uncertainty in the soil carbon response to climate change and predicting how stocks will change in the future has been identified as an important area of current climate research. The uncertainty is a result of difficulties in the representation of related processes within models and limitations to empirical experiments. Significant variations in future projections of the soil carbon responses to climate change are also partly a result of an inconsistent representation of carbon cycle parameters amongst ESMs (Bradford et al., 2016; Nishina et al., 2014; Arora et al., 2013).

The Coupled-Model Intercomparison Project (CMIP) was established to create a common framework for multi-model evaluation (Meehl et al., 2000), where previous generations are known as CMIP5 (Taylor et al., 2012) and CMIP3 (Meehl et al., 2007). CMIP is now in phase 6, known as CMIP6 (Eyring et al., 2016; Meehl et al., 2014), which is the ensemble of ESMs used in the most recent Intergovernmental Panel on Climate Change (IPCC) report (AR6) (IPCC, 2021a). CMIP provides consistent climate variables and climate scenarios which enable modelling centres to complete comparable simulations, and allows for multi-model evaluation of models within CMIP generations. Specific projects such as Coupled Climate-Carbon Cycle Model Intercomparison Project (C4MIP), have a specific focus on understanding and quantifying future changes in the global carbon cycle, and the potential feedbacks on the climate system (Jones et al., 2016). Multi-model evaluation can help reveal key differences between models and empirical data which can help address some uncertainty; critically assessing and improving ESMs is required to help improve our knowledge of future climate change.

As new generations of models are developed, the aim is to improve the representation of climate system processes. This includes making improvements to the representation of soil carbon in biogeochemical models in order to help reduce the uncertainty related to future projections of soil carbon. However, the uncertainty due to the soil carbon feedback did not reduce significantly between the CMIP3 and CMIP5 model generations (Knutti and Sedláček, 2013). To date, limited studies have investigated the response of soil carbon in the CMIP6 models. Therefore, a robust and in-depth evaluation of soil carbon and the related processes that control the input and output fluxes in the most up-to-date ESMs within CMIP6 is required to help identify areas for future research. Identifying areas for future research, specifically key areas for future model development, is a useful step towards reducing uncertainty in future climate change projections.

1.5 Emergent constraints

A key method to reduce uncertainty in future climate change projections is through observational constraints. A specific recent variant of this general approach, called 'Emergent Constraints' (sometimes referred to as ECs), aims to reduce uncertainty in climate change projections by identifying relationships between uncertain future changes and observable trends or variability, which are evident across an ensemble of models. This technique was first used by Hall and Qu (2006), who used a relationship deduced from an ESM ensemble to constrain the future snow albedo feedback to climate change using the present day observable seasonal cycle. Since this study, emergent constraints have successfully been used to evaluate ESMs in CMIP5 (Cox et al., 2018; Wenzel et al., 2014; Qu and Hall, 2007) and are now being used for CMIP6 (Nijsse et al., 2020; Thackeray et al., 2021).

The technique requires two main criteria for the possibility of an emergent constraint. Firstly, it relies on a strong statistical relationship existing between an aspect of the current climate and an aspect of the future climate, across the ensemble of models, such as a CMIP ensemble. Secondly, observational measurements on the aspect of the current climate, where the uncertainty is less than the uncertainty from the projected model spread in the ensemble. If these conditions hold, then uncertainty in future climate projections can be reduced by defining a 'constraint' on a specific, measurable climate variable (Hall et al., 2019; Eyring et al., 2019). This is discussed in more detail below.

1.5.1 The concept of emergent constraints

The premise of an emergent constraint is to use a trend or variation that can be measured in the real world, to help constrain a future response of the Earth system that cannot be measured but would like to predict. For this to be possible, a relationship between the observable trend/variation and the uncertain future response is required - called an *emergent relationship*. Emergent relationships are typically derived from a model ensemble, and when combined with an observation of the trend/variation it is possible to define an *emergent constraint* on the future response.

The concept can be further explained using Figure 1.4, which has been taken from Eyring et al. (2019). The idea is there exists an 'Earth system sensitivity', which is simply how sensitive an aspect of the Earth system (such as soil carbon) is to climate change. This is shown on the y-axis of the figure and is unknown in the real world. Each ESM projects a sensitivity, which is shown by the blue

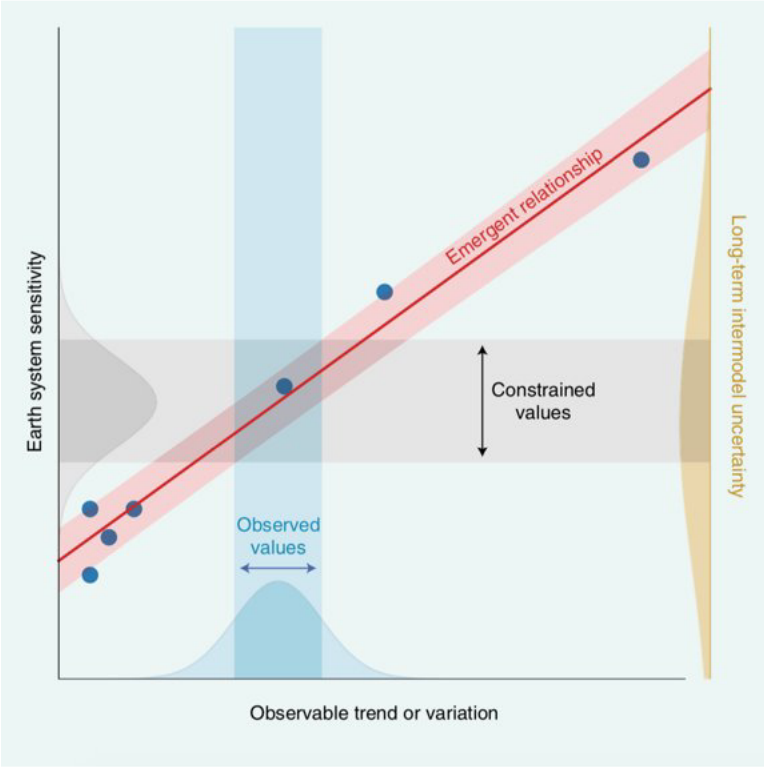

Figure 1.4: Schematic illustrating the concept of emergent constraints taken from Eyring et al. (2019).

dots on the figure. As the future sensitivity is unknown, each future ESM projection is seen to have an equal possibility of being the actual future Earth system sensitivity. If each ESM projects a different sensitivity, it can result in a 'Long-term intermodel uncertainty', which is represented by the yellow distribution on the right-hand side of the figure. This is a result of a large range of projections of an Earth system sensitivity seen across a model ensemble. The premise of an emergent constraint is the aim to reduce this uncertainty by relating the unknown Earth system sensitivity variable to an 'Observable trend or variation'. This is shown on the x-axis of the figure and is measurable in the real world.

In order to do this, relationships between the sensitivity (y-axis) and trends or variations (x-axis) based on a fundamental understanding of the Earth system are considered. This relationship is shown by the red line between the x and y axis on the figure, labelled 'Emergent relationship'. If such a relationship emerges from the model ensemble, meaning the relationship becomes apparent when considering all the ESMs within the ensemble, this relationship can be used together with real world measured values of the x-axis variable - the observable trend or variation - to find a reduced range of projections of the Earth system sensitivity. This assumes that the uncertainty of the measurable observed values, shown on the figure by the blue distribution, is less than the spread in the model predicted x-axis values (blue markers). It is also required for the success of an

emergent constraint, that the uncertainty on the observational values (blue distribution) combined with the uncertainty surrounding the emergent relationship (red distribution), are less then the uncertainty associated with the long-term intermodel uncertainty (yellow distribution). If these conditions hold, a reduction in the long-term model uncertainty can be obtained, which is shown on the figure by the grey distribution of 'Constrained values' (Hall et al., 2019).

1.5.2 Existing emergent constraints on the carbon cycle

The emergent constraint technique has been successfully used to find constraints on aspects of climate change within the Earth system across model ensembles. Hall et al. (2019) provided a table of all existing emergent constraints from CMIP5 and CMIP3 published at the time of the study (see Table 1 in Hall et al. (2019)). The most commonly constrained Earth system sensitivity is 'equilibrium climate sensitivity', which is a measure of the warming to the Earth's climate under a given CO_2 concentration. However, more recently emergent constraints have been used to successfully constrain uncertainties related to terrestrial carbon cycle responses to climate change (Cox, 2019). These carbon cycle emergent constraints presented in Hall et al. (2019) are listed and explained below.

Sensitivity of tropical carbon to climate change constrained by carbon dioxide variability (Cox et al., 2013).

In this study, the emergent constraint technique was used to constrain the uncertain release of carbon from tropical forests. As previously discussed, the future land carbon storage is uncertain due to an unknown magnitude of the net affect from increased carbon input and output as a response to climate change. Tropical forests are thought to be particularly sensitive due to a potential moisture limitation in the future, which could lead to dieback of the forests (Cox et al., 2004). It was found in the study that ESMs disagree on the changes expected in tropical forests, where tropical land carbon storage projections by ESMs range from a loss of 11 PgC to a gain of 319 PgC by the year 2099, adding to the uncertainty surrounding carbon cycle projections under climate change. The emergent constraint was obtained by deducing an emergent relationship from an ensemble of models between the sensitivity of CO_2 interannual variability to tropical temperature anomalies and the sensitivity of tropical land carbon storage to climate change. The use of atmospheric CO_2 and tropical temperature measurements from the real world were used together with the emergent relationship, to constrain the predicted carbon loss in the tropics. This study constrained the carbon loss from the tropics (30°N - 30°S), where a carbon loss of 53 $\pm$ 17 PgC per degree of warming was predicted, as opposed to the 69 $\pm$ 39 PgC per degree of

warming projected by ESMs. The original Cox et al. (2013) study was completed with the C4MIP ensemble of models, but has more recently been shown to hold for the CMIP5 ensemble in Wenzel et al. (2014), where an overlapping carbon loss of 44 $\pm$ 14 PgC per degree of warming was found.

Projected land photosynthesis constrained by changes in the seasonal cycle of atmospheric CO_2 (Wenzel et al., 2016).

Increased plant productivity is expected due to increased rates of land photosynthesis under elevated atmospheric CO_2 concentrations. However, the extent of this increase is uncertain with global projections from ESMs ranging from a 20% to a 60% increase in productivity to a doubling of CO_2. This study presented an emergent constraint on the global CO_2 fertilisation effect by relating the increasing amplitude of the CO_2 seasonal cycle to the magnitude of CO_2 fertilisation effect. The terrestrial Gross Primary Productivity (GPP, a measure of increased plant photosynthesis) is used to represent the magnitude of the CO_2 fertilisation effect. A constraint on GPP increase under a doubling of atmospheric CO_2 concentrations is deduced for different regions. An increase of 37 $\pm$ 9 % was estimated for high latitude ecosystems (60°N – 90°N) and an increase of 32 $\pm$ 9 % was estimated for extra-tropical ecosystems (30°N – 90°N), using respective observational measurements.

An observation-based constraint on permafrost loss as a function of global warming (Chadburn et al., 2017).

This constraint on permafrost loss under global warming was presented as an emergent constraint in the Table of the Hall et al. (2019) study, although it does not use the conventional emergent constraint method introduced by Hall and Qu (2006). Instead, the spatial relationship between temperature and permafrost cover was investigated using observational data. This spatial relationship is said to represent the temperature sensitivity of permafrost and can be used to predict the sensitivity of permafrost to future changes in temperature (ΔT). The validity of this method was investigated by testing whether these permafrost-T relationships in models were able to predict the sensitivity of permafrost to temperature in the future, implying the temperature relationships remain consistent under climate change. Permafrost is stated to cover 15 million km^2 of the land surface and is one of the most sensitive components of the Earth system to warming. Using the observation-based constraint, a sensitivity of permafrost area loss to global mean warming was estimated at $40^{+1.0}_{-1.1}$ km^2 per degree of warming. This derived sensitivity was found to be greater than previous studies, such that the stabilisation of warming at 1.5°C opposed to 2°C would result in a reduced area

of permafrost thaw by approximately 2 million km^2.

1.5.3 Credibility of emergent constraints

Despite this progress and common use of the emergent constraint technique, the robustness and utility have been questioned in the literature (Sanderson et al., 2021; Williamson and Sansom, 2019). One criticism seen regarding emergent constraint research is that a data mining approach could be used to obtain a false emergent constraint (Caldwell et al., 2014). Some climate scientists have argued that if enough Earth system sensitivities were plotted against observable trends and variations, statistically relationships would be found between these variables. However, not all of these relationships will be valid.

Klein and Hall (2015) discusses the use of criteria which can be used to assess the credibility of such emergent constraints, such as categorising emergent constraints. They propose three different categories: (1) potential emergent constraints, where simply a relationship is found between the x and y axis, (2) promising emergent constraints, where the emergent relationship is also based on a physical understanding of the Earth system, and (3) confirmed emergent constraints, where they suggest the need for physical evidence when determining the emergent relationship between Earth system variables. Hall et al. (2019) later suggest a classification of emergent constraints into two categories: (1) proposed emergent constraints, and (2) confirmed emergent constraints. These categories follow a similar premise to those defined in Klein and Hall (2015), where the difference between a proposed and confirmed emergent constraint is a physical or theoretical mechanism behind the statistical relationship. Hall et al. (2019) suggest the categorising of emergent constraints is necessary due to the increasing number being reported in the literature. These categories also highlight the importance of emergent constraints being based on fundamental understanding of the Earth system, where only realistic relationships that are based on theoretical knowledge of the Earth system should be considered.

Moreover, an additional method which would improve the credibility of an emergent constraint is if the constraint exists across different ensembles (Hall et al., 2019). With a finite number of climate models, the best way to achieve this is to investigate emergent constraints across different CMIP generations. For example, testing the emergent constraint in both the CMIP5 and CMIP6 ensembles (Thackeray et al., 2021; Schlund et al., 2020). Sanderson et al. (2021) state that emergent constraints could be found due to common structural assumptions within an ensemble, which implies an improved credibility of a constraint if it remains statistically valid after model improvements in a new generation. However,

it is highlighted that the use of emergent constraints alone to estimate uncertainties in unknown climate projections could potentially lead to unrealistic biases (Sanderson et al., 2021). Overall, emergent constraints provide promise in helping to reduce uncertainty in key projections of climate change. However, appropriate considerations must be taken to ensure valid emergent constraints with a good level of credibility (Hall et al., 2019).

1.6 Concluding remarks

Major uncertainties exist in projections of future soil carbon stocks, and this is of significant importance in determining future climate. Evaluation of the most up-to-date ESMs within CMIP6 and techniques such as emergent constraints, can help reduce uncertainty in future projections of climate change. ESMs are tools to predict future changes to the climate, and evaluation enables us to see what the most up-date models are predicting, as well as helping to identify key areas which require future development. Emergent constraints provide promise for reducing carbon cycle related uncertainty, allowing for a clearer idea of soil carbon change in future. Quantifying future climate change and reducing uncertainty in predictions is required to improve our understanding of how climate change will affect both ecosystems and people on Earth. This in turn increases the chance of successful adaptation and mitigation to climate change.

1.7 Thesis outline

Chapter 2 is an evaluation of soil carbon and related controls in the newest generation of CMIP6 models, as well as the previous generation of CMIP5 models. The evaluation is completed against empirical datasets for global soil carbon, as well as for NPP and soil carbon turnover time. The results from Chapter 2 are published in Varney et al. (2022).

Chapter 3 investigates future projections of soil carbon change in CMIP5 and CMIP6 ESMs. The response is broken down into changes due to increases in NPP and reductions in soil carbon turnover time, to isolate the differing responses influencing changes to future soil carbon storage.

Chapter 4 presents a ‘spatial emergent constraint’. A successful emergent constraint is deduced on the sensitivity of soil carbon turnover to global warming, where present day spatial temperature relationships of soil carbon turnover times are used to constrain the future sensitivity to climatic changes in global temperatures. This spatial emergent constraint is then used to deduce future changes in

soil carbon turnover to differing levels of global warming, reducing the uncertainty surrounding future projections of this response. The results from Chapter 4 are published in Varney et al. (2020).

Chapter 5 introduces the C4MIP simulations in more detail, which allow for the isolation of effects on soil carbon due to changes in atmospheric CO_2 and changes in global temperatures. In this Chapter, soil carbon specific carbon-concentration (β_s) and carbon-climate (γ_s) feedback parameters are defined and evaluated for CMIP6 ESMs.

Chapter 6 sees the analysis of Chapter 3 and Chapter 5 combined, where the individual sensitivities of soil carbon controls (NPP and soil carbon turnover time) to changes in both atmospheric CO_2 and global temperatures are investigated in CMIP6 ESMs.

Finally, Chapter 7 summarises the main findings from the thesis, and highlights the potential future research questions that have arisen from the evaluation and analysis presented in the previous chapters.

Chapter 2

Evaluation of soil carbon simulation in CMIP5 and CMIP6 Earth System Models

Abstract As discussed in Chapter 1, the response of soil carbon (C_s) to CO_2-induced global warming has the potential to provide a significant feedback on climate change, but this feedback is currently poorly known and is associated with uncertainties in Earth System Model (ESM) projections. In order to improve the reliability of future projections of climate change, it is key to realistically represent present-day carbon stores and spatial controls. In this chapter, the representation of late 20^{th} century soil carbon stores and controls via Net Primary Productivity (NPP) and soil carbon turnover time (τ_s), are evaluated in the CMIP5 and CMIP6 generations of ESMs. This chapter is based on a paper published in *Biogeosciences* (Varney et al., 2022).

2.1 Introduction

The latest generation of the Coupled Model Intercomparison Project (CMIP), CMIP6 (Eyring et al., 2016), includes an ensemble of Earth System Models (ESMs), which are used in the most recent Intergovernmental Panel on Climate Change (IPCC) report (AR6) (IPCC, 2021a). The relationships between carbon and environmental drivers used in models help to determine the response of the carbon cycle to climate change (Todd-Brown et al., 2013). Therefore, representing present-day carbon stores and spatial controls realistically within models is key for estimating carbon emission cuts required for Paris agreement targets (Friedlingstein et al., 2020).

Present-day soil carbon can be approximately broken down into above-ground

and below-ground controls, which influence the spatial distribution of soil carbon stocks (Koven et al., 2015). The above-ground control of soil carbon can be considered as the input flux of carbon into the soil from vegetation. Both the amount of carbon from plant and root litter (known as litterfall) and the fraction of this that is converted to longer-lived soil carbon pools will influence the storage of soil carbon. Net Primary Productivity (NPP, Π_N) can be used as a proxy for the litterfall flux, where the fluxes are equal when vegetation is in a steady state. The below-ground control of soil carbon can be quantified simply in terms of the soil carbon turnover time (τ_s), which is defined as the time carbon resides in the soil (Koven et al., 2017; Carvalhais et al., 2014). τ_s can be considered as a proxy for below-ground controls on soil carbon storage (Koven et al., 2015; Todd-Brown et al., 2014, 2013).

In this chapter, the representation of late 20^{th} century soil carbon stores and these related controls (NPP and τ_s) are evaluated in CMIP6 ESMs. Previously, similar studies have been conducted to evaluate soil carbon in the preceding generations of ESMs, for example: Anav et al. (2013) and Todd-Brown et al. (2013) for CMIP5. There are some existing CMIP6 soil carbon related studies; for example, Burke et al. (2020) evaluates the representation of permafrost in models and Ito et al. (2020) investigate future soil carbon stocks under specific land-use conditions. This study is the first to specifically focus on global and spatial soil carbon and related controls in CMIP6, with a thorough evaluation against empirical datasets and comparison against the preceding CMIP5 ensemble.

2.2 Methods

2.2.1 Earth system models

Soil carbon stores and related controls are examined in eleven CMIP6 ESMs (Eyring et al., 2016; Meehl et al., 2014), as listed Table 2.1. Throughout the chapter, comparisons are made with ten ESMs from the previous CMIP generation (CMIP5; Taylor et al. (2012)), as listed in Table 2.2. The ESMs included in this chapter were chosen due to the availability of the required data in the online repository at the time of analysis (https://esgf-node.llnl.gov/search/cmip6/ and https://esgf-node.llnl.gov/search/cmip5/).

Tables 2.1 (CMIP6) and 2.2 (CMIP5) present information about the included ESMs, specifically more details about the associated land surface model (LSM). It should be noted that there are similarities between some of the LSMs within the ESMs - either advances from earlier models or even the same LSM within different ESMs. For example, CESM2 and NorESM2-LM both use the Community Land Model

version 5 (CLM5) (Arora et al., 2020). For some modelling centres, both the CMIP5 and CMIP6 versions of the models are included and in these cases direct comparisons can be made to determine changes from CMIP5 to CMIP6. These generationally related CMIP5 and CMIP6 models are: CanESM2 and CanESM5, CCSM4 and CESM2, GFDL-ESM2G and GDFL-ESM4, IPSL-CM5A-LR and IPSL-CM6A-LR, MIROC-ESM and MIROC-ES2L, MPI-ESM-LR and MPI-ESM1.2-LR, NorESM1-M and NorESM2-LM, and HadGEM2-ES and UKESM1-0-LL, respectively. The models where only either the CMIP5 or CMIP6 version from the modelling centre was included are: BNU-ESM and GISS-E2-R from CMIP5 and ACCESS-ESM1.5, BCC-CSM2-MR and CNRM-ESM2-1 from CMIP6. A key general change to note is that CMIP6 has more models that include an interactive nitrogen cycle compared with CMIP5: ACCESS-ESM1.5, CESM2, MIROC-ES2L, MPI-ESM1.2-LR, NorESM2-LM and UKESM1-0-LL in CMIP6 compared with CCSM4 and NorESM1-M in CMIP5 (the CMIP5 model BNU-ESM includes carbon-nitrogen interactions, however this process was turned off in CMIP5 simulations; Ji et al. (2014)). Additionally, an increased number of soil carbon pools is seen in some CMIP6 models (e.g. CLM5 has 29 carbon pools compared with 20 in CLM4). Arora et al. (2020) include a comprehensive overview of the updates seen in the individual CMIP6 models, which is presented in the 'Model descriptions' section of the associated Appendix.

Todd-Brown et al. (2013) include a summary of the temperature and moisture dependencies of soil respiration/decomposition as assumed in the CMIP5 models (see Table 1 in Todd-Brown et al. (2013)). The most common representation of the temperature sensitivity of decomposition is the Q_{10} equation, which is defined by $f(T) = Q_{10}^{(T-T_0)/10}$, where T is temperature and T_0 is a reference temperature. With the Q_{10} equation, decomposition increases exponentially with temperature (Davidson and Janssens, 2006). The majority of other models within CMIP5 used the Arrhenius equation to represent the temperature sensitivity, where the main difference from the Q_{10} representation is that the rate of decomposition levels off at higher temperature levels (Lloyd and Taylor, 1994). Of the remaining CMIP5 models, the GFDL model simulates an increased rate of decomposition with temperature until some optimal temperature, above which the rate of decomposition decreases (Shevliakova et al., 2009) (which Todd-Brown et al. (2013) defined as a 'hill' function) and the GISS model implement a linear increase of respiration to temperature up to a maximum value (Del Grosso et al., 2005). The representation of the decomposition sensitivity to soil moisture was found to be to be represented in two ways amongst the CMIP5 models, where either decomposition was assumed to increase monotonically with increasing soil moisture, or less commonly to increase to some optimum moisture level and then decrease (again

described as a 'hill' function by Todd-Brown et al. (2013)). In this study, it is found that the representation of temperature and moisture functions remain similar from CMIP5 from CMIP6. The Q_{10} equation remains the most common representation of soil temperature sensitivity in models, followed by the Arrhenius equation and then 'hill' functions. Similarly, the most common representation of the sensitivity of soil to moisture in CMIP6 is a monotonically increasing function, followed by 'hill' functions of various sorts.

2.2.2 Defining soil carbon variables

CMIP defines common output variables (Meehl et al., 2000), which allows for consistent comparison between the models, and for cleaner evaluation of models to observational data. These common output variables also allow for consistent comparison between model generations, in this case between CMIP6 and CMIP5. This chapter focuses on evaluation of near present-day soil carbon and related controls. Therefore, the results presented in this chapter use the CMIP standard historical simulation (CMIP scenario *historical*), for both the CMIP6 and CMIP5 analyses. The historical simulation runs from 1850-2015 in CMIP6 and from 1850-2005 in CMIP5, where the selected dates for each variable (stated below) were chosen to allow for consistent comparison between CMIP5 and CMIP6 and to best match the modelled data to the observational data.

To evaluate soil carbon, this chapter uses 'Soil Carbon' (CMIP variable *cSoil*), which represents the carbon stored in soils, and where applicable 'Litter Carbon' (CMIP variable *cLitter*), which represents carbon stored in the vegetation litter. Total soil carbon (C_s) is defined as the sum of these soil carbon and litter carbon variables (*cSoil* + *cLitter*), where for models that do not report a separate litter carbon pool, the total soil carbon is taken to be simply the *cSoil* variable. This allows for a more consistent comparison between the models and between the models and empirical data due to differences in how soil carbon and litter carbon are simulated (Arora et al., 2020; Todd-Brown et al., 2013). Modelled C_s is time-averaged between the years 1950 to 2000 of the historical simulation and is considered spatially (units of kg m^{-2}) and as global totals (units of PgC), where global totals are calculated as an area-weighted sum using the model land surface fraction (CMIP variable *sftlf*). To calculate northern latitude totals, a sum between the latitudes 60° N and 90° N was considered.

The CMIP6 ESMs CESM2 and NorESM2-LM have two different variables to represent soil carbon: (1) CMIP variable *cSoil*, which represents the full vertical soil profile, and (2) CMIP variable *cSoilAbove1m*, which represents soil carbon in the top 1 m of soil. This is due to the representation of vertically resolved soil carbon

Table 2.1: The 11 CMIP6 Earth System Models included in this chapter, and relevant features of their land carbon cycle components (Arora et al., 2020; Eyring et al., 2016).

Earth System Model	Modelling Centre	Land Surface Model	Nitrogen cycle	No. of live carbon pools	No. of dead carbon pools	Temperature & Moisture	References
ACCESS-ESM1.5	CSIRO	CABLE2.4 + CASA-CNP	Yes	3	6	Arrhenius & Hill	Ziehn et al. (2020), Haverd et al. (2018), Trudinger et al. (2016)
BCC-CSM2-MR	BCC	BCC-AVIM2	No	3	8	Hill & Hill	Wu et al. (2019), Ji et al. (2008)
CanESM5	CCCma	CLASS-CTEM	No	3	2	Q_{10} & Hill	Swart et al. (2019), Melton et al. (2020), Seiler et al. (2021)
CESM2	CESM	CLM5	Yes	22	7	Arrhenius & Increasing	Danabasoglu et al. (2020), Lawrence et al. (2019)
CNRM-ESM2-1	CNRM	ISBA-CTRIP	No	6	7	Q_{10} & Increasing	Séférian et al. (2019), Delire et al. (2020)
GFDL-ESM4	GFDL	LM4.1	No	6	4	Hill & Increasing	Dunne et al. (2020), Zhao et al. (2018)
IPSL-CM6A-LR	IPSL	ORCHIDEE, branch 2.0	No	8	3	Q_{10} & Increasing	Boucher et al. (2020), Cheruy et al. (2020), Guimberteau et al. (2018)
MIROC-ES2L	JAMSTEC	MATSIRO VISIT-s	Yes	3	6	Arrhenius & Increasing	Hajima et al. (2020), Ito and Oikawa (2002)
MPI-ESM1.2-LR	MPI	JSBACH3.2	Yes	3	18	Q_{10} & Increasing	Mauritsen et al. (2019), Goll et al. (2017), Goll et al. (2015)
NorESM2-LM	NCC	CLM5	Yes	22	7	Arrhenius & Increasing	Seland et al. (2020), Lawrence et al. (2019)
UKESM1-0-LL	UK	JULES-ES-1.0	Yes	3	4	Q_{10} & Hill	Sellar et al. (2020), Wiltshire et al. (2021)

Table 2.2: The 10 CMIP5 Earth System Models included in this chapter, and relevant features of their land carbon cycle components (Friedlingstein et al., 2014; Arora et al., 2013; Anav et al., 2013; Taylor et al., 2012). Including temperature and moisture functions presented in Todd-Brown et al. (2013).

Earth System Model	Modelling Centre	Land Surface Model	Nitrogen cycle	No. of live & dead carbon pools	Temperature & Moisture	References
BNU-ESM	BNU	CoLM + BNU-DGVM	Yes	-	Q_{10} & Increasing	Ji et al. (2014), Dai et al. (2003)
CCSM4	CCSM	CLM4	Yes	20	Arrhenius & Increasing	Gent et al. (2011), Lawrence et al. (2011)
CanESM2	CCCma	CLASS2.7 + CTEM1	No	5	Q_{10} & Hill	Arora et al. (2009), Arora and Boer (2010)
GFDL-ESM2G	GFDL	LM3	No	10	Hill & Increasing	Dunne et al. (2012), Dunne et al. (2013), Shevliakova et al. (2009)
GISS-E2-R	NASA-GISS	YIBs, version 1.0	No	12	Increasing & Increasing	Schmidt et al. (2014), Yue and Unger (2015)
HadGEM2-ES	MOHC	JULES + TRIFFID	No	7	Q_{10} & Hill	Jones et al. (2011), Best et al. (2011), Clark et al. (2011)
IPSL-CM5A-LR	IPSL	ORCHIDEE	No	7	Q_{10} & Increasing	Dufresne et al. (2013), Krinner et al. (2005)
MIROC-ESM	JAMSTEC	MATSIRO + SEIB-DGVM	No	6	Arrhenius & Increasing	Watanabe et al. (2011), Ito and Oikawa (2002), Sato et al. (2007)
MPI-ESM-LR	MPI	JSBACH + BETHY	No	6	Q_{10} & Increasing	Raddatz et al. (2007), Knorr (2000)
NorESM1-M	NCC	CLM4	Yes	20	Arrhenius & Increasing	Bentsen et al. (2013), Iversen et al. (2013), Lawrence et al. (2011)

in these models, which means there are separate carbon pools in the model that represent different soil depths (Lawrence et al., 2019). In this chapter, the CMIP variable *cSoilAbove1m* is used throughout to represent soil carbon for the models CESM2 and NorESM2-LM, unless otherwise stated. The use of this variable is to enable a more consistent comparison with both the other CMIP6 models and the CMIP5 models. Therefore, an assumption of a 1 m depth of soil for modelled soil carbon allows for the fairest evaluation, and evaluation is considered against empirical datasets down to a depth of 1 m (see below). However, comparisons with the *cSoil* variable for both CESM2 and NorESM2-LM are included in Tables 2.4 and 2.6 of the Results.

In order to obtain a clean separation between above-ground and below-ground drivers of soil carbon variations, a quasi-equilibrium approximation is made. To begin, the definition of the effective soil carbon turnover time (τ_s) is shown by Equation 2.1 (Varney et al., 2020; Koven et al., 2017; Carvalhais et al., 2014), which represents the average time carbon resides in the soil:

$$\tau_s = \frac{C_s}{R_h} \tag{2.1}$$

where, R_h is the output flux of carbon from the soil known as the heterotrophic respiration, which is described as the carbon loss from the decomposition by microbes. This definition of the turnover time implicitly neglects other processes that may release soil carbon, but which are not yet routinely included in ESMs (e.g. peat fires or dissolved organic carbon fluxes).

The definition of the effective turnover time (Equation 2.1) ensures that the soil carbon at any one time is given by $C_s = R_h \tau_s$. In an unperturbed steady state (i.e. neglecting disturbances from land use change, fires, insect outbreaks, etc.), there is no net exchange of carbon between land and atmosphere, and therefore R_h is equal to litterfall, known as fallen organic material from plants. When vegetation and soil carbon are close to a steady state, litterfall and R_h are also approximately equal to NPP, where NPP is defined as the net carbon assimilated by plants via photosynthesis minus loss due to plant respiration. In the contemporary period considered in this study, R_h has been found to be well approximated by NPP (Varney et al., 2020). This is because the difference between NPP and R_h, which represents the Net Ecosystem Productivity (NEP, F_L), is a small fraction of the NPP over the historical period (NPP $\approx$ 60 PgC yr^{-1}; NEP $\approx$ 3 PgC yr^{-1}). Therefore the present-day soil carbon can be approximated by:

$$C_s \approx \Pi_N \, \tau_s \tag{2.2}$$

to a good accuracy. This allows for a clean separation of soil carbon variation into the above (NPP, Π_N) and below (τ_s) ground drivers of soil carbon spatial patterns, following the approach of previous published studies (Koven et al., 2015; Todd-Brown et al., 2013).

To evaluate these soil carbon controls on C_s, NPP and τ_s are evaluated separately. This chapter uses modelled 'Net Primary Productivity' (CMIP variable *npp*), which is defined as the mass flux of carbon out of the atmosphere due to NPP on land. NPP is also considered spatially (kg m^{-2} yr^{-1}), and as an area-weighted global total flux (PgC yr^{-1}). By definition, τ_s is defined by Equation 2.1 and therefore is calculated by soil carbon (as defined above) divided by R_h. For R_h, the variable 'Heterotrophic Respiration' (CMIP variable *rh*) is used, which is defined as the mass flux of carbon into the atmosphere due to heterotrophic respiration on land, primarily due to the microbial respiration that occurs in the soil and the units of R_h are the same as that of NPP. The carbon fluxes (NPP and R_h) are time-averaged over the period 1995-2005 for consistency between the CMIP generations and the empirical datasets. τ_s can be considered on a spatial level, or as an effective global τ_s, which is defined as average τ_s=mean(C_s)/mean(R_h) (where the mean represents an area-weighted global average). The advantage of defining an effective global τ_s is that it is not dominated by large spatial outlying values. Using either method, the units for τ_s are in years (yr) by definition.

The relationships of soil carbon, C_s, NPP and τ_s, with both temperature and soil moisture are also considered. For temperature, the variable 'near surface air temperature' (CMIP variable *tas*), representing atmospheric temperature at the surface is considered, where the dates 1995-2005 where chosen to be consistent with the carbon fluxes. The variable for atmospheric temperature was considered opposed to soil temperature as equivalent global observational datasets are required for the analysis. For soil moisture, the variable 'Moisture in Upper Portion of Soil Column' (CMIP variable *mrsos*), which is defined as the mass content of water in the soil layer in the upper portion of the soil (0cm-10cm depth) was considered, where the dates 1978-2000 were considered to match the empirical data. The standard output *mrsos* is in units of kg m^{-2}, however in this chapter a volumetric soil moisture, referred to as θ, is used to allow for consistent comparison with the benchmark data. θ is calculated as *mrsos* divided by the depth of the soil layer in mm, which in this case is θ = mrsos/100. The variable *mrsos* for soil moisture was considered opposed to the full soil column moisture (CMIP variable

mrso) as this better matched the available empirical dataset for soil moisture. It is noted that this represents surface soil moisture and does not match the depth over which soil carbon is evaluated (0 – 1 m). This is due to deeper soil moisture products not being as readily available due to limitations of remote sensing methods in penetrating deeper ground. It is expected that the surface soil moisture will be related to deeper soil moisture to some extent but will be influenced by different processes. For example, high surface soil moisture after rainfall events could run off and thus not always reach the deeper soil.

2.2.3 Empirical datasets

2.2.3.1 Soil carbon

Observational soil carbon, C_s, to a depth of 1 m, was obtained by combining the empirical Harmonized World Soils Database (HWSD) (FAO and ISRIC, 2012) and Northern Circumpolar Soil Carbon Database (NCSCD) (Hugelius et al., 2013) soil carbon datasets, where NCSCD was used where overlap of the datasets occurs. This is a commonly used method when considering empirical soil carbon and has been previously used in multiple studies, such as: Varney et al. (2020), Koven et al. (2017), and Todd-Brown et al. (2013). This dataset is referred to here as the 'Benchmark dataset'.

The 95% confidence intervals given by Todd-Brown et al. (2013) are used to derive standard deviations about the global mean soil carbon obtained by this dataset. To do this, the constructed 95% confidence intervals where used to calculate upper and lower bounds around the mean value. Then assuming the data is normally distributed, these derived 95% confidence intervals were halved to obtain confidence intervals equivalent to a standard deviation error on the mean (1412 $\pm$ 215 PgC). The uncertainty analysis completed in Todd-Brown et al. (2013) is used for the benchmark soil carbon dataset as no quantitative uncertainty has been previously or since defined for the HWSD and NCSCD datasets (Anav et al., 2013).

Additionally, the benchmark dataset was compared with empirical estimates found in the literature to improve the robustness of the evaluation. Todd-Brown et al. (2013) find that this derived uncertainty is consistent with other empirical estimates of global soil carbon: for example, 1576 PgC in Eswaran et al. (1993), 1220 PgC in Sombroek et al. (1993), and 1502 PgC in Jobbágy and Jackson (2000). This study further compares with empirical estimates of 1395 PgC in Post et al. (1982) and 1515 PgC in Raich and Schlesinger (1992). These empirical estimates are within one standard deviation of the global mean soil carbon

given by the benchmark dataset (Table 2.3).

Moreover, additional empirical datasets are considered to improve the reliability of the benchmark dataset (Table 2.3). These include: (1) the World Inventory of Soil property Estimates (WISE30sec) dataset down to a depth of 2 m (Batjes, 2016), which includes a given standard deviation on the global total soil carbon consistent with the derived benchmark uncertainty, (2) the named 'S2017' from Sanderman et al. (2017) soil carbon estimate (1 m and 2 m), which uses a data-driven statistical model and the History Database of the Global Environment (HYDE) land use data, (3) the Global Soil Dataset for use in Earth System Models (GSDE), which provides a estimates for observational soil carbon down to a depth of up to 2.3 m (Shangguan et al., 2014), and (4) the Global Gridded Surfaces of Selected Soil Characteristics (IGBP-DIS) estimate of soil carbon to a depth of 1 m, derived by the Oak Ridge National Laboratory Distributed Active Archive Centre (ORNL DAAC) (IGBP, 2000). These datasets were combined to obtain a mean estimate for observational soil carbon down to a depth of 1 m, where a global total soil carbon value of 1560 $\pm$ 214 PgC was found. This estimate is consistent with the benchmark dataset estimate (Table 2.3), and further improves the confidence in the benchmark soil carbon estimate.

Furthermore, the spatial correlation coefficients between these additional datasets and the benchmark dataset are considered, where the following values correspond to the above datasets: (1) 0.554, (2) 0.625, (3) 0.482, and (4) 0.622. Map plots comparing the empirical soil carbon datasets are shown in Figure 2.1. The estimate for northern latitude total soil carbon has greater uncertainties associated with it, where the standard deviation deduced by combining the empirical datasets is 83 PgC. To account for this increased uncertainty, the deduced standard deviation of 83 PgC is used on the benchmark soil carbon throughout this chapter, opposed to the 61 PgC derived using the Todd-Brown et al. (2013) uncertainty analysis.

2.2.3.2 Carbon fluxes

To estimate a benchmark NPP, the commonly used MODIS NPP (2000-2010) dataset (Zhao et al., 2005) is used. The MODIS NPP dataset does not have associated uncertainty estimates, so this chapter estimates a standard deviation error on benchmark NPP as derived by Ito (2011). The MODIS NPP dataset was found to be consistent with 251 empirical present-day estimates of NPP found in the literature, which Ito (2011) used to estimate a global value of 56.2 $\pm$ 14.3 PgC yr^{-1} (compared with a derived MODIS mean value of 56.6 yr^{-1}).

Table 2.3: Table of global total and northern latitude total (northern latitudes defined as 60° N - 90° N) soil carbon estimates from multiple empirical datasets, for varying soil depths where applicable.

Empirical dataset	Depth	Global total C_s (PgC)	Northern latitude total C_s (PgC)	Reference
HWSD + NCSCD	1 m	1412 ± 215	401 ± 61	FAO and ISRIC (2012) Hugelius et al. (2013)
WISE30sec	1 m	1371 ± 129	314	Batjes (2016)
	2 m	1952 ± 198	468	
S2017	1 m	1966	515	Sanderman et al. (2017)
	2 m	3141	893	
GSDE	1 m	1682	526	Shangguan et al. (2014)
	2.3 m	2593	849	
IGBP DIS	1 m	1567	377	IGBP (2000)

Moreover, due to the limited choice of observational derived NPP datasets (Harper et al., 2018), models can be further evaluated against using a benchmark dataset for Heterotrophic respiration (R_h), where R_h is estimated using the CARDAMOM (2001–2010) heterotrophic respiration dataset (Bloom et al., 2015). The empirical CARDAMOM R_h has associated estimates of error, which were used to derive a standard deviation uncertainty on the empirical average R_h (51.7 ± 21.8 PgC yr^{-1}). This chapter includes map plots comparing the two empirical datasets, which is shown in Figure 2.2, and global totals for R_h are also considered for comparison against NPP for both the CMIP6 and CMIP5 ESMs.

2.2.3.3 Soil carbon turnover time

To estimate a benchmark soil carbon turnover time (τ_s), the estimate of observational soil carbon can be divided by the estimate of heterotrophic respiration (R_h) (see above). To estimate an uncertainty on effective global τ_s, this study derived upper (τ_s^+) and lower (τ_s^-) bounds based on the derived C_s and R_h uncertainty estimates. The upper bound was calculated using the following: $\tau_s^+ = C_s^+ \,/\, R_h^-$, where C_s^+ is equal to the mean soil carbon plus one standard deviation and R_h^- is equal to the mean heterotrophic respiration minus one standard deviation. The lower bound was calculated using the following: $\tau_s^- = C_s^- \,/\, R_h^+$, where similarly C_s^- is equal to the mean soil carbon minus one standard deviation and R_h^+ is equal to the mean heterotrophic respiration plus one standard deviation.

This method gives a large uncertainty bound around the derived mean estimate

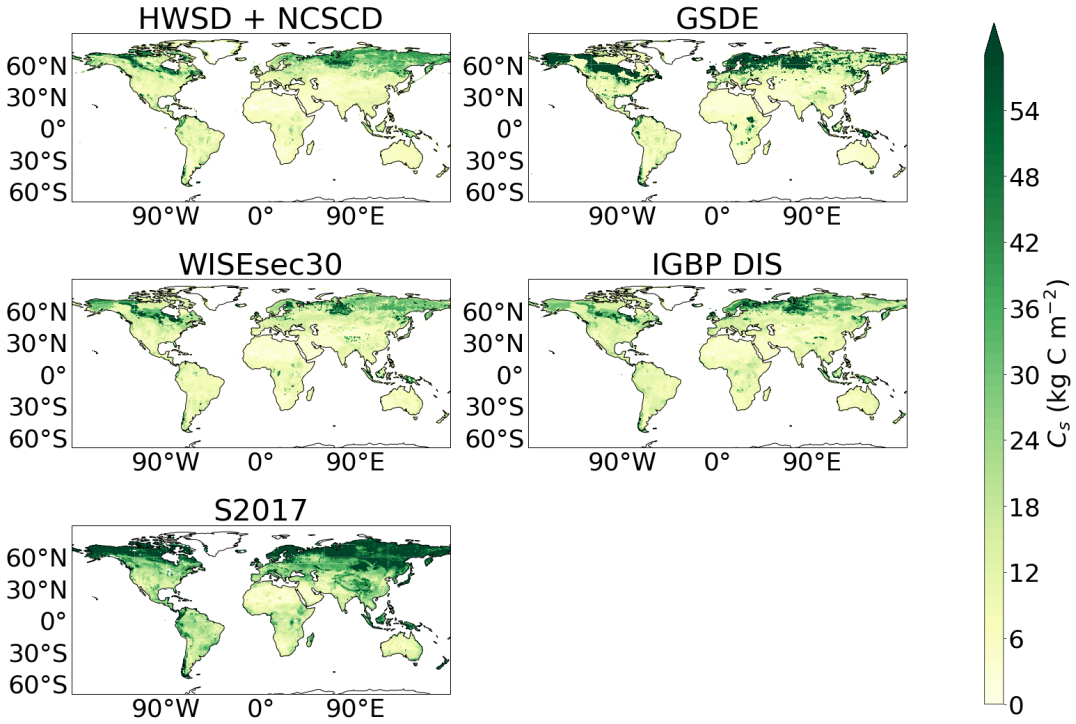

Figure 2.1: Maps comparing empirical datasets of soil carbon (C_s). The benchmark dataset is a map plot showing C_s approximated to a depth of 1 m by combining the Harmonized World Soils Database (HWSD) (FAO and ISRIC, 2012) and Northern Circumpolar Soil Carbon Database (NCSCD) (Hugelius et al., 2013), where NCSCD was used where overlap occurs. Additional map plots are shown for empirical C_s estimated by: the World Inventory of Soil property Estimates (WISE30sec) (Batjes, 2016), the named 'S2017' from Sanderman et al. (2017), the Global Soil Dataset for use in Earth System Models (GSDE) (Shangguan et al., 2014), and the Global Gridded Surfaces of Selected Soil Characteristics (IGBP-DIS) (IGBP, 2000).

(27.0^{+27}_{-11} yr), so the benchmark data is further compared to empirical estimates. Raich and Schlesinger (1992) derive an estimate of mean soil carbon turnover of 32 years, using estimates for mean soil carbon pools and mean soil respiration rates. More recently, Carvalhais et al. (2014) derive an estimate for the mean global ecosystem carbon turnover time of 23^{+7}_{-4}, which is a spatially explicit and observation based estimate. Ito et al. (2020) derived an observational uncertainty range on soil carbon turnover time of 18.5 to 45.8 years, which was derived using similar empirical estimates found in the literature. These estimates increase the certainty on the values closer to the derived empirical mean value for τ_s.

2.2.3.4 Soil moisture and air temperature

To estimate soil moisture (θ), the Copernicus Climate Change Service (C3S) 'Soil moisture gridded data from 1978 to present' dataset (published 2018-10-25) was used, where the years 1978 to 2000 are considered. This dataset is based on the ESA Climate Change Initiative soil moisture, and estimates global surface soil

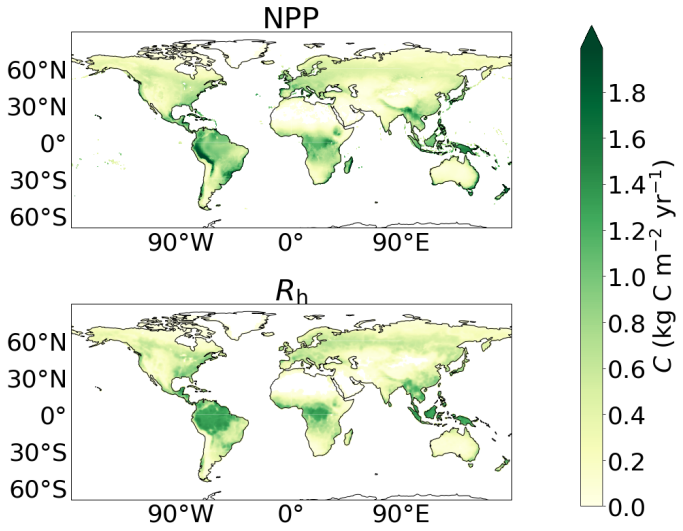

Figure 2.2: Maps of empirical carbon flux datasets. Net Primary Productivity (NPP) is approximated using the MODIS NPP dataset (Zhao et al., 2005), and Heterotrophic Respiration (R_h) is approximated using the CARDAMOM R_h dataset (Bloom et al., 2015).

moisture from a large set of satellite sensors (Copernicus Climate Change Service, 2021; Gruber et al., 2017; Dorigo et al., 2017; Liu et al., 2012; Wagner et al., 2012; Liu et al., 2011). The WFDEI Meteorological Forcing dataset was used to represent observational air temperatures (1995-2005) (Weedon et al., 2014), where dates are chosen to allow for consistency between CMIP generations. This chapter includes no uncertainty analysis on the soil moisture and air temperature empirical datasets as these datasets are only used to evaluate spatial correlations with modelled data and not to evaluate soil moisture and air temperature in the models.

2.2.4 Regridding

To allow direct comparisons between the empirical data and model output data, the model data was regridded to match the observational grid. In this case, the observational grid is a 0.5° by 0.5° resolution, 720 longitude and 360 latitude grid. The regridding was done using Iris - the community-driven Python package for analysing and visualising Earth science data (Met Office, 2013). The regidding method assumed conservation of mass and used linear extrapolation, where extrapolation points will be calculated by extending the gradient of the closest two points. Moreover, model land masks are used to calculate the fraction of land in each coastal grid cell (CMIP variable *sftlf*).

2.2.5 Statistical analysis

It is difficult to evaluate the spatial distributions of modelled soil carbon and related spatial controls against empirical data with a single metric, so the evaluation for both CMIP6 and CMIP5 involves multiple methods. These include: coefficients of variation, spatial standard deviations, spatial Pearson correlation coefficients and Root Mean Square Errors (RMSEs). These methods can be combined to give a more thorough evaluation of spatial soil carbon and associated controls in the CMIP6 models compared to the previous generation of CMIP5 models.

The coefficient of variation is defined as the ratio of the ensemble standard deviation (std) to the ensemble mean in each grid cell. This is used to show the amount of variability amongst the models in the ensemble scaled to the size of the ensemble mean, so represents the variability spatially in the ensemble and shows how much variation is present across the ensemble in specific regions. It is presented as hatching on a map figure (Figure 2.6), where shaded 'hatched' regions show regions of high variability within the ensemble. These regions show areas where there is disagreement in the ensemble as there is large spread compared with the mean, and was defined as where $std/mean > 0.75$. The regions where spatial $C_s < 5$ kg m^{-2} were discounted as the low values of soil carbon are present in these regions.

The spatial standard deviation is a measure of the spread in the data across the globe compared to the mean value. Pearson correlation coefficients (r-values) were used as a spatial measure of the linear correlation between the empirical and modelled data, where a high r-value (near 1 or -1) represents a high correlation in the data and a low r-value (near 0) represents a negligible correlation. RMSE were used as an absolute measure of the difference between the modelled data and empirical data, where the lower the value the lower the difference error. The RMSE can be considered as the standard deviation of the difference, and it is a measure to show the deviation of the modelled data in relation to the empirical data. This statistical data: spatial standard deviations, Pearson correlation coefficients, and RMSEs, can be presented using a Taylor diagram. A Taylor diagram is a mathematical graph used to indicate the performance of a model compared with a benchmark, which in this case is the empirical datasets (Taylor, 2001).

2.3 Results

2.3.1 Soil carbon stocks

2.3.1.1 Global total evaluation

Global total soil carbon (in the top 1 m of soil) is shown to vary amongst the ESMs in CMIP6, with a range of 1294 PgC between the models with the lowest and highest values (Table 2.4). The global total soil carbon for two (CanESM5 and MIROC-ES2L) out of the eleven CMIP6 models falls within the benchmark soil carbon uncertainty range, 1197–1627 PgC (mean $\pm$ stand deviation). The models with the largest global total soil carbon are CNRM-ESM2-1 (1810 PgC), BCC-CSM2-MR (1770 PgC), and UKESM1-0-LL (1760 PgC), values greater than the benchmark dataset but not the additional empirical datasets (Table 2.3). The models GFDL-ESM4 (516 PgC) and IPSL-CM6A-LR (639 PgC) have the lowest global total soil carbon values in the ensemble, with global totals significantly lower (approximately 50% less) than the global totals seen in empirical data. It is noted that, if the full soil carbon profile is considered for CESM2 and NorESM2-LM opposed to a depth of 1 m, the global total soil carbon values are increased to 1870 PgC from 991 PgC in CESM2 and to 2430 PgC from 969 PgC in NorESM2-LM.

Both the CMIP5 and CMIP6 ensemble mean global totals fall within the benchmark uncertainty range (Tables 2.4 and 2.5). The ensemble mean global total soil carbon is found to have decreased in CMIP6 from CMIP5 (1206 $\pm$ 445 PgC vs. 1480 $\pm$ 810 PgC). However, a significant reduction is seen in the associated standard deviation of the ensemble mean global totals in CMIP6 compared with CMIP5 ($\pm$ 445 PgC in CMIP6 from $\pm$ 810 PgC in CMIP5) and a reduced range of global total values (a range of 1294 PgC is seen in CMIP6 as opposed to 2493 PgC in CMIP5). This suggests that, although a significant range in global soil carbon still exists amongst the CMIP6 ESMs, there is an improved consistency between the models seen in CMIP6 compared with the models in CMIP5, although it is noted that this may be a factor of the selection of models included in each ensemble rather than any change in process representation.

It is found from comparing the previous generation models in CMIP5 with the updated CMIP6 equivalent that multiple models in CMIP6 have lower quantities of soil carbon than in CMIP5, such as GFDL-ESM4 from GFDL-ESM2G, IPSL-CM6A-LR from IPSL-CM5A-LR, MIROC-ES2L from MIRCO-ESM, and MPI-ESM1.2-LR from MPI-ESM-LR. For example, the CMIP5 model MPI-ESM-LR is reported to have the largest soil carbon magnitude amongst the CMIP5 models,

with a global total of 3000 PgC (Table 2.5), whereas the updated CMIP6 model MPI-ESM1.2-LR has a reduced global total soil carbon value of 970 PgC amongst the lowest values reported in CMIP6 and below the observationally derived range (Table 2.4). Conversely, these reductions are negated in the ensemble mean by the remaining models, which have greater quantities of soil carbon in CMIP6 compared with their CMIP5 equivalent, such as CanESM5 from CanESM2, CESM2 from CCSM4, NorESM2-LM from NorESM1-M, and UKESM1-0-LL from HadGEM2-ES. For example, the CMIP5 model NorESM1-M is amongst the lowest soil carbon values presented in this ensemble at 538 PgC (Table 2.5), whereas the updated CMIP6 model NorESM2-LM has an increased global total of 969 PgC (down to 1 m) (Table 2.4).

2.3.1.2 Northern latitude total evaluation

Northern latitude soil carbon (down to a depth of 1 m and where northern latitudes are defined as 60° N - 90° N) is found to be underestimated in CMIP6, with eight out of the eleven CMIP6 models having lower northern latitude soil carbon values than the derived observational range (Table 2.4). A total of two of the eleven CMIP6 models (CNRM-ESM2-1 and MIROC-ES2L) have northern latitude totals that fall within the uncertainty range derived from the benchmark data, 318–484 PgC (mean $\pm$ stand deviation). The CMIP6 models with the greatest northern latitude total soil carbon are BCC-CSM2-MR (575 PgC), CNRM-ESM2-1 (440 PgC), and MIROC-ES2L (347 PgC). The CMIP6 models with the lowest northern latitude soil carbon are IPSL-CM6A-LR (66 PgC), ACCESS-ESM1.5 (151 PgC), GFDL-ESM4 (163 PgC), MPI-ESM1.2-LR (175 PgC), and UKESM1-0-LL (194 PgC), values significantly lower than the totals seen in empirical data.

The northern latitude soil carbon total was also under-estimated in CMIP5, with six out of the ten CMIP5 models estimating northern latitude totals lower than the empirical estimates (Table 2.5). The ensemble mean total northern latitude soil carbon is lower in CMIP6 (266 $\pm$ 139 PgC seen in Table 2.4) than in CMIP5 (318 $\pm$ 246 PgC seen in Table 2.5), which is consistent with the global total results; however, both the CMIP5 and CMIP6 mean values fall below the benchmark range. Similarly, as with global soil carbon, a smaller standard deviation on the mean is found for CMIP6 compared with CMIP5, and there is a reduced range in simulated northern latitude total values amongst the CMIP6 models, where despite a large range seen (66 to 575 PgC), an even greater range is seen in CMIP5 (28.1 to 742 PgC). Moreover, improvements are seen amongst models from CMIP5 to CMIP6. For example, the CMIP5 model NorESM1-M had a northern latitude total soil carbon value of 31.0 PgC, which is significantly lower than what is expected based on the benchmark dataset (Table 2.5). However, the updated CMIP6 ver-

Table 2.4: Table presenting global soil carbon (C_s) values for the 11 CMIP6 models included in this chapter and the benchmark datasets. Including: global total C_s in PgC, and northern latitude total (90°N - 60°N) C_s in PgC, and the spatial mean value of C_s and corresponding standard deviation in kg m^{-2}.

Earth System Model	Global total C_s (PgC)	Northern latitude total C_s (PgC)	Mean $C_s \pm$ std (kg m^{-2})
ACCESS-ESM1.5	900	151	5.86 $\pm$ 5.35
BCC-CSM2-MR	1770	575	11.6 $\pm$ 16.6
CanESM5	1500	218	3.87 $\pm$ 6.52
CESM2 (cSoilAbove1m)	991	294	7.05 $\pm$ 16.6
CESM2 (cSoil)	*1870*	*1036*	*13.8 $\pm$ 51.7*
CNRM-ESM2-1	1810	440	12.2 $\pm$ 9.98
GFDL-ESM4	516	163	1.36 $\pm$ 3.43
IPSL-CM6A-LR	639	66.0	4.80 $\pm$ 3.37
MIROC-ES2L	1460	347	9.31 $\pm$ 10.7
MPI-ESM1.2-LR	970	175	6.68 $\pm$ 5.23
NorESM2-LM (cSoilAbove1m)	969	300	2.61 $\pm$ 6.97
NorESM2-LM (cSoil)	*2430*	*1563*	*6.60 $\pm$ 41.3*
UKESM1-0-LL	1760	194	12.0 $\pm$ 10.9
Ensemble mean	1206 $\pm$ 445	266 $\pm$ 139	2.80 $\pm$ 5.15
Benchmark dataset	1412 $\pm$ 215	401 $\pm$ 83	10.7 $\pm$ 9.28

Table 2.5: Table presenting global soil carbon (C_s) values for the 10 CMIP5 models included in this chapter and the benchmark datasets. Including: global total C_s in PgC, and northern latitude total (90°N - 60°N) C_s in PgC, and the spatial mean value of C_s and corresponding standard deviation in kg m^{-2}.

Earth System Model	Global total C_s (PgC)	Northern latitude total C_s (PgC)	Mean $C_s \pm$ std (kg m^{-2})
BNU-ESM	681	135	5.31 $\pm$ 4.55
CCSM4	507	28.1	4.03 $\pm$ 3.24
CanESM2	1540	300	9.16 $\pm$ 9.11
GFDL-ESM2G	1420	635	9.47 $\pm$ 13.2
GISS-E2-R	2150	609	15.9 $\pm$ 20.8
HadGEM2-ES	1080	148	8.19 $\pm$ 6.24
IPSL-CM5A-LR	1350	346	9.77 $\pm$ 7.64
MIROC-ESM	2550	742	20.5 $\pm$ 15.1
MPI-ESM-LR	3000	204	23.5 $\pm$ 14.8
NorESM1-M	538	31.0	3.61 $\pm$ 3.34
Ensemble mean	1480 $\pm$ 810	318 $\pm$ 246	10.5 $\pm$ 6.02
Benchmark dataset	1412 $\pm$ 215	401 $\pm$ 83	10.7 $\pm$ 9.28

sion of this model, NorESM2-LM, has a northern latitude total soil carbon value of 300 PgC, which is much more in line with the expected observational values (Table 2.4). An improved representation of northern latitude soil carbon is also seen in CESM2 (compared with CCSM4), which has the same land surface model as NorESM2-LM (CLM5; Lawrence et al. (2019)).

The CMIP6 models with the lowest global total values for soil carbon do not always correspond to the lowest northern latitude values for soil carbon. For example, UKESM1-0-LL global total soil carbon is amongst the highest global totals seen in CMIP6; however, low quantities of soil carbon are seen in the northern latitudes (approximately 10% of the global total). Conversely, BCC-CSM2-MR, CESM2, GFDL-ESM4, and NorESM2-LM have approximately 30% of their global total stocks in the northern latitude region, which is consistent with the ratio seen in the benchmark dataset. This result suggests that representing global total soil carbon stocks consistently with the benchmark soil carbon does not imply consistency in the representation of northern latitude soil carbon stocks, and these should be evaluated separately. However, the large uncertainties associated with the empirical datasets for the northern latitudes are noted (Table 2.3).

2.3.1.3 Spatial evaluation

A lack of consistency in the simulation of soil carbon was found amongst the CMIP5 models, which can be seen in Figure 2.3(a), where differences between the empirical and modelled data is shown. Northern latitude soil carbon was found to be underestimated in CMIP5, where areas of blue can be seen in the northern latitudes of the CMIP5 soil carbon map in Figure 2.3(a). This underestimation of CMIP5 northern latitude soil carbon is accompanied by significant overestimations seen in mid-latitude soil carbon. Specifically, large quantities of soil carbon which are inconsistent with our benchmark dataset can be seen in the mid-latitude regions in the following CMIP5 models: CanESM2, GFDL-ESM2G, GISS-E2-R, MIROC-ESM, and MPI-ESM-LR, and less significant overestimations are seen in HadGEM2-ES and IPSL-CM5A-LR (Figure 2.5). Systematic errors remain in the CMIP6 models, however there are some improvements seen in the spatial simulation of soil carbon from CMIP5. Soil carbon is still underestimated in the northern latitudes, where the areas of blue still remain the northern latitudes of the CMIP6 soil carbon map in Figure 2.3(a), though regions of overestimations in the northern latitudes are also seen amongst the CMIP6 models in BCC-CSM2-MR, CESM2, CNRM-ESM2-1, and NorESM2-LM (Figure 2.4), but it is noted that this representation might be more consistent with observations if a dataset including deeper soil carbon stocks was considered. CMIP6 shows improvements in the representation of mid-latitude soil carbon, where less of an overestimation

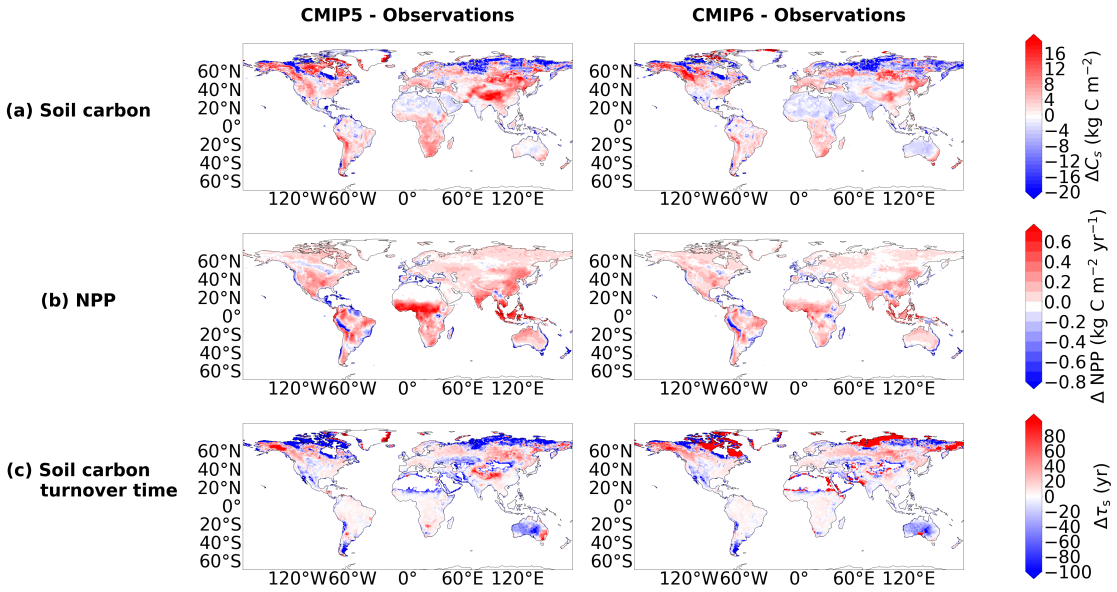

Figure 2.3: Maps presenting the difference between the modelled and benchmark data for the CMIP5 and CMIP6 ensembles, for: (a) C_s (kg m^{-2}), (b) NPP (kg m^{-2} yr^{-1}), and (c) τ_s (yr).

is seen in CMIP6 compared with CMIP5 (Figure 2.3(a)). This overestimation can still be seen in four of the eleven CMIP6 models: ACCESS-ESM1.5, CanESM2, MIROC-ES2L and UKESM1-0-LL, however the overestimations in CMIP6 are less inconsistent than when compared with CMIP5 and the number of models showing this limitation in CMIP6 has been reduced (Figure 2.4).

Despite the differences seen in the spatial representation of soil carbon between the individual models in CMIP6, the ensemble mean has more areas of agreement within the ensemble compared with the ensemble mean in CMIP5. This can be seen in Figure 2.6(a), where there is less hatching (where hatched shaded areas represent regions of low agreement amongst the models in the ensemble, see Methods) in the CMIP6 map compared with the CMIP5 map. Specifically, ensemble mean C_s in CMIP6 has more areas of agreement in the mid-latitude region compared with the CMIP5 ensemble mean, where significant areas of disagreement are seen. This disagreement is likely due to the overestimation which exists in some of the CMIP5 models (Figure 2.5). Also, a reduction in the area of disagreement is seen in the northern latitudes in CMIP6 compared with CMIP5, however this remains the region where the most disagreement exists across the generations. It is noted that this is a measure of agreement within the ensemble, and not between the models and empirical data.

The inconsistency of the simulation of spatial soil carbon in CMIP6 is further evaluated using the spatial standard deviations, the spatial Pearson correlation coefficients and RMSEs (see Methods), where the Taylor Diagram (Figure 2.7(a))

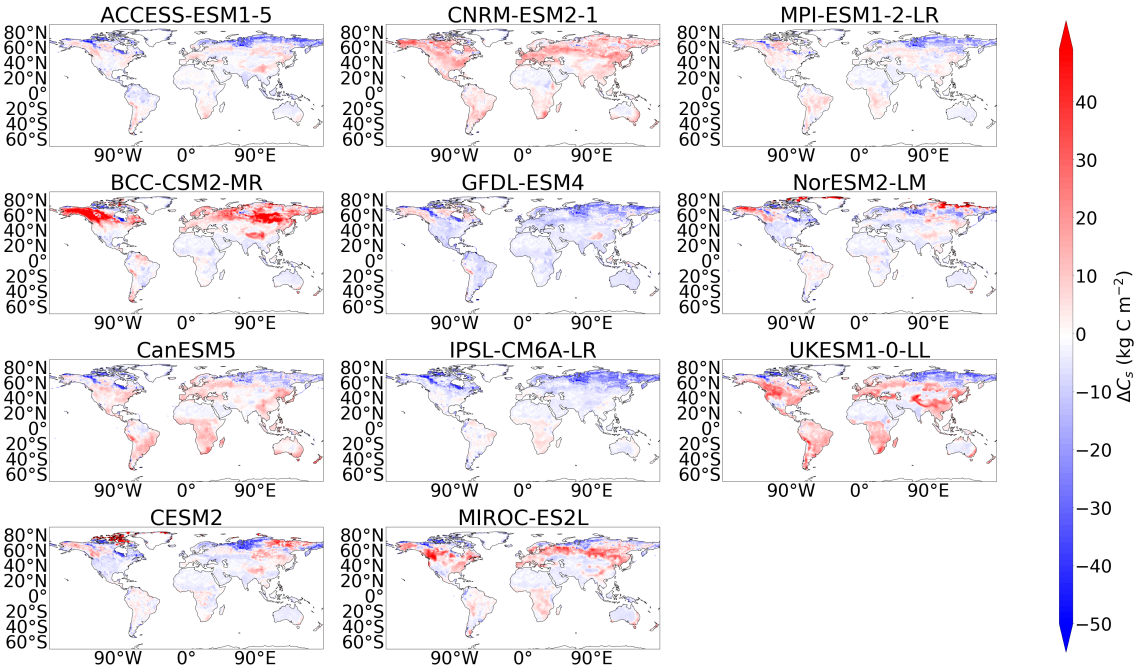

Figure 2.4: Maps of the difference in soil carbon (C_s) between the historical simulation of each CMIP6 model and the benchmark data.

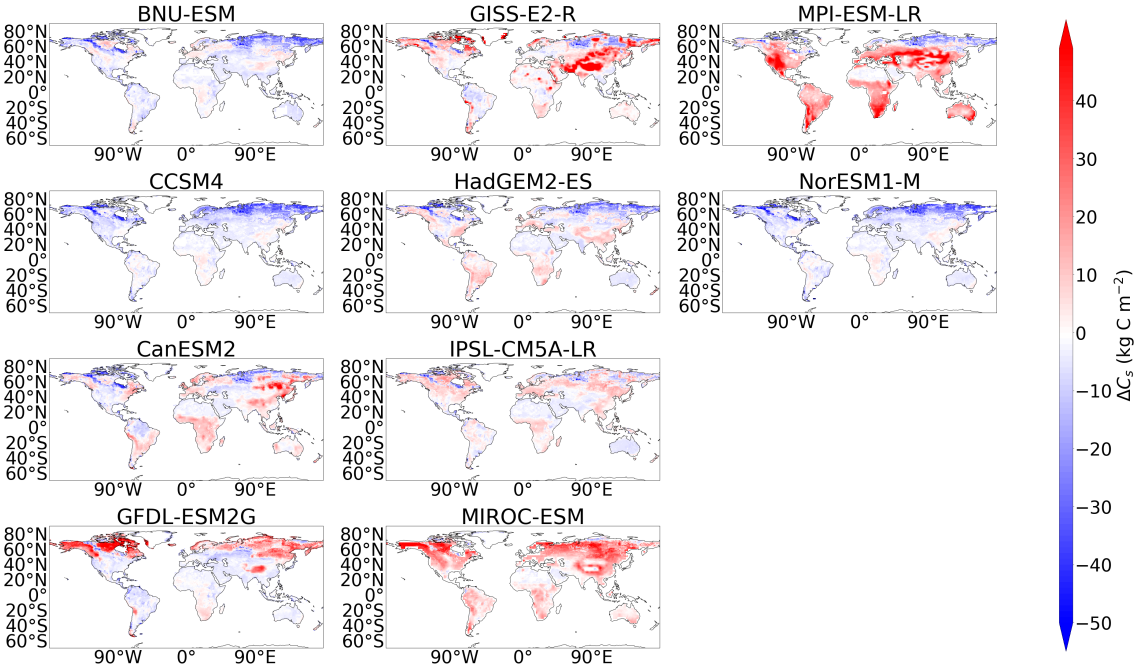

Figure 2.5: Maps of the difference in soil carbon (C_s) between the historical simulation of each CMIP5 model and the benchmark data.

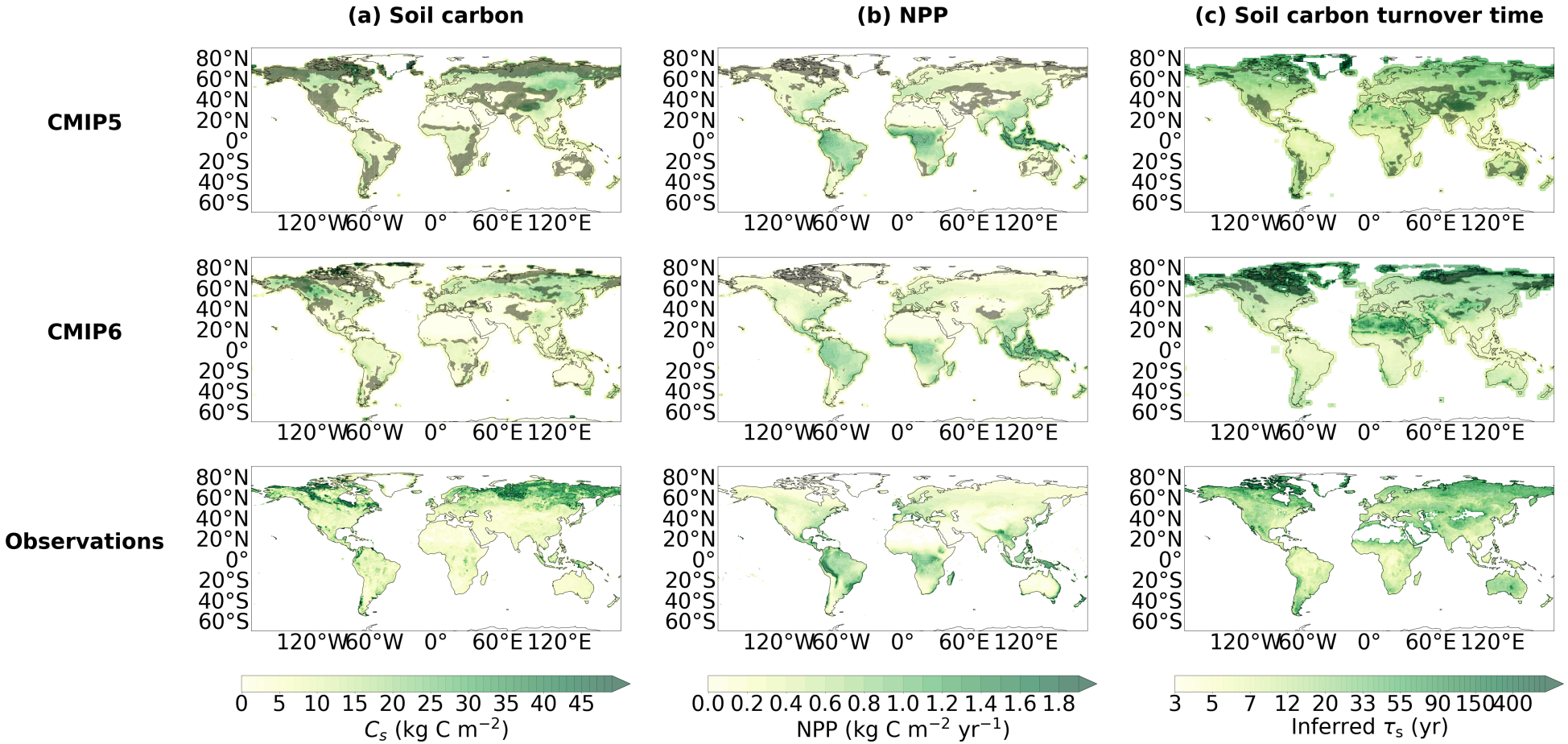

Figure 2.6: Ensemble mean maps for (a) C_s (kg m^{-2}), (b) NPP (kg m^{-2} yr^{-1}), and (c) τ_s (yr), presented for the CMIP6 ensemble, CMIP5 ensemble and the benchmark datasets. The hatched areas are used to show regions of low agreement within the ensemble, where regions of low soil carbon ($<$ 5 kg m^{-2}) have been excluded.

presents all three statistical assessments. The spatial standard deviation for soil carbon is shown on the radial axis between standard x and y axes in Figure 2.7(a). The range of spatial standard deviations amongst the CMIP6 models sees a slight reduction from the range amongst the CMIP5 models, though significant differences remain. The CMIP6 models CNRM-ESM2-1, MIROC-ES2L and UKESM1-0-LL best match the spatial standard deviation derived from the benchmark dataset (Tables 2.4 and 2.5). It is found that the spatial representation of modelled soil carbon in CMIP6 is poorly correlated to the empirical soil carbon, where the CMIP6 ensemble spatial correlation coefficient with the empirical data is found to be 0.250. The spatial correlation coefficients between the individual CMIP6 and CMIP5 models with the empirical data can also be seen in Figure 2.7(a), where the low spatial correlation coefficients are shown by the curved correlation axis. The lowest spatial correlation coefficients amongst the CMIP6 models were r-values of 0.104 in IPSL-CM6A-LR and 0.115 in UKESM1-0-LL. The CMIP6 model that was the most spatially consistent with the empirical data is CNRM-ESM2-1, with an r-value of 0.630. The CMIP6 ensemble sees a slight reduction in the RMSE compared to the CMIP5 ensemble, suggesting a slight improvement (Figure 2.8(a)). Significant improvements in the RMSE are seen in MIROC-ES2L from MIROC-ESM and MPI-ESM1.2-LR from MPI-ESM-LR. These results suggest small improvements in the simulation of soil carbon across this CMIP generation, however the low spatial correlation coefficients and variable RMSEs seen across the models in CMIP6 suggest inconsistencies with the benchmark data remain.

2.3.2 Net Primary Productivity

2.3.2.1 Global total evaluation

Global total NPP amongst the CMIP6 models appears to be consistent with the benchmark dataset (Table 2.6), where the CMIP6 ensemble mean for NPP is approximately 95% of the benchmark mean. The CMIP6 ensemble mean global total NPP (53.0 $\pm$ 9.39 PgC yr^{-1}) is found to be slightly lower than the derived mean benchmark value, however it is comfortably within the observational uncertainty range (56.6 $\pm$ 14.3 PgC yr^{-1}). The equivalent values for the CMIP5 models can be seen in Table 2.7, where the CMIP5 ensemble total is also found to be within the observational uncertainty range (56.3 $\pm$ 15.4 PgC yr^{-1}).

The standard deviation surrounding the CMIP5 ensemble mean is greater than in CMIP6. This reduced standard deviation in CMIP6 is because several of the models have a simulated global total NPP that more closely matches the benchmark NPP global total value compared with the previous CMIP5 generation. For

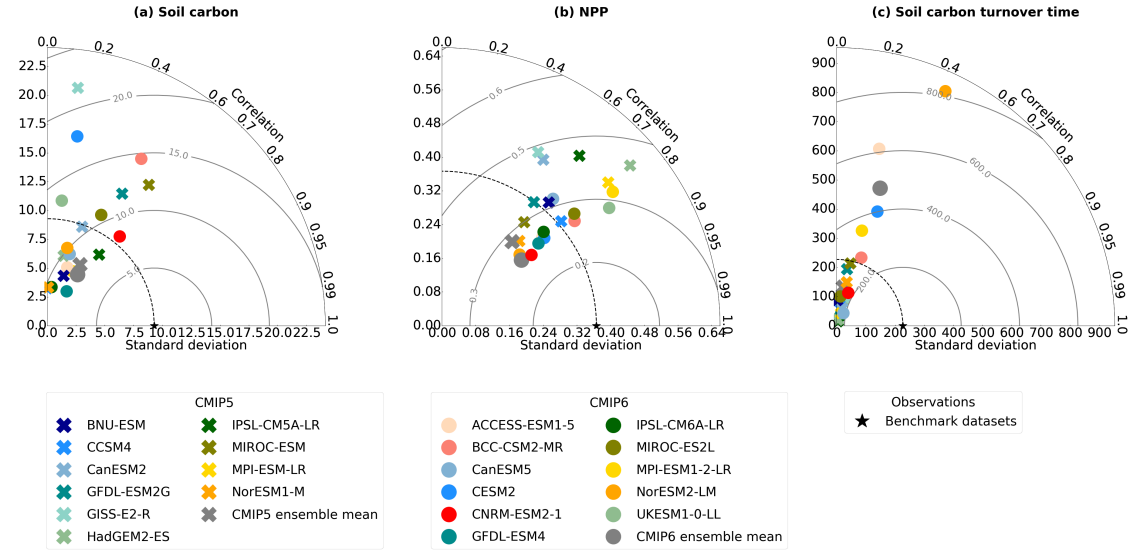

Figure 2.7: Taylor diagrams showing the spatial standard deviation (shown by the radial axis between standard x and y axes), the Pearson correlation coefficients (shown by the curved correlation axis), and the RMSE (show by the grey contours), for the ESMs in both CMIP5 and CMIP6 compared to the benchmark datasets, for (a) soil carbon (C_s), (b) NPP, and (c) soil carbon turnover time (τ_s).

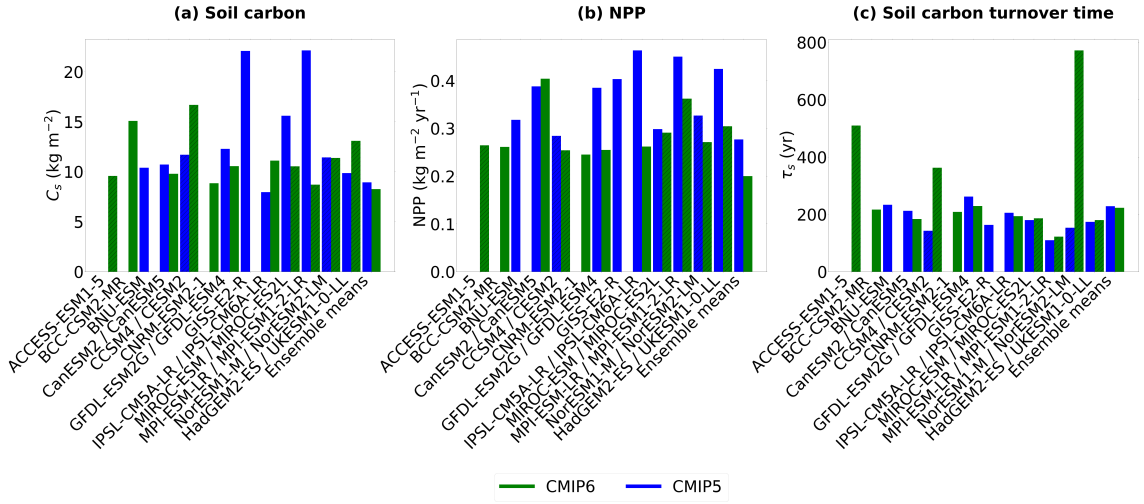

Figure 2.8: Bar charts comparing the Root Mean Squared Errors (RMSEs) in CMIP6 and CMIP5, for (a) soil carbon (C_s), (b) NPP, and (c) soil carbon turnover time (τ_s).

example, GFDL-ESM4 from GFDL-ESM2G, IPSL-CM6A-LR from IPSL-CM5A-LR, MIROC-ES2L from MIROC-ESM, MPI-ESM1.2-LR from MPI-ESM1-M, and UKESM1-0-LL from HadGEM2-ES. The majority of CMIP6 models see a reduction in NPP from the CMIP5 equivalent model, which in general reduces the overestimation of NPP that was seen in the CMIP5 models (Table 2.7 and 2.6). However, is was not the case for CanESM5 from CanESM2 which sees an increase in the magnitude of NPP from CMIP5 to CMIP6, resulting in a consequent overestimation compared to the benchmark data. A reduced range of modelled global total NPP values is also seen in CMIP6 from CMIP5, where the range is reduced from 48.5 PgC yr^{-1} in CMIP5 to 32.7 PgC yr^{-1} in CMIP6. These results suggest that overall the representation of carbon fluxes in CMIP6 ESMs is more consistent than in CMIP5.

Table 2.6: Table presenting global carbon fluxes and turnover time values for the 11 CMIP6 models included in this chapter and the benchmark datasets. Including: global total NPP (PgC yr^{-1}), global total R_h (PgC yr^{-1}) and effective average soil carbon turnover time (yr).

Earth System Model	NPP (PgC yr^{-1})	R_h (PgC yr^{-1})	τ_s (yr)
ACCESS-ESM1.5	45.6	45.1	19.0
BCC-CSM2-MR	51.2	48.9	34.1
CanESM5	75.5	75.0	18.1
CESM2 (cSoilAbove1m)	43.9	38.3	25.8
CESM2 (cSoil)	-	-	50.4
CNRM-ESM2-1	45.6	40.3	41.5
GFDL-ESM4	52.6	43.7	11.2
IPSL-CM6A-LR	46.4	39.9	14.6
MIROC-ES2L	59.1	52.7	24.5
MPI-ESM1.2-LR	58.9	53.4	15.4
NorESM2-LM (cSoilAbove1m)	43.5	38.2	24.0
NorESM2-LM (cSoil)	-	-	*60.8*
UKESM1-0-LL	60.8	57.5	28.1
Ensemble mean	53.0 $\pm$ 9.39	48.4 $\pm$ 10.5	23.3 $\pm$ 8.59
Benchmark datasets	56.6 $\pm$ 14.3	51.7 $\pm$ 21.8	27.0^{+27}_{-11}

Table 2.7: Table presenting global carbon fluxes and turnover time values for the 10 CMIP5 models included in this chapter and the benchmark datasets. Including: global total NPP (PgC yr^{-1}), global total R_h (PgC yr^{-1}) and effective average soil carbon turnover time (yr).

Earth System Model	NPP (PgC yr^{-1})	R_h (PgC yr^{-1})	τ_s (yr)
BNU-ESM	44.3	42.5	16.6
CCSM4	42.9	41.4	14.3
CanESM2	59.0	58.8	72.9
GFDL-ESM2G	74.4	62.7	57.3
GISS-E2-R	31.0	39.5	47.1
HadGEM2-ES	69.1	67.0	16.8
IPSL-CM5A-LR	76.6	62.4	19.4
MIROC-ESM	47.1	41.2	56.8
MPI-ESM-LR	73.5	59.9	42.7
NorESM1-M	45.0	41.3	34.5
Ensemble mean	56.3 $\pm$ 15.4	52.8 $\pm$ 10.7	37.8 $\pm$ 19.7
Benchmark datasets	56.6 $\pm$ 14.3	51.7 $\pm$ 21.8	27.0^{+27}_{-11}

2.3.2.2 Spatial evaluation

Modelled NPP in CMIP6 is spatially more consistent with empirical data than CMIP5. This can be seen in Figure 2.3(b), where the difference between the modelled and benchmark NPP is shown for both CMIP5 and CMIP6. It can be seen in the CMIP5 map that NPP is overestimated in the tropical regions, specifically in Africa and South East Asia, and the equivalent CMIP6 difference map shows a clear reduction in this overestimation. This tropical overestimation of NPP prominent in CMIP5 (Figure 2.10), is still seen in the CMIP6 models CanESM5, MPI-ESM1.2-LR and UKESM1-0-LL. However, this is not seen in the CMIP6 ensemble mean as it is likely negated by underestimations seen in CESM2, CNRM-ESM2-1, and NorESM2-LM (Figure 2.9). CMIP6 also sees more consistency with the benchmark dataset in the northern and mid-latitudes compared with CMIP5, where more white areas are seen in the CMIP6 map in Figure 2.3(b). An underestimation of NPP is seen in both CMIP5 and CMIP6 on the west side of South America, though unusually high NPP is seen in this region in the MODIS NPP dataset (Figure 2.2). Moreover, greater agreement amongst the

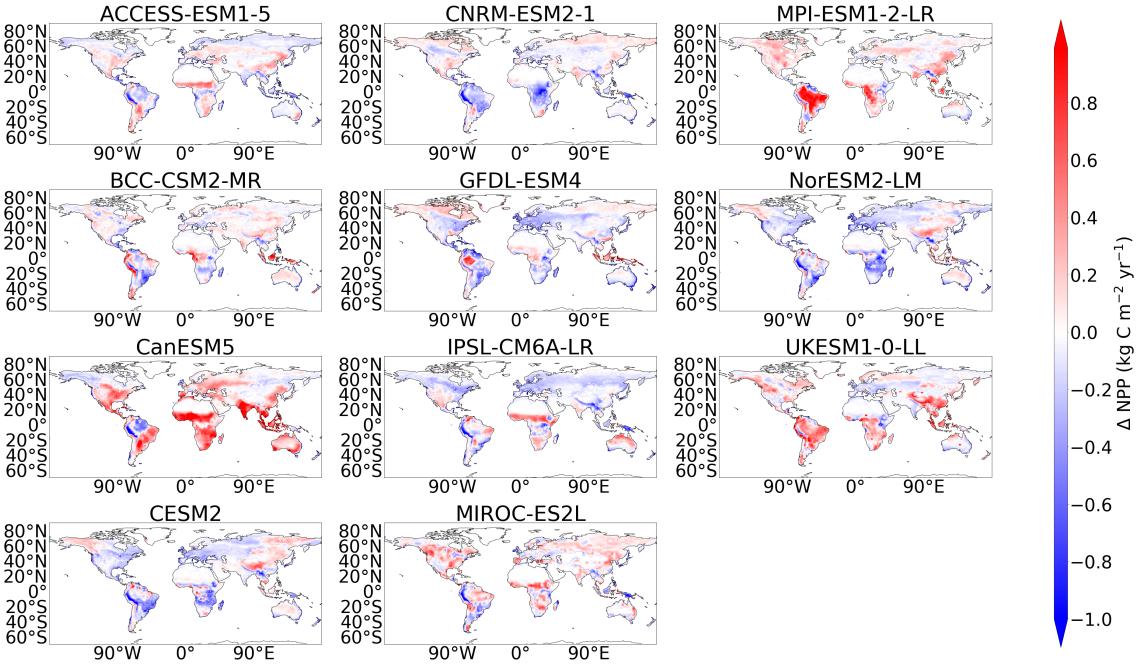

Figure 2.9: Maps of the difference in Net Primary Productivity (NPP) between the historical simulation of each CMIP6 model and the benchmark dataset.

models within CMIP6 is seen compared with the models in CMIP5. This can be seen in Figure 2.6(b), where less hatching representing areas of disagreement within the ensemble is seen in the CMIP6 compared with CMIP5. Specifically, CMIP6 sees less hatching in the northern latitudes, the Middle East and South East Europe, as well as regions in South America, South Africa and Australia.

The improved empirical consistency of modelled NPP in CMIP6 is also found when further evaluated using the same spatial metrics as with soil carbon. Despite a small range remaining in the spatial standard deviations amongst the CMIP6 models (shown by the radial axis in Figure 2.7(b)), robust improvements in the spatial correlation coefficients (shown by the curved axis in Figure 2.7(b)) and RMSEs are seen across the ensemble compared with CMIP5 (Figure 2.8(b)). Notable improvements in the representation of NPP are seen in GFDL-ESM4 compared with GFDL-ESM2G, IPSL-CM6A-LR compared with IPSL-CM5A-LR, and UKESM1-0-LL compared with HadGEM2-ES, with reduced RMSEs seen in each updated model. A general improvement in the spatial correlation coefficients is seen across all the CMIP6 models, where the circle markers (CMIP6 models) in Figure 2.7(b), have higher correlation values than the cross markers (CMIP5 models). The general improvement has resulted in the CMIP6 ensemble correlation coefficient (0.836) being greater compared with the equivalent CMIP5 value (0.711). The lowest correlations between modelled and observed NPP amongst the CMIP5 models are GISS-E2-R (0.274) and CanESM2 (0.469). The updated version CanESM5 remains the lowest correlation seen in CMIP6 (0.655), how-

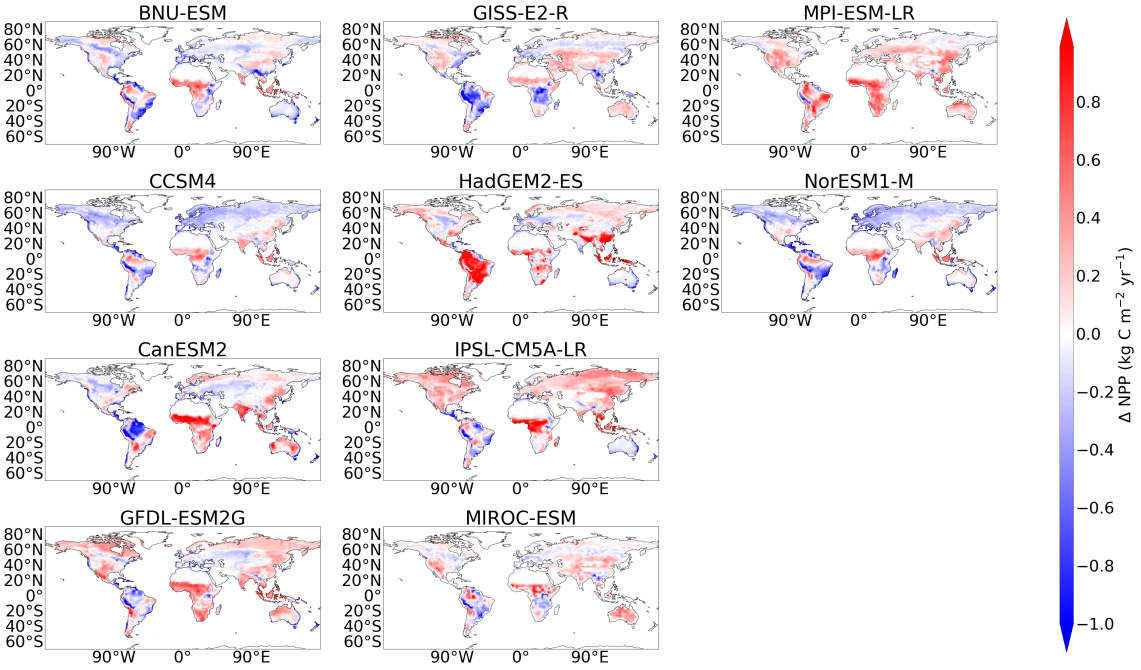

Figure 2.10: Maps of the difference in Net Primary Productivity (NPP) between the historical simulation of each CMIP5 model and the benchmark dataset.

ever an improvement in the correlation is seen. The updated version of the GISS model is not included in the CMIP6 ensemble considered in this chapter, which could be a reason for the increased ensemble mean correlation. However, this effect does not take away from the improvements seen across the CMIP6 models. HadGEM2-ES (0.764) and MPI-ESM-LR (0.764) were the CMIP5 models with the highest correlation to the benchmark NPP, and the updated CMIP6 equivalents of these models remain the models with the greatest correlations, but again improvements in the correlations are seen (0.816 in UKESM1-0-LL and 0.785 MPI-ESM1.2-LR).

2.3.3 Soil carbon turnover time

2.3.3.1 Global evaluation

There are minor improvements suggested in the simulated effective global τ_s amongst select CMIP6 models (Table 2.6) compared with CMIP5 (Table 2.7). The ensemble mean effective global τ_s was overestimated in CMIP5 (37.8 $\pm$ 19.7 yr) when compared with the derived mean τ_s using the benchmark datasets (27.0^{+27}_{-11} yr), which is reduced to a less significant underestimation in CMIP6 (23.3 $\pm$ 8.59 yr). Though both the CMIP5 and CMIP6 estimates fall within the observational uncertainty range. The associated ensemble spread on effective mean τ_s is less in CMIP6 compared with CMIP5, with a ensemble standard deviation of approximately 50% less. A significant range is seen in the effective global τ_s values amongst the CMIP5 models, with 5 fold difference between the lowest and the

highest values (Table 2.7). This range is mostly due to large overestimations seen amongst the CMIP5 models, for example in CanESM2, GFDL-ESM2G and MIROC-ESM. A reduced range is seen in amongst the models in CMIP6, however a 4 fold range still exists between the lowest and the highest values (Table 2.6). This reduced range is partly due to reductions in the effective global τ_s values in CMIP6 models compared to the equivalent model in CMIP5, specifically, CanESM5 from CanESM2, GFDL-ESM4 from GFDL-ESM2G, MIROC-ES2L from MIROC-ESM, and MPI-ESM1.2-LR from MPI-ESM-LR. Though overestimations do remain in CMIP6, for example in CNRM-ESM2-1, where the slowest effective turnover time was seen. Moreover, the range is also reduced due to improvements seen in models which underestimated τ_s in CMIP5, such as UKESM1-0-LL from HadGEM2-ES and CESM2 from CCSM4.

2.3.3.2 Spatial evaluation

The comparison of spatial soil carbon turnover times (τ_s) in CMIP6 with CMIP5 has more varied results than comparing simulated NPP. The CMIP5 ensemble showed an underestimation of τ_s in the northern latitudes, which is replaced with an overestimation of τ_s in CMIP6 when compared with the benchmark data (Figure 2.3(c)). This northern latitude overestimation in the CMIP6 ensemble is a result of the overestimations of τ_s in CESM2 and NorESM2-LM (Figure 2.11), which dominate in the CMIP6 ensemble mean. It is noted that this result may differ if deeper soil carbon stocks were considered. The northern latitude underestimation of τ_s is still seen within the CMIP6 models, such as CanESM5, CNRM-ESM2-1, GFDL-ESM4, IPSL-CM6A-LR, MIROC-ES2L, MPI-ESM1.2-LR, and UKESM1-0-LL (Figure 2.11). An overestimation of mid-latitude τ_s was seen in the CMIP5 models MIROC-ESM and MPI-ESM-LR (Figure 2.12), which is no longer seen in the updated CMIP6 models MIROC-ES2L and MPI-ESM1-2-LR, respectively. However, an overestimation of mid-latitude τ_s is seen in CMIP6 models BCC-CSM2-MR, CNRM-ESM2-1 and UKESM1-0-LL (Figure 2.11). The uncertainty in simulated northern latitude τ_s is also apparent in Figure 2.6(c), where the hatching shows the lack of agreement within the CMIP6 ensemble in this region. However, more agreement within the CMIP6 ensemble is seen in the same figure in the mid-latitudes and tropical regions compared with CMIP5.

The simulation of spatial τ_s in CMIP6 is further evaluated against the empirical data with the additional statistical metrics. Modelled τ_s is found to be poorly spatially correlated to empirical τ_s in both the CMIP5 and CMIP6 models (shown by the curved axis in Figure 2.7(c)). A slight increase in the ensemble mean spatial correlations is seen from CMIP5 (0.188) to CMIP6 (0.267), due to increases seen amongst individual models between CMIP5 and CMIP6, such as CESM2 from

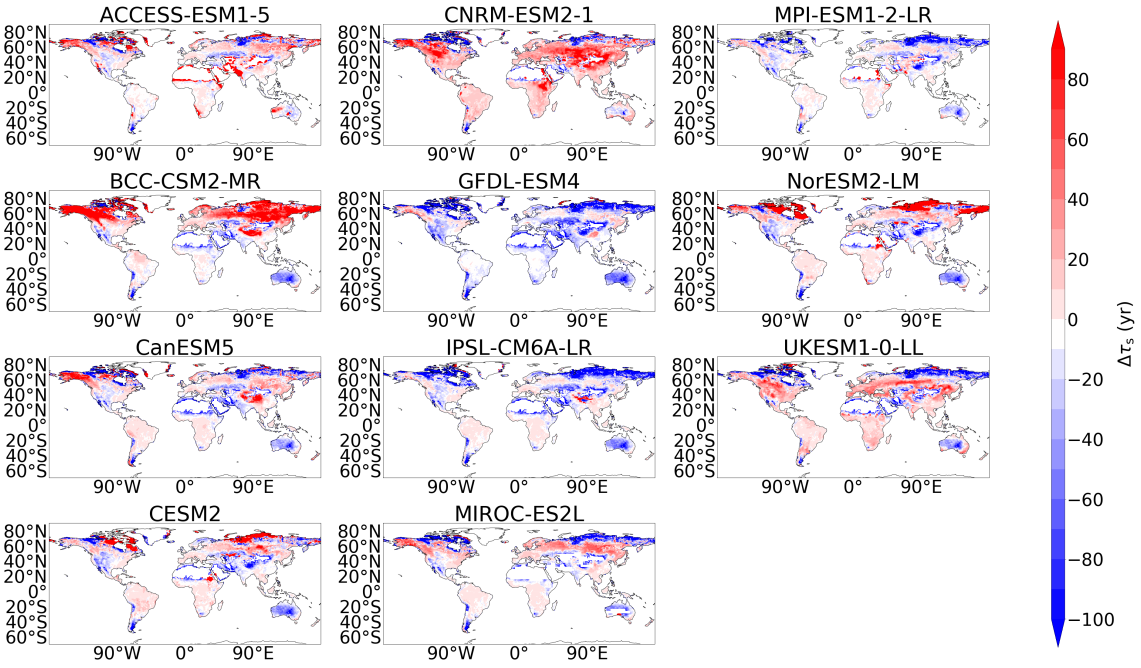

Figure 2.11: Maps of the difference in soil carbon turnover time (τ_s) between the historical simulation of each CMIP6 model and the benchmark datasets.

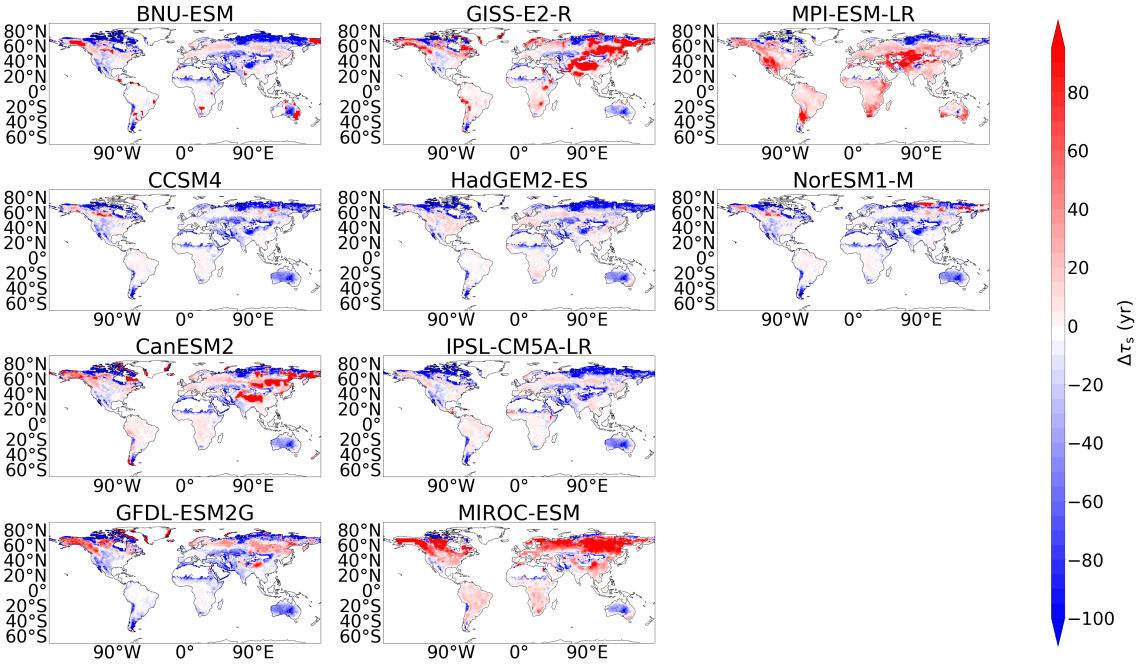

Figure 2.12: Maps of the difference in soil carbon turnover time (τ_s) between the historical simulation of each CMIP5 model and the benchmark datasets.

CCSM4, MPI-ESM1.2-LR from MPI-ESM-LR, and NorESM2-LM from NorESM1-M. However, the consistency of modelled τ_s with the benchmark datasets remains low. A particularly large range is seen in the spatial standard deviations of τ_s amongst the CMIP6 models, which is an increased range from CMIP5 (shown by the radial axis in Figure 2.7(c)). The CMIP6 models with the most extreme overestimations of the spatial standard deviations compared with the derived benchmark value (NorESM2-LM, CESM2, and ACCESS-ESM1.5), are also found to have large RMSEs (Figure 2.8(c)). Amongst the remaining CMIP6 models, the RMSEs for modelled τ_s remain relatively consistent between CMIP5 and CMIP6.

2.3.4 Drivers of soil carbon spatial patterns

2.3.4.1 Global drivers

A negligible correlation (≈ 0) is found between the benchmark estimates of soil carbon and NPP, suggesting that soil carbon is not spatially correlated to NPP in the real world. On the other hand, soil carbon and NPP (C_s-NPP) are found to be significantly correlated in the models in both CMIP5 and CMIP6. The C_s-NPP spatial correlation was found to be greater than 0.5 for six out of the ten CMIP5 ESMs and eight out of the eleven models in CMIP6 (Figure 2.13(a)). However, a low spatial correlation is found in the CMIP6 models CESM2 (0.134), NorESM2-LM (0.261), and BCC-CSM2-MR (0.214), values most consistent with the benchmark datasets. The C_s-τ_s spatial correlations found in the CMIP6 models tend to underestimate the positive correlation seen in the benchmark datasets (Figure 2.13(a)). The majority of CMIP6 models see a negligible or slightly negative C_s-τ_s spatial correlation, despite a low positive correlation produced by the benchmark datasets. The models BCC-CSM2-MR, MIROC-ES2L, and NorESM2-LM are most consistent with the benchmark C_s-τ_s correlation.

The modelled NPP to temperature (NPP-T) spatial correlations in CMIP6 are consistent with the positive relationship seen in the benchmark datasets, however the magnitude of this positive correlation varies amongst the models (Figure 2.13(b)). The magnitude of the positive NPP-T correlation is underestimated in CanESM5, GFDL-ESM4, and NorESM2-LM, but is otherwise relatively consistent amongst the CMIP6 models. Nonetheless, a much greater range in the modelled NPP-T correlations is seen amongst the CMIP5 models, suggesting an improved representation of this relationship in CMIP6. The variation in modelled NPP-θ correlations remains in CMIP6, with models disagreeing in the sign and magnitude of the correlation of NPP to soil moisture. The modelled NPP-θ correlation is the most consistent with the benchmark correlations in GFDL-ESM4, MPI-ESM1.2-LR and UKESM1-0-LL (Figure 2.13(b)).

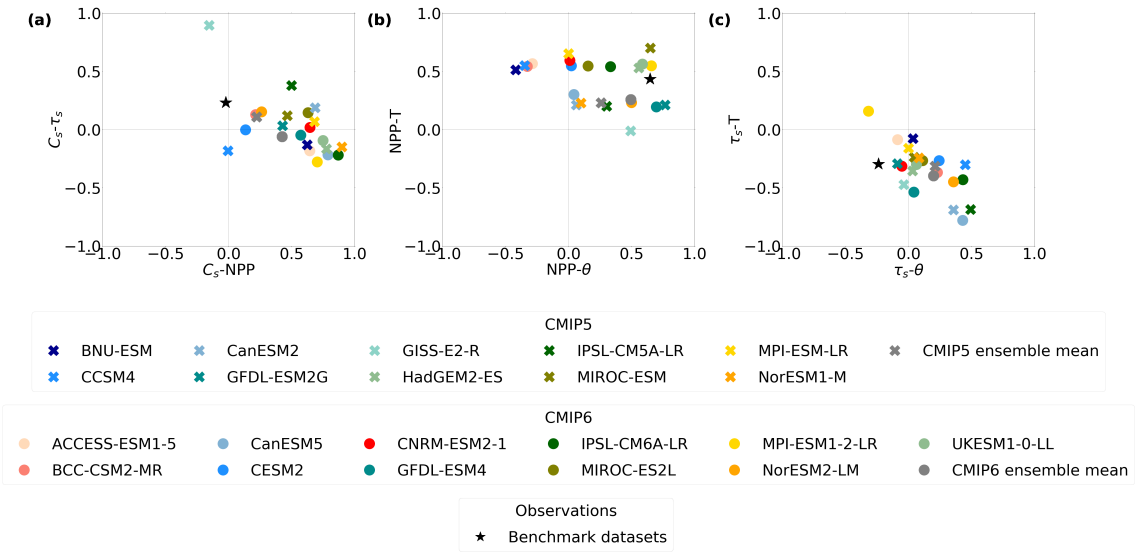

Figure 2.13: Scatter plots investigating the relationships between different Pearson correlation coefficients of climate variables, (a) C_s-τ_s against C_s-NPP, (b) NPP-T against NPP-θ, (c) τ_s-T against τ_s-θ.

It is generally agreed across the models in CMIP6 and CMIP5 that τ_s and temperature (T) are negatively correlated, with the exception of MPI-ESM1.2-LR where a slight positive correlation is seen (Figure 2.13(c)). This is consistent with the negative τ_s-T correlation derived in the benchmark dataset. There is variation amongst the models in the magnitude of the negative correlation, with a significant overestimation seen in CanESM5. A negative correlation is also seen in the τ_s-θ correlation derived with the benchmark datasets. Inconsistencies with this empirical relationship are seen amongst the models in both CMIP5 and CMIP6, with many negligible and positive correlations deduced (Figure 2.13(c)). The exception is again MPI-ESM1.2-LR, which in this case is the model most consistent with the benchmark τ_s-θ correlation.

2.3.4.2 Regional drivers

The spatial correlations of modelled C_s-NPP are shown to be overestimated at every latitude in both CMIP6 and CMIP5, compared with the equivalent correlations derived from the empirical datasets. It can be seen that the CMIP6 ensemble mean C_s-NPP correlation has an even larger positive bias compared with the benchmark correlation than in CMIP5. The empirical data sees a reduced C_s-NPP correlation in the northern latitudes, whereas a slight but less significant reduction is seen in the models (Figure 2.14(a)). The spatial correlation between C_s-τ_s is shown to vary against latitude in the empirical datasets, where a greater correlation is seen in the tropical and northern latitude regions, and a negligible correlation is seen in the mid-latitudes (Figure 2.14(b)). The CMIP6 models simulate the negligible C_s-τ_s seen in the mid-latitudes relatively consistently with the

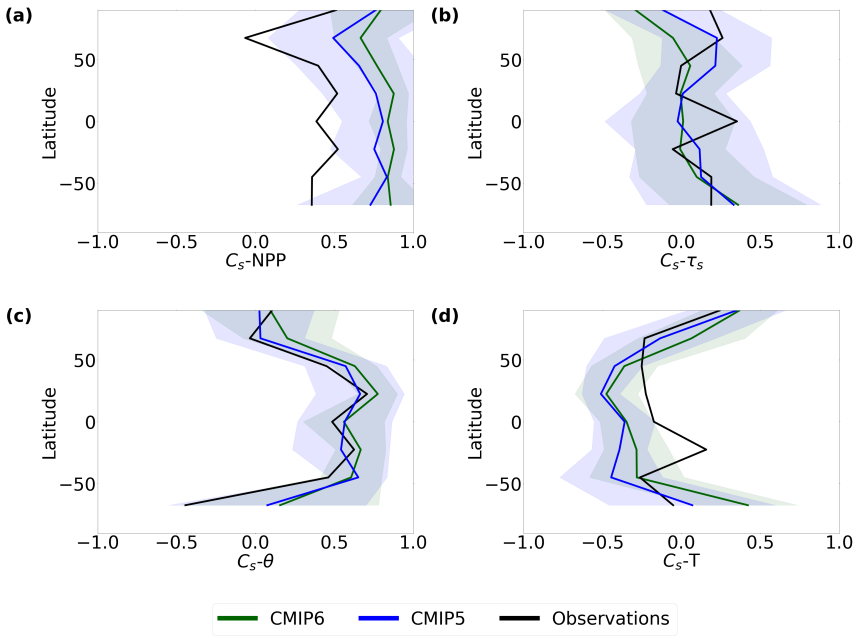

Figure 2.14: The latitudinal profiles of the Pearson correlation coefficients between soil carbon and (a) NPP (C_s-NPP), (b) soil carbon turnover time (C_s-τ_s), (c) soil moisture (C_s-θ), and (d) temperature (C_s-T).

benchmark data, where an improved consistency is seen from CMIP5. However, the CMIP6 models do not simulate the tropical and northern latitude positive C_s-τ_s correlations, where a negligible modelled correlation remains in these regions. CMIP5 is more consistent with the benchmark correlations than in CMIP6, where a positive modelled correlation C_s-τ_s is seen (Figure 2.14(b)).

The spatial correlation between modelled soil carbon and soil moisture (C_s-θ) is consistent with the correlations seen in the benchmark datasets at every latitude, with an improvement seen in the tropical correlation patterns in CMIP6 compared with CMIP5 (Figure 2.14(c)). Both the CMIP5 and CMIP6 ensembles span the benchmark C_s-θ correlation, though large model ranges in the C_s-θ sensitivity are seen across all latitudes. However, there is a reduced ensemble uncertainty in the C_s-θ correlation from CMIP5 to CMIP6 in low and mid latitudes. An overestimation of the negative C_s-T correlation seen in the benchmark datasets is present in both the CMIP5 and CMIP6 models, except the high latitudes (Figure 2.14(d)). This modelled C_s-T correlation is particularly underestimated in the lower tropical latitudes, where a greater positive correlation is seen here in the benchmark datasets. Figure 2.14(d) suggests a slight improvement in the modelled tropical C_s-T correlation in CMIP6, and a worsening of modelled C_s-T in the high latitudes than in CMIP5, when compared with the C_s-T correlations in the benchmark datasets.

2.4 Discussion

2.4.1 Soil carbon stocks

2.4.1.1 Global total soil carbon

Simulating global soil carbon stocks that are consistent with empirical data is required to produce reliable projections of future soil carbon storage and emission (Todd-Brown et al., 2013). This study deduces a CMIP6 ensemble mean global total soil carbon of 1206 $\pm$ 445 PgC (Table 2.4), using regridded model resolutions (see Methods). It is noted that Ito and Oikawa (2002) states a CMIP6 ensemble of 1553 $\pm$ 672 PgC; however, the full soil carbon profile is considered for CESM2 and NorESM2-LM, as opposed to a depth of 1 m considered in this study. Additionally, this study deduces a comparable CMIP5 ensemble mean global soil carbon value of 1480$\pm$ 810 PgC (Table 2.5) using equivalent dates in the historical simulation (1950–2000). Todd-Brown et al. (2013) state an ensemble mean soil carbon value of 1520 $\pm$ 770 PgC in CMIP5; however, the Todd-Brown et al. (2013) study includes the models BCC-CSM1.1, CESM1-CAM5, and INM-CM4, which are missing from the analysis in this study due to data availability. Anav et al. (2013) present a CMIP5 ensemble mean soil carbon value of 1502 $\pm$ 798 PgC, but this calculation includes multiple model versions (for example, LR and MR) from the same modelling centre in their ensemble. A caveat of this evaluation study is the non-independent nature of CMIP ESMs, where for example CESM2 and NorESM2-LM share the same Land Surface Model (LSM). Additionally, the ensembles included here do not necessarily represent all models that exist within each CMIP generation. However, the evaluation completed here allows for general improvements in the simulation of soil carbon stocks and fluxes between the CMIP5 and CMIP6 generations to be noted and key areas for future model development to be highlighted.

Despite a suggestion of a reduced spread in model estimates of global total soil carbon within CMIP6 relative to CMIP5, discrepancies remain in the consistency of these estimates with the observations between the two CMIP generations. It should also be noted that CMIP6 does not simply contain updated versions of every model in CMIP5: some new models are included and some CMIP5 models not included in CMIP6. These factors together with the uncertainty associated with empirical datasets have resulted in no robust conclusion being drawn on the improvement of soil carbon simulation in CMIP6 compared with CMIP5. Due to the potential significant feedback that exists between soil carbon and global climate, this lack of consistency reduces our confidence in future projections of climate change (Friedlingstein et al., 2006; Gregory et al., 2009; Arora et al., 2013;

Friedlingstein et al., 2014).

2.4.1.2 Spatial soil carbon patterns

Modelled soil carbon was found to be poorly spatially correlated with the empirical data amongst models in both CMIP5 and CMIP6 (Figure 2.7(a)). An improvement in CMIP6 ESMs was seen in the spatial patterns across the mid-latitudes, which were generally overestimated in CMIP5. However, significant underestimations of modelled soil carbon in the northern latitudes still remain, which have a significant impact on model predictions of global total soil carbon stocks (Figure 2.3(a)). This systematic underestimation was previously reported in the literature as a limitation of the CMIP5 models, where Todd-Brown et al. (2013) found northern latitude soil carbon to be less consistent with the empirical data than on a global scale. This limitation remains amongst models in the CMIP6 generation, where it was found that the majority of CMIP6 models underestimate northern latitude soil carbon stocks regardless of whether the global soil carbon stocks are underestimated.

However, an exception to this northern latitude underestimation is seen within CMIP6 in the models CESM2 and NorESM2-LM. These ESMs include the land surface model (LSM) CLM5 (Lawrence et al., 2019), which is the first LSM to include the representation of vertically resolved soil carbon in their CMIP simulations. This representation enables the inclusion of separate carbon pools at varying depths in the soil, which aims to more consistently simulate soil carbon with the real world (Koven et al., 2013). This is of particular importance in the northern latitudes, where carbon stocks are expected to exist at much greater depths than the 1 m considered in this study (Tarnocai et al., 2009; Ran et al., 2021). This can be seen in Table 2.3, where increased magnitudes of soil carbon stocks are shown when increased depths are considered using the empirical datasets. A more thorough evaluation of soil carbon in both CESM2 and NorESM2-LM is suggested for future research, with a particular focus on this improved northern latitude soil carbon stocks simulation, however this evaluation of deeper soil carbon stocks (below 1 m) is beyond the scope of this study.

Accurately simulating soil carbon in the northern latitude regions is of particular importance as it is a major part of the total global soil carbon pool (Jackson et al., 2017). Additionally, much of the carbon stored in these soil is held within permafrost, which is known to be particularly sensitive to climate change. Permafrost thaw under climate change has the potential to release significant amounts of carbon into the atmosphere over a short period of time with increased warming (Schuur et al., 2015; Zimov et al., 2006; Burke et al., 2017; Hugelius et al., 2020), representing a significant feedback within the climate system. Permafrost

dynamics are generally poorly represented in ESMs, where Burke et al. (2020) found CMIP6 ESMs to have a similar representation compared with CMIP5. Underestimating soil carbon in the northern latitudes may result in underestimating the impact of this feedback in future climate change projections. Future improvements are needed to improve the simulation of soil carbon stocks globally, but particularly within the northern latitudes.

2.4.2 Drivers of soil carbon change

To allow for a more in-depth understanding of the inconsistencies found between modelled and empirical soil carbon, the simulation of above and below-ground controls of soil carbon were also evaluated. Simulations of contemporary soil carbon can be disaggregated into the effects of litterfall, which is well approximated by plant Net Primary Productivity (NPP), and effective soil carbon turnover time (τ_s), which is affected by both temperature and moisture of the soil (Koven et al., 2015). If models are to reliably simulate soil carbon in a way that is consistent with empirical data, the spatial drivers of soil carbon, NPP and τ_s, must also be simulated consistently with empirical data. Isolating the effects of NPP and τ_s on soil carbon helps us to break down the simulation of soil carbon to help understand the limitations and inconsistencies seen amongst the models.

2.4.2.1 NPP

An improved simulation of NPP is suggested in the ESMs included from CMIP6, compared with the ESMs from CMIP5. This conclusion is suggested by: an increased number of models in our CMIP6 ensemble have global total NPP values consistent with empirical data (Table 2.6), the overestimation of tropical NPP amongst CMIP5 models is seen to be reduced amongst the CMIP6 models (Figure 2.3(b)), and more agreement is seen within CMIP6 relative to CMIP5 in the simulation of mid and northern latitude NPP (Figure 2.6(b)). Modelled NPP was found to be robustly more consistent with the empirical data in our CMIP6 ensemble compared with the CMIP5 ensemble in all statistical evaluation metrics. Since CMIP5, multiple models have seen an addition of a dynamic nitrogen cycle (Davies-Barnard et al., 2020), where the models with nitrogen cycles are highlighted in Figure 2.8 by the shaded bars. The results suggest an improvement in the simulation of NPP with the addition of dynamic nitrogen in models. However, CMIP6 models that do not represent a nitrogen cycle also mostly see improvements in the simulation of NPP, suggesting NPP is more constrained by observations in the newest generation of models. CanESM5 is the only ESM within CMIP6 included here to not see an overall improvement in the simulation of NPP, where NPP is found to be overestimated compared with the benchmark dataset. It is likely that the inclusion of a nitrogen cycle in this model would limit this overes-

timated NPP and improve consistency with the observations (Zhang et al., 2014; Exbrayat et al., 2013a).

Despite this apparent improved simulation of NPP in CMIP6, the spatial correlation between modelled soil carbon and NPP was found to be inconsistent with the equivalent empirically derived relationship. This result was previously shown for the CMIP5 models (Todd-Brown et al., 2013), and has been more recently shown for the CMIP6 models (Georgiou et al., 2021), both agreeing with the results found here. The majority of CMIP6 models were found to have positive C_s-NPP spatial correlations, opposed to a negligible spatial correlation found in the observations (Figure 2.13(a)). Despite NPP driving the spatial pattern of soil carbon stocks due to carbon input from vegetation, a positive correlation was not expected in the real world due to regions with high soil carbon not correlating with regions of high NPP. For example, in the observational derived data soil carbon stocks are greatest in the northern latitudes due to long turnover times in these regions, whereas NPP is lower due to cold temperatures in these regions limiting vegetation growth. The three CMIP6 models which did not significantly overestimate this correlation (CESM2, NorESM2-LM, and BCC-CSM2-MR) are three of the models with the most empirically consistent proportion of soil carbon stocks in the northern latitudes. Conversely the tropical regions see high NPP values, but warmer temperatures result in faster turnover times and lower soil carbon stocks. NPP is expected to increase in the future under climate change (Kimball et al., 1993; Friedlingstein et al., 1995; Amthor, 1995), which means an overly positive correlation in models could result in a subsequent increase in modelled projections of soil carbon stocks. An overestimation of future soil carbon storage could result in an overestimation of the future carbon sink and an inaccurate global carbon budget (Todd-Brown et al., 2013; Friedlingstein et al., 2022).

2.4.2.2 Soil carbon turnover time

The systematic improvements suggested from the evaluation of NPP simulation within our CMIP6 ensemble are not suggested for the simulation of τ_s, where the simulation of τ_s appears to remain inconsistent with the empirical data in CMIP6 from CMIP5. Improvements are suggested within CMIP6 relative to CMIP5, such as more agreement within the ensemble in the mid-latitudes and tropical regions, however less agreement is seen in the northern latitudes (Figure 2.6(c)). Northern latitude τ_s is generally underestimated in models, which corresponds to the underestimation of soil carbon seen in these regions. This has been previously identified in ESMs, where it was found that the underestimation of global τ_s amongst the CMIP5 models is primarily due to low values in the northern latitudes (Wu et al., 2018). The reduced agreement in CMIP6 is due to long τ_s values existing

in the northern latitudes of CESM2 and NorESM2-LM, alongside the general ensemble underestimations (Figure 2.11). The increased northern latitude τ_s values in CESM2 and NorESM2-LM are likely to be due to the representation of vertically resolved soil carbon pools, which allows for differential τ_s values for pools at varying depths. Despite these individual improvements since CMIP5, large discrepancies exist within the CMIP6 ensemble between modelled and empirical τ_s.

To simulate τ_s consistently with observations, the relationship of τ_s to both temperature (T) and moisture (θ) must also be simulated in a way that is consistent with observations. Generally, the τ_s-T relationship is consistently simulated, however there is variation in the modelled temperature sensitivity of τ_s across the ensemble. The τ_s-θ relationship is less consistently represented, where the majority of CMIP6 models do not match the empirically derived relationship. Despite a positive dependence of soil respiration on soil moisture in the empirical data, many of the CMIP6 models display a contradictory positive τ_s-θ correlation (Figure 2.13). Many of the models use functions that increase respiration with soil moisture (see Section 2.2.1) so the increase of τ_s with increasing soil moisture indicated by positive τ_s-θ correlations in the models is unexpected. It is noted that this effect occurs most strongly in the models with a very strongly negative τ_s-T relationship (Figure 2.13(c)), so it could in fact be an artefact of a negative correlation between temperature and soil moisture. In this context it is also important to consider what soil moisture in LSMs represents (Koster et al., 2009). The aim within models is to act as the lower boundary condition for atmospheric models, therefore their soil parameters may historically have been tuned to give appropriate evaporation rates and not necessarily to represent the soil moisture itself in an accurate way, so it may be more relevant to consider the large-scale emergent patterns of τ_s than the direct relationships between soil moisture and respiration. It is noted that the empirical relationship shows τ_s reducing with higher soil moisture, which suggests that the observations are picking up more on longer turnover times in dry areas rather than in saturated areas such as peatlands. This may be due to having only surface soil moisture information, whereas peatlands, while saturated at depth, typically have a water table $\sim$10 cm below the surface and can be very dry at the surface (Evans et al., 2021). Thus while models do not include the necessary processes for peat formation (Chadburn et al., 2022), this is unlikely to be the cause of the discrepancy since it would lead to even more of a positive τ_s-θ correlation in the models.

Different processes control soil carbon formation in different ecosystems, including stabilisation by clay particles, transformation by microbes, nitrogen and phosphorous availability, etc. (Witzgall et al., 2021). In the present study, the largest

discrepancies in both soil carbon and turnover times are seen in permafrost and peatland areas (see Figure 2.4 and Figure 2.11). For example, the west Siberian peatland complex stands out on the majority of the panels in these figures as an area of high model error. This is partly because the soil carbon turnover times and quantities of soil carbon are largest in these regions, but also partly due to the specific controlling processes in these ecosystems. A key part of soil carbon development in permafrost regions is the fact that organic material can be preserved in frozen soil, including via cryoturbation and yedoma deposits, which have not yet been thoroughly represented in models (Beer, 2016; Zhu et al., 2016). There are a variety of other factors, such as plants storing significantly more of their carbon below-ground instead of above-ground in cold climates, and recalcitrant vegetation such as mosses, which are not represented in most ESMs (Sulman et al., 2021). Peatland formation is controlled primarily by waterlogging, which reduces oxygen available for decomposition, but there are a huge number of additional physical and biogeochemical feedbacks that take place (Waddington et al., 2015). These kinds of small-scale processes and inhomogeneities are difficult to resolve in global models with $\sim$100 km^{-2} grid cells, and this should be weighed up against their relative impact on global carbon budgets when considering including these processes in ESMs. However, it is suggested that the large-scale discrepancies such as in the permafrost and large peatland areas can and should be resolved in future model versions.

The results found here suggest much of the uncertainty associated with modelled soil carbon stocks can be attributed to the simulation of below-ground processes. The apparent improved consistency of NPP with empirical data suggests considerable efforts have been made to achieve an improved representation of above-ground processes in CMIP6 ESMs since the release of the CMIP5 ensemble. However, the same improvements are not apparent in the simulation of τ_s as systemic limitations remain in the new generation of ESMs considered in this study, suggesting the same progress on the model development of below-ground processes has not been achieved between CMIP5 and CMIP6. Moreover, focus on above-ground processes without consideration of below-ground processes can result in inconsistencies of soil carbon stocks. For example, the inclusion of a nitrogen cycle has been shown to lead to a reduction in soil carbon in the model, see Figure 6 in Wiltshire et al. (2021), so tuning of the baseline turnover rates is required to keep soil carbon stocks consistent with observed values.

The required improvement of soil carbon pool turnover rates has previously been identified for the CMIP5 ensemble (Nishina et al., 2014), and more recently, Ito et al. (2020) find that the difference in turnover times amongst the CMIP6 models

is responsible for approximately 88% of the variation seen in global soil carbon stocks amongst the models and state that constraining key parameters which control soil carbon turnover processes is a key area for future model development. A key development seen in CMIP6 since CMIP5 is the representation of vertically resolved soil carbon. Models which simulate non-vertically resolved soil carbon typically turn over all the carbon based on the temperature near the soil surface. This could lead to reduced quantities of soil carbon and an underestimation of northern latitude soil carbon stocks, due to near surface soil being warmer than the deeper soil, and as turnover is known to respond exponentially to temperature (Davidson and Janssens, 2006). Overall, further improvements in the representation of soil carbon turnover time, with a particular focus on the northern latitudes, is identified as a key area for future model development.

2.5 Conclusions

The ability of Earth System Models (ESMs) to simulate present-day soil carbon (C_s) is vital to help produce reliable long term projections of climate change. In this chapter the most up-to-date ESMs, which are part of the CMIP6 ensemble, have been evaluated against empirical datasets to assess their ability to represent C_s and related controls: Net Primary Productivity (NPP) and the effective soil carbon turnover time ($\tau_s = C_s/R_h$). The evaluation is completed by comparison with the previous generation of CMIP5 ESMs, to assess where improvements have been made and to identify priorities for future model development. Below the key conclusions from this chapter are listed:

1. The spatial patterns of soil carbon in CMIP6 models appear to be more in agreement with each other than they were in CMIP5 and are more consistent with observations in the mid-latitudes, although caveats around the uncertainty in observations and the ensemble design make this conclusion uncertain. However, soil carbon is still heavily underestimated in high northern latitudes (with the exception of two CMIP6 models that represent deep soil carbon).

2. Overall no significant improvements are suggested in the simulation of the observed spatial pattern of C_s across the globe from the CMIP5 to the CMIP6 generation.

3. There is good evidence that spatial patterns of contemporary NPP are better simulated in CMIP6 than in CMIP5 generation models, when compared to satellite-derived estimates.

4. However, spatial patterns of τ_s continue to be poorly represented in CMIP6 models, in comparison to estimates derived from observational datasets of soil carbon and heterotrophic respiration (R_h).

5. Importantly, soil carbon simulations in both the CMIP5 and CMIP6 ESM generations seem to be spuriously highly-correlated with NPP, which may make soil carbon in these models over responsive to future projected changes in NPP.

Taken together, these conclusions point to a need for a much greater emphasis on improving the representation of below-ground soil processes in next generation (CMIP7) of ESMs. In the next chapter, the future trajectories of C_s in these CMIP models will be analysed, to investigate the uncertainties associated with the future soil carbon response to climate change.

Chapter 3

Projections of soil carbon in CMIP6 Shared Socioeconomic Pathways

Abstract

As discussed in Chapter 1, the overall response of soil carbon to human-induced climate change is uncertain due to competing soil carbon driven feedbacks. In Chapter 2, present day simulations of soil carbon within ESMs were evaluated against observational datasets. In this chapter, projections of future changes to soil carbon storage during the 21$^{\mathrm{st}}$ century are investigated in CMIP6 ESMs, with comparisons to CMIP5 ESMs, to assess the uncertainty of the soil carbon induced feedback to climate change. This chapter includes a breakdown into contributions from changes in Net Primary Productivity (NPP) and soil carbon turnover time (τ_s).

3.1 Introduction

The global response of soil carbon presents one of the greatest uncertainties in determining the overall response of land carbon storage to CO_2-induced climate change (Bradford et al., 2016; Nishina et al., 2015). Global soils represent the largest store of terrestrial carbon in the Earth's climate system (Canadell et al., 2021; Ciais et al., 2013; Jobbágy and Jackson, 2000), and the carbon fluxes involved in the exchange of CO_2 between the soil and atmosphere are sensitive to changes in climate. However, the overall effect of climate change on soil carbon is not very well constrained due to competing soil carbon driven feedbacks (Arora et al., 2020; Todd-Brown et al., 2014).

Soil carbon driven feedbacks to climate change include the negative CO_2 fertilisation feedback, which results from increased carbon inputs from increased Net Primary Productivity (NPP, Π_N) (Schimel et al., 2015), and the positive

climate feedback due to increased carbon losses via heterotrophic respiration and reduced soil carbon turnover time (τ_s) (Crowther et al., 2016). The balance between these effects will determine the future response of soil carbon stocks under a changing climate (Todd-Brown et al., 2014; Friedlingstein et al., 2003). During the 20$^{\text{th}}$ century, the Earth's terrestrial surface has been a carbon sink which results in the land surface providing a negative feedback to climate change (Canadell et al., 2021; Ciais et al., 2013; Cox et al., 2000). However, to understand the long term potential terrestrial carbon storage, the response of global soil carbon to climate change must be quantified (Friedlingstein et al., 2020).

Earth System Models (ESMs) are used to predict changes to soil carbon stocks and to help quantify the feedback to climate change. Previously, analysis has been completed using ESMs from the Coupled Model Intercomparison Project phase 5 (CMIP5) (Taylor et al., 2012), for which Todd-Brown et al. (2014) found variations in ESM projections of 21$^{\text{st}}$ century changes in soil carbon, NPP and τ_s. In this study, projections of future soil carbon change (ΔC_s) are analysed in the next phase of CMIP ESMs, known as CMIP6, with the aim to evaluate estimates of ΔC_s during the 21$^{\text{st}}$ century and to make comparisons with the previous generation of CMIP5 ESMs. Additionally, the input and output carbon fluxes to and from the soil (which are controlled by NPP and τ_s) are considered, along with how they contribute to overall soil carbon changes.

3.2 Methods

3.2.1 Earth system models

This chapter uses output data from ten CMIP6 ESMs (Eyring et al., 2016; Meehl et al., 2014). The CMIP6 ESMs included in this study are: ACCESS-ESM1-5, BCC-CSM2-MR, CanESM5, CESM2, CNRM-ESM2-1, IPSL-CM6A-LR, MIROC-ES2L, MPI-ESM1-2-LR, NorESM2-LM, and UKESM1-0-LL. Additionally, output data from nine CMIP5 ESMs is used to allow for comparison between the CMIP generations (Taylor et al., 2012). The CMIP5 ESMs included in this chapter are: BNU-ESM, CanESM2, GFDL-ESM2G, GISS-E2-R, HadGEM2-ES, IPSL-CM5A-LR, MIROC-ESM, MPI-ESM-LR, and NorESM1-M. The ESMs included were chosen due to the availability of the data required for the analysis presented below (CMIP6: https://esgf-node.llnl.gov/search/cmip6/ and CMIP5: (https://esgf-node.llnl.gov/search/cmip5/).

Information about the ESMs, including the Land Surface Model (LSM) component, are presented for both the CMIP6 and CMIP5 models in Tables 2.1

and 2.2 in Chapter 2. It was noted in Chapter 2 that the modelled responses of soil decomposition to climate remained similar between CMIP6 and CMIP5 (Todd-Brown et al., 2013). The sensitivity of decomposition to temperature within CMIP6 ESMs is represented variously by the Q_{10} equation, the Arrhenius equation, 'hill' functions (defined to increase to an optimal point and then decrease) or some linear approximation of these functions. Similarly, the representation of the sensitivity of decomposition to moisture in CMIP6 ESMs is by a monotonically increasing function or by 'hill' functions of various sorts (Todd-Brown et al., 2014). A key change highlighted in CMIP6 ESMs from CMIP5 ESMs is the inclusion of an interactive nitrogen cycle, which is much more commonly included in CMIP6 compared with CMIP5. For example, the following CMIP6 models include nitrogen limitations: ACCESS-ESM1.5, CESM2, MIROC-ES2L, MPI-ESM1.2-LR, NorESM2-LM and UKESM1-0-LL, whereas NorESM1-M is the only CMIP5 model included in this study which simulates this process. An additional update in CMIP6 is the representation of vertically resolved soil carbon in CESM2 and NorESM2-LM (Lawrence et al., 2019).

Using ESM output variables, soil carbon (C_s) is defined as the sum of carbon stored in soils and the carbon stored in the vegetation litter (CMIP variable *cSoil* $+$ CMIP variable *cLitter*). This allows for a more consistent comparison between the models due to differences in how soil carbon and litter carbon are defined (Arora et al., 2020; Todd-Brown et al., 2013). For models that do not report a separate litter carbon pool (*cLitter*), soil carbon is taken to be simply the *cSoil* variable. Spatial C_s is given in units of kg m^{-2}, and global total C_s are given in units of PgC, which are calculated using an area weighted sum (using the model land surface fraction, CMIP variable *sftlf*).

$$\tau_s = \frac{C_s}{R_h} \tag{3.1}$$

Additionally, ESM output variables were used to define the soil carbon driven climate feedbacks. Net Primary Productivity (NPP, CMIP variable *npp*) is defined as the net carbon assimilated by plants via photosynthesis minus loss due to plant respiration, and is used to represent the net carbon input flux to the system. Heterotrophic Respiration (R_h, CMIP variable *rh*) is defined as the microbial respiration within global soils, and was used to define an effective global soil carbon turnover time (τ_s), see Equation 3.1. τ_s is defined as the ratio of mean soil carbon to mean heterotrophic respiration (where the mean represents an area weighted global average). Carbon fluxes (NPP and R_h) are considered as area

weighted global totals in units of PgC yr^{-1}, and therefore effective τ_s has units of yr^{-1}.

3.2.2 Future climate scenarios

The analysis in this study considers three future climate scenarios defined by CMIP, which are used to consider different levels of global warming. The future scenarios are designed to relate future releases of greenhouse gases and aerosols to different socioeconomic projections. The CMIP6 'Shared Socioeconomic Pathways' (SSPs) considered in this chapter are: SSP126, SSP245, SSP585, which run from 2015 to 2100 (O'Neill et al., 2014; O'Neill et al., 2016). These pathways are chosen to allow for comparison with the CMIP5 'Representative Concentration Pathways' (RCPs): RCP2.6, RCP4.5 and RCP8.5, which run from 2005 to 2100 (Meinshausen et al., 2011). It is noted that the SSP and RCP concentration scenarios are not identical, but they are similar enough to enable helpful comparisons between CMIP5 and CMIP6 projections.

Descriptions of the different SSPs and RCPs are given below. (1) The RCP2.6 and SSP126 pathways represent a future where action is taken to reduce emissions of greenhouse gases. SSP126 follows approximately RCP2.6 global forcing pathway with SSP1 socioeconomic conditions. The SSP1 conditions represents a future drive in sustainable action and the RCP2.6 forcing is approximately a radiative forcing of 2.6 W m^{-2} by 2100 relative to pre-industrial conditions. (2) The RCP4.5 and SSP245 pathways represent a middle pathways in terms of climate action. SSP245 follows approximately RCP4.5 global forcing pathway with SSP2 socioeconomic conditions. The SSP2 conditions represents a more mixed climate driven future and the RCP4.5 forcing is approximately a radiative forcing of 4.5 W m^{-2} by 2100 relative to pre-industrial conditions. (3) The RCP8.5 and SSP585 pathways represent a fossil fuel intensive future, where little effort is taken to reduce anthropogenic emissions of greenhouse gases. SSP585 follows approximately RCP8.5 global forcing pathway with SSP5 socioeconomic conditions. The RCP8.5 forcing is approximately a radiative forcing of 8.5 W m^{-2} by 2100 relative to pre-industrial conditions.

For the reference period from which change is calculated, the CMIP 'Historical' simulation was considered, where the simulation runs from 1850 to 2005 in CMIP5 and from 1850 to 2015 in CMIP6. A change, $\triangle$, was defined as the difference between the last decade of the 21^{st} century (time averaged between 2090 and 2100), and the last decade of the CMIP5 historical simulation (time averaged between 1995-2005). These dates are considered to allow for consistency between the CMIP generations. If a timeseries is considered, the historical

reference period (historical simulation time averaged between 1995-2005) was taken away from the entire future climate simulation (e.g. SSP126 minus the historical reference period).

3.2.3 Isolating the controls of soil carbon change

Soil carbon (C_s) can be defined as the product of the heterotrophic respiration (R_h) and the soil carbon turnover time (τ_s) as shown by Equation 3.2, based on the definition of τ_s seen in Equation 3.1. Future soil carbon stocks can be defined as initial soil carbon ($C_{s,0}$) plus a change in soil carbon (ΔC_s), as shown by Equation 3.3, where the subscript 0 denotes the initial state (historical simulation time averaged between 1995-2005). Equation 3.3 can be expanded to give Equation 3.4, which can be simplified to give Equation 3.5. It is common to assume linearity and neglect the product of change term ($\Delta R_h \Delta \tau_s$), however in this study the term was included in the breakdown analysis.

$$C_s = R_h \tau_s \tag{3.2}$$

$$C_{s,0} + \Delta C_s = (R_{h,0} + \Delta R_h)(\tau_{s,0} + \Delta \tau_s) \tag{3.3}$$

$$C_{s,0} + \Delta C_s = R_{h,0}\tau_{s,0} + \tau_{s,0}\Delta R_h + R_{h,0}\Delta \tau_s + \Delta R_h \Delta \tau_s \tag{3.4}$$

$$\Delta C_s = \tau_{s,0}\Delta R_h + R_{h,0}\Delta \tau_s + \Delta R_h \Delta \tau_s \tag{3.5}$$

To isolate the above and below ground effects on soil carbon, the separate effects due to changes in Net Primary Productivity (NPP, Π_N) and changes due to soil carbon turnover (τ_s) are considered (Todd-Brown et al., 2014). However, to converse carbon the difference between the global fluxes NPP and R_h in a transient climate must be taken into account. The difference is defined as the Net Ecosystem Productivity (NEP, F_L), as shown in Equation 3.6.

$$F_L = \Pi_N - R_h \tag{3.6}$$

Equation 3.6 can be substituted into Equation 3.5, to obtain an equation for ΔC_s in terms of Π_N, F_L and τ_s (Equation 3.7).

$$\Delta C_s = \tau_{s,0}\Delta(\Pi_N - F_L) + (\Pi_{N,0} - F_{L,0})\Delta \tau_s + \Delta(\Pi_N - F_L)\Delta \tau_s \tag{3.7}$$

It is noted that at equilibrium the initial NEP ($F_{L,0}$) will equal zero, as initial NPP ($\Pi_{N,0}$) and initial R_h ($R_{h,0}$) will equal one another. However, due to defining our ini-

tial state as the start of the historical simulation, some amount of climate change has already occurred and $F_{L,0}$ will be therefore be small but non-negligible. Moreover, ESMs include additional carbon fluxes that cause changes to the resultant soil carbon inputs include terms, such as: grazing, harvest, land use change, and fire (Todd-Brown et al., 2014). Due to including the NEP term which accounts for the difference between NPP and R_h, these affects are included within the terms in Equation 3.7 which make up the overall soil carbon response in ESMs.

Finally, Equation 3.7 can expanded to give Equation 3.8, and the individual responses which make up the total change in soil carbon (ΔC_s) can be broken-down into six components:

$$\begin{aligned}\Delta C_s = \tau_{s,0}\Delta\Pi_N \; - \; \tau_{s,0}\Delta F_L \; + \; \Pi_{N,0}\Delta\tau_s \; - \; F_{L,0}\Delta\tau_s \\ + \; \Delta\Pi_N\Delta\tau_s \; - \; \Delta F_L\Delta\tau_s\end{aligned} \tag{3.8}$$

Equation 3.7 is exact for given time-varying values of Π_N, τ_s and F_L, but in this form it does not cleanly separate into contributions due to changes in each of these factors. A linear approximation is therefore made (assuming $\Delta\Pi_N/\Pi_N \; << \; 1$ and $\Delta\tau_s/\tau_s \; << \; 1$), which allows for the cross terms to be neglected ($\Delta NPP\Delta\tau_s \approx \Delta\Pi_N\Delta\tau_s$ and $\Delta NEP\Delta\tau_s \approx \Delta F_L\Delta\tau_s$). The additional terms in Equation 3.8 are defined as given below.

$$\Delta C_{s,NPP} \approx \tau_{s,0}\Delta\Pi_N \tag{3.9}$$

$$\Delta C_{s,NEP} \approx -\tau_{s,0}\Delta F_L \tag{3.10}$$

$$\Delta C_{s,\tau} \approx \Pi_{N,0}\Delta\tau_s \tag{3.11}$$

$$\Delta C_{s,\tau_{NEP}} \approx -F_{L,0}\Delta\tau_s \tag{3.12}$$

3.3 Results

3.3.1 Projected changes in soil carbon

A reduced spread in projected end of 21$^{\text{st}}$ century estimates of soil carbon change (ΔC_s) is seen in CMIP6 compared to CMIP5. This reduced spread is seen in Figure 3.1, where projections of ΔC_s by 2100 in CMIP6 are compared with CMIP5 across the different future scenarios. The reduced range of projec-

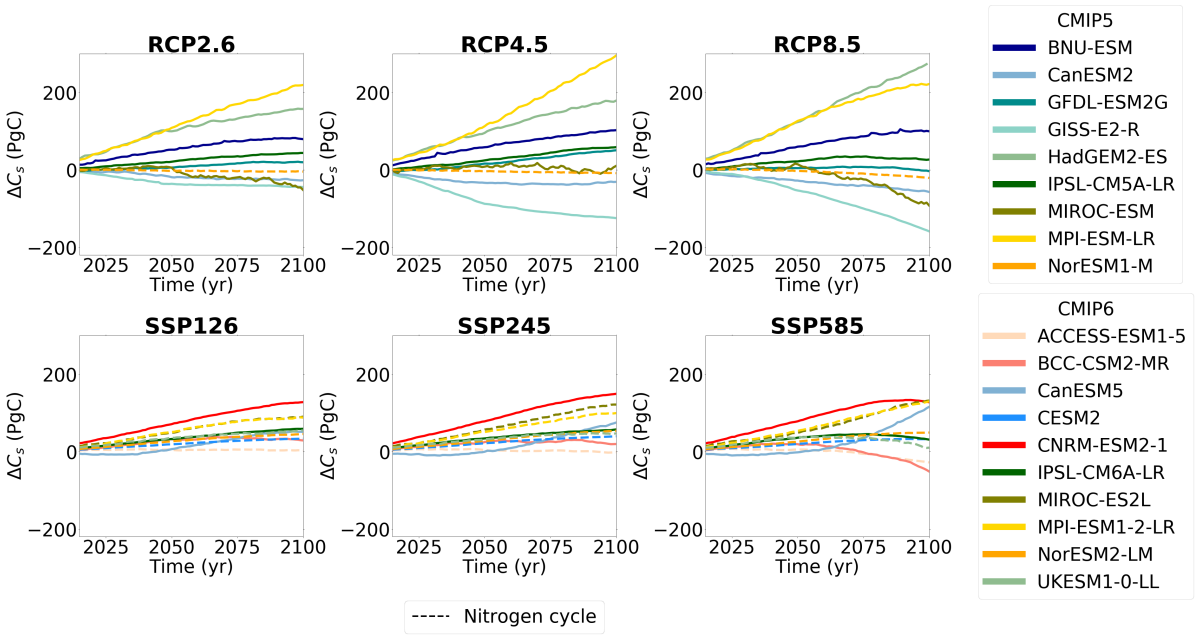

Figure 3.1: Projected future change in soil carbon (ΔC_s) in CMIP5 (top row) and CMIP6 (bottom row) ESMs, for future scenarios SSP126 and RCP2.6, SSP245 and RCP4.5, SSP585 and RCP8.5.

tions is seen across all future scenarios (SSP126 and RCP2.6, SSP245 and RCP4.5, SSP585 and RCP8.5), where the range in CMIP6 is consistently less than 50% the equivalent range in CMIP5 (Figure 3.1). This reduced uncertainty is also suggested by a reduced standard deviation about the ensemble mean ΔC_s in CMIP6 from CMIP5, which is also consistently reduced by 50% across all future climate scenarios (Tables 3.1 and 3.2).

It is noted that the large range in the CMIP5 projected estimates of ΔC_s is a result of the large increases in soil carbon storage in HadGEM2-ES and MPI-ESM-LR, and the large soil carbon losses in GISS-E2-R (Figure 3.1). The updated equivalent CMIP6 models UKESM1-0-LL (from HadGEM2-ES) and MPI-ESM1-2-LR (from MPI-ESM-LR) have projected estimates of ΔC_s which are more consistent with the other models in the CMIP6 ensemble. However, an updated CMIP6 version of the GISS-E2-R model is not included in this analysis of this study, which could contribute to the reduced uncertainty.

CMIP6 projections more robustly estimate an increase in C_s by 2100, compared with CMIP5 where both increases and decreases in C_s are projected (Figure 3.1). The future responses of soil carbon in CMIP5 range from an increase of 23.2% (HadGEM2-ES) to a decrease of 6.50% (GISS-E2-R) in RCP8.5, with approximately half of the models showing increases and half showing decreases in soil carbon across all future scenarios (Table 3.2). In CMIP6, the future responses of soil carbon range from an increase of 12.5% (MPI-ESM1-2-LR) to

a decrease of 2.25% (ACCESS-ESM1.5) in SSP585, however the majority of models predict an increase in soil carbon across all future scenarios (Table 3.1).

Despite this, larger CO_2 increases in CMIP6 (SSP585 compared with SSP126), does not always relate to an increased soil carbon storage. By contrast the majority of CMIP5 models project an increased magnitude in estimated ΔC_s with increased forcing (Figure 3.1). In SSP585, half the CMIP6 models (CESM2, CNRM-ESM2-1, IPSL-CM6A-LR, NorESM2-LM, and UKESM1-0-LL) estimate a smaller increase or a greater decrease in ΔC_s, when compared with SSP126. This effect is most prominent in UKESM1-0-LL, where a turning point from increasing to decreasing soil carbon is seen in the mid-century of the SSP585 projections (Figure 3.2). This is opposed to an estimated increase in soil carbon storage with increased forcing, which is generally seen in CMIP5 and the remaining CMIP6 models (CanESM5, MIROC-ES2L, and MPI-ESM1-2-LR).

CMIP6 sees a notable variation amongst the spatial pattern of estimated ΔC_s (Figure 3.3). More commonly positive ΔC_s values are seen in the northern latitudes (ACCESS-ESM1-5, CNRM-ESM2-1, IPSL-CM6A-LR, MIROC-ES2L, MPI-ESM1-2-LR, and UKESM1-0-LL), where the greatest increases are seen in models which saw large global increases (CNRM-ESM2-1 and MIROC-ES2L) (Table 3.1). However negative values are seen in three ESMs (BCC-CSM2-MR, CESM2, and NorESM2-LM). Variation amongst the ESMs is also seen in the tropical regions, where increases in soil carbon can be seen in six of the CMIP6 ESMs (BCC-CSM2-MR, CanESM5, CESM2, MIROC-ES2L, and NorESM2-LM), but decreases are seen in the remaining four ESMs (ACCESS-ESM1-5, CNRM-ESM2-1, IPSL-CM6A-LR, and UKESM1-0-LL).

3.3.2 Future changes to soil carbon controls

The projected change in soil carbon (ΔC_s) is a result of the changing input and output fluxes under climate change. To a first order, the response of C_s will be determined by changes to Net Primary Productivity (NPP) and the soil carbon turnover time (τ_s). In this section, future projections of these soil carbon fluxes are analysed in CMIP6 and CMIP5 ESMs.

3.3.2.1 Net Primary Productivity

Net Primary Productivity (NPP) is projected by CMIP6 ESMs to increase during the 21$^{\text{st}}$ century, with a greater increase with increasing climate forcing (increased CO_2). This result is consistent with the projections of ΔNPP amongst the CMIP5 models (Figure 3.4). However, projections in CMIP6 ESMs show disagreement in the magnitude of ΔNPP by 2100 across all future climate scenarios, where a

Table 3.1: Table presenting the absolute (PgC) and relative (%) change in 21$^{\text{st}}$ century soil carbon for each CMIP6 model, for each future SSP scenario.

Earth System Model	Absolute ΔC_s (PgC)			Relative ΔC_s (%)		
	SSP126	SSP245	SSP585	SSP126	SSP245	SSP585
ACCESS-ESM1.5	3.44	-0.98	-23.4	0.38	-0.108	-2.55
BCC-CSM2-MR	31.8	22.3	-35.2	1.76	1.23	-1.95
CanESM5	50.6	66.7	97.7	3.41	4.49	6.59
CESM2	32.7	38.3	32.4	1.77	2.08	1.76
CNRM-ESM2-1	126	145	132	6.79	7.85	7.11
IPSL-CM6A-LR	57.6	55.0	35.5	8.86	8.45	5.46
MIROC-ES2L	87.3	118	126	5.88	7.94	8.5
MPI-ESM1-2-LR	86.2	97.9	123	8.79	9.98	12.5
NorESM2-LM	44.1	52.0	48.7	1.81	2.13	1.99
UKESM1-0-LL	52.3	46.9	17.5	2.96	2.65	0.988
Ensemble mean	55.4 $\pm$ 31.8	58.3 $\pm$ 44.3	50.3 $\pm$ 57.8	4.53 $\pm$ 2.95	4.24 $\pm$ 3.51	3.67 $\pm$ 4.50

Table 3.2: Table presenting the absolute (PgC) and relative (%) change in 21st century soil carbon for each CMIP5 model, for each future RCP scenario.

Earth System Model	Absolute ΔC_s (PgC)			Relative ΔC_s (%)		
	RCP2.6	RCP4.5	RCP8.5	RCP2.6	RCP4.5	RCP8.5
BNU-ESM	81.4	99.7	100	11.6	14.2	14.3
CanESM2	-25.4	-32.7	-53.5	-1.65	-2.12	-3.47
GFDL-ESM2G	19.9	47.9	0.278	1.40	3.37	0.020
GISS-E2-R	-43.1	-122	-146	-1.92	-5.43	-6.50
HadGEM2-ES	154	174	258	13.9	15.6	23.2
IPSL-CM5A-LR	42.5	57.1	28.4	3.14	4.22	2.10
MIROC-ESM	-39.9	-1.53	-80.0	-1.55	-0.059	-3.11
MPI-ESM-LR	211	277	219	6.94	9.09	7.19
NorESM1-M	-3.94	-7.60	-17.7	-0.723	-1.40	-3.26
Ensemble mean	44.1 $\pm$ 84.2	54.7 $\pm$ 111	34.3 $\pm$ 127	3.45 $\pm$ 5.66	4.17 $\pm$ 6.97	3.38 $\pm$ 9.24

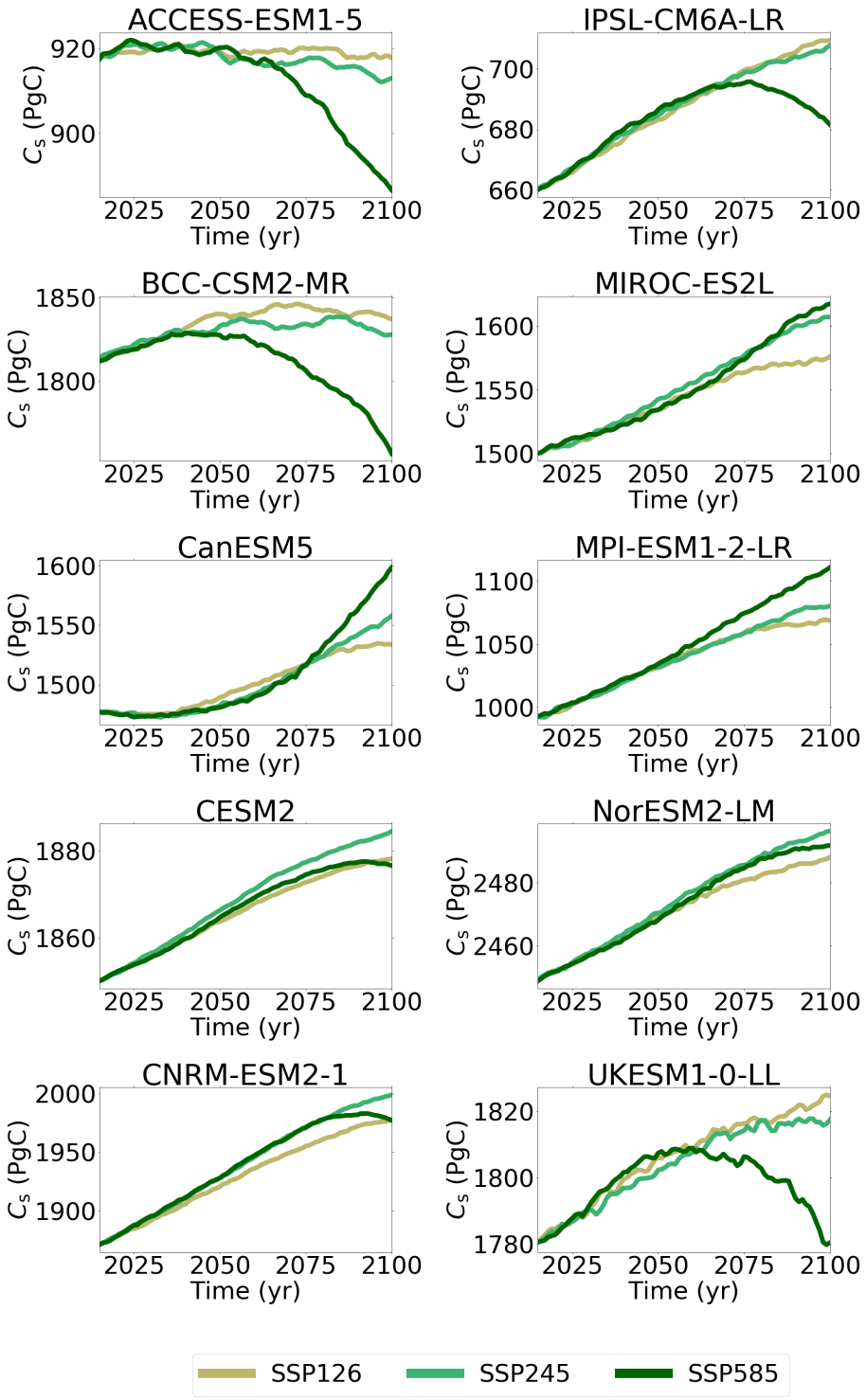

Figure 3.2: Timeseries of projected future soil carbon (C_s) in CMIP6 ESMs for future scenarios SSP126, SSP245, SSP585.

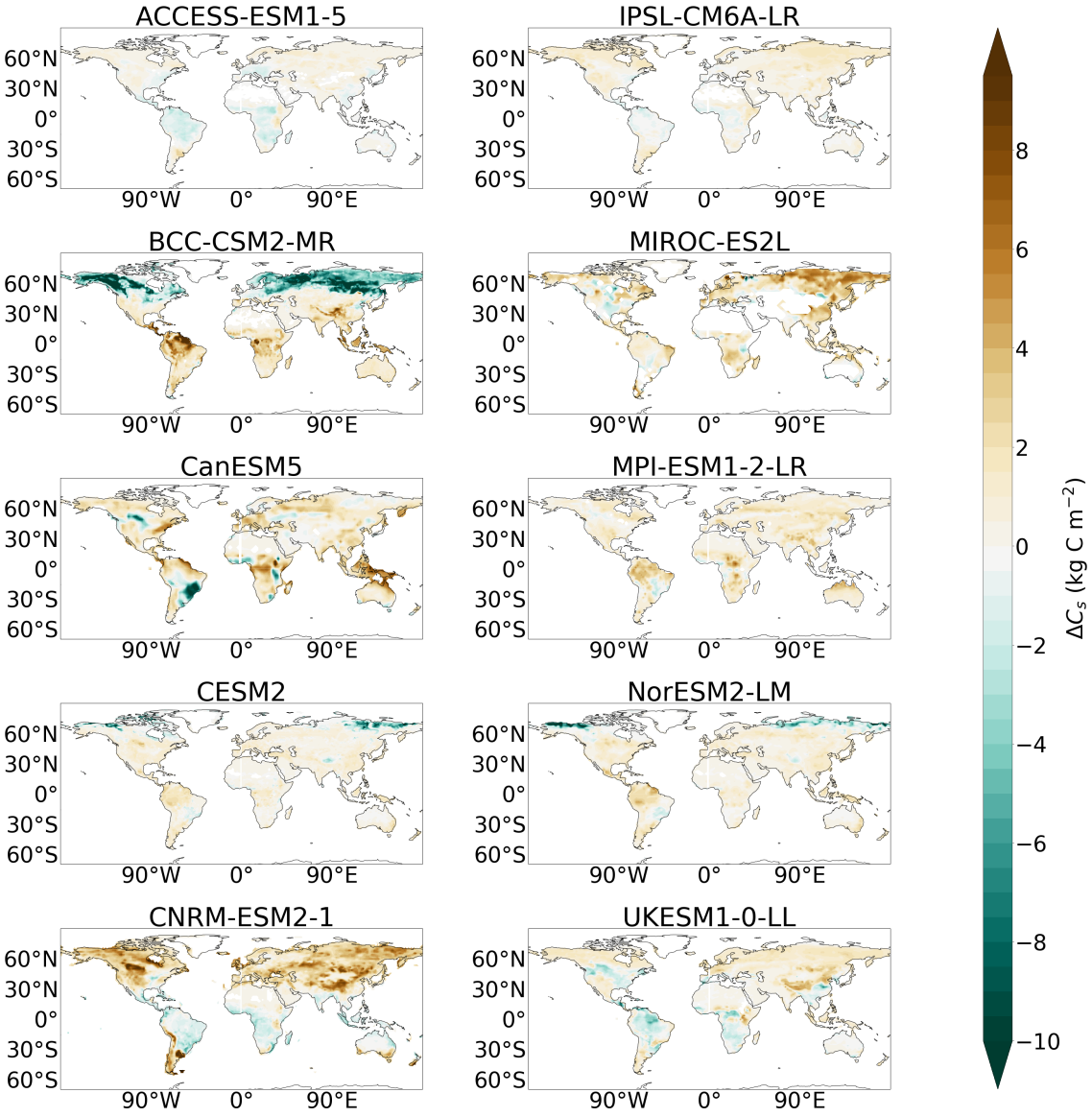

Figure 3.3: Map plots showing the change in soil carbon (ΔC_s) in SSP585 for each CMIP6 ESM.

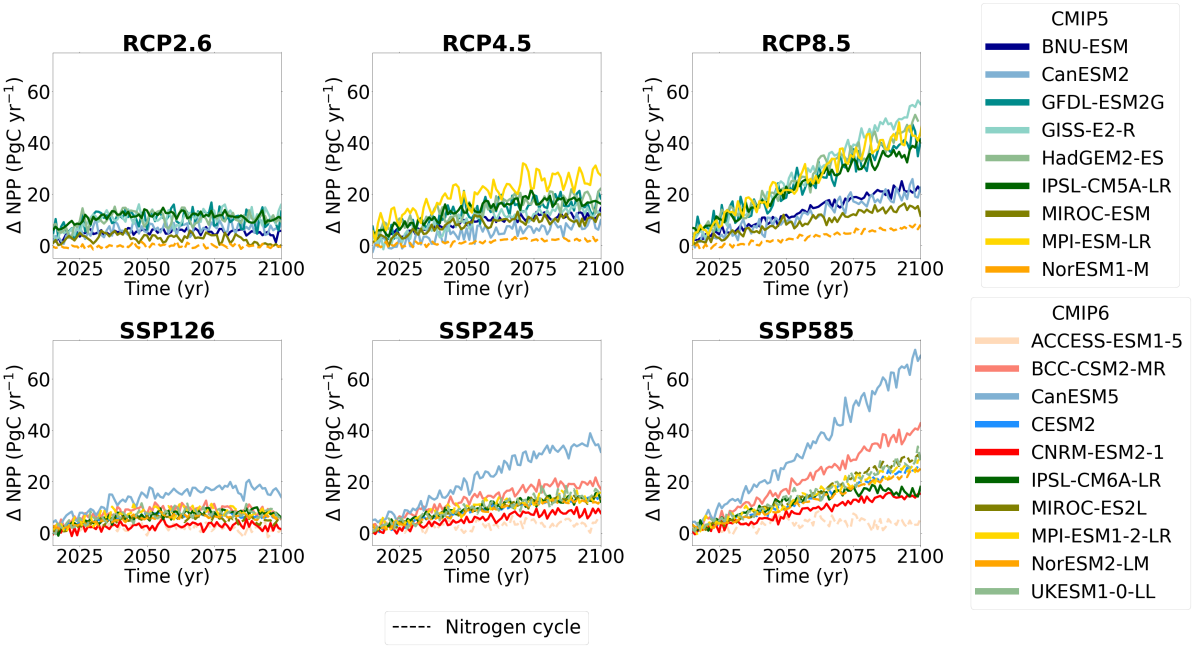

Figure 3.4: Projected future change in Net Primary Production (Δ NPP) in CMIP5 (top row) and CMIP6 (bottom row) ESMs, for future scenarios SSP126 and RCP2.6, SSP245 and RCP4.5, SSP585 and RCP8.5.

projected CMIP6 ensemble increase of 24.6 $\pm$ 16.9 PgC yr^{-1} is seen in SSP585. The largest projections of ΔNPP amongst the CMIP6 models are seen in CanESM5 and BCC-CSM2-MR, where increases of 65.8 PgC yr^{-1} and 39.4 PgC yr^{-1}, respectively, are projected by 2100 under SSP585. This is compared to ACCESS-ESM1-5 which has the lowest projected changes amongst the CMIP6 models, where an increase of 4.07 PgC yr^{-1} projected by 2100 under SSP585 (Table 3.3).

The CMIP6 ensemble sees a slightly increased range in end of century ΔNPP compared with CMIP5, across all future scenarios (Tables 3.3 and 3.4). This is slightly surprising, as there is a reduced range of present day NPP in CMIP6, as shown in Chapter 2. Figure 3.4 suggests the increased range is mostly due to outlying projections of ΔNPP. A cluster of ESMs in CMIP6 which have similar projections of ΔNPP is seen (CESM2, MIROC-ES2L, MPI-ESM1-2-LR, NorESM2-LM, and UKESM1-0-LL), which is made up of ESMs which simulate an interactive nitrogen cycle. ACCESS-ESM1-5 is the only model which simulates interactive nitrogen and does not predict consistent ΔNPP with the other nitrogen ESMs in CMIP6. The projections of ΔNPP in ACCESS-ESM1-5 is consistent with the projections of NorESM1-M in CMIP5, which is the only CMIP5 model considered here which simulates interactive nitrogen.

Table 3.3: Table presenting the change in 21$^{\text{st}}$ century NPP and τ_s for each CMIP6 model.

Earth System Model	Δ NPP (PgC yr^{-1})			$\Delta\tau_s$ (yr)		
	SSP126	SSP245	SSP585	SSP126	SSP245	SSP585
ACCESS-ESM1.5	1.66	3.58	4.07	-0.828	-1.69	-2.35
BCC-CSM2-MR	8.37	19.7	39.4	-4.53	-8.52	-14.0
CanESM5	17.4	35.4	65.8	-3.09	-5.01	-7.10
CESM2	6.46	13.7	24.5	-5.05	-8.63	-14.1
CNRM-ESM2-1	2.28	7.96	14.3	-1.624	-4.19	-8.05
IPSL-CM6A-LR	8.40	13.9	16.2	-0.938	-1.81	-2.83
MIROC-ES2L	4.90	13.9	29.0	-1.52	-3.37	-6.23
MPI-ESM1-2-LR	7.84	14.3	25.9	-0.555	-1.27	-2.30
NorESM2-LM	6.33	12.6	23.3	-7.16	-11.0	-18.9
UKESM1-0-LL	8.08	15.2	28.1	-2.37	-4.52	-8.25
Ensemble mean	7.44 $\pm$ 4.01	13.6 $\pm$ 8.71	24.6 $\pm$ 16.9	-2.30 $\pm$ 2.047	-4.55 $\pm$ 3.35	-7.65 $\pm$ 5.65

Table 3.4: Table presenting the change in 21st century NPP and τ_s for each CMIP5 model.

Earth System Model	Δ NPP (PgC)			$\Delta\tau_s$ (yr)		
	RCP2.6	RCP4.5	RCP8.5	RCP2.6	RCP4.5	RCP8.5
BNU-ESM	4.52	11.7	21.9	-0.165	-1.36	-3.42
CanESM2	6.94	8.73	20.4	-2.95	-2.71	-6.23
GFDL-ESM2G	9.47	16.4	40.13	-1.53	-3.31	-6.38
GISS-E2-R	11.5	13.6	51.4	-2.26	-3.88	-8.03
HadGEM2-ES	10.4	18.2	45.5	-0.40	-1.24	-3.66
IPSL-CM5A-LR	10.4	16.9	37.0	-1.50	-2.91	-5.31
MIROC-ESM	0.350	9.98	14.4	-2.66	-8.32	-12.4
MPI-ESM-LR	-	26.6	43.0	-0.280	-5.00	-8.17
NorESM1-M	-0.388	2.25	6.94	-0.151	-0.645	-1.55
Ensemble mean	5.32 $\pm$ 4.74	12.4 $\pm$ 7.42	28.1 $\pm$ 16.8	-1.26 $\pm$ 1.13	-3.26 $\pm$ 2.21	-6.13 $\pm$ 3.03

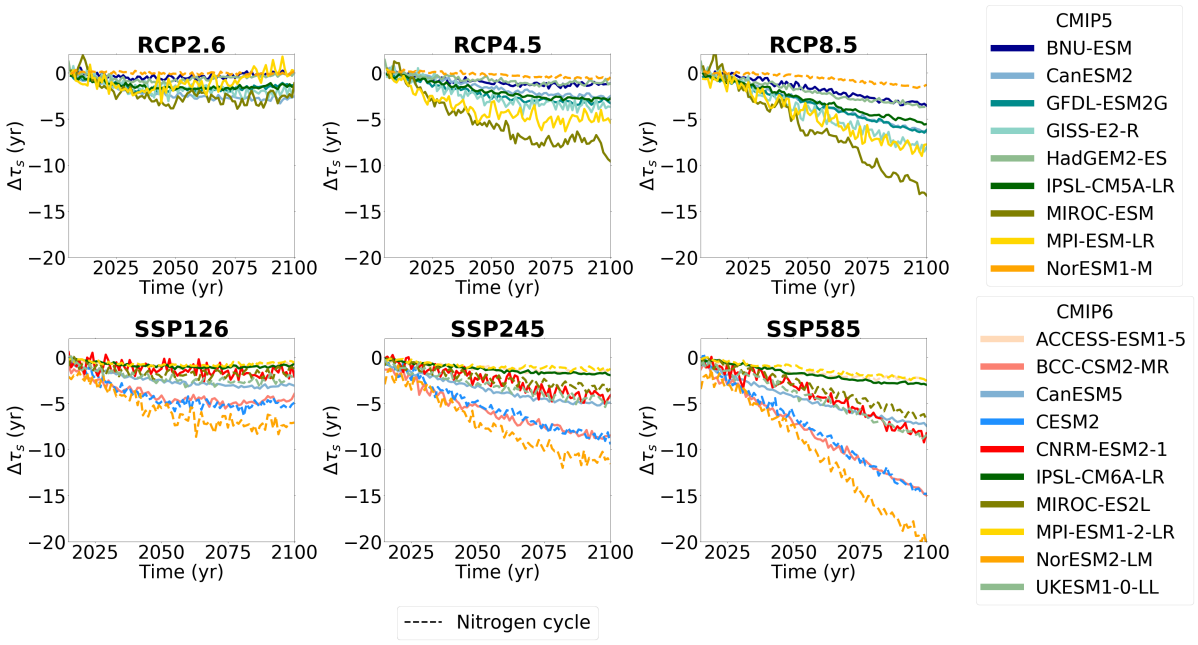

Figure 3.5: Projected future change in soil carbon turnover time ($\Delta\tau_s$) in CMIP5 (top row) and CMIP6 (bottom row) ESMs, for future scenarios SSP126 and RCP2.6, SSP245 and RCP4.5, SSP585 and RCP8.5.

3.3.2.2 Soil carbon turnover time

Soil carbon turnover time (τ_s) is projected by CMIP6 ESMs to decrease by 2100, with a greater reduction seen with increase climate forcing scenario. This result is consistent with the projections of $\Delta\tau_s$ amongst the CMIP5 models (Figure 3.5). However, it is found that variation exists amongst the CMIP6 ESMs end of century estimates, where a projected CMIP6 ensemble reduction of -7.65 $\pm$ 5.65 years is seen in SSP858. The greatest reductions in end of century effective global τ_s amongst the CMIP6 models is seen in BCC-CSM2-MR, CESM2 and NorESM2-LM, with reductions of at least 14 years in SSP585. The CMIP6 models with the least change in effective global τ_s are ACCESS-ESM1-5, IPSL-CM6A-LR, and MPI-ESM1-2-LR, with reductions of only around 2 years under SSP585 (Table 3.1).

The range of $\Delta\tau_s$ estimates by 2100 is not reduced in CMIP6 compared with CMIP5 in any of the climate forcing scenarios (Tables 3.3 and 3.4). The increased range is primarily due to the τ_s reductions seen in the CMIP6 models NorESM2-LM, CESM2 and BCC-CSM2-MR (Figure 3.5). These three ESMs have large present day soil carbon stocks, especially in the northern latitudes (see Table 2.4 in Chapter 2), and subsequently large turnover times in these regions (see Table 2.6 in Chapter 2). Additionally, CESM2 and NorESM2-LM are the only models within CMIP6 to simulate vertically resolved soil carbon.

3.3.3 Breaking down the projected changes in soil carbon

To understand the projected end of century changes in soil carbon storage (ΔC_s) in ESMs, the individual responses of soil carbon due to changes in NPP ($\Delta C_{s,NPP}$) and the response due to changes in τ_s ($\Delta C_{s,\tau}$) were diagnosed, as shown in Figure 3.6. Future ΔC_s (blue bars) is mostly a result of the net effect of the linear terms: $\Delta C_{s,NPP}$ (dark green bars) and $\Delta C_{s,\tau}$ (red bars). However, there are also non-negligible contributions from the non-linear term: $\Delta NPP \Delta \tau_s$ (black bars), and a small addition due to the non-equilibrium terms: $\Delta C_{s,NEP}$ (light green bars), $\Delta C_{s,\tau_{NEP}}$ (pink bars), and ΔNEP$\Delta \tau_s$ (grey bars).

The magnitudes of the changes due to each of these terms varies amongst the ESMs in CMIP6. Specifically, the ΔNPP and $\Delta \tau_s$ contributions to changes in future soil carbon stocks ($\Delta C_{s,NPP}$ and $\Delta C_{s,\tau}$, respectively) are generally greater than the subsequent ΔC_s projected by the model, especially in the more extreme climate scenarios. For example, in SSP585 there is range of approximately 170 PgC in overall soil carbon change (ΔC_s), from +132 PgC in CNRM-ESM2-1 to -35 PgC in BCC-CSM2-MR. However, the $\Delta C_{s,NPP}$ contribution has a much larger range of 1442 PgC, from +95 PgC in ACCESS-ESM1-5 to +1517 PgC in NorESM2-LM. Similarly, $\Delta C_{s,\tau}$ has a range of 756 PgC, from -115 PgC in ACCESS-ESM1-5 to -871 PgC in NorESM2-LM (Figure 3.6).

The magnitude of change seen from the individual feedbacks ($\Delta C_{s,NPP}$ and $\Delta C_{s,\tau}$) is not obviously related to the resultant magnitude of soil carbon change (Figure 3.7). For example, NorESM2-LM projects large $\Delta C_{s,NPP}$ and $\Delta C_{s,\tau}$ values (+1517 PgC and -871 PgC in SSP585, respectively), however a relatively small overall change in soil carbon (+49 PgC in SSP585). Conversely, CNRM-ESM2-1 projects smaller $\Delta C_{s,NPP}$ and $\Delta C_{s,\tau}$ values (+667 PgC and -413 PgC in SSP585, respectively), but a larger overall change in soil carbon (+132 PgC in SSP585). The change in soil carbon is determined by the relationship between all the contributing terms to the overall ΔC_s response, as opposed to the absolute size of a given contribution (Figure 3.6).

Surprisingly, a very strong correlation is found amongst the ESMs in CMIP6 (r^2 value of 0.97), between the linear terms $\Delta C_{s,NPP}$ and $\Delta C_{s,\tau}$ (Figure 3.8(a)). This leads to these terms partially cancelling each other, with a resultant relatively small net change in soil carbon. A correlation of this type is not seen in CMIP5 (r^2 value of 0.084, Figure 3.8(a)). This correlation amongst CMIP6 ESMs results in ΔC_s being more clustered in CMIP6 compared to CMIP5, despite a similarly large variation in the individual contributions. The strong CMIP6 correlation ($r^2 = 0.97$) remains when the fractional changes ($\Delta C_{s,NPP}/C_{s,0}$ and $\Delta C_{s,\tau_{NPP}}/C_{s,0}$, where

$C_{s,0}$ is initial soil carbon stocks) are plotted instead (Figure 3.8(b)).

The differences in ESM projections of ΔC_s are also found to be partly due to differing magnitudes of the non-linear term ($\Delta NPP \Delta \tau_s$). ESM projected magnitudes of $\Delta NPP \Delta \tau_s$ are found to be relatively large, especially in the more extreme climate scenario SSP585 (Figure 3.6). In SSP585, a range from a reduction of 11 PgC (ACCESS-ESM1-5) to a reduction of 599 PgC (BCC-CSM2-MR) is found amongst the CMIP6 models, and in some cases values greater than the overall change in soil carbon are seen (BCC-CSM2-MR, CanESM5, CESM2, NorESM2-LM, and UKESM1-0-LL). This term is significant when there are large and counteracting magnitudes of ΔNPP and $\Delta \tau_s$ (Figures 3.4 and 3.5, respectively), which results in a non-negligible product.

Additionally, to obtain the overall change in soil carbon seen in the models, contributions from the non-equilibrium terms ($\Delta C_{s,NEP}$, $\Delta C_{s,\tau_{NEP}}$, and ΔNEP$\Delta \tau_s$) must also be included (Figure 3.6). The non-equilibrium terms are due to the difference between NPP and R_h under transient climate change. The contribution from these terms is found to be relatively small in most models, but not in all. The change in soil carbon due to the change in NEP ($\Delta C_{s,NEP}$, where $NEP = NPP - R_h$) is often found to be greater in the models which see greater magnitudes of $\Delta C_{s,NPP}$ and $\Delta C_{s,\tau}$. In SSP585, projections of $\Delta C_{s,NEP}$ amongst CMIP6 models range from a reduction of 333 PgC in NorESM2-LM to a gain of 8.74 PgC in ACCESS-ESM1-5. In CMIP5, exceptions where greater $\Delta C_{s,NEP}$ terms are found in the GISS-E2-R and MPI-ESM-LR models, implying the models are far from equilibrium at the end of the century.

3.4 Discussion

The response of soil carbon storage to CO_2-induced climate change remains a major uncertainty in ESMs projections (Canadell et al., 2021). Projected changes in soil carbon (ΔC_s) have previously been investigated for CMIP5 ESMs, where Todd-Brown et al. (2014) found disagreement in projected ΔC_s amongst ESMs within the ensemble. The results presented in this chapter suggest a reduced spread in end of 21$^{\text{st}}$ century projections of ΔC_s amongst CMIP6 ESMs compared to the previous generation of CMIP5 ESMs (Figure 3.1). This chapter presented a breakdown of ΔC_s into components arising from changes in Net Primary Productivity (NPP, Π_N) and soil carbon turnover time (τ_s), named $\Delta C_{s,NPP}$ and $\Delta C_{s,\tau}$, respectively. CMIP6 ESMs were found to predict a wider range of magnitudes of $\Delta C_{s,NPP}$ and $\Delta C_{s,\tau}$ than in CMIP5, despite the apparent reduction in ΔC_s projection uncertainty within the CMIP6

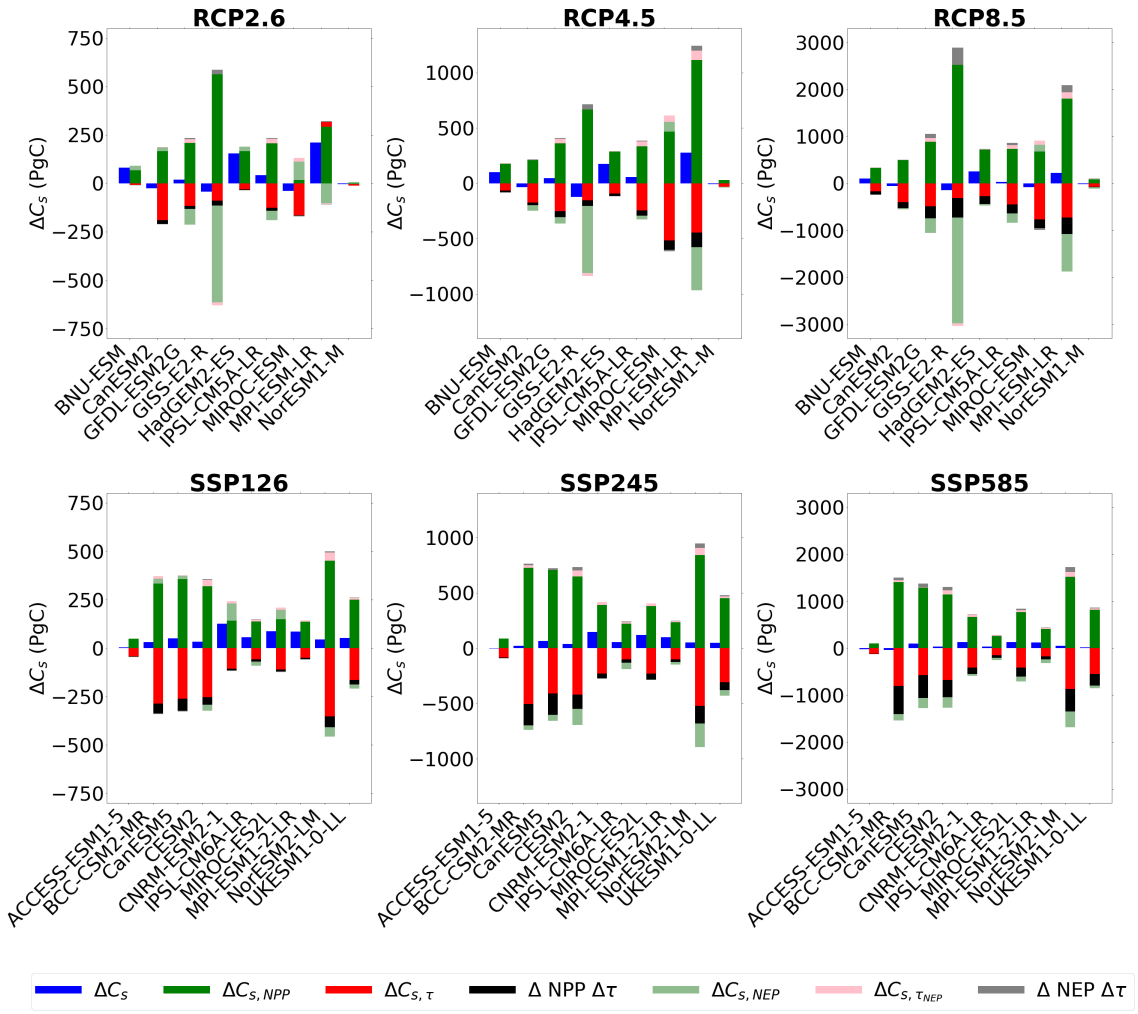

Figure 3.6: A bar chart showing the contributions of NPP and τ_s to end of 21st century changes in soil carbon (ΔC_s) in CMIP5 (top row) and CMIP6 (bottom row) ESMs, for future scenarios SSP126 and RCP2.6, SSP245 and RCP4.5, SSP585 and RCP8.5. The included terms are: the linear term representing changes in soil carbon due to the changes in NPP ($\Delta C_{s,NPP}$), the linear term representing changes in soil carbon due to the changes in τ_s ($\Delta C_{s,\tau}$), the non-linear term ($\Delta NPP \Delta \tau_s$), and then additional terms to account for the non-equilibrium climate in 2100 ($\Delta C_{s,NEP}$, $\Delta C_{s,\tau_{NEP}}$, and ΔNEP$\Delta \tau_s$).

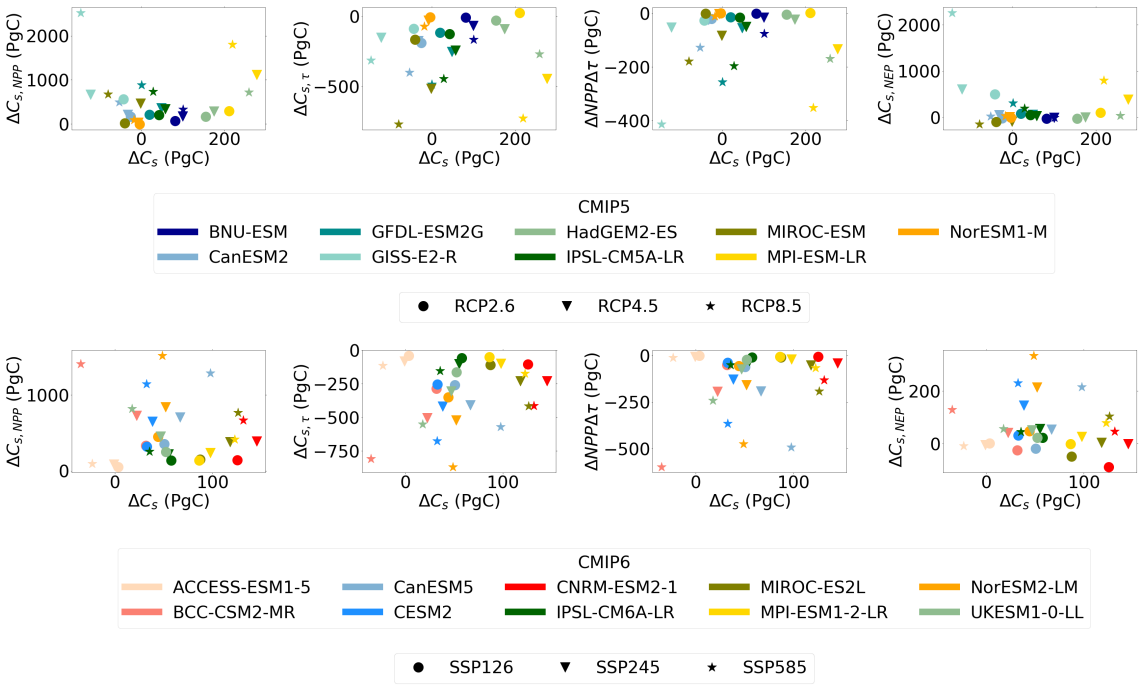

Figure 3.7: Scatter plot comparing the relationship between $\Delta C_{s,NPP}$, $\Delta C_{s,\tau}$, $\Delta NPP\Delta\tau_s$, and $\Delta C_{s,\tau_{NEP}}$, each against ΔC_s, for CMIP5 (top row) and CMIP6 (bottom row) ESMs, for future scenarios SSP126 and RCP2.6, SSP245 and RCP4.5, SSP585 and RCP8.5.

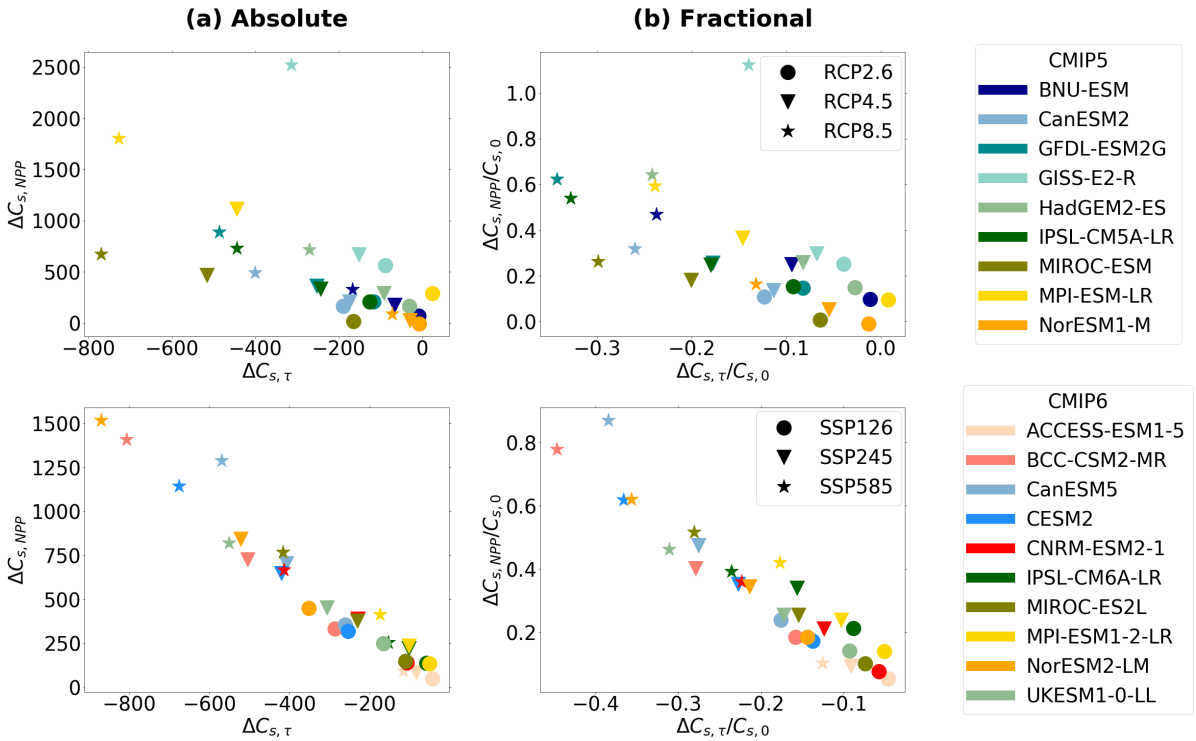

Figure 3.8: Scatter plot comparing the relationship between $\Delta C_{s,NPP}$ and $\Delta C_{s,\tau}$ for CMIP5 (top row) and CMIP6 (bottom row) ESMs in future scenarios SSP126 and RCP2.6, SSP245 and RCP4.5, SSP585 and RCP8.5, for (a) absolute changes, and (b) fractional changes.

ensemble (Figure 3.6). This effect was found to be largely due to a strong correlation between these linear soil carbon driven feedbacks in CMIP6, which was not seen as strongly in CMIP5 (Figure 3.8(a)). This correlation results in a a cancellation effect between $\Delta C_{s,NPP}$ and $\Delta C_{s,\tau}$, which causes more consistent predicted changes to overall soil carbon across the ensemble. The reasons for this correlation will be investigated in Chapter 6.

The net future change in soil carbon (ΔC_s) was also found to be a result of a non-linear term between changes in NPP and τ_s ($\Delta NPP \Delta \tau_s$) and a transient term ($\Delta C_{s,NEP}$). The non-linear $\Delta NPP \Delta \tau_s$ term was found to have a non-negligible contribution to future changes in soil carbon, meaning the initial $\Delta \Pi_N / \Pi_N << 1$ and $\Delta \tau_s / \tau_s << 1$ assumption was not valid in this case. This is due to both the ΔNPP and $\Delta \tau_s$ terms being found to have large and counteracting magnitudes, especially at more extreme levels of climate change (Figure 3.6). The $\Delta C_{s,NEP}$ term represents the net carbon sink during the 21$^{\text{st}}$ century, which exists whilst the climate is in a transient state due to continuous climate change. By definition, the magnitude of $\Delta C_{s,NEP}$ is negative if ΔNEP is positive, which implies a greatest or faster increase in NPP with respect to R_h seen in the majority of ESMs. The greater magnitudes of $\Delta C_{s,NEP}$ in the more extreme climate scenarios implies that soil carbon is further from equilibrium in these simulations (Figure 3.6), due to a greater CO_2 forcing in the same time period. The long-term response of NEP is key to determining the temporal evolution of the land carbon sink over the 21$^{\text{st}}$ century.

3.4.1 Reliability of CMIP6 projections and comparisons with CMIP5

This chapter has highlighted the importance of understanding the individual processes which contribute to soil carbon feedbacks in determining the overall ΔC_s response. This has previously been identified using the CMIP5 ensemble, where Todd-Brown et al. (2014) found that variation in projections of ΔC_s amongst CMIP5 ESMs was explained by initial soil carbon stocks and the relative changes in soil inputs and outputs. To improve the robustness and reliability of future ΔC_s estimates, it is important to achieve more agreement amongst ESM projections of future changes to the controls of the inputs and outputs of soil carbon (NPP and τ_s). Between CMIP5 and CMIP6 generations, model development has focused on improving the representation of these processes. However, no robust reductions in the projected range of ΔNPP (Figure 3.4) and $\Delta \tau_s$ (Figure 3.5) are seen across the ensemble, suggesting that major limitations remain within the CMIP6 ESMs.

One common new addition within the CMIP6 models is the inclusion of an interactive nitrogen cycle (Davies-Barnard et al., 2020), which is more commonly represented within CMIP6 models compared to CMIP5 models (ACCESS-ESM1.5, CESM2, MIROC-ES2L, MPI-ESM1-2-LR, NorESM2-LM and UKESM1-0-LL). Figure 3.4 suggests that the inclusion of a nitrogen cycle (shown by the dashed lines throughout this chapter) constrains future estimates of ΔNPP, where the majority of ESMs which include the representation of interactive nitrogen agree on future predictions of ΔNPP. However, there is some debate on how soil carbon will respond to NPP changes and how nitrogen interacts with this (Todd-Brown et al., 2014). Firstly, climate warming results in a liberation of nitrogen from microbial respiration, which can alleviate limitations within plants (Bai et al., 2013). Secondly, the effect of land use change has been shown to influence future soil carbon storage (Ito et al., 2020; Brovkin et al., 2013). Ito et al. (2020) attribute a change in soil carbon of 48 $\pm$ 32 PgC to land use change in SSP126 across the CMIP6 ensemble, where land use specific CMIP experiments were used. Finally, it has previously been found that soil carbon and NPP are too highly correlated amongst models in both CMIP5 and CMIP6, when compared to relationships derived in observational data (Varney et al. (2022); Georgiou et al. (2021); Todd-Brown et al. (2013), see Chapter 2), which suggests the potential for an overestimation of increased ΔC_s due to productivity increases within ESM projections.

It has been found in CMIP5 ESMs that high accumulation of C_s was predicted in the northern latitude regions, however this response was not seen in empirical studies (Todd-Brown et al., 2014). In CMIP6 ESMs, this chapter found this effect remains in the majority of ESMs (Figure 3.3), although reductions in northern latitude soil carbon stocks were found in three CMIP6 ESMs (BCC-CSM2-MR, CESM2 and NorESM2-LM). The ESMs where these predicted northern latitude reductions were found were also found to simulate northern latitude soil carbon stocks the most consistently with empirical datasets (see Table 2.4 in Chapter 2). This finding suggests that accurately modelling northern latitude soil carbon stocks in the present day is important in determining the net future response of soil carbon. Reducing the uncertainty surrounding the fate of northern latitude soil carbon stocks is particularly important due to the large magnitude of carbon stored in these regions (Jackson et al., 2017).

It has previously been discussed that missing below-ground processes within CMIP5 ESMs could result in a reduced reliability in future projections of soil carbon (Koven et al., 2015; Todd-Brown et al., 2014), for example: permafrost dynamics (Koven et al., 2011), microbial dynamics (Koven et al., 2015), and

mineral stabilisation (Koven et al., 2015; Todd-Brown et al., 2014; Six et al., 2002). The need for the inclusion of these processes within models is increasingly highlighted within literature (Chadburn et al., 2020; Walker et al., 2018), however progress is still needed for the inclusion of these within CMIP ESMs (Burke et al., 2020). In this chapter, τ_s is used as a proxy to investigate the future response of below-ground processes predicted by ESMs and high uncertainty is found to remain within CMIP6 ESMs (Figure 3.5). To improve the uncertainty in future τ_s predictions a focus on improving the representation of these missing below-ground processes is required (Chadburn et al., 2020; Ito et al., 2020).

3.5 Conclusions

In this chapter, future projections of soil carbon change (ΔC_s) have been analysed using ESM output from the latest CMIP6 ensemble and were investigated under differing levels of climate change (future scenarios SSP126, SSP245 and SSP585). The future projections made by CMIP6 ESMs were also compared against equivalent projections made by the previous generation of ESMs in the CMIP5 ensemble (future scenarios RCP2.6, RCP4.5 and RCP8.5) to investigate whether recent model improvements have reduced the uncertainty surrounding the future soil carbon response. Below the key conclusions from this chapter are listed:

1. An apparent reduction in uncertainty of end of 21$^{\text{st}}$ century ΔC_s projections is suggested in CMIP6 compared to CMIP5.

2. However, the same reduction in projection uncertainty is not suggested surrounding the soil carbon controls: Net Primary Productivity (NPP) and the effective soil carbon turnover time ($\tau_s = C_s/R_h$), and the subsequent effects on future soil carbon storage ($\Delta C_{s,NPP}$ and $\Delta C_{s,\tau}$).

3. The results in this study suggest the inclusion of a interactive nitrogen cycle constrains the future responses to NPP and shows progress in CMIP6 models. However, future work is required to further improve the representation of soil carbon input from increases in NPP and the subsequent response of soil carbon to reductions in soil carbon turnover time (τ_s) under climate change.

4. The linear terms which make up the response of soil carbon under climate change, the response of soil carbon due to changes in NPP ($\Delta C_{s,NPP}$) and the response due to changes in τ_s ($\Delta C_{s,\tau}$), are found to be strongly correlated in CMIP6, which was not the case in CMIP5. This correlation is likely to

be a cause of the reduction in the ΔC_s projection spread across the CMIP6 ensemble.

5. The results suggest that a linear approximation may not be appropriate when considering future changes to land carbon storage within global soils, due to a relatively large magnitude of the non-linear term ($\Delta NPP \Delta \tau_s$).

Understanding and quantifying soil carbon feedbacks is critical for calculating an accurate global carbon budget, which is required if Paris agreement targets are to be met (Friedlingstein et al., 2020). This chapter highlights the importance of considering the individual soil driven carbon feedbacks under climate change when determining the overall response of global soil carbon storage, and suggests the need for constraints on the magnitudes of the feedbacks from controls (NPP and τ_s) to improve reliability and reduce uncertainty in future changes in soil carbon. In Chapter 4, a spatial emergent constraint on $\Delta C_{s,\tau}$ will be presented.

Chapter 4

Spatial emergent constraint on the sensitivity of soil carbon turnover to global warming

Abstract

Carbon cycle feedbacks represent large uncertainties in climate change projections, and it is the response of soil carbon to climate change that contributes the greatest uncertainty. It has been seen in Chapter 3 that future changes in soil carbon depend on changes in carbon inputs from plants and on reductions in the turnover time of soil carbon (τ_s) with warming. In this chapter, an emergent constraint on the sensitivity of τ_s to global warming is presented, based on both CMIP5 and CMIP6 Earth System Model (ESM) projections. This makes use of current heterotrophic respiration and the spatial variability of τ_s inferred from observations of carbon in the top one metre of soil. The resulting spatial emergent constraint approximately halves the uncertainty in the response of soil carbon due to reductions in τ_s under climate change. This chapter is based on a paper published in *Nature Communications* (Varney et al., 2020).

4.1 Introduction

Uncertain carbon cycle feedbacks must be understood and quantified if the Paris agreement targets are to be met (UNFCCC, 2015). Moreover, with the potential to significantly reduce the carbon budget for climate stabilisation at 2°C global warming, the response of soil carbon to climate change presents a significant uncertainty in future climate change projections (Jones et al., 2013). The uncertainty of the soil carbon feedback was not found to reduce significantly between the CMIP3 and CMIP5 model generations and in Chapter 3, it was shown that similar uncertainty remains in the latest ensemble of CMIP6 models.

This study attempts to obtain a constraint on ESM projections of soil carbon change using an alternative method. In more recent years, emergent constraints have become increasingly common and have been used to successfully constrain terrestrial carbon cycle processes (Barkhordarian et al., 2021; Xu et al., 2020; Winkler et al., 2019). However, in these studies the emergent constraints have been based on temporal trends and variations to reduce uncertainty in climate change projections (Hall et al., 2019; Hall and Qu, 2006). The approach of this study follows the method used in Chadburn et al. (2017), where a spatial temperature sensitivity is used to constrain the future response to climate change - which is termed here as a *spatial emergent constraint*. This study combines the Chadburn et al. (2017) method with the soil carbon turnover analysis of Koven et al. (2017) to get a constraint on the resultant change in soil carbon due to the sensitivity of soil carbon turnover to global warming.

Soil carbon (C_s) is increased by the flux of organic carbon into the soil from plant litter and roots, and decreased by the breakdown of the organic matter by soil microbes, which releases CO_2 into the atmosphere as the heterotrophic respiration flux (R_h). If the vegetation carbon is at a steady state, litterfall (Λ) will equal the Net Primary Production of plants (NPP). If the soil carbon is also near to a steady state - and in the absence of significant fire fluxes and other non-respiratory carbon losses - the litterfall, NPP, and R_h will all be approximately equal to one another. Even over the historical period, when atmospheric CO_2 has been increasing and there has been a net land carbon sink, this approximation holds well (see Figure 4.4). In order to separate the effects of changes in NPP from the effects of climate change on R_h, an effective turnover time for soil carbon, $\tau_s = C_s/R_h$, is defined (Koven et al., 2017; Carvalhais et al., 2014). The turnover time of soil carbon is known to be especially dependent on temperature (Jenkinson et al., 1991). A common assumption is that τ_s decreases by about 7% per degree of warming, which is equivalent to assuming that $\mathrm{q}_{10} = 2$ (Davidson and Janssens, 2006). However, this sensitivity differs between models, and also between models and observations.

The long-term change in soil carbon (ΔC_s) can be written as the sum of a term arising from changes in litterfall ($\Delta C_{s,\Lambda}$), and a term arising from changes in the turnover time of soil carbon ($\Delta C_{s,\tau}$). Model projections of the first-term ($\Delta C_{s,\Lambda}$) differ primarily because of differences in the extent of CO_2 fertilisation of NPP and associated nutrient limitations. The second-term ($\Delta C_{s,\tau}$) differs across models because of differences in the predicted future warming and because of differences in the sensitivity of soil carbon decomposition to temperature

(which includes an influence from faster equilibration of fast-turnover compared to slow-turnover carbon pools under changing inputs (Koven et al., 2015)). This study provides an observational constraint on the uncertainty in the latter term. As the vast majority of the CMIP6 and CMIP5 models do not yet represent vertically resolved deep soil carbon in permafrost or peatlands, the constraint focuses on carbon change in the top 1 metre of soil. To ensure a fair like-for-like comparison, the two CMIP6 models that do represent vertically-resolved soil carbon (CESM2 and NorESM2) are excluded, although this has an negligible effect on the overall result. This study therefore applies to soil carbon loss in the top 1 metre of soil only. In this chapter, it is shown that it is possible to significantly reduce the uncertainty in this key feedback to climate change using current-day spatial data to constrain the sensitivity to future warming.

4.2 Methods

4.2.1 Equation for the τ_s component of soil carbon change

Soil carbon turnover time (τ_s) is the residence time of carbon in the soil and therefore was defined as the time it takes for carbon to be transferred from the atmosphere into the soil via the land surface, then to exist in the soil and to be released back into the the atmosphere. This can be defined using Equation 4.1, where τ_s is equal to the ratio of soil carbon stocks (C_s) to the output flux heterotrophic respiration flux (R_h).

$$\tau_s = \frac{C_s}{R_h} \tag{4.1}$$

Equation 4.1 can be rearranged to obtain an equation for soil carbon (C_s), as shown by Equation 4.2.

$$C_s = R_h \, \tau_s \tag{4.2}$$

The long-term change in soil carbon (ΔC_s) can be written as the sum of a term arising from changes in litterfall ($\Delta C_{s,\Lambda}$) and a term arising from changes in the turnover time of soil carbon ($\Delta C_{s,\tau}$), plus an additional non-linear term ($\Delta R_h \Delta \tau_s$), which is generally smaller than the first two (see Chapter 3), as shown by Equation 4.3. These terms representing the change in soil carbon can be approximated as a sum involving the change in R_h and the change in τ_s, using a substitution of Equation 4.2.

$$\Delta C_s = \Delta C_{s,\Lambda}(\mathrm{t}) + \Delta C_{s,\tau}(\mathrm{t}) \approx \Delta(R_h\,\tau_s) \approx \tau_{s,0}\,\Delta R_h + R_{h,0}\,\Delta\tau_s + \Delta R_h\,\Delta\tau_s \quad (4.3)$$

The focus and aim of this study was to find a constraint on the change in soil carbon due to the change in soil carbon turnover time ($\Delta C_{s,\tau}$). Hence, an equation for the component of soil carbon change $\Delta C_{s,\tau}$ can be obtained by taking the $\Delta\tau_s$ component of Equation 4.3. The equation in the final form is shown by Equation 4.4, where $R_{h,0}$ was used to represent R_h from the reference period ('present day', defined below) to isolate the response of $\Delta C_{s,\tau}$ as a result of the response of τ_s to climate change.

$$\Delta C_{s,\tau} = R_{h,0}\,\Delta\tau_s \quad (4.4)$$

Note: In Chapter 3, $\Delta C_{s,\tau}$ was defined with NPP$_0$ opposed to $R_{h,0}$, and we had an additional term $\Delta C_{s,\tau_{NEP}}$. As in this case we are isolating the τ_s response to climate change (below-ground response), $R_{h,0}$ can be used, where $\Delta C_{s,\tau_{rh}}$ = $\Delta C_{s,\tau_{NPP}}$ - $\Delta C_{s,\tau_{NEP}}$, as R_h = NPP - NEP.

4.2.2 Obtaining spatial relationships

The method used in this study was motivated by the observational-based constraint method used in Chadburn et al. (2017), where a spatial temperature sensitivity was used to constrain a future response to global warming. Koven et al. (2017) first investigated the relationship between soil carbon turnover time (τ_s) and temperature, where differing climatological sensitivities in different temperature ranges were found. The method used in Koven et al. (2017) was followed here to derive relationships that represent the sensitivity of τ_s to temperature (T) on a spatial level, for both CMIP ESMs and observational data.

4.2.2.1 CMIP ESMs

This study uses ESMs from both the CMIP6 and CMIP5 ensembles, where the included CMIP6 models are: ACCESS-ESM1-5, BCC-CSM2-MR, CanESM5, CNRM-ESM2-1, IPSL-CM6A-LR, MIROC-ES2L, and UKESM1-0-LL (Eyring et al., 2016), and the included CMIP5 models are: BNU-ESM, CanESM2, CESM1-CAM5, GFDL-ESM2G, GISS-ES-R, HadGEM2-ES, IPSL-CM5A-LR, MIROC-ESM, and NorESM-M (Taylor et al., 2012). The ESMs are presented in Tables 2.1 (CMIP6) and 2.2 (CMIP5) of Chapter 2. The ESMs included were chosen due to their availability of required data available on the online repository at the time of analysis (CMIP6: https://esgf-node.llnl.gov/search/cmip6/ and

CMIP5: (https://esgf-node.llnl.gov/search/cmip5/).

To obtain model specific spatial τ_s-temperature relationships, the following method was used. A reference time period was considered (1995-2005), which was taken as the last decade of the CMIP5 historical simulation to allow consistency within CMIP generations and to best match the observational data time frame considered. Then, monthly model output data was time averaged over this period, for the output variables 'soil carbon content' (C_s) in kg m^{-2}, 'heterotrophic respiration carbon flux' (R_h) in kg m^{-2}s^{-1}, and 'air temperature' in K. The variables C_s and R_h were used to obtain values for soil carbon turnover time (τ_s) in years, using Equation 4.1. The model temperature variable units were converted from K to °C to match observational units.

For each ESM, values of $\log \tau_s$ for each latitude and longitude were plotted against the corresponding spatial temperature data to obtain the spatial $\log \tau_s$-temperature plot. Then, quadratic fits (using the python package numpy polyfit) were calculated for each model, which represent the spatial $\log \tau_s$ relationship and sensitivity to temperature. These model specific relationships are shown by Figure 4.1 for CMIP6 and by Figure 4.2 for CMIP5 (and by the colourful lines in Figure 4.7(a) in the Results section).

4.2.2.2 Observations

Following Koven et al. (2017), observational soil carbon data (to a depth of 1 m) was estimated by combining the Harmonized World Soils Database (HWSD) (FAO and ISRIC, 2012) and Northern Circumpolar Soil Carbon Database (NCSCD) (Hugelius et al., 2013) soil carbon datasets, where NCSCD was used where overlap occurs. To calculate τ_s, this estimate for observational soil carbon was used together with a global observational dataset for heterotrophic respiration, where CARDAMOM (2001-2010) heterotrophic respiration (R_h) was used (Bloom et al., 2015). The WFDEI dataset was used for observational air temperatures (2001-2010) (Weedon et al., 2014).

These datasets can be used to obtain the inferred observational $\log \tau_s$-temperature relationship by plotting $\log \tau_s$ against temperature for each latitude and longitude point, and using the quadratic fitting method described above. This represents the 'real world' spatial temperature sensitivity of $\log \tau_s$, and is shown by Figure 4.3 (as well as the thick-dotted-black line in Figure 4.7(a) of the Results section).

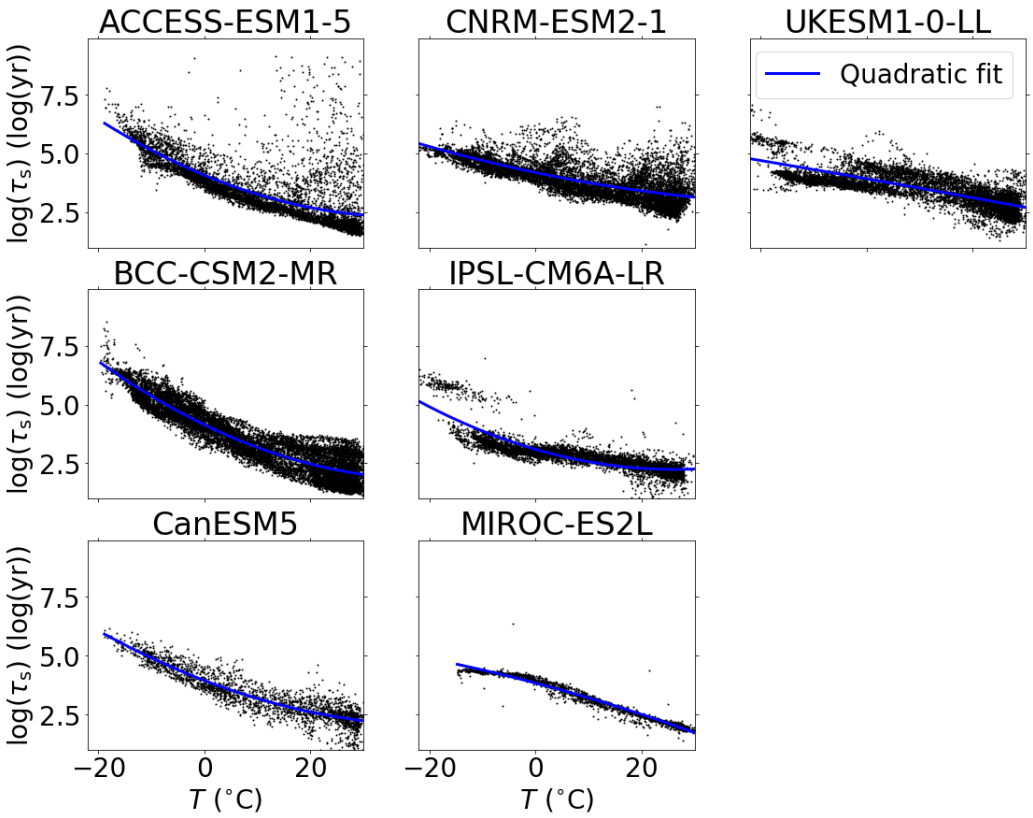

Figure 4.1: Scatter plots of the relationship between soil carbon turnover ($\log \tau_s$) and near surface air temperature (T) for each CMIP6 ESM considered in the study. The black points represent the individual grid points of data, and the blue lines show the spatial $\log \tau_s$-temperature quadratic fits.

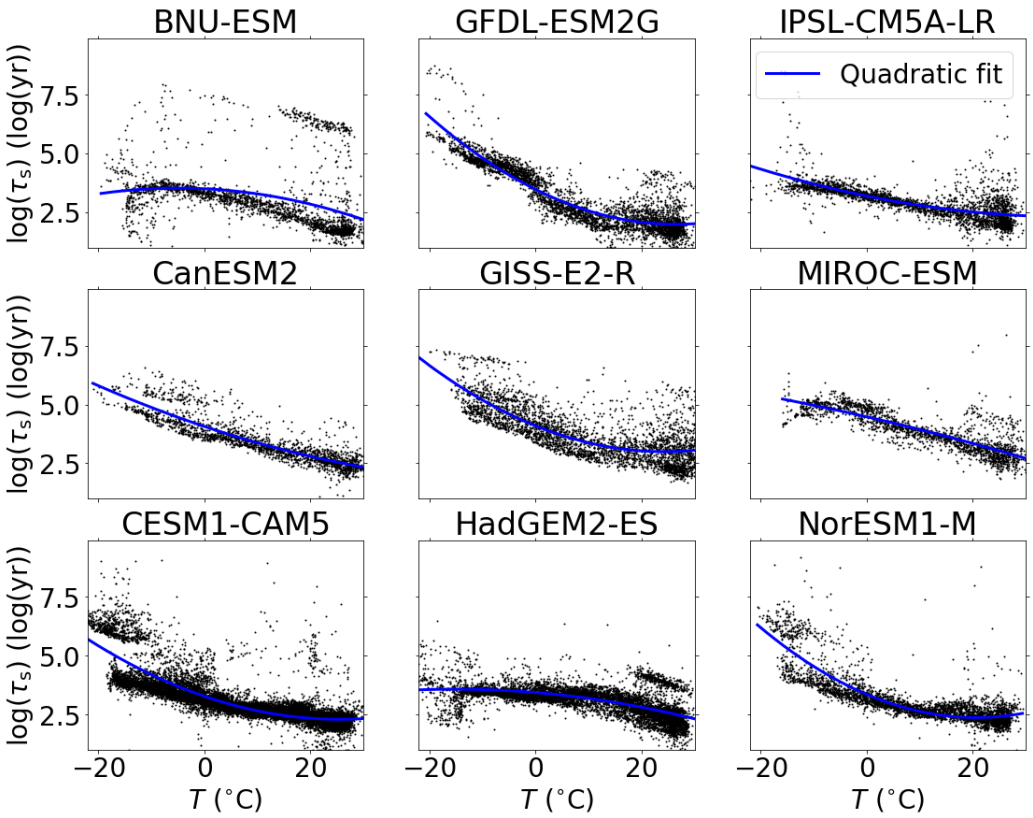

Figure 4.2: Scatter plots of the relationship between soil carbon turnover ($\log \tau_s$) and near surface air temperature (T) for each CMIP5 ESM considered in the study. The black points represent the individual grid points of data, and the blue lines show the spatial $\log \tau_s$-temperature quadratic fits.

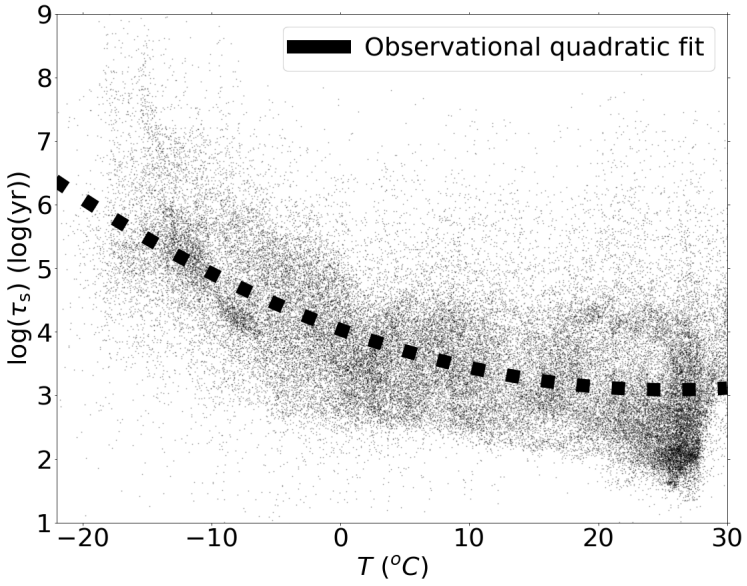

Figure 4.3: A scatter plot of the relationship between soil carbon turnover ($\log \tau_s$) and near surface air temperature (T) for the observational datasets considered in this study: C_s (FAO and ISRIC, 2012; Hugelius et al., 2013), R_h (Bloom et al., 2015), and temperature (Weedon et al., 2014). The black points represent the individual grid points of data and the thick-dotted black line shows the spatial $\log \tau_s$-temperature quadratic fit.

4.2.3 Proof of concept for the method

The concept of the spatial emergent constraint method relies on the idea that the spatial temperature sensitivity, which gives a relationship of τ_s to temperature, can be used to project and constrain the temporal sensitivity of τ_s to temperature (i.e. a space-for-time substitution). To do this, the change in soil carbon due to the change in soil carbon turnover time ($\Delta C_{s,\tau}$) was calculated using Equation 4.4, using two different methods to obtain $\Delta\tau_s$. (1) The first method is shown by Equation 4.5. With this method, $\Delta\tau_s$ was calculated using Equation 4.1, where a future (τ_s^{f}) and historical (τ_s^{h}) were calculated using model output data. (2) The second method is shown by Equation 4.6. With this method, $\Delta\tau_s$ was derived using the quadratic $\log\tau_s$-temperature relationships with the modelled spatial temperature profiles. In this equation, T is near surface air temperature, T^{f} represents a future temperature, and T^{h} represents historical (present day) temperature from the reference period (1995-2005). The exponential ($\exp$) were taken to turn $\log\tau_s$ values to τ_s values. q(T) represents the quadratic $\log\tau_s$-temperature relationship as a function of temperature to obtain the estimated $\log\tau_s$.

$$\Delta\tau_s = \tau_s^{\mathrm{f}} - \tau_s^{\mathrm{h}} \tag{4.5}$$

$$\Delta\tau_s = \exp(\mathrm{q}(T^{\mathrm{f}})) - \exp(\mathrm{q}(T^{\mathrm{h}})) \tag{4.6}$$

The calculation of $\Delta\tau_s$ requires a future reference point. In this case, the end of the 21$^{\mathrm{st}}$ century (2090-2100) warming, for each future CMIP6 SSP scenario (SSP126, SSP245, SSP585) (O'Neill et al., 2016) or equivalent future CMIP5 RCP scenario (RCP2.6, RCP4.5, and RCP8.5) (Meinshausen et al., 2011), was compared with the reference period from the historical simulation (1995-2005), for each CMIP6 ESM and CMIP5 ESM respectively. To calculate the corresponding values for $\Delta C_{s,\tau}$, the different $\Delta\tau_s$ values were used in Equation 4.4 with the model-specific $R_{h,0}$. The resultant spatial $\Delta C_{s,\tau}$ values from each method were summed over the values from the individual grid cells to get a global total, which were then compared. The premise of the method is that if the two different $\Delta C_{s,\tau}$ values obtained from each method are approximately the same, then this implies that the derived $\log\tau_s$-temperature relationships, with prescribed future modelled temperatures alone, can predict the change in soil carbon due to the change in soil carbon turnover time to climate change (the results of this test are shown in Figure 4.7(b)).

4.2.4 Calculating constrained values

To isolate the uncertainty due to differences in the sensitivity of modelled τ_s to temperature, as opposed to the climate sensitivity of the models to CO_2, an emergent constraint for specific degrees of global mean warming in each model were considered. To consider a specific degree of global warming (Figure 4.8), the future spatial temperature profiles at these specific global mean warming levels were calculated, for example: 1°C, 2°C, and 3°C global mean warming. The temperature change was calculated from the reference period (1995-2005), and then a 5-year rolling mean of global temperature was taken to remove some of the interannual variability. Once the year that the given temperature increase had been reached is obtained, a time average including -5 and +5 years was taken, and the spatial temperature distribution of that model averaged over the deduced time period was used for the calculations of future τ_s.

This study now follows the previously defined emergent constraint method (Hall and Qu, 2006), which was explained in Figure 1.4 within Chapter 1 of this thesis. The 'Earth system sensitivity' (conventionally represented by the y-axis), was defined as the sensitivity of soil carbon to future changes in soil carbon turnover ($\Delta C_{s,\tau}$). This can be predicted with ESMs using Equation 4.5 (method 1) for different degrees of global warming. Then the 'observed variation' (conventionally represented by the x-axis) was defined in this case as the predicted sensitivity of soil carbon to future changes in soil carbon turnover using the spatial temperature sensitivity of soil carbon turnover time, calculated using Equation 4.6 (method 2) for different degrees of global warming, for each ESM. In doing this, a set of x and y values were obtained, corresponding to the modelled values and relationship-derived of $\Delta C_{s,\tau}$ respectively, for each ESM. In this case, an emergent relationship was found between the model predicted x and y values for each degree of global warming. The emergent relation was found using linear regression between the x and y data points. The linear regression was completed using the least-squares linear regression technique, which mathematically best fits the x and y data points and minimises the sum of the squares of the residuals of the points from the line.

To obtain the observationally-constrained values of $\Delta C_{s,\tau}$ on the x-axis, a spatial profile for the 'observational' future temperature was required. Due to the uncertainty associated with climate sensitivity, which results in each model projecting different future warming scenarios for the same amount of climate forcing, an anomaly correction for future temperature projections was used. This spatial future temperature anomaly was projected using each model and each respective future SSP/RCP scenario separately. To calculate this, the

temperature at the reference time frame (1995-2005), which overlaps the WFDEI observational temperature data time frame (2001-2010), was subtracted from the future temperature profile for each model (as calculated above), to calculate the temperature change. Then, this temperature anomaly was added onto the observational temperature dataset to give a model-derived future 'observational' temperature for each model. This was then be used together with the observational derived $\log \tau_s$-temperature relationship, to project values for future τ_s. Then this together with relationship-derived historical τ_s deduced using the observational temperature dataset, was used to calculate $\Delta\tau_s$. Finally, global $\Delta C_{s,\tau}$ was obtained by multiplying $\Delta\tau_s$ by the observational dataset for $R_{h,0}$, using Equation 4.4, and then calculating a weighted-global total. As each model-derived future 'observational' temperature was considered separately, a range of projected observational-constrained $\Delta C_{s,\tau}$ values were obtained. This range was used to define x_{obs}, which represents the mean observational-constrained $\Delta C_{s,\tau}$ value, and a corresponding standard deviation due to the uncertainty in the modelled spatial profiles of future temperatures.

$$P(y) = \int_{-\infty}^{\infty} P\{ y \mid x\} \, P(x) \, dx \tag{4.7}$$

The emergent relationship and the observational constraint was combined to obtain an emergent constraint on the model predicted sensitivity of $\Delta C_{s,\tau}$ to global warming (y-axis). To do this, Equation 4.7 was used to obtain a constrained probability density function on the y-axis. In Equation 4.7, P(y) defines the constrained probability density function, P{ y | x} represents the emergent relationship, which is a probability of y given x defined using linear regression, and P(x) represents the observational-constrained x_{obs} and associated uncertainty, which represents the probability of x. P(y) was then deduced by integrating across all possible x values to estimate y at any given point, and hence obtaining the constrained probability density function on $\Delta C_{s,\tau}$. It is noted that the probability distributions are assumed to be normal. In the Results, the spatial emergent constraint is first presented on 2°C global warming (Figure 4.8), and then for 1°C and 3°C global warming (Figure 4.10).

4.2.5 Observational sensitivity study

An observational sensitivity study on the spatial emergent constraint was considered for the following two reasons: (1) to test the robustness of the constraint, and (2) to investigate the constraint dependence on the choice of observational dataset. This sensitivity study involved repeating the above analysis with different

observational-derived datasets to represent the output flux in Equation 4.1, to reproduce the emergent constraint on $\Delta C_{s,\tau}$ at 2°C of global warming.

To calculate τ_s using Equation 4.1, an observational dataset for global heterotrophic respiration was required. In the main results section, CARDAMOM (2001-2010) heterotrophic respiration was used (Bloom et al., 2015). The CARDAMOM R_h dataset was used in the main results for the following two main reasons: firstly, τ_s was defined using heterotrophic respiration which allows for consistency between models and observations, and secondly, the dataset does not use a prescribed q_{10} sensitivity (Bloom et al., 2015). Instead, the CARDAMOM R_h dataset was derived by explicitly assimilating observations into a process-based diagnostic land-surface model. In the sensitivity study, the following additional observational datasets were considered: NDP-08 'Inter-annual Variability in Global Soil Respiration on a 0.5 Degree Grid Cell Basis' dataset (1980-1994) (Raich et al., 2002), 'Global spatiotemporal distribution of soil respiration modelled using a global database' (Hashimoto et al., 2015), and MODIS Net Primary Productivity (NPP) (2000-2014) (Zhao et al., 2005). Figure 4.4 shows scatter plots showing one-to-one comparisons of each observational datasets against one another.

The emergent constraint analysis was repeated with the MODIS NPP (Zhao et al., 2005) and Raich 2002 R_s (Raich et al., 2002) datasets, for both CMIP6 and CMIP5 together as one ensemble and as separate model ensembles. It is noted that the historical conditions under which these datasets are measured are non-stationary, which means there is therefore an imbalance between NPP and R_h which leads to the land carbon sink. However, this sink is a relatively small fraction of these fluxes (less than 5%), so in most locations it is expected that R_h and NPP will be close to being in balance (which can be seen in Figure 4.4).

The decision was made not to complete the spatial emergent constraint analysis using the Hashimoto dataset (Hashimoto et al., 2015). This was because not only is it inconsistent with the three other datasets considered, it also shows an arbitrary maximum respiration level (Figure 4.4), which likely results from the assumed temperature-dependence of soil respiration in this dataset which takes a quadratic form. The quadratic form is justified based on a site-level study in which it is used to fit temporal dynamics. However, the parameters for the quadratic function that are fitted in the Hashimoto study are very different from those in the site-level study, which therefore suggests that the same relationship does not apply to the global distribution of mean annual soil respiration.

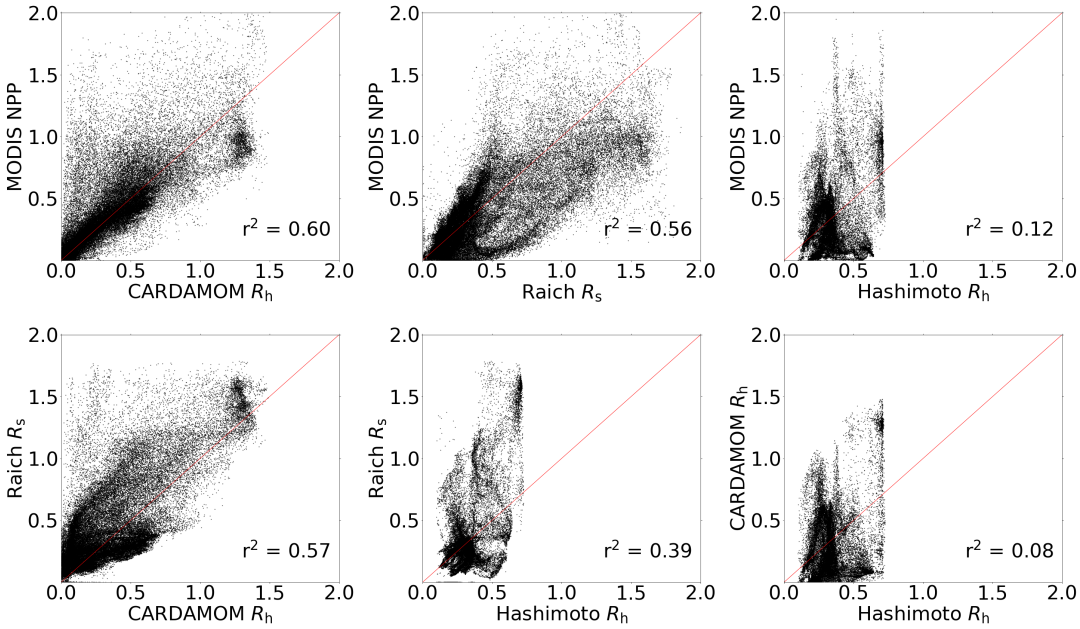

Figure 4.4: Scatter plots showing one-to-one comparisons of all the observational datasets which where considered in this study against one another, including: CARDAMOM heterotrophic respiration (R_h) (Bloom et al., 2015), MODIS net primary production (NPP) (Zhao et al., 2005), Raich 2002 soil respiration (R_s) (Raich et al., 2002), and Hashimoto 2015 heterotrophic respiration (R_h) (Hashimoto et al., 2015). The black data points represent the spatial data for each grid point, and the red lines show a one-to-one comparison. The respective r^2 correlation coefficients are stated on each figure panel.

4.2.6 Calculating effective q_{10} for change in soil carbon

Simple models of soil carbon turnover (τ_s) are often based on a Q_{10} function, which means that τ_s depends on temperature as shown by Equation 4.8. The results for $\Delta C_{s,\tau}$ that would be derived from considering a simple Q_{10} function (with q_{10}=2, q_{10}=2.5, q_{10}=3), can be compared with the emergent constrained value for $\Delta C_{s,\tau}$. This enables an estimation of an effective q_{10} sensitivity of heterotrophic respiration.

$$\tau_s = \tau_{s,0} \exp\left((-0.1 \log q_{10}) \Delta T\right) \tag{4.8}$$

To do this, an equation for $\Delta\tau_s$ can be derived from Equation 4.8. This was done by considering Equation 4.9, where $\tau_{s,0}$ is an initial τ_s, and substituting in τ_s in temperature sensitivity form (Equation 4.8) to obtain an equation for $\Delta\tau_s$ in temperature sensitivity form, as shown by Equation 4.10.

$$\Delta\tau_s = \tau_s - \tau_{s,0} \tag{4.9}$$

$$\Delta\tau_s = \tau_{s,0} \exp\left((-0.1 \log \mathrm{q}_{10})\Delta T\right) - \tau_{s,0} \tag{4.10}$$

The equation for $\Delta\tau_s$ in temperature sensitivity form (Equation 4.10), can be used to obtain a temperature sensitivity form of the equation for the component of soil carbon change due to the change in soil carbon turnover time ($\Delta C_{s,\tau}$).

$$\Delta C_{s,\tau} = R_{h,0}\tau_{s,0}[\exp\left((-0.1 \log \mathrm{q}_{10})\Delta T\right) - 1] \tag{4.11}$$

$$\Delta C_{s,\tau} = C_{s,0}[\exp\left((-0.1 \log \mathrm{q}_{10})\Delta T\right) - 1] \tag{4.12}$$

This was done by substituting Equation 4.10 into Equation 4.4, and obtains Equation 4.11. This equation was then simplified to obtain an equation relating $\Delta C_{s,\tau}$ and ΔT, where the final form is shown by Equation 4.12.

4.3 Results

4.3.1 Proof of concept

To start, the spatial temperature sensitivity of soil carbon turnover time (τ_s) is investigated. For each ESM, effective τ_s can be calculated using time-averaged (1995-2005) values of C_s and R_h at each grid-point, and applying the definition (Equation 1). Similarly, this can be done for the observational datasets, using soil carbon (C_s) in the top 1 metre (FAO and ISRIC, 2012; Hugelius et al., 2013) and time-averaged (2001-2010) heterotrophic respiration (R_h) (Bloom et al., 2015), as shown in Figure 4.5. Figure 4.5(c) shows the map of inferred values of τ_s from these observations, with a notable increase from approximately 7 years in the warm tropics to over 100 years in the cooler high northern latitudes. This map shows that carbon resides in the soils for longer periods of time in the northern latitudes compared with the topical regions where the turnover of carbon is much faster.

Similar maps can be diagnosed for each of year of data, for each ESM, and for each future scenario, giving time and space varying values of τ_s for each model run. This enables the estimation of $\Delta C_{s,\tau}$, via the last term on the right of Equation 4.3. For each ESM, the $R_{h,0}$ value was taken as the mean over the decade 1995-2005, to overlap with the time period of the observations and to maintain consistency across CMIP generations. Individual grid-point τ_s values were calculated for each year before calculating area-weighted global totals of $\Delta C_{s,\tau}$.

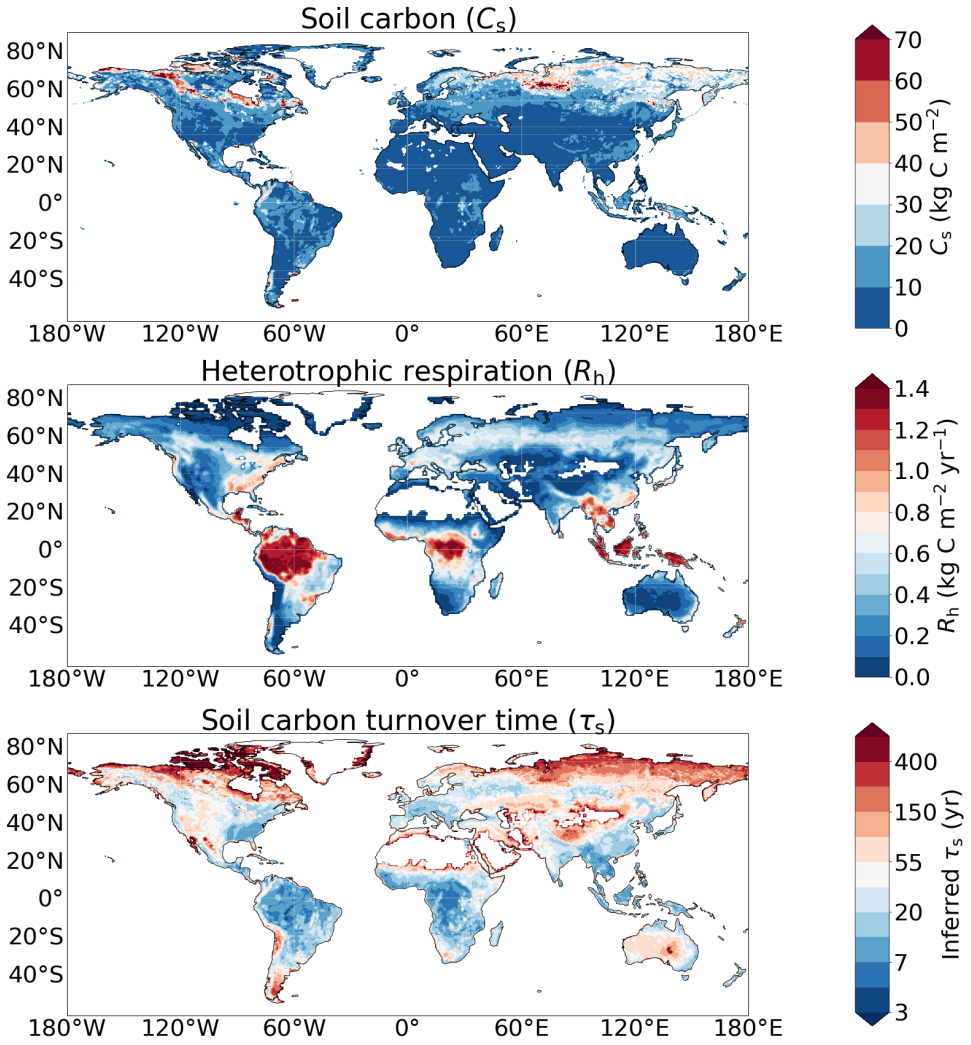

Figure 4.5: Maps of (a) observed soil carbon (C_s) to a depth of 1 m (kg C m^{-2}) (FAO and ISRIC, 2012; Hugelius et al., 2013), (b) observed heterotrophic respiration ($R_{h,0}$) (kg C m^{-2} yr^{-1}) (Bloom et al., 2015), and (c) inferred soil carbon turnover time (τ_s) (yr).

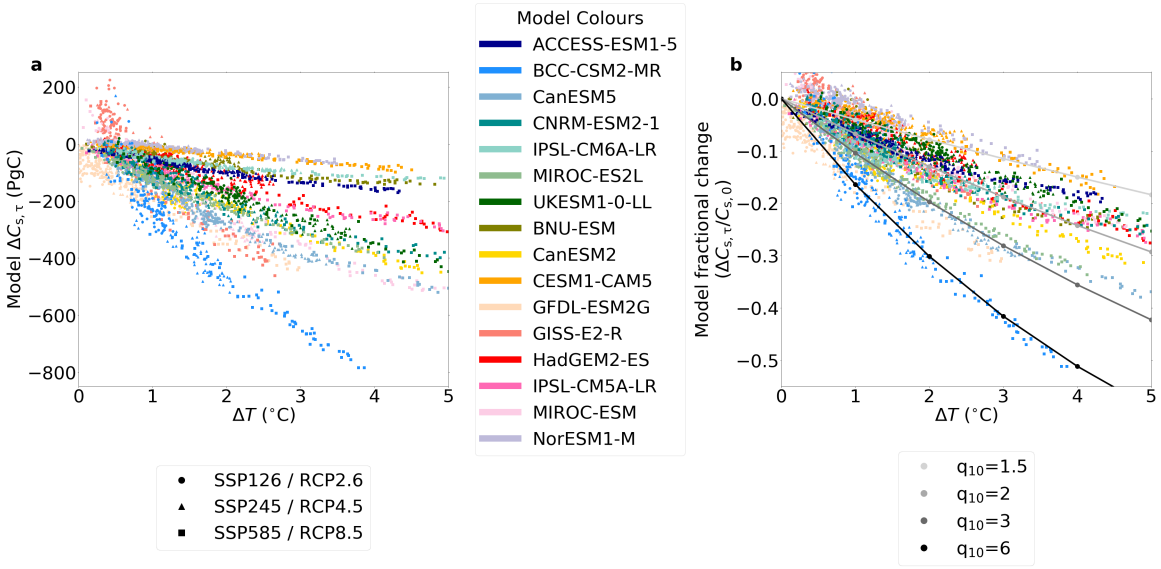

Figure 4.6: $\Delta C_{s,\tau}$ vs ΔT plot diagnosed from sixteen Earth System Models (seven CMIP6 ESMs and nine CMIP5 ESMs), for three different future scenarios: SSP126, SSP245, SSP585, or RCP2.6, RCP4.5, RCP8.5, respectively. (a) The change in soil carbon due to the change in soil carbon turnover time against change in global mean temperatures; (b) The fractional change in soil carbon due to the change in soil carbon turnover time against change in global mean temperatures, and compared to different effective q_{10} sensitivities.

The uncertainty of $\Delta C_{s,\tau}$ stems from the uncertainty in modelled τ_s, and the uncertainty due to differing climate sensitivities of the models. In this study, the aim was to quantify and constrain the uncertainty in τ_s. To isolate the uncertainty in the latter term, $\Delta C_{s,\tau}$ was considered for differing levels of global mean warming in each model. The resulting dependence of global total $\Delta C_{s,\tau}$ on global warming is shown in Figure 4.6(a), for each of the ESMs considered in both CMIP6 and CMIP5 (seven CMIP6 ESMs and nine CMIP5 ESMs), and for three Shared Socioeconomic Pathways (SSP): SSP126, SSP245 and SSP585 (CMIP6) (O'Neill et al., 2016), or the equivalent Representative Concentration Pathways (RCP): RCP2.6, RCP4.5, and RCP8.5 (CMIP5) (Meinshausen et al., 2011). In all cases $\Delta C_{s,\tau}$ is negative, which is consistent with the soil carbon turnover time decreasing with warming. The more surprising thing to note is the huge range in the projections, with a spread at 2°C global mean warming of approximately 400 PgC, regardless of future SSP/RCP scenario. Figure 4.6(b) plots the fractional change in soil carbon $\Delta C_{s,\tau}/C_{s,0}$, showing that there is a large range of effective q_{10} sensitivities between the model projections.

ESMs in both CMIP5 and CMIP6 can be used to test whether the spatial variation in τ_s reveals the sensitivity of soil carbon turnover to temperature. Figure 4.7(a) is a scatter plot of $\log \tau_s$ against temperature, using the τ_s values shown in Figure

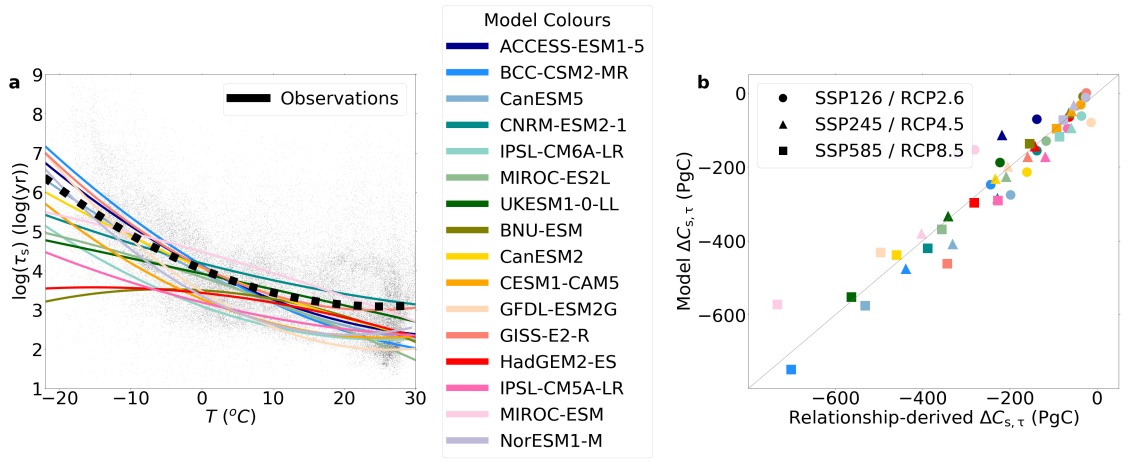

Figure 4.7: Figure showing the use of the spatial variability of τ_s to estimate $\Delta C_{s,\tau}$. (a) Scatter plot of the relationship between $\log \tau_s$ and air temperature from observations (FAO and ISRIC, 2012; Hugelius et al., 2013; Bloom et al., 2015; Weedon et al., 2014) (black points), and a quadratic fit (black-dotted line) representing the observational temperature sensitivity of $\log \tau_s$. The equivalent quadratic fits for the ESMs are shown by the coloured lines; (b) The proof of principle for the method, showing an actual vs estimated comparison, representing the modelled against the relationship-derived values of the $\Delta C_{s,\tau}$, where the change is considered between the start (1995-2005) and the end (2090-2100) of 21$^{\text{st}}$ century and is assumed to relate to the top 1 metre of soil.

4.5(c) and mean temperatures from the empirical WFDEI dataset over the period 2001-2010 (Weedon et al., 2014). The thick black-dotted line is a quadratic fit through these points. Also shown for comparison are equivalent quadratic fits for each model (colourful lines), using the model $\log \tau_s$ and mean near-surface air temperature (T) values for each grid-point, over an overlapping period with the observations (1995-2005). There is a spread in the data points due to variation in soil moisture, soil type, and other soil parameters (Exbrayat et al., 2013b). The model specific spread in the data can be seen for the CMIP6 and CMIP5 models in Figures 4.1 and 4.2, respectively. Although models do not account for every possible factor contributing to this spread, the spread of points in the models is generally similar to the observations (Figure 4.3). However, differences between the best-fit functions relating τ_s to T are evident between the models, and between the models and the observations (Koven et al., 2017).

This suggests that it may be possible to constrain $\Delta C_{s,\tau}$ using the observed τ_s vs T fit from the observations, but only if it can show that such functions can be used to predict $\Delta C_{s,\tau}$ under climate change. In order to test this premise, it is attempted to reconstruct the time-varying $\Delta C_{s,\tau}$ projection for each model using the time-invariant τ_s vs T fit across spatial points (Figure 4.7(a)), and the time-invariant $R_{h,0}$ field. The change in soil carbon turnover time ($\Delta \tau_s(\mathrm{t})$) for a given model run is estimated at each point based-on the

τ_s vs T curve, and the time-varying projection of T at that point. A local estimate of the subsequent change in soil carbon can then be made based-on the farthest right-hand term of Equation 4.4 ($R_{h,0}\,\Delta\tau_s$), which can be integrated up to provide an estimated change in global soil carbon in the top 1 metre ($\Delta C_{s,\tau}$).

Figure 4.7(b) shows the result of this test for all models and all respective SSP and RCP scenarios. The axes of this plot show equivalent variables which represent the global $\Delta C_{s,\tau}$, change between the mean value for 2090-2100 and the mean value for 1995-2005. The y-axis represents the actual values for each model as shown in Figure 4.6, and the x-axis represents the estimate derived from spatial variability (as in Figure 4.7(a)). As hoped, actual vs estimated values cluster tightly around a one-to-one line with an r^2 correlation coefficient value of 0.90.

The proof of concept investigation takes into account the extrapolation of the $\log\tau_s$-temperature relationship. As global warming will lead to the warmest areas on Earth to have increased maximum temperatures in the future compared with the same areas in the present day, some amount of extrapolation will be required from the $\log\tau_s$ vs T curve inferred from the present day spatial patterns, in order to infer the change in $\log\tau_s$ in the future. However, the extrapolations are expected to be small relative to the range covered by the present day spatial variability. The percentage of data points where modelled temperatures went beyond observational spatial temperatures was investigated in the most extreme future warming scenarios for CMIP6 and CMIP5, SSP585 and RCP8.5 respectively. It was found that the mean percentage value of spatial data points in this case was 0.51% for CMIP6 and 4.4% for CMIP5. Moreover, given the near linearity of the $\log\tau_s$ vs T curve, and the success of the estimates of the soil carbon changes ($\Delta C_{s,\tau}$) in each model using the $\log\tau_s$ vs T curve derived from spatial variability, it suggests that the extrapolations at the hottest locations are not affecting the success of the method.

4.3.2 The spatial emergent constraint

4.3.2.1 Spatial emergent constraint on 2°C of global warming

The tight cluster seen in Figure 4.7(b) gives confidence to use the τ_s vs T fit and $R_{h,0}$ from observations to constrain future projections of $\Delta C_{s,\tau}$. To remove the uncertainty in future $\Delta C_{s,\tau}$ due to the climate sensitivity of the models, a common amount of global mean warming in each model was investigated. Figure 4.8(a) is similar to Figure 4.7(b) but instead for the more policy-relevant case of 2°C of global warming. As before, the y-axis represents the modelled $\Delta C_{s,\tau}$ and the

x-axis is the estimate derived from spatial variability. Once again, the actual and estimated values of $\Delta C_{s,\tau}$ cluster around the one-to-one line (with $\mathrm{r}^2 = 0.87$). The model range arises partly from differences in the initial field of heterotrophic respiration ($R_{h,0}$), and partly from differences in $\Delta\tau_s$.

The vertical green line in Figure 4.8(a) represents the mean estimate when the τ_s vs T relationship and the $R_{h,0}$ field from the model are replaced with the equivalents from the observations. The spread shown by the shaded area represents the relatively small impact on $\Delta C_{s,\tau}$ of differences in modelled spatial climate change patterns at 2°C of global warming. In order to estimate the remaining uncertainty in $\Delta C_{s,\tau}$, this spread is considered to be equivalent to an observational uncertainty in an emergent constraint approach (Eyring et al., 2019; Cox et al., 2018). A standard statistical approach (see methods, Cox et al. (2013); Wenzel et al. (2016)) is applied to estimate the probability density function of the y-axis variable (model $\Delta C_{s,\tau}$), accounting for both this observational spread and the quality of the emergent relationship. The analysis was completed with both CMIP6 and CMIP5 models to show that the result is also robust to the choice of model ensemble (see Table 4.1).

Figure 4.8(b) shows the resulting emergent constraint (blue line), and compares this with the unweighted histogram of model values (grey blocks), and a Gaussian fit to that prior distribution (black line), representing the distribution of the range of projections before and after the constraint. The spatial emergent constraint reduces the uncertainty in $\Delta C_{s,\tau}$ at 2°C of global warming from -196 $\pm$ 117 PgC to -232 $\pm$ 52 PgC (where these are mean values $\pm$ one standard deviation for the top 1 metre).

4.3.2.2 Observational sensitivity study

The analysis was completed with additional observational datasets used in the definition of τ_s (Equation 1) to test the robustness and sensitivity of the emergent constraint. A comparison of the derived observational relationships from the sensitivity study is presented in Figure 4.9, where differences are more prominent in the coldest and hottest temperature regions. The derived quadratic relationships and the corresponding observational dataset were each then used with Equation 4.4 as before to obtain a spatial emergent constraint on $\Delta C_{s,\tau}$.

The results for each observational dataset are presented in Table 4.1, which shows the constrained values of $\Delta C_{s,\tau}$ at 2°C global mean warming. It was found that strongly-overlapping emergent constraints where found, despite the use of different observational dataset. The constraint produced using Raich 2002 R_s

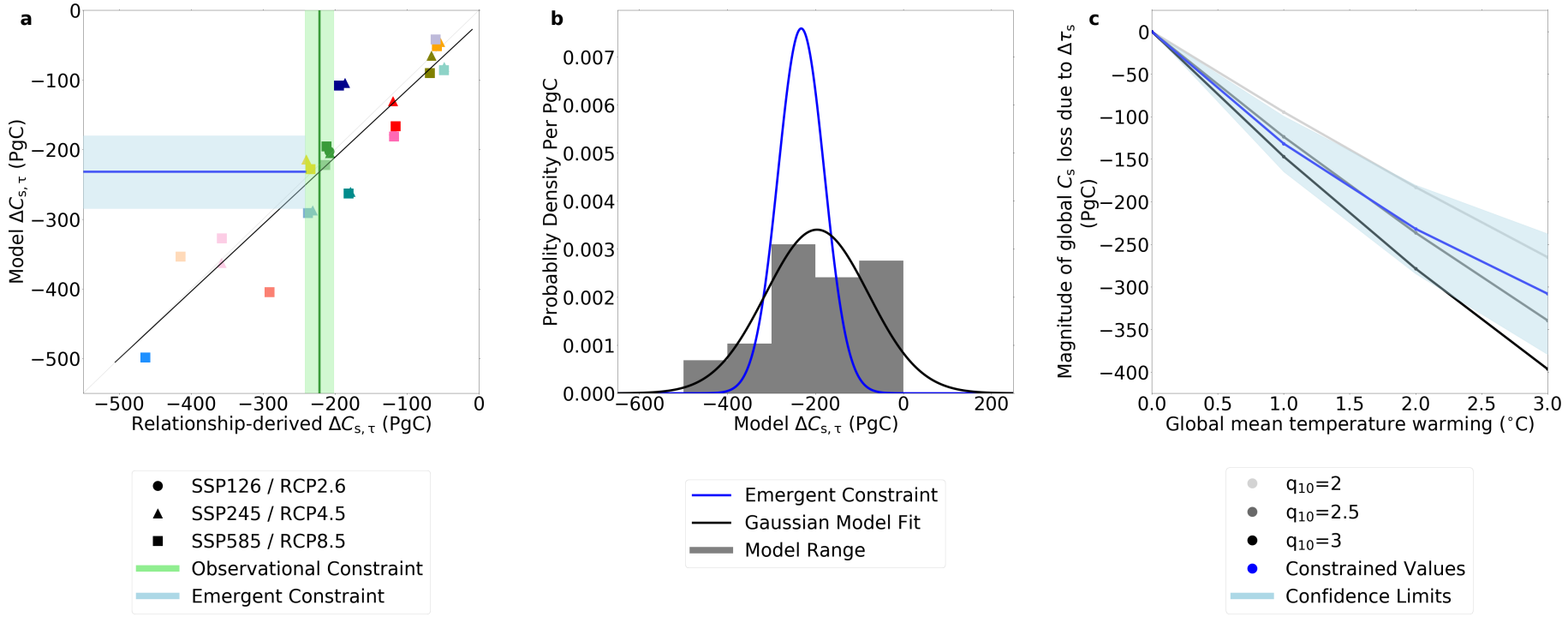

Figure 4.8: Figure showing the emergent constraint on $\Delta C_{s,\tau}$ as a function of global warming. (a) Actual vs estimated scatter plot for $\Delta C_{s,\tau}$ for 2°C of global warming. The vertical green line defines the observational constraint which is derived using observational data and the future spatial temperature field of each model (decadal average), and the shaded region represents the corresponding uncertainty ($\pm$1 standard deviation). The horizontal blue line represents the emergent constraint, with the shaded region showing the corresponding uncertainty ($\pm$1 standard deviation) which results from the differing future spatial warming patterns seen in the future spatial temperature fields across the ESMs, and the emergent relationship between the model data points (black line). (b) Probability density function showing the Gaussian distribution of $\Delta C_{s,\tau}$ values from the unweighted prior model ensemble (black line) and the emergent constraint (blue line). (c) Constrained $\Delta C_{s,\tau}$ values at different levels of global warming (blue line), including the likely ($\pm$1 standard deviation) uncertainty bounds (shaded blue). Different effective global q_{10} values shown for comparison; the emergent constraint is consistent with an effective $q_{10} \approx 2.5 \pm 0.6$.

Table 4.1: The table presents the sensitivity of the emergent constraint on $\Delta C_{s,\tau}$ to model ensemble: CMIP5, CMIP6, or CMIP5 and CMIP6 combined (columns), and to the observational dataset for heterotrophic respiration used in the calculation of τ_s (rows). The penultimate row presents the constraint using the observational τ_s v T fit and model $R_{h,0}$, opposed to observational $R_{h,0}$, to isolate the uncertainty reduction from these different components. For comparison, the last row shows the mean and standard deviation of the unconstrained model ensemble.

Constrained $\Delta C_{s,\tau}$ at 2°C global mean warming			
	Combined	CMIP6	CMIP5
CARDAMOM R_h	-232 ± 52	-238 ± 62	-227 ± 48
MODIS NPP	-201 ± 53	-206 ± 63	-196 ± 49
Raich 2002 R_s	-243 ± 50	-249 ± 59	-238 ± 46
CARDAMOM R_h (Observational τ_s v T fit, model $R_{h,0}$)	-227 ± 95	-220 ± 75	-230 ± 109
Unconstrained $\Delta C_{s,\tau}$	-196 ± 117	-216 ± 109	-180 ± 121

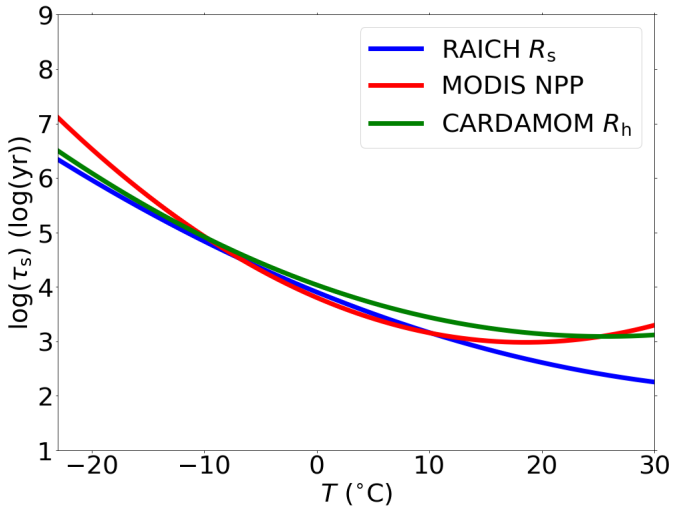

Figure 4.9: Comparison of the spatial $\log \tau_s$-temperature quadratic fits derived using the different observational datasets: CARDAMOM R_h (Bloom et al., 2015), MODIS NPP (Zhao et al., 2005), and Raich 2002 R_s (Raich et al., 2002).

has a slightly higher mean constrained value, and the constraint obtained using MODIS NPP obtains a lower mean constrained value, when compared to the constrained value using CARDAMOM R_h. However, both constraints are within the uncertainty range of the CARDAMOM R_h emergent constraint and the result suggests the constraint is not sensitive to the choice of observational dataset.

4.3.2.3 Breakdown of the spatial emergent constraint

The success of the constraint on $\Delta C_{s,\tau}$ under global warming is partly due to the correction from using observational R_h, and partly due to the use of the observational spatial temperature sensitivity of 'real world' τ_s, which is shown by Equation 4.4. To investigate the extent of which the constraint is dependent on each of the observational corrections, the constraint on $\Delta C_{s,\tau}$ at 2°C warming was considered with each component individually. The results are shown in the penultimate row of Table 4.1, and can be compared with the final emergent constraint values in the first row, and the unconstrained values in the final row.

The results from this investigation show that the constraint on the CMIP6 ensemble is mostly due to the correction from the observational τ_s-T relationship, where this results in a reduced standard deviation $\pm$ 75 PgC compared with $\pm$ 109 PgC unconstrained and $\pm$ 62 PgC using the full constraint method. Conversely, when only considering the CMIP5 ensemble, the reduced uncertainty mostly comes from the correction from the use of the observational initial heterotrophic respiration field, where this results in a reduced standard deviation of $\pm$ 109 PgC compared with $\pm$ 121 PgC unconstrained and $\pm$ 48 PgC using the full constraint method.

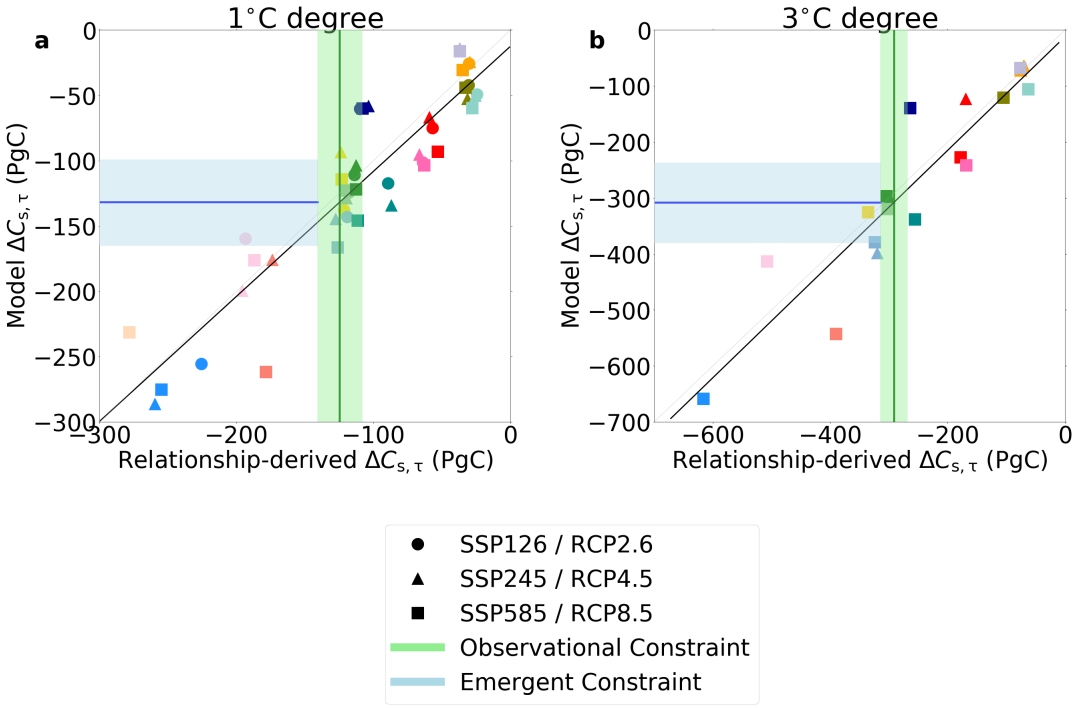

Figure 4.10: The emergent constraint plot, showing actual vs estimated $\Delta C_{s,\tau}$ for 1°C and 3°C of global warming, as shown in Figure 4.8(a) for 2°C of global warming.

4.3.2.4 Spatial emergent constraint applied to differing levels of global warming

The same method can be applied to find constrained values of $\Delta C_{s,\tau}$ for other values of global warming, where the correlation in the data was also tested (r^2 values for were as follows: 1°C is 0.84 and 3°C is 0.87). Spatial emergent constraints on $\Delta C_{s,\tau}$ are found for 1°C global warming, where the uncertainty is reduced from -115 $\pm$ 70 PgC to -132 $\pm$ 32 PgC, and 3°C global warming, where the uncertainty is reduced from -270 $\pm$ 161 PgC to -308 $\pm$ 71 PgC. The corresponding emergent constraint plots are shown in Figure 4.10, with Figure 4.10(a) showing the constraint on 1°C global warming and 4.10(b) on 3°C global warming.

Figure 4.8(c) shows the constrained range of $\Delta C_{s,\tau}$ as a function of global warming, which was found using the resultant constrained mean value of $\Delta C_{s,\tau}$ obtained for each °C of global mean warming, and the corresponding uncertainty bounds at the 68% confidence limits ($\pm$1 standard deviation). Also shown on the Figure 4.8(c) are different $\Delta C_{s,\tau}$-ΔT sensitivity curves based on different values of q_{10}, for example $q_{10} = 2$, calculated using Equation 4.12. Here the different degrees of global warming represent ΔT, and initial observational soil carbon stocks ($C_{s,0}$) are used. These curves can also be seen on Figure 4.6(b). It is important to note that there is no direct relationship between the effective

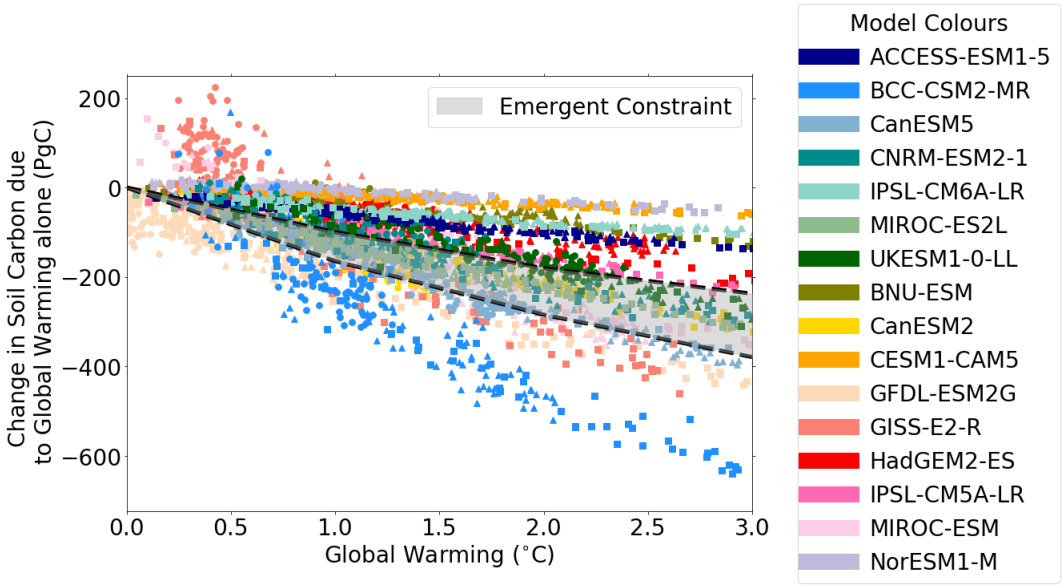

Figure 4.11: The constrained values of $\Delta C_{s,\tau}$ for differing levels of global mean warming (ΔT), diagnosed from sixteen Earth System Models (seven CMIP6 ESMs and nine CMIP5 ESMs), for three different future scenarios: SSP126, SSP245, SSP585, or RCP2.6, RCP4.5, RCP8.5, respectively. The shaded grey region, outlined by the black dotted line, shows the new constrained projected range of $\Delta C_{s,\tau}$ for increasing levels of global mean warming.

q_{10} for soil carbon change shown in Figures 4.6(b) and 4.8(c), and the spatial τ_s-T relationships in Figure 4.7(a). The q_{10} value derived here is an effective q_{10} value that indicates the sensitivity of global soil carbon (in the top 1 metre) to global mean temperature, where it can be seen that the emergent constraint is consistent with an effective $q_{10} \approx 2.5 \pm 0.6$.

Figure 4.11 shows the equivalent plot seen in Figure 4.6(a), which presented the large range of projections seen in $\Delta C_{s,\tau}$ by the ESMs in CMIP6 and CMIP5. However, Figure 4.11 includes the new constrained projections shown by the shaded grey region and outlined by the black dotted line. This shaded region shows the new reduced uncertainty in the projected change in soil carbon due to the change in soil carbon turnover for given degrees of global warming from this spatial emergent constraint method.

4.4 Discussion

The motivation for this study was due to the significant uncertainties found in projections of future soil carbon storage under climate change, which have been prominent across generations of ESMs (CMIP3, CMIP5 and CMIP6). It was found in Chapter 3 that the uncertainty surrounding this response was mostly due to uncertainties in the individual feedbacks, such as the changes from plants inputs and reductions in soil carbon turnover time (τ_s). The importance of con-

straining soil carbon turnover times in ESMs has been stated in the literature for both CMIP5 (Todd-Brown et al., 2014) and CMIP6 (Ito et al., 2020) generations. In this study, the response of soil carbon to climate change was separated into the response from changes in litter and root inputs from plants and on reductions in the turnover time of soil carbon (τ_s) with warming. The constraint focused on the latter-term, which was defined as the change in soil carbon due to the response of soil carbon turnover to climate change in the top 1 metre of soil ($\Delta C_{s,\tau}$).

This study defines the term 'spatial emergent constraint', which is the term used to describe an emergent constraint which is based on using a spatial temperature sensitivity to obtain a sensitivity to global warming. In previous emergent constraint studies, temporal trends, such as annual variability Cox et al. (2013) and seasonable cycles (Wenzel et al., 2014), have been used as the observable variable upon which the constraint is based. Unfortunately, time-varying observational datasets of C_s and R_h do not exist, which might have allowed a direct constraint on the projected uncertainty in global total $\Delta C_{s,\tau}$ to global warming (Figure 4.6). Instead it is explored whether the observed spatial variability in τ_s (as shown in Figure 4.5(c)) provides some observational constraint on the sensitivity of τ_s to temperature. In doing so, this premise is motivated by Chadburn et al. (2017) who used the correlation between the observed geographical distributions of permafrost and air temperature to constrain projections of future permafrost area under global warming. The concept relies on inferring how sensitive an Earth system variable is to temperature by the spatial temperature sensitivity, which you can then use to predict the sensitivity to future global warming based on this derived relationship to temperature. A spatial to temporal substitution can then be used to help constrain projections of the sensitivity of an Earth system variable to climate change.

As discussed in Chapter 1, for an emergent constraint to be credible the premise must be based on a physical understanding of the Earth system. In this case, the success and robustness of the method relies on the response of an Earth system variable to increased global temperatures under global warming to be the primary source of change at a global scale, opposed to the other associated climate change affects such as increased atmospheric CO_2 concentrations. In this case, the investigation took place using soil carbon turnover time (τ_s) which has previously been found to be especially dependent on temperature (Crowther et al., 2016; Davidson and Janssens, 2006; Trumbore et al., 1996; Jenkinson et al., 1991). Additionally, the spatial patterns of τ_s to temperature in CMIP5 simulations and observations were previously shown in Koven et al. (2017), where it was presented that a higher climatological temperature sensitivity was

seen in cold regions compared to warmer regions on Earth. The result found in Koven et al. (2017) suggested the potential for the spatial relationship of τ_s to temperature to infer the temperature sensitivity of τ_s, and the potential to use this with the emergent constraint technique.

Another method discussed in Chapter 1 to improve the credibility of an emergent constraint is the robustness to model ensemble. The deduced emergent constraint in this study included investigations into the sensitivity of the constraint to both model ensemble and observational dataset. Firstly, it was found that the spatial emergent constraint was consistent across CMIP generations, where the constraint held between CMIP5 and CMIP6 ensemble generations of ESMs (Table 4.1). Secondly, the spatial emergent constraint was found to be robust for different observational datasets, where overlapping constraints where found at 2° global warming (Table 4.1). A result of this improves the confidence and robustness of the constraint and the consequent constrained projections of $\Delta C_{s,\tau}$ under global warming.

4.5 Conclusions

Emergent constraints provide promise in helping to reduce the uncertainty surrounding the feedback of the carbon cycle to climate change. Projections of the future response to soil carbon due to reductions in turnover time ($\Delta C_{s,\tau}$) using CMIP6 and CMIP5 ESMs were found to span a large range even at 2°C of global warming (-196 $\pm$ 117 PgC). This study presented a constraint on $\Delta C_{s,\tau}$, which makes use of current heterotrophic respiration and the spatial variability of τ_s inferred from observations. This spatial emergent constraint resulted in successfully halving the uncertainty in $\Delta C_{s,\tau}$ at 2°C global warming to -232 $\pm$ 52 PgC.

The result suggests a potential release of approximately 230 billions tonnes of carbon into the atmosphere from the soil, if not negated by increased carbon input from plant productivity. To obtain a constraint on the overall response of soil carbon to climate change, further research on constraining this input flux of carbon to the soil under climate change is required. The result for the projected change in soil carbon due to reductions in soil carbon turnover rules out the most extreme projections, but nonetheless suggests substantial soil carbon losses due to climate change even in the absence of losses of deeper permafrost carbon.

Chapter 5

Soil carbon-concentration and carbon-climate feedbacks in CMIP6 Earth System Models

Abstract

Throughout this thesis, the aim has been to quantify and understand uncertainty surrounding the future response of soil carbon storage under climate change. The most commonly used approach to quantify changes in land carbon storage is the $\{\beta, \gamma\}$ formulation which breaks-down the changes in land carbon storage into two distinct linear feedback terms: carbon-concentration (β_L) and carbon-climate (γ_L) feedbacks (Friedlingstein et al., 2006). In this chapter, we use a similar approach specifically to examine projected changes in soil carbon storage.

5.1 Introduction

The future response of terrestrial carbon storage to anthropogenic CO_2 emissions is fundamental in understanding future changes to the Earth's climate system (Friedlingstein et al., 2020). Carbon cycle feedbacks are defined to describe the carbon cycle responses to increases in atmospheric CO_2 concentrations and the associated impact of climate change, such as through increases to atmospheric temperatures and changes in precipitation patterns (Canadell et al., 2021). Quantification of carbon cycle feedbacks is required to determine the overall response of the climate system to given atmospheric CO_2 emissions (Gregory et al., 2009). Land carbon cycle feedbacks are commonly broken-down into carbon-concentration feedbacks (β_L), which are a measure of how terrestrial carbon responds to an increased atmospheric CO_2 concentration, and carbon-climate feedbacks (γ_L), which are a measure of how terrestrial carbon responds to subsequent changes in climate (Friedlingstein et al., 2003, 2006).

These feedbacks are used to isolate the sensitivities of land carbon storage to changes in atmospheric CO_2 (ΔCO_2) and global temperatures (ΔT), which is assumed to represent the overall impacts of climate change on large spatial scales (Arora et al., 2020). The feedback parameters β_L and γ_L have previously been calculated for Earth System Models (ESMs) of both the CMIP5 generation (Arora et al., 2013) and CMIP6 generation (Arora et al., 2020) of the Coupled Model Intercomparison Project (CMIP). An advantage of using this formulation is that it allows for the quantification of the feedbacks for a given atmospheric CO_2 concentration, which can then be used as a simplified measure to compare amongst ESMs, despite the increasing ESM complexities (Arora et al., 2020, 2013; Gregory et al., 2009). Additionally, the technique can be used for concentration-driven and emission-driven simulations and removes the differences due to different climate sensitivities amongst the models (Arora et al., 2020; Boer and Arora, 2013; Friedlingstein et al., 2006). In this chapter, the focus is on quantifying soil carbon driven feedbacks in CMIP6 ESMs, and the sensitivity of soil carbon storage to future changes in the climate system. To do this, soil carbon carbon-concentration and carbon-climate feedbacks, $\{\beta_s, \gamma_s\}$, are estimated. In order to remove the complicating impacts of land-use change, Coupled Climate-Carbon Cycle Model Intercomparison Project (C4MIP) idealised experiments are considered (Arora et al., 2020, 2013; Jones et al., 2016). The aim of the chapter is to compare β_s and γ_s between models across the CMIP6 generation, and to look for evidence of non-linearities that are not captured by this approach.

5.2 Methods

5.2.1 C4MIP simulations

The Coupled Climate-Carbon Cycle Model Intercomparison Project (C4MIP) was set up to ease comparison of carbon cycle feedbacks in the climate system projected by ESMs, with the first results being presented in Friedlingstein et al. (2006). Since then, C4MIP has provided a common framework to allow for comparison and consistent evaluation of ESMs in each generation of the Coupled Model Intercomparison Project (CMIP). This framework includes a set of idealised experiments to simplify and quantify the impact of increasing atmospheric CO_2 on the climate system, where additional effects such as land-use change, aerosols, or non-CO_2 greenhouse gases are not included (Arora et al., 2020, 2013). The main simulation is known as the 1% CO_2 run (CMIP simulation *1pctCO2*), and is a simulation which sees a 1% increase in atmospheric CO_2 per year (referred to in this chapter as the full 1% CO_2 simulation), starting from

pre-industrial concentrations and running for 150 years.

Additional versions of this model experiment were designed to evaluate carbon cycle feedbacks, where the 'CO_2' effects and 'climate' effects are isolated (Arora et al., 2020, 2013). These are known as: biogeochemically coupled (referred to in this Chapter as BGC simulation) and radiatively coupled (referred to in this chapter as RAD simulation) 1% CO_2 runs. In the BGC runs (CMIP6 simulation *1pctCO2-bgc* and CMIP5 simulation *esmFixClim1*), the 1% CO_2 increase per year only affects the carbon cycle component of the ESM while the atmospheric radiation code continues to see pre-industrial CO_2 values. Conversely, in the RAD runs (CMIP6 simulation *1pctCO2-rad* and CMIP5 simulation *esmFdbk1*), the 1% CO_2 increase per year affects only the radiation code, and the carbon cycle component of the ESM continues to see just the pre-industrial CO_2 value (285 ppm). In both runs, nitrogen deposition is also fixed at pre-industrial values (Jones et al., 2016).

In this chapter, the full 1% CO_2, BGC, and RAD C4MIP experiments are analysed from ten Coupled Model Inter-comparison Project Phase 6 (CMIP6) ESMs (Eyring et al., 2016; Meehl et al., 2014). The CMIP6 ESMs included in this study are: ACCESS-ESM1-5, BCC-CSM2-MR, CanESM5, CESM2, GFDL-ESM4, IPSL-CM6A-LR, MIROC-ES2L, MPI-ESM1-2-LR, NorESM2-LM, and UKESM1-0-LL. Information about the ESMs is presented in Table 2.1 of Chapter 2.

5.2.2 Soil carbon-concentration and carbon-climate feedbacks

5.2.2.1 Friedlingstein et al. (2006) $\{\beta, \gamma\}$ formulation

Friedlingstein et al. (2003) were first to perform a feedback analysis to estimate the feedbacks of the carbon cycle under a changing climate using a linear approximation. Friedlingstein et al. (2006) adopted a similar approach, assuming ΔC_L can be approximated using feedback parameters which define separate sensitivities to changes in atmospheric CO_2 (ΔCO_2) and changes in global temperatures (ΔT), defined as the land carbon-concentration (β_L) and carbon-climate (γ_L) (Equation 5.1).

$$\Delta C_L \approx \beta_L \Delta CO_2 + \gamma_L \Delta T \tag{5.1}$$

The Friedlingstein et al. (2006) methodology (referred to in this chapter as the $\{\beta, \gamma\}$ formulation) uses time-integrated fluxes, which represent the global total

change in size of the land carbon pool (ΔC_L). This is presented for the full 1% CO_2 simulation (Equation 5.2), BGC simulation (Equation 5.3), and RAD simulation (Equation 5.4) below, where ΔC_L, ΔC_L^{BGC}, and ΔC_L^{RAD} are the changes in global land carbon pools (PgC), and F_L, F_L^{BGC}, and F_L^{RAD} represent the changes to the carbon fluxes (PgC yr^{-1}), for each simulation respectively.

$$\Delta C_L = \int F_L \, dt = \beta_L \Delta CO_2 + \gamma_L \Delta T \tag{5.2}$$

$$\begin{aligned} \Delta C_L^{BGC} = \int F_L^{BGC} \, dt = \beta_L \Delta CO_2 + \gamma_L \Delta T^{BGC} \\ \approx \beta_L \Delta CO_2 \end{aligned} \tag{5.3}$$

$$\Delta C_L^{RAD} = \int F_L^{RAD} \, dt = \gamma_L \Delta T^{RAD} \tag{5.4}$$

In these equations, $\Delta CO_2(t)$ is identical in the full 1% CO_2 and BGC simulations (Equations 5.2 and 5.3, respectively), as the carbon cycle sees increases in CO_2 in both cases. However, ΔCO_2 can be neglected in the RAD simulation (Equation 5.4), as the carbon cycle sees no increased CO_2 in this case. ΔT, ΔT^{BGC}, and ΔT^{RAD} are the changes in global temperatures, in the full 1% CO_2, BGC, and RAD simulations, respectively. In Equation 5.3, ΔT^{BGC} is assumed to be negligible, following Friedlingstein et al. (2006) where the small temperature change in the BGC simulation (ΔT^{BGC}) was ignored. The radiation code in the BGC simulation does not see an increase in CO_2, however Arora et al. (2020) explain that changes in the carbon cycle arising from increases in CO_2 affect latent and sensible heat fluxes at the land surface including changes to evaporative fluxes from stomatal closure over land and changes in vegetation structure and coverage if dynamic vegetation is included in the ESM. In this study, the temperature changes in the BGC simulation are assumed to be negligible in the context of the $\{\beta, \gamma\}$ formulation.

5.2.2.2 Defining soil carbon-concentration and carbon-climate feedbacks

The changes in land carbon storage, ΔC_L, can be written as the sum of the changes in vegetation carbon (ΔC_v) and changes in soil carbon (ΔC_s). This assumption allows for a similar breakdown of the land carbon-concentration and carbon-climate feedback parameters, where $\beta_L = \beta_v + \beta_s$ and $\gamma_L = \gamma_v + \gamma_s$ (Figure 5.5).

$$\Delta C_L \approx (\beta_v + \beta_s)\Delta CO_2 + (\gamma_v + \gamma_s)\Delta T \tag{5.5}$$

$$\Delta C_s \approx \beta_s \Delta CO_2 + \gamma_s \Delta T \tag{5.6}$$

Therefore, an equation for ΔC_s can be obtained, with soil specific carbon-concentration (β_s) and carbon-climate (γ_s) feedback parameters, which represent the sensitivity of ΔC_s to CO_2 and T, respectively (Equation 5.6).

5.2.3 Calculation of carbon-concentration and carbon-climate feedback parameters

5.2.3.1 Defining climate variables

For each of the CMIP6 ESMs, the CMIP output variables: *cSoil*, *cLitter*, and *cVeg* are considered in the analysis for future land carbon storage. Soil carbon (C_s) is defined as the sum of carbon stored in soils and the carbon stored in the vegetation litter (CMIP variable *cSoil* $+$ CMIP variable *cLitter*), allowing for a more consistent comparison between the models due to differences in how soil carbon and litter carbon are simulated (Arora et al., 2020; Todd-Brown et al., 2013). For models that do not report a separate litter carbon pool (CMIP variable *cLitter*), soil carbon is taken to be simply the CMIP variable *cSoil*. Land carbon (C_L) is defined as the sum of carbon stored in soil + litter (C_s), plus the carbon stored in vegetation (C_v, CMIP variable *cVeg*). Global total values for C_s and C_L are given in units of PgC, which are calculated using an area weighted sum (using the model land surface fraction, CMIP variable *sftlf*).

Increases in global temperatures (ΔT) are considered using CMIP variable *tas*, which is defined as the change in near-surface air temperature in °C. To calculate changes in atmospheric CO_2 (ΔCO_2) in the C4MIP 1% CO_2 simulations, initial pre-industrial CO_2 concentrations are considered as 285 ppm, and then cumulatively increased by 1% each year, for 71 years ($\approx$ 2xCO_2) or 141 years ($\approx$ 4xCO_2).

5.2.3.2 Carbon-concentration feedback parameter (β)

To calculate the soil carbon-concentration feedback parameter (β_s), the BGC run was used. For each ESM, soil carbon in the BGC run (C_s^{BGC}, PgC) was plotted against calculated CO_2 concentrations (ppm). To calculate β_s (expressed in units of carbon uptake or release per unit change in CO_2, PgC ppm^{-1}), the gradient was found using linear regression (using the python package numpy polyfit) between C_s^{BGC} and CO_2, for both 2xCO_2 and 4xCO_2. β_s is defined to be the gradient.

To calculate the land carbon-concentration feedback parameter (β_L), the same method was used but replacing C_s^{BGC} with C_L^{BGC}.

5.2.3.3 Carbon-climate feedback parameter (γ)

To calculate the soil carbon-climate feedback parameter (γ_s), the RAD run was used. For each ESM, soil carbon in the RAD run (C_s^{RAD}, PgC) was plotted against changing temperature T (°C) of each model. To calculate γ_s (expressed in units of carbon uptake or release per unit change in temperature, PgC °C^{-1}), the gradient was found using linear regression (using the python package numpy polyfit) between C_s^{RAD} and T, for both 2xCO_2 and 4xCO_2. γ_s is defined to be the gradient. To calculate the land carbon-climate feedback parameter (γ_L), the same method was used but replacing C_s^{RAD} with C_L^{RAD}.

5.2.3.4 Validity of method

In designing the C4MIP experiments, the purpose of the BGC simulation was to isolate the sensitivities to CO_2 for the calculation of β, and the purpose of the RAD simulation was to isolate the sensitivities to T for the calculation of γ. Therefore, this is the methodology chosen in this study for an initial investigation into soil carbon specific β and γ feedback parameters. However, to test the validity of the method used here, the land carbon-concentration (β_L) and carbon-climate (γ_L) feedback parameters derived in this study for the CMIP6 ESMs are compared with the equivalent values presented in Arora et al. (2020) (named β_L^{A2020} and $\gamma_L^{*,A2020}$), for both 2xCO_2 and 4xCO_2 (Table 5.1). Note, the land carbon feedback parameters are considered to test the validity of the method as this is the first study to calculate soil specific feedback parameters in this way (where, $C_L = C_s + C_v$).

Arora et al. (2020) chose an adapted method to calculate the land carbon-climate feedback parameters with the CMIP6 ESMs (referred to here as γ^*). To calculate γ^*, the full 1% CO_2 and BGC simulations were used, opposed to the RAD simulation (see the BGC-COU approach, Table 1 in Arora et al. (2020)). Therefore, γ_L^* was calculated and compared with $\gamma_L^{*,A2020}$, where if linearity is assumed, $\gamma \approx \gamma^*$. To calculate γ_L^*, land carbon in the BGC run (C_L^{BGC}) is subtracted from land carbon in the full 1% CO_2 run (C_L), then the resultant land carbon was plotted against changing temperature T (°C) from the full 1% CO_2 simulation for each model. To calculate γ_L^* (PgC °C^{-1}), the gradient was found using linear regression (using the python package numpy polyfit) between $C_L - C_L^{BGC}$ and T, for both 2xCO_2 and 4xCO_2, where γ_s^* is defined to be the gradient.

The β_L values calculated in this chapter are consistent with the Arora et al. (2020) values, but there are some differences in the γ_L^* values (Table 5.1). Future studies should investigate the sensitivity of β_s and γ_s to different calculation methods, but this is beyond the scope of this chapter.

5.3 Results

5.3.1 Investigating projections of soil carbon in the 1% CO_2 simulations

Projections of soil carbon change (ΔC_s) in CMIP6 ESMs for the full 1% CO_2, biogeochemically coupled 1% CO_2 (BGC) and radiatively coupled 1% CO_2 (RAD) simulations, are presented in Figure 5.1. Soil carbon is projected to increase in the full 1% CO_2 simulation amongst CMIP6 ESMs (ensemble mean +88.2$\pm$40.4 PgC at 2xCO_2 and +177$\pm$141 PgC at 4xCO_2). However, the magnitude of the increase varies amongst the ESMs, with a range of +38 PgC (NorESM2-LM) to +145 PgC (BCC-CSM2-MR) at 2xCO_2, and a range of +15 PgC (ACCESS-ESM1-5) to +502 PgC (CanESM5) at 4xCO_2. Six of the ESMs (CanESM5, CESM2, IPSL-CM6A-LR, MIROC-ES2L, MPI-ESM1-2-LR, NorESM2-LM) see an increased ΔC_s value with increasing climate forcing, however the remaining four ESMs (ACCESS-ESM1-5, BCC-CSM2-MR, GFDL-ESM4, UKESM1-0-LL) see a saturation affect on the increase or a turning point, where carbon starts to decrease again from 70 years ($\approx$ 2xCO_2) in the simulation (Figure 5.1(a)).

The projected increase in ΔC_s is the net effect of the increases projected in the BGC run (ensemble mean +132$\pm$66.5 PgC at 2xCO_2 and +348$\pm$203 PgC at 4xCO_2, Figure 5.1(b)) and the decreases projected in the RAD run (ensemble mean -45.5$\pm$22.9 PgC at 2xCO_2 and -170$\pm$94.7 PgC at 4xCO_2, Figure 5.1(c)), where the response due to increases in atmospheric CO_2 (BGC simulation) dominate the overall response (full 1% CO_2 simulation) in the majority of models. In the BGC simulation, projected ΔC_s values range from +49 PgC (NorESM2-LM) to +267 PgC (BCC-CSM2-MR) at 2xCO_2, and from +113 PgC (ACCESS-ESM1-5) to +721 PgC (BCC-CSM2-MR) at 4xCO_2. In the RAD simulation, lower magnitudes are seen, where projected ΔC_s values range from -16 PgC (CESM2) to -84 PgC (BCC-CSM2-MR) at 2xCO_2, and from -60 PgC (MPI-ESM1-2-LR) to -372 PgC (BCC-CSM2-MR) at 4xCO_2.

Figure 5.2 shows patterns of changes in soil carbon (ΔC_s) at 4xCO_2, for the full 1% CO_2, biogeochemically coupled 1% CO_2 (BGC) and radiatively coupled 1% CO_2 (RAD) simulations. In the BGC simulation, increases in ΔC_s are seen

Table 5.1: Table presenting the calculated land carbon-concentration (β_L, PgC ppm^{-1}) and carbon-climate (γ_L^*, PgC °C^{-1}) feedback parameters for 2xCO_2 and 4xCO_2, compared to the values presented Arora et al. (2020) for the CMIP6 ESMs.

	Land carbon							
Earth System Model	2xCO_2				4xCO_2			
	β_L	β_L^{A2020}	γ_L^*	$\gamma_L^{*,A2020}$	β_L	β_L^{A2020}	γ_L^*	$\gamma_L^{*,A2020}$
ACCESS-ESM1.5	0.694	0.75	-8.19	-12	0.301	0.37	-15.5	-21.1
BCC-CSM2-MR	1.80	2.22	-83.3	-132.84	1.54	1.81	-141	-163.1
CanESM5	1.47	1.42	-5.89	-6.22	1.43	1.28	+10.2	+15.95
CESM2	0.930	0.98	-8.36	-12.76	0.869	0.9	-16.1	-21.6
GFDL-ESM4	1.13	1.08	-42.4	-50.69	0.986	0.93	-72.4	-80.06
IPSL-CM6A-LR	1.18	1.11	-12.8	-12.24	0.713	0.62	-8.88	-8.67
MIROC-ES2L	1.50	1.45	-48.7	-63.36	1.21	1.12	-67.8	-69.57
MPI-ESM1-2-LR	1.16	1.08	-1.71	-0.81	0.773	0.71	-6.43	-5.17
NorESM2-LM	0.899	0.94	-13.4	-15.61	0.816	0.85	-17.2	-20.95
UKESM1-0-LL	1.10	1.00	-22.6	-24.01	0.815	0.75	-34.9	-38.4
Ensemble mean	1.19	1.22	-27.3	-34.10	0.95	0.97	-37.0	-45.07
Ensemble std	± 0.31	± 0.40	± 27.5	± 38.39	± 0.35	± 0.40	± 45.0	± 50.59

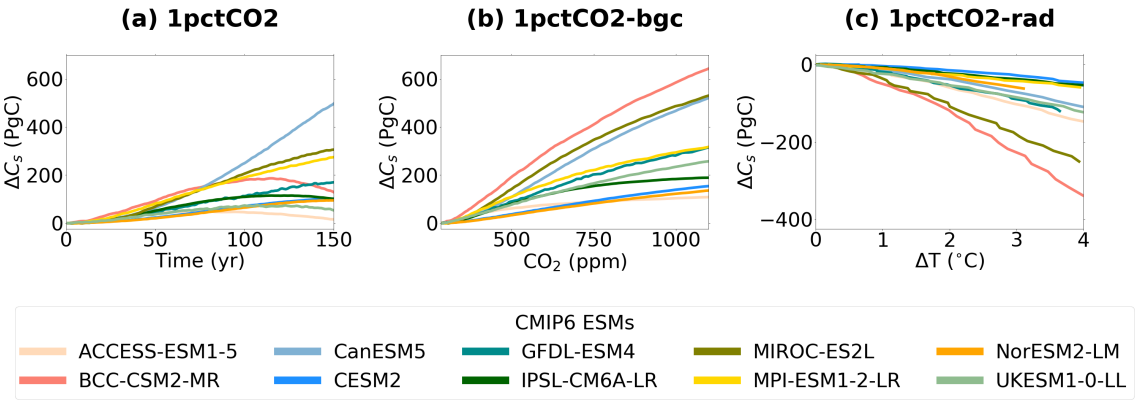

Figure 5.1: Timeseries of projected changes in soil carbon (ΔC_s) in CMIP6 ESMs for the idealised 1% CO_2 (left column), biogeochemically coupled 1% CO_2 (BGC, middle column) and radiatively coupled 1% CO_2 (RAD, right column) simulations.

across all regions in CMIP6 ESMs, apart from slight decreases found in the northern latitudes of the CanESM5 and NorESM2-LM models. The projected increases in ΔC_s have spatially varying magnitudes, but generally the greatest increases are seen in the tropical regions. In the RAD simulation, ΔC_s is found to be more spatially variable compared with the BGC simulation. In the RAD simulation, generally ΔC_s decreases globally, with the greatest decreases seen in the tropical regions. However, the greatest disagreement is seen in the northern latitudes, where four models (ACESS-ESM1-5, CanESM5, MIROC-ES2L, UKESM1-0-LL) see an increase in ΔC_s, but three models (BCC-CSM2-MR, CESM2, NorESM2-LM) see a decrease in ΔC_s. The overall ΔC_s values seen in the full 1% CO_2 simulation are again found to be mostly dominated by the BGC simulation (Figure 5.2). However, exceptions are seen where the RAD simulation dominates for certain regions in some CMIP6 ESMs. Specifically, the decrease in ΔC_s in the RAD simulation dominates the overall response of ΔC_s in the northern latitudes of BCC-CSM2-MR, CESM2, and NorESM2-LM (the only models where decreases where seen), as well as ΔC_s in tropical regions of ACCESS-ESM1-5, GFDL-ESM4, and UKESM1-0-LL.

5.3.2 Soil carbon-concentration and carbon-climate feedback parameters

The sensitivity of soil carbon to changes in atmospheric CO_2 (BGC simulation) and global temperatures (RAD simulation) can be quantified using soil carbon specific carbon-concentration (β_s) and carbon-climate (γ_s) feedback parameters. The soil carbon-concentration (β_s) and carbon-climate (γ_s) feedback parameters were calculated for each CMIP6 ESM, and the values are presented in Table 5.2. β_s is found to be positive amongst the CMIP6 ESMs, consistent with increased C_s with increasing CO_2, and γ_s is found to be negative, consistent with decreased

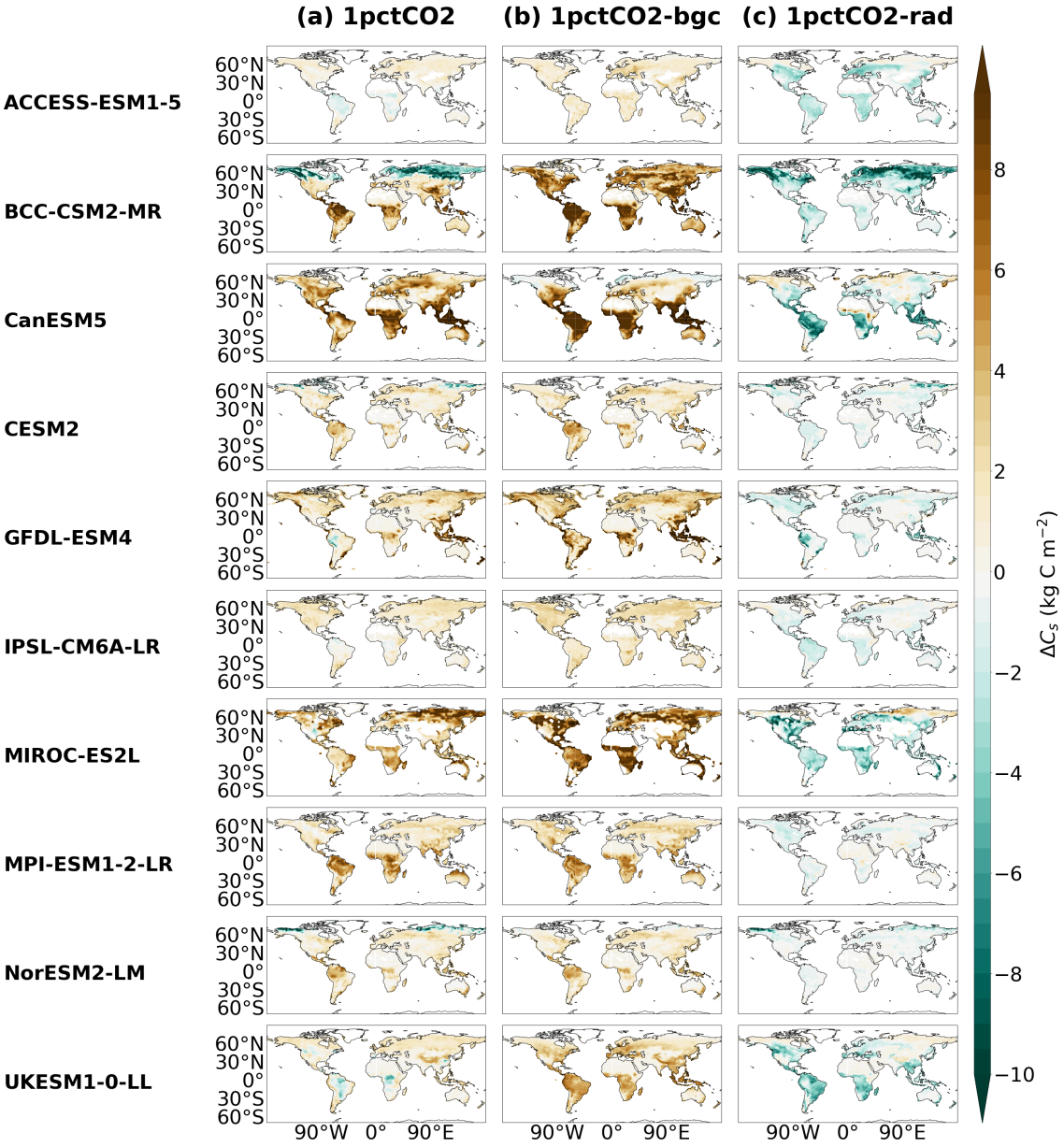

Figure 5.2: Maps of changes in soil carbon (ΔC_s) at 4xCO_2 in CMIP6 ESMs for the idealised simulations 1% CO_2 (left column), biogeochemically coupled 1% CO_2 (BGC, middle column) and radiatively coupled 1% CO_2 (RAD, right column).

C_s with increasing temperature.

The climate feedback (γ_s) is found to be slightly more uncertain amongst the CMIP6 ESMs compared with the concentration feedback (β_s), where the γ_s ensemble standard deviation has a magnitude of 61% of the mean, compared to 57% in β_s projections at 4xCO_2. The β_s parameters varied from 0.174 PgC ppm^{-1} (NorESM2-LM) to 0.957 PgC ppm^{-1} (BCC-CSM2-MR) at 2xCO_2, and from 0.127 PgC ppm^{-1} (ACCESS-ESM1-5) to 0.837 PgC ppm^{-1} (BCC-CSM2-MR) at 4xCO_2. The γ_s parameters are found to be less consistent between 2xCO_2 and 4xCO_2, and varied from -7.87 PgC $^{\circ}$C^{-1} (CESM2) to -53.7 PgC $^{\circ}$C^{-1} (BCC-CSM2-MR) at 2xCO_2, and from -15.1 PgC $^{\circ}$C^{-1} (CESM2) to -83.7 PgC $^{\circ}$C^{-1} (BCC-CSM2-MR) at 4xCO_2 (Table 5.2). Generally, models with higher sensitivities to CO_2 (β_s), also have higher sensitivities to temperature (γ_s), where an r^2 value of 0.6 is found between the β_s and γ_s values.

The calculation of the soil carbon-concentration (β_s) and carbon-climate (γ_s) feedback parameters for 2xCO_2 are shown in Figure 5.3. Projections of soil carbon in the BGC simulation (C_s^{BGC}) are shown in Figure 5.3(a) and projections of soil carbon in the RAD simulation (C_s^{RAD}) are shown in Figure 5.3(b). Soil carbon responds approximately linearly to both CO_2 (ΔC_s^{BGC}) and temperature (ΔC_s^{RAD}) up until 2xCO_2. However, above 2xCO_2, the changes seen in many of the models diverge from this linear behaviour.

In the BGC simulation, C_s^{BGC} is found to have a continuous linearity with CO_2 in the CESM2, CanESM5, and NorESM2-LM models, with a relatively consistent β_s factor for both 2xCO_2 and 4xCO_2 (Table 5.2). However, the majority of the CMIP6 ESMs (ACESS-ESM1-5, BCC-CSM2-MR, GFDL-ESM4, IPSL-CM6A-LR, MIROC-ES2L, MPI-ESM1-2-LR, and UKESM1-0-LL) see a saturation to the increase, and the projected C_s^{BGC} at 4xCO_2 is less than the estimated sensitivity by the 2xCO_2 β_s line (Figure 5.3(a)).

In the RAD simulation, the ESMs in CMIP6 suggest an increased sensitivity of C_s^{RAD} to temperature (T) with increased climate forcing. However, the magnitude of this affect varies amongst the models. The CESM2 and NorESM2-LM models have amongst the lowest sensitivities to T at 2xCO_2, however approximately a 50% increase is seen in γ_s between 2xCO_2 and 4xCO_2 (Table 5.2). Also amongst the lowest sensitivities to T are the IPSL-CM6A-LR and MPI-ESM1-2-LR models, but this remains the case with increased forcing and only a small difference is seen between γ_s at 2xCO_2 and 4xCO_2 in these models. The models with the greatest sensitivities to T are BCC-CSM2-MR and

Table 5.2: Table presenting the land carbon-concentration (β_L, PgC ppm^{-1}) and carbon-climate (γ_L and γ_L^*, PgC °C^{-1}) feedback parameters, and the soil carbon-concentration (β_s, PgC ppm^{-1}) and carbon-climate (γ_s and γ_s^*, PgC °C^{-1}) feedback parameters, for 2xCO_2 and 4xCO_2 for the CMIP6 ESMs.

	Land carbon				**Soil carbon**			
Earth System Model	2xCO_2		4xCO_2		2xCO_2		4xCO_2	
	β_L	γ_L	β_L	γ_L	β_s	γ_s	β_s	γ_s
ACCESS-ESM1.5	0.694	-67.5	0.301	-83.0	0.274	-30.7	0.127	-40.0
BCC-CSM2-MR	1.80	-65.6	1.54	-98.9	0.957	-53.7	0.837	-83.7
CanESM5	1.47	-20.3	1.43	-35.9	0.593	-20.2	0.697	-31.6
CESM2	0.930	-18.6	0.869	-30.2	0.192	-7.87	0.203	-15.1
GFDL-ESM4	1.13	-42.2	0.986	-59.9	0.446	-25.3	0.410	-33.0
IPSL-CM6A-LR	1.18	-17.6	0.714	-24.4	0.405	-11.6	0.258	-15.4
MIROC-ES2L	1.50	-48.1	1.21	-74.3	0.765	-43.7	0.717	-63.5
MPI-ESM1-2-LR	1.16	-10.5	0.773	-9.30	0.554	-14.2	0.415	-15.4
NorESM2-LM	0.899	-19.5	0.816	-37.1	0.174	-10.9	0.179	-20.2
UKESM1-0-LL	1.10	-34.6	0.815	-52.1	0.371	-23.8	0.332	-32.3
Ensemble mean	1.19	-34.5	0.945	-50.5	0.474	-24.2	0.418	-35.0
Ensemble std	± 0.308	± 19.6	± 0.345	± 26.9	± 0.237	± 14.1	± 0.237	± 21.5

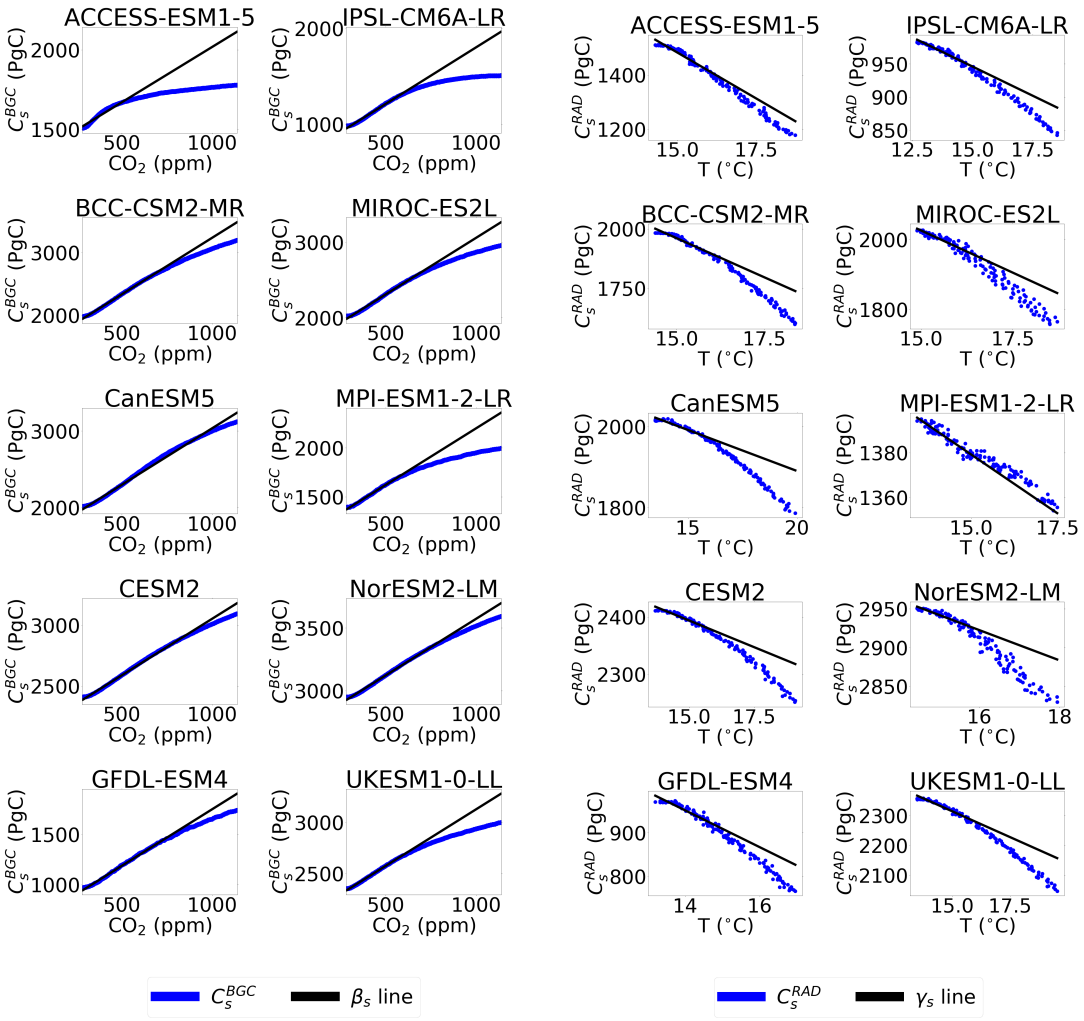

(a) β_s (b) γ_s

Figure 5.3: Timeseries plots showing the calculation of the soil carbon-concentration feedback parameters (a) β_s, and soil carbon-climate feedback parameters (b) γ_s, to 2xCO_2 for each CMIP6 ESM.

MIROC-ES2L at both 2xCO_2 and 4xCO_2 (Figure 5.3(b)).

5.3.3 Investigating the non-linearity in soil carbon sensitivities to climate change

The projected change in soil carbon (ΔC_s) in ESMs in the full 1% CO_2 simulations was compared with the estimated ΔC_s derived using Equation 5.6, which uses the derived β_s and γ_s feedback parameters together with model specific ΔT, with estimates for both 2xCO_2 and 4xCO_2 (Figure 5.4). At 2xCO_2, the $\{\beta, \gamma\}$ approximation is found to predict ΔC_s within 15% of the actual projected values in the 1% CO_2 simulation for seven out of the ten CMIP6 ESMs (CanESM5, CESM2, GFDL-ESM4, IPSL-CM6A-LR, MPI-ESM1-2-LR, NorESM2-LM, and UKESM1-0-LL). The remaining models where the linear approximation is less consistent with projected ΔC_s changes are ACCESS-ESM1-5, BCC-CSM2-MR, and MIROC-

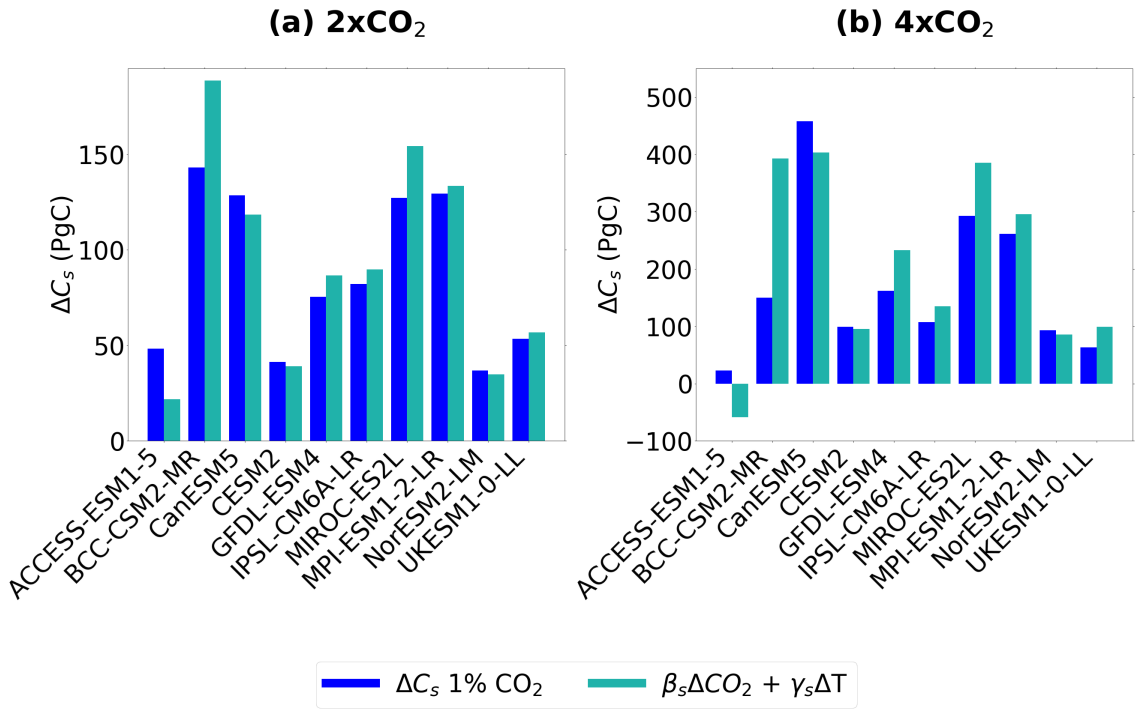

Figure 5.4: Bar charts comparing ΔC_s (PgC) in the full 1% CO_2 simulations with estimated ΔC_s using the calculated β_s and γ_s feedback parameters for each CMIP6 ESM, where estimated $\Delta C_s \approx \beta_s \Delta CO_2 + \gamma_s \Delta T$, for (a) 2x$CO_2$ and (b) 4xCO_2.

ES2L (Figure 5.4(a)). At 4xCO_2, the $\{\beta, \gamma\}$ approximation is found to be less robust at predicting consistent changes in soil carbon. The linear approximation is most robust in the CESM2 and NorESM2-LM models, where $\beta_s \Delta CO_2 + \gamma_s \Delta T$ is within 10% of the projected ΔC_s, followed by the CanESM5 and MPI-ESM1-2-LR models which were within 15%. The models where the linear approximation is the least consistent with projected ΔC_s are ACCESS-ESM1-5 and BCC-CSM2-MR, where it is shown that the linear approximation is not suitable at 4xCO_2 (Figure 5.4(b)).

5.3.4 Comparisons with land carbon-concentration and carbon-climate feedback parameters

The contribution of the sensitivity of soil carbon stocks (C_s) to the total sensitivity of future land carbon stocks (C_L) was investigated, where comparisons are made between the soil and land carbon-concentration feedback parameters, β_s and β_L, and the soil and land carbon-climate feedback parameters, γ_s and γ_L (Figure 5.5). For the carbon-concentration feedback (β), the portion of the β_L response that is due to global soils (β_s) ranges from 19% (NorESM2-LM) to 53% (BCC-CSM2-MR), with a mean of 38 $\pm$ 11 % seen across the CMIP6 ESMs at 2xCO_2 (Figure 5.5(a)). At 4xCO_2 the range is from 22% (NorESM2-LM) to 59% (MIROC-ES2-L), with a mean of 42 $\pm$ 12 % seen across the CMIP6 ESMs (Figure 5.5(b)). The

portion of β_L due to β_s remains consistent between 2xCO_2 and 4xCO_2, suggesting consistent sensitivities with increased forcing. For the carbon-climate feedback (γ), the portion of the γ_L response that is due to global soils (γ_s) ranges from approximately 26% (CESM2) to 153% (MPI-ESM1-2-LM), with a mean of 55 $\pm$ 32 % seen across the CMIP6 ESMs at 2xCO_2 (Figure 5.5(a)), and at 4xCO_2 the ranges is from 50% (CESM2) to 165% (MPI-ESM1-2-LM), with a mean of 76 $\pm$ 33 % seen across the CMIP6 ESMs (Figure 5.5(b)). Therefore, the portion of γ_L due to γ_s increases with increasing climate forcing, suggesting that soil dominates the response of land carbon to climate, especially at more extreme levels of climate change.

5.4 Discussion

Quantifying future changes in soil carbon under climate change is vital in order to understand future changes in the Earth's climate system (Canadell et al., 2021; Ciais et al., 2013). Changes in soil carbon (ΔC_s) are generally assumed to result from either changes in atmospheric CO_2 or changes in global temperatures (T), approximately controlled by increased soil carbon due to the CO_2 fertilisation effect and decreased soil carbon by increases in heterotrophic respiration (R_h), respectively (Todd-Brown et al., 2014). By separating the effects of increasing CO_2 and T, the C4MIP (Jones et al., 2016) ESM simulations allow the effects of these two processes to be examined individually. Consistent increases in soil carbon across the CMIP6 ESMs in the BGC simulations ('CO_2 only'), and consistent decreases in soil carbon in the RAD simulations ('climate only') (Figure 5.1), demonstrate these two processes, and are consistent with ESM predictions seen for changes in the overall land carbon responses (Arora et al., 2020, 2013).

Understanding how these two processes relate to the overall soil carbon response under climate change is crucial to quantifying changes to soil carbon stocks in the future. The commonly used $\{\beta, \gamma\}$ formulation allows for the quantification of sensitivities to both CO_2 and T, and assumes that the overall response can be approximated as a linear combination of the individual feedbacks (Friedlingstein et al., 2006). This formulation has previously been used to quantify both land and ocean responses in both CMIP5 and CMIP6 generation of ESMs (Arora et al., 2020, 2013; Boer and Arora, 2009), but has yet to be used to approximate the sensitivity of soil carbon and quantify the soil carbon feedback in ESMs. In this study, the Friedlingstein et al. (2006) $\{\beta, \gamma\}$ formulation is adapted to define soil carbon specific feedback parameters and quantify the sensitivity of soil carbon to CO_2 and T. The work in this chapter shows that the

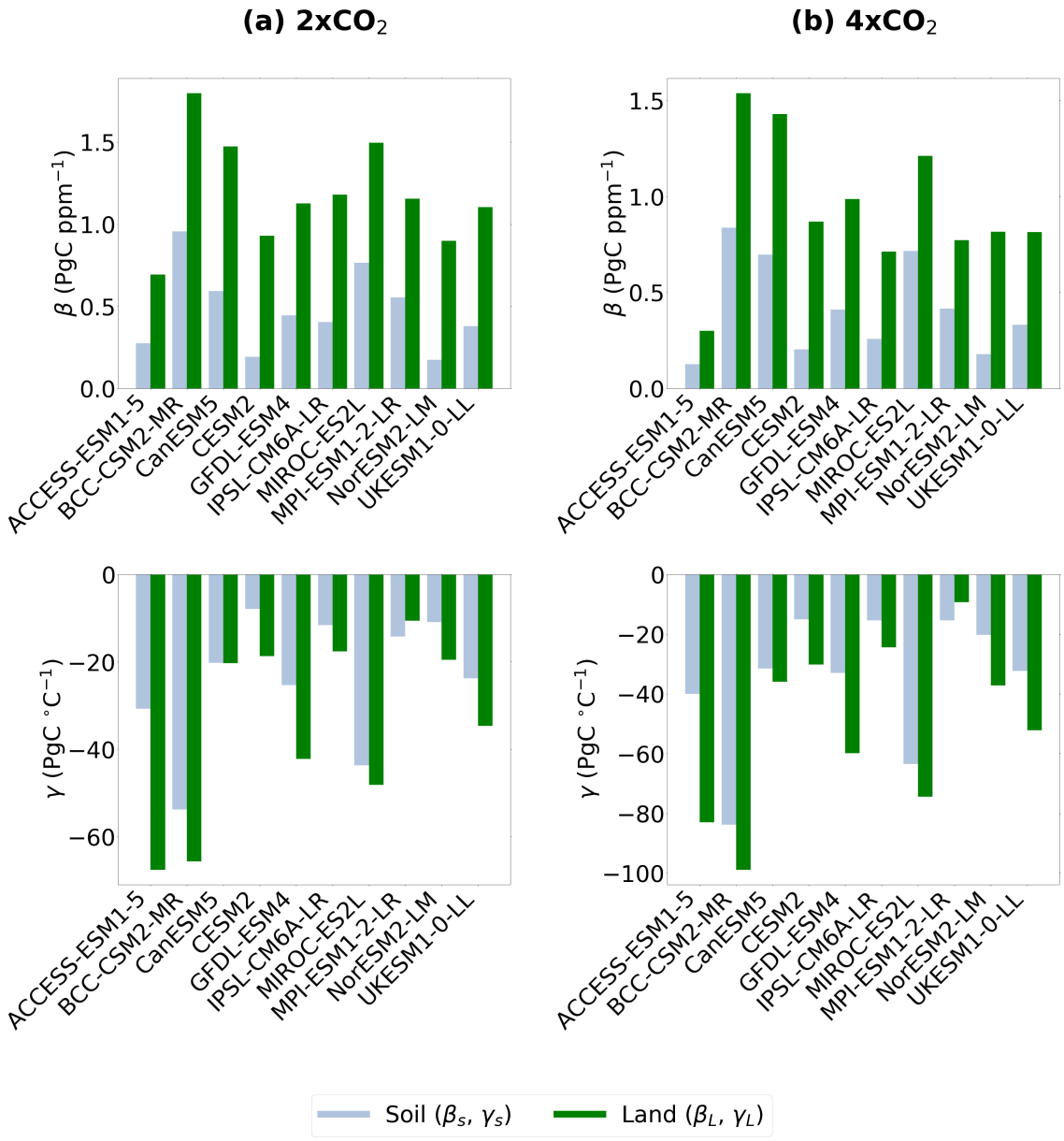

Figure 5.5: Bar charts comparing the land carbon-concentration (β_L) feedback parameters with the soil carbon-concentration (β_s) feedback parameters (top row), and the land carbon-climate (γ_L) feedback parameters with the soil carbon-climate (γ_s) feedback parameters (bottom row), for (a) 2xCO_2 and (b) 4xCO_2.

linear approximation into CO_2 and T sensitivities is a good approximation to predict soil carbon changes in CMIP6 ESMs up until approximately a doubling of pre-industrial CO_2 values. However, as the change in CO_2 increases beyond a doubling of CO_2, the linear approximation breaks down in approximately six out of ten ESMs within the ensemble, and significant divergences are seen between the actual soil carbon predicted by CMIP6 ESMs and the change in soil carbon predicted by the $\{\beta, \gamma\}$ formulation. This is seen both in terms of the response to T or CO_2 individually (Figure 5.3) and in terms of the additive nature of the T and CO_2 responses in giving the response in the full simulation (Figure 5.4).

The breakdown of the $\{\beta, \gamma\}$ approximation at high CO_2 in CMIP6 ESMs may imply cross-terms between the CO_2 and T responses. Non-linearities in the future land and ocean carbon responses have previously been found in ESMs (Arora et al., 2020; Schwinger et al., 2014; Zickfeld et al., 2011; Gregory et al., 2009). Zickfeld et al. (2011) suggest that the non-linearity in the land response is due to significantly differing vegetation responses which depend on whether or not climate effects are combined with the CO_2 fertilization effect, for example forest dieback. However, this is found to be model dependent, for example not all models simulate dynamic vegetation. The spatial variations in the response of soil carbon to CO_2 and climate that are seen in Figure 5.2 could also contribute to the non-linearity. For example, a different spatial pattern of soil carbon under elevated CO_2 could lead to a different overall temperature response, e.g. if more carbon is in the high latitudes where greater temperature changes are seen.

Arora et al. (2020) find that climate responses in the BGC simulation account for a difference of 1% - 5% in the calculation of the feedbacks, suggesting a small but non-negligible effect of climate in the BGC runs. This response was shown to be dependent on the representation of vegetation within the model, as with the non-linearities found in Zickfeld et al. (2011). Model dependency was also found here, with the first-order linear approximation remaining a valid formulation for four out of the ten ESMs within CMIP6, even at 4xCO_2 (Figure 5.4). Therefore, a non-linearity in CO_2 and T is not robustly found amongst the CMIP6 models. Conversely, the non-linearity presented in Chapter 3, which suggested a future non-linearity between Net Primary Productivity (NPP) and soil carbon turnover time (τ_s), was found to be consistent amongst CMIP6 ESMs and was seen at all levels of climate change across the future SSP scenarios. To further investigate the sensitivities of soil carbon to individual CO_2 and T responses, an investigation into the sensitivities of the soil carbon controls using the C4MIP simulations is suggested (see Chapter 6).

5.5 Conclusions

The Friedlingstein et al. (2006) methodology adapted in this chapter suggests that β_s and γ_s is a valid assumption for projected soil carbon changes in ESMs up until a doubling of CO_2. However, under more extreme levels of climate change, the results here suggest the need for the non-linearity in feedbacks to be further investigated. Soil carbon is found to have a greater impact on carbon-climate feedbacks than vegetation carbon responses, which means that the sensitivity of soil to changes in global temperature is the dominant response of the land surface. Therefore, further understanding and quantifying the sensitivity of global soils under global warming is necessary to quantify future changes in the climate system. Moreover, the sensitivity of soil carbon to temperature increased with increasing climate forcing, suggesting that soil carbon is particularly important in the long-term response of land carbon storage under extreme levels of global warming. This result suggests the need for future model development to focus on the simulation of soil carbon in ESMs, with a specific focus on below-ground processes.

Chapter 6

Relating the $\{\beta, \gamma\}$ formulation to the $\{NPP, \tau_s\}$ formulation

Abstract

In Chapter 5, the response of soil carbon in CMIP6 models was broken-down using the $\{\beta, \gamma\}$ formulation, separating the responses to increases in atmospheric CO_2 and global warming (Friedlingstein et al., 2006). By contrast in Chapter 3, the soil carbon response was analysed in terms of above-ground (NPP) and below-ground (τ_s) processes, called here the '$\{NPP, \tau_s\}$ formulation'. In this chapter, these two different formulations are compared to understand the reasons for the effectiveness of the linear $\{\beta, \gamma\}$ approach. This investigation then further revealed the importance of 'false priming' (Koven et al., 2015), which leads to an apparent sensitivity of the effective soil carbon turnover time (τ_s) to NPP, and therefore to atmospheric CO_2.

6.1 Introduction

The overall response of soil carbon to climate change can be quantified by understanding the response of carbon exchange between the land and the atmosphere to increases in anthropogenic CO_2. The carbon fluxes which control the fate of carbon stored in global soils are known to be sensitive to changes in climate, which results in soil carbon driven feedbacks to climate change (Canadell et al., 2021). The input flux of carbon to the soil can be approximated as Net Primary Productivity (NPP) (Todd-Brown et al., 2014, 2013), defined as the net rate of accumulation of carbon by vegetation arising from photosynthesis minus the loss from plant respiratory fluxes. NPP is projected to increase under increased atmospheric CO_2 due to a CO_2 fertilization effect (Schimel et al., 2015; Todd-Brown et al., 2014), which can result in an increased soil carbon storage. The output flux of carbon from the soil is approximated as heterotrophic respi-

ration (R_h), defined as the carbon losses due to decomposition from microbes in the soil. R_h is projected to increase under global warming, where increased global temperatures result in an increased rate of microbial decomposition. Soil carbon turnover time (τ_s) is defined as the ratio of soil carbon stocks to the output flux of carbon, is often considered as a proxy for this increased R_h (Todd-Brown et al., 2014, 2013), where the increased R_h is known to reduce global τ_s and results in an increased release of carbon from the soil into the atmosphere (Crowther et al., 2016).

On a global scale, it was assumed that as a first-order approximation the future response of NPP could be approximated as the linear response to increases in atmospheric CO_2 and the future response of τ_s could be approximated as the linear response to increases in global temperatures (T). This assumption was made due to NPP being known to be especially dependent on atmospheric CO_2 concentrations (De Kauwe et al., 2016; Schimel et al., 2015; Woodward et al., 1998; Cao and Woodward, 1998) and turnover time being known to be especially dependent on temperature (Exbrayat et al., 2013a; Hartley and Ineson, 2008; Trumbore et al., 1996; Lloyd and Taylor, 1994). However, Chapter 3 found a strong correlation between soil carbon changes due to NPP increases and soil carbon changes due to τ_s reductions, in each CMIP6 ESM included in the investigation. This finding indicates a strong relationship between changes in NPP and changes in τ_s, and suggests that this assumption should be called into question, which is investigated here.

In Chapter 5, the future change in soil carbon (ΔC_s) was linearly approximated into the sensitivities due to CO_2 and temperature (T) using the $\{\beta, \gamma\}$ formulation to quantify the carbon cycle feedbacks (Friedlingstein et al., 2006), a metric presented in Intergovernmental Panel on Climate Change (IPCC) reports. The non-linearity in CO_2 and T was not found to be as significant as expected (Chapter 5), from what was implied by the NPP-τ_s non-linearity (Chapter 3). In this chapter, the non-linearity found in Chapter 3 named the $\{NPP, \tau_s\}$ formulation, is further investigated using CMIP6 ESM output from Coupled Climate-Carbon Cycle Model Intercomparison Project (C4MIP) idealised simulations, which exclude additional processes such as land-use change.

6.2 Methods

6.2.1 C4MIP simulations

This chapter uses the framework set up by the Coupled Climate-Carbon Cycle Model Intercomparison Project (C4MIP) to allow for the comparison of projected

carbon cycle feedbacks in ESMs. The model experiments include a 'full 1% CO_2 simulation' (CMIP simulation *1pctCO2*), which is a simulation that sees a 1% increase in atmospheric CO_2 per year, starting from pre-industrial concentrations and running for 150 years. A biogeochemically coupled 'BGC simulation' (CMIP6 simulation *1pctCO2-bgc*), where the 1% CO_2 increase per year only affects the carbon cycle component of the ESM and the radiative code remains at pre-industrial CO_2 values. A radiatively coupled 'RAD simulation' (CMIP6 simulation *1pctCO2-rad*), where the 1% CO_2 increase per year affects only the radiative code, and the carbon cycle component on the ESM remains at pre-industrial CO_2 values (285 ppm). This experiment framework is described in more detail in the Methods section of Chapter 5.

As in the previous chapter, the full 1% CO_2, BGC, and RAD C4MIP experiments are used with ten Coupled Model Inter-comparison Project Phase 6 (CMIP6) ESMs (Eyring et al., 2016; Meehl et al., 2014). The CMIP6 ESMs included in this study are: ACCESS-ESM1-5, BCC-CSM2-MR, CanESM5, CESM2, GFDL-ESM4, IPSL-CM6A-LR, MIROC-ES2L, MPI-ESM1-2-LR, NorESM2-LM, and UKESM1-0-LL. Information about the ESMs is presented in Table 2.1 of Chapter 2. Descriptions of the output variables used are given in Chapter 3 and Chapter 5.

6.2.2 Partial derivatives relating the $\{\beta, \gamma\}$ formulation to the $\{NPP, \tau_s\}$ formulation

The $\{\beta, \gamma\}$ formulation can be summarised as a linear approximation of the form:

$$\Delta C_s = \frac{\partial C_s}{\partial CO_2} \Delta CO_2 + \frac{\partial C_s}{\partial T} \Delta T = \beta_s \, \Delta CO_2 + \gamma_s \, \Delta T \tag{6.1}$$

where, $\beta_s = \partial C_s / \partial CO_2$ and $\gamma_s = \partial C_s / \partial T$.

In Chapter 3, an effective soil carbon turnover time (τ_s) was defined such that:

$$C_s = R_h \, \tau_s \tag{6.2}$$

where, C_s is soil carbon and R_h is the heterotrophic respiration rate.

By taking partial derivatives of Equation 6.2 with respect to CO_2 and temperature, it is therefore possible to derive equations for β_s:

$$\beta_s = \tau_s \frac{\partial R_h}{\partial CO_2} + R_h \frac{\partial \tau_s}{\partial CO_2} \tag{6.3}$$

and for γ_s:

$$\gamma_s = \tau_s \frac{\partial R_h}{\partial T} + R_h \frac{\partial \tau_s}{\partial T} \tag{6.4}$$

As in Chapter 3, it was chosen to rewrite R_h as the difference between NPP (Π_N) and the land carbon sink (F_L), as $R_h = \Pi_N - F_L$. This is to isolate the impact of changes in NPP with the Net Ecosystem Productivity (NEP, F_L) representing the additional impact of a net carbon sink (positive NEP) or carbon source (negative NEP).

Equations 6.3 and 6.4 for β_s and γ_s therefore become:

$$\beta_s = \tau_s \frac{\partial \Pi_N}{\partial CO_2} + \Pi_N \frac{\partial \tau_s}{\partial CO_2} - \tau_s \frac{\partial F_L}{\partial CO_2} - F_L \frac{\partial \tau_s}{\partial CO_2} \tag{6.5}$$

and:

$$\gamma_s = \tau_s \frac{\partial \Pi_N}{\partial T} + \Pi_N \frac{\partial \tau_s}{\partial T} - \tau_s \frac{\partial F_L}{\partial T} - F_L \frac{\partial \tau_s}{\partial T} \tag{6.6}$$

In both of these equations, the last two terms on the right-hand side are negligible if the carbon sink (NEP) is a small fraction of NPP. It is also often implicitly assumed that the $\partial \Pi_N / \partial CO_2$ term dominates in Equation 6.5 (representing the NPP response to CO_2), and that the $\partial \tau_s / \partial T$ term dominates in Equation 6.6 (representing the τ_s response to climate). However, in many models the sensitivity of NPP to climate ($\partial \Pi_N / \partial T$) is not negligible, and in models with multiple soil carbon pools it might be expected to see false priming (Koven et al., 2015), which implies that $\partial \tau_s / \partial CO_2$ is not negligible. In the rest of this chapter, the contribution from each of these terms will be estimated from the CMIP6 C4MIP experiments. In order to do this, Equations 6.5 and 6.6 need first to be rewritten in a discrete form.

6.2.3 Discrete equations relating the $\{\beta, \gamma\}$ formulation to the $\{NPP, \tau_s\}$ formulation

Future soil carbon can be defined as initial soil carbon ($C_{s,0}$, where initial is represented by a subscript 0) plus a change in soil carbon (ΔC_s), as shown by Equation 6.7. Equation 6.7 can be expanded to give Equation 6.8, which can be simplified to give Equation 6.9, as shown below.

$$C_{s,0} + \Delta C_s = (R_{h,0} + \Delta R_h)(\tau_{s,0} + \Delta\tau_s) \tag{6.7}$$

$$C_{s,0} + \Delta C_s = R_{h,0}\tau_s + \tau_{s,0}\Delta R_h + R_{h,0}\Delta\tau_s + \Delta R_h\Delta\tau_s \tag{6.8}$$

$$\Delta C_s = \tau_{s,0}\Delta R_h + R_{h,0}\Delta\tau_s + \Delta R_h\Delta\tau_s \tag{6.9}$$

Again, Net Ecosystem Productivity (NEP, F_L) can be substituted into Equation 6.9 to give Equation 6.10, and expanded to give an equation for ΔC_s in terms of NPP (Π_N), NEP (F_L) and τ_s (Equation 6.11).

$$\Delta C_s = \tau_{s,0}\Delta(\Pi_N - F_L) + (\Pi_{N,0} - F_{L,0})\Delta\tau_s + \Delta(\Pi_N - F_L)\Delta\tau_s \tag{6.10}$$

$$\begin{aligned}\Delta C_s = \tau_{s,0}\Delta\Pi_N \; + \; \Pi_{N,0}\Delta\tau_s \; + \; \Delta\Pi_N\Delta\tau_s \\ - \; \tau_{s,0}\Delta F_L \; - \; F_{L,0}\Delta\tau_s \; - \; \Delta F_L\Delta\tau_s\end{aligned} \tag{6.11}$$

Previously in Chapter 3, it was found that a linear approximation (where assuming $\Delta\Pi_N/\Pi_N << 1$ and $\Delta\tau_s/\tau_s << 1$) was not suitable here due to a non-negligible $\Delta\Pi_N\Delta\tau_s$ product (named the $\Delta NPP\Delta\tau_s$ term). Therefore, in this chapter this assumption is not made and all terms are considered in the breakdown analysis. As in Chapter 3, the following terms are defined: the change in soil carbon due to NPP changes ($\Delta C_{s,NPP} \approx \tau_{s,0}\Delta\Pi_N$), the NEP transient term ($\Delta C_{s,NEP} \approx -\tau_{s,0}\Delta F_L$), the change in soil carbon due to τ_s changes ($\Delta C_{s,\tau} \approx \Pi_{N,0}\Delta\tau_s$), the transient affect on τ_s ($\Delta C_{s,\tau_{NEP}} \approx -F_{L,0}\Delta\tau_s$), and the non-linear cross terms ($\Delta NPP\Delta\tau_s \approx \Delta\Pi_N\Delta\tau_s$ and $\Delta NEP\Delta\tau_s \approx -\Delta F_L\Delta\tau_s$).

Similarly, the equation for ΔC_s (Equation 6.11) can also be defined for the change in soil carbon in the BGC simulation (ΔC_s^{BGC}), shown by Equation 6.12, and for the change in soil carbon in the RAD simulation (ΔC_s^{RAD}), shown by Equation 6.13. Where, superscripts denotes the BGC and RAD simulations, respectively.

$$\begin{aligned}\Delta C_s^{BGC} = \tau_{s,0}^{BGC}\Delta\Pi_N^{BGC} \; + \; \Pi_{N,0}^{BGC}\Delta\tau_s^{BGC} \; + \; \Delta\Pi_N^{BGC}\Delta\tau_s^{BGC} \\ - \; \tau_{s,0}^{BGC}\Delta F_L^{BGC} \; - \; F_{L,0}^{BGC}\Delta\tau_s^{BGC} \; - \; \Delta F_L^{BGC}\Delta\tau_s^{BGC}\end{aligned} \tag{6.12}$$

$$\begin{aligned}\Delta C_s^{RAD} = \tau_{s,0}^{RAD}\Delta\Pi_N^{RAD} \; + \; \Pi_{N,0}^{RAD}\Delta\tau_s^{RAD} \; + \; \Delta\Pi_N^{RAD}\Delta\tau_s^{RAD} \\ - \; \tau_{s,0}^{RAD}\Delta F_L^{RAD} \; - \; F_{L,0}^{RAD}\Delta\tau_s^{RAD} \; - \; \Delta F_L^{RAD}\Delta\tau_s^{RAD}\end{aligned} \tag{6.13}$$

These equations can be used to investigate the sensitivity of the soil carbon controls to both changes in atmospheric CO_2 and global T. The sensitivity of the components in Equation 6.12 to CO_2 are tested, as shown by Equation 6.14, and the sensitivity of the components in Equation 6.13 to T are tested, as shown by Equation 6.15. This is done by explicit differentiation of Equations 6.12 and 6.13 with respect to CO_2 and T, respectively.

$$\Delta C_s^{BGC} = \frac{\partial}{\partial CO_2}\left[\Delta C_s^{BGC}\right]\Delta CO_2 \tag{6.14}$$

$$\Delta C_s^{RAD} = \frac{\partial}{\partial T}\left[\Delta C_s^{RAD}\right]\Delta T \tag{6.15}$$

Equations 6.14 and 6.15 can be used to relate these sensitivities to CO_2 and T to the $\{\beta, \gamma\}$ formulation. Recall Equation 6.1, which defines ΔC_s in terms of the soil carbon-concentration (β_s) and carbon-climate (γ_s) feedback parameters, first defined in Chapter 5 (Friedlingstein et al., 2006). This can be rewritten as shown in Equation 6.16, by substituting in Equations 6.14 and 6.15 to represent the sensitivity of soil carbon to both CO_2 and T, respectively. In this case, therefore β_s and γ_s can be defined as the contributions to ΔC_s based on the individual sensitivities of the soil carbon controls to CO_2 and T (by substituting Equations 6.12 and 6.13 into Equations 6.14 and 6.15, respectively), as shown by Equations 6.17 and 6.18.

$$\begin{aligned}\Delta C_s &= \beta_s \Delta CO_2 + \gamma_s \Delta T \\ &= \frac{\partial}{\partial CO_2}\left[\Delta C_s^{BGC}\right]\Delta CO_2 + \frac{\partial}{\partial T}\left[\Delta C_s^{RAD}\right]\Delta T\end{aligned} \tag{6.16}$$

Where,

$$\beta_s = \tau_{s,0}^{BGC}\frac{\partial \Pi_N^{BGC}}{\partial CO_2} + \Pi_{N,0}^{BGC}\frac{\partial \tau_s^{BGC}}{\partial CO_2} + \frac{\partial \Delta\Pi_N^{BGC}\Delta\tau_s^{BGC}}{\partial CO_2} - \tau_{s,0}^{BGC}\frac{\partial F_L^{BGC}}{\partial CO_2} - F_{L,0}^{BGC}\frac{\partial \tau_s^{BGC}}{\partial CO_2} - \frac{\partial \Delta F_L^{BGC}\Delta\tau_s^{BGC}}{\partial CO_2} \quad (6.17)$$

$$\gamma_s = \tau_{s,0}^{RAD}\frac{\partial \Pi_N^{RAD}}{\partial T} + \Pi_{N,0}^{RAD}\frac{\partial \tau_s^{RAD}}{\partial T} + \frac{\partial \Delta\Pi_N^{RAD}\Delta\tau_s^{RAD}}{\partial T} - \tau_{,0s}^{RAD}\frac{\partial F_L^{RAD}}{\partial T} - F_{L,0}^{RAD}\frac{\partial \tau_s^{RAD}}{\partial T} - \frac{\partial \Delta F_L^{RAD}\Delta\tau_s^{RAD}}{\partial T} \quad (6.18)$$

Therefore, Equations 6.17 and 6.18 are discretised forms of Equations 6.5 and 6.6, respectively. Where, Equations 6.5 and 6.6 have been linearised about an initial state. The Equations 6.17 and 6.18 are more suitable for application to the C4MIP outputs.

Equations 6.17 and 6.18 can be rewritten by defining β_s and γ_s contribution terms, where each component of the equations make up the total β_s and γ_s sensitivities. As shown below for β_s (Equation 6.19) and γ_s (Equation 6.20).

$$\beta_s = \beta_{NPP} + \beta_\tau + \beta_{\Delta NPP\Delta\tau} - \beta_{NEP} - \beta_{NEP_\tau} - \beta_{\Delta NEP\Delta\tau} \quad (6.19)$$

$$\gamma_s = \gamma_{NPP} + \gamma_\tau + \gamma_{\Delta NPP\Delta\tau} - \gamma_{NEP} - \gamma_{NEP_\tau} - \gamma_{\Delta NEP\Delta\tau} \quad (6.20)$$

Each carbon-concentration feedback parameter contribution (β) and the carbon-climate feedback parameter contribution (γ) are calculated for each CMIP6 ESM using the BGC and RAD simulations, as expressed in Equations 6.17 and 6.18, respectively. To calculate gradients with respect to CO_2 and T, the methodology presented in the 'Calculation of carbon-concentration and carbon-climate feedback parameters' section of Chapter 5 was used (for example, linear regression of the relevant component against CO_2 or T), together with Equations 6.17 and 6.18. The β_s contributions are expressed in units of carbon uptake or release per unit change in CO_2 (PgC ppm^{-1}), and the γ_s contributions are expressed in units of carbon uptake or release per unit change in temperature (PgC $^\circ$C^{-1}).

6.3 Results

6.3.1 Investigating projections in the 1% CO_2 simulations

6.3.1.1 Net Primary Productivity

Projections of changes in Net Primary Productivity (ΔNPP) in the CMIP6 ESMs for the simulations full 1% CO_2, biogeochemically coupled 1% CO_2 (BGC) and radiatively coupled 1% CO_2 (RAD), are presented in the top row of Figure 6.1. NPP is projected to increase in the full 1% CO_2 simulation amongst CMIP6 ESMs (ensemble mean +24.4$\pm$8.75 PgC yr^{-1} at 2xCO_2 and +45.2$\pm$21.5 PgC yr^{-1} at 4xCO_2). The magnitude of the increase varies from 8.7 to 36.2 PgC yr^{-1} at 2xCO_2 and 5.1 to 85.9 PgC yr^{-1} at 4xCO_2. Generally, the ESMs see an increased ΔNPP with increasing CO_2, however a saturation in the increase is seen in the ACCESS-ESM1-5 and IPSL-CM6A-LR models (Figure 6.1(a)).

The projected increase in ΔNPP is largely driven by increases in atmospheric CO_2, as seen in the BGC simulation (ensemble mean +24.2$\pm$9.88 PgC yr^{-1} at 2xCO_2 and +44.2$\pm$21.9 PgC yr^{-1} at 4xCO_2, Figure 6.1(b)). However an additional climate affect in NPP is seen in the RAD simulation (ensemble mean -2.00$\pm$3.59 PgC yr^{-1} at 2xCO_2 and -6.33$\pm$5.88 PgC yr^{-1} at 4xCO_2, Figure 6.1(c)). While ΔNPP in the BGC simulation is consistently positive across all models (increase of 9.9 to 41.7 PgC yr^{-1} at 2xCO_2 and 12.4 to 81.5 PgC yr^{-1} at 4xCO_2), the climate effects on NPP in the RAD simulation are less certain, ranging from a significant decrease (up to -20.8 PgC yr^{-1} at 4xCO_2) to a small increase of only $\sim$ 2 to 3 PgC yr^{-1} for both 2xCO_2 and 4xCO_2.

Figure 6.2 shows spatial changes in ΔNPP at 4xCO_2, for the simulations full 1% CO_2, biogeochemically coupled 1% CO_2 (BGC) and radiatively coupled 1% CO_2 (RAD). Again as expected, the response of NPP is seen to be dominated by the BGC simulation, where increases in ΔNPP are seen in all regions and the greatest magnitude of increase is seen in the tropical regions. In the RAD simulation, a consistent pattern of ΔNPP is seen, where NPP decreases in the tropical regions and increases in the northern latitudes. In the full 1% CO_2 simulation, the decrease in Amazonian ΔNPP from the RAD simulation dominates in the ACCESS-ESM1-5, IPSL-CM6A-LR, and UKESM1-0-LL models. Otherwise, increases in ΔNPP are seen in all regions.

6.3.1.2 Soil carbon turnover time

Projections of changes in soil carbon turnover time ($\Delta\tau_s$) in the CMIP6 ESMs for the simulations full 1% CO_2, biogeochemically coupled 1% CO_2 (BGC) and

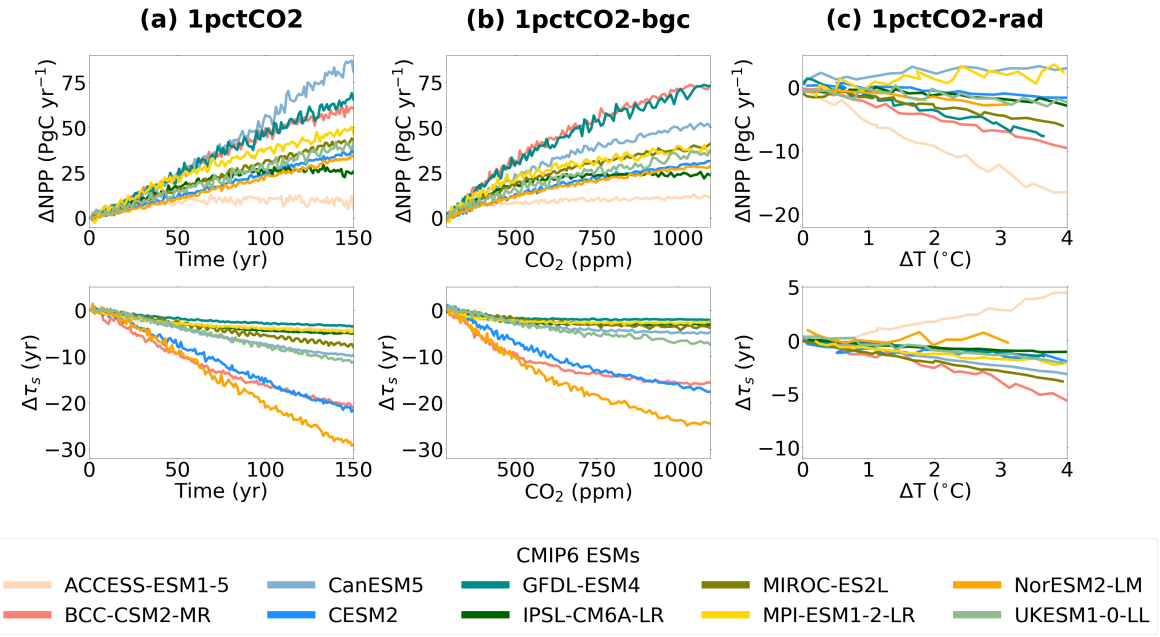

Figure 6.1: Timeseries of projected changes in Net Primary Productivity (ΔNPP, top row), and soil carbon turnover time ($\Delta\tau_s$, bottom row), in CMIP6 ESMs for the idealised simulations 1% CO_2 (left column), biogeochemically coupled 1% CO_2 (BGC, middle column) and radiatively coupled 1% CO_2 (RAD, right column).

radiatively coupled 1% CO_2 (RAD), are presented in the bottom row of Figure 6.1. As expected, projected $\Delta\tau_s$ in ESMs is shown to decrease under climate change, with reductions predicted in the full 1% CO_2 simulation amongst CMIP6 ESMs (ensemble mean -6.79±4.39 yr at 2xCO_2 and -11.8±8.42 yr at 4xCO_2). The magnitude of the reduction varies amongst ESMs, from -2.31 to -15.1 yr at 2xCO_2 and -3.51 to -29 yr at 4xCO_2 (Figure 6.1(a)).

Surprisingly, the projected decrease in $\Delta\tau_s$ is found to be a result of both the CO_2 effect seen in the BGC simulation (ensemble mean -5.41±4.13 yr at 2xCO_2 and -8.87±8.01 yr at 4xCO_2, Figure 6.1(b)), and the climate effect seen in the RAD simulation (ensemble mean -0.73±0.97 yr at 2xCO_2 and -1.68±3.19 yr at 4xCO_2, Figure 6.1(c)), amongst ESMs. In the BGC simulation, the greatest projected $\Delta\tau_s$ changes are seen in the BCC-CSM2-MR, CESM2, and NorESM2-LM models (-16.5 yr, -19.0 yr, and -25.7 yr, respectively at 4xCO_2). Amongst the remaining ESMs, a range of -1.95 to -3.80 yr at 2xCO_2 and -1.99 to -8.38 yr at 4xCO_2 is found. In the RAD simulation, generally decreases are seen in $\Delta\tau_s$, where a range of -0.17 to -1.97 yr at 2xCO_2 and a range of -0.12 to -5.77 yr at 4xCO_2 (excluding ACCESS-EMS1-5). The model ACCESS-EMS1-5 projects increases in $\Delta\tau_s$ during the RAD simulation (+6.22 yr at 4xCO_2), which is an anomaly amongst the models in the ensemble.

Figure 6.3 shows spatial changes in $\Delta\tau_s$ at 4xCO_2, for the simulations full

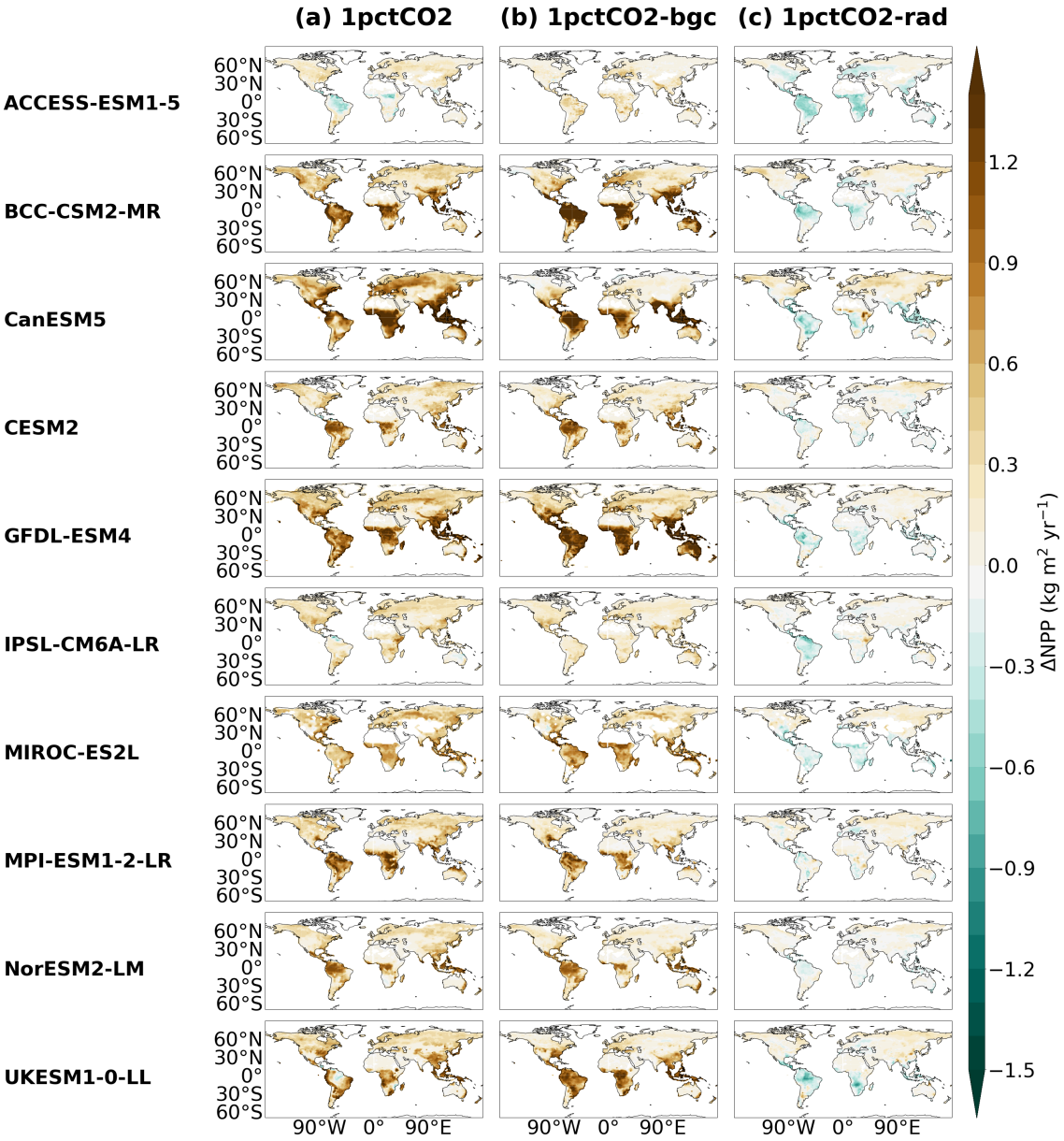

Figure 6.2: Maps of changes in Net Primary Productivity (ΔNPP) at 4xCO_2 in CMIP6 ESMs for the idealised simulations 1% CO_2 (left column), biogeochemically coupled 1% CO_2 (BGC, middle column) and radiatively coupled 1% CO_2 (RAD, right column).

1% CO_2, biogeochemically coupled 1% CO_2 (BGC) and radiatively coupled 1% CO_2 (RAD). For projections of $\Delta\tau_s$, it is less clear whether the BGC or RAD simulation dominates the overall future response. Generally, large reductions in $\Delta\tau_s$ are seen in the northern latitudes in the full 1% CO_2 run, which is a result of large $\Delta\tau_s$ reductions in the RAD run. Conversely in the BGC run, areas of increased τ_s are seen within the northern latitudes of seven of the CMIP6 ESMs (BCC-CSM2-MR, CanESM5, GFDL-ESM4, IPSL-CM6A-LR, MPI-ESM1-2-LR, NorESM2-LM, UKESM1-0-LL). Within the tropical regions, the predicted changes see no robust pattern across the CMIP6 ensemble, and both increases and decreases are seen in the BGC and RAD simulations.

6.3.1.3 Breakdown of soil carbon feedbacks

In Chapter 3, it was found that the projected changes in soil carbon (ΔC_s) in ESMs could be successfully broken down into the individual feedbacks which make up the total response. In this chapter, it was investigated whether the same breakdown could be used in the idealised C4MIP simulations, where it was found that this was the case for the full 1% CO_2 simulation (ΔC_s), as well as the BGC (ΔC_s^{BGC}) and RAD (ΔC_s^{RAD}) simulations (Figure 6.4). The total ΔC_s (blue bars) response in ESMs were similarly found to be a result of the linear terms: the response due to changes in NPP ($\Delta C_{s,NPP}$, green bars) and response due to changes in τ_s ($\Delta C_{s,\tau}$, red bars), as well as non-negligible contributions from the non-linear term: $\Delta NPP\Delta\tau_s$ (black bars), and the non-equilibrium terms: $\Delta C_{s,NEP}$ (light green bars), $\Delta C_{s,\tau_{NEP}}$ (pink bars), and ΔNEP$\Delta\tau_s$ (grey bars).

In the full 1% CO_2 simulation (Figure 6.4(a)), the contributions of change are similar to the changes seen in the SSP simulations (see Figure 3.6 in Chapter 3), where ΔC_s is mostly a result of the net effect between NPP changes ($\Delta C_{s,NPP}$), τ_s changes ($\Delta C_{s,\tau}$), non-linearity in NPP and τ_s ($\Delta NPP\Delta\tau_s$), and the resultant NEP affect ($\Delta C_{s,NEP}$). Amongst the ESMs in CMIP6, there is variation in the magnitude of changes in each term, which is often larger than the variation in the overall soil carbon response (suggesting some cancellation of errors). In the full 1% CO_2 simulation, there is range of approximately 103 PgC in overall soil carbon change (ΔC_s) at 2xCO_2, from +34.6 to +137 PgC. However, the $\Delta C_{s,NPP}$ contribution has a much larger range of 1094 PgC, from +206 to +1300 PgC at 2xCO_2. Similarly, $\Delta C_{s,\tau}$ has a range of 422 PgC, from -117 PgC to -538 PgC at 2xCO_2. These large positive and negative contributions cancel to give a smaller net change in soil carbon.

The projected contributions from the BGC simulation are shown to dominate in the overall response seen in the full 1% CO_2 simulation (Figure 6.4(b)).

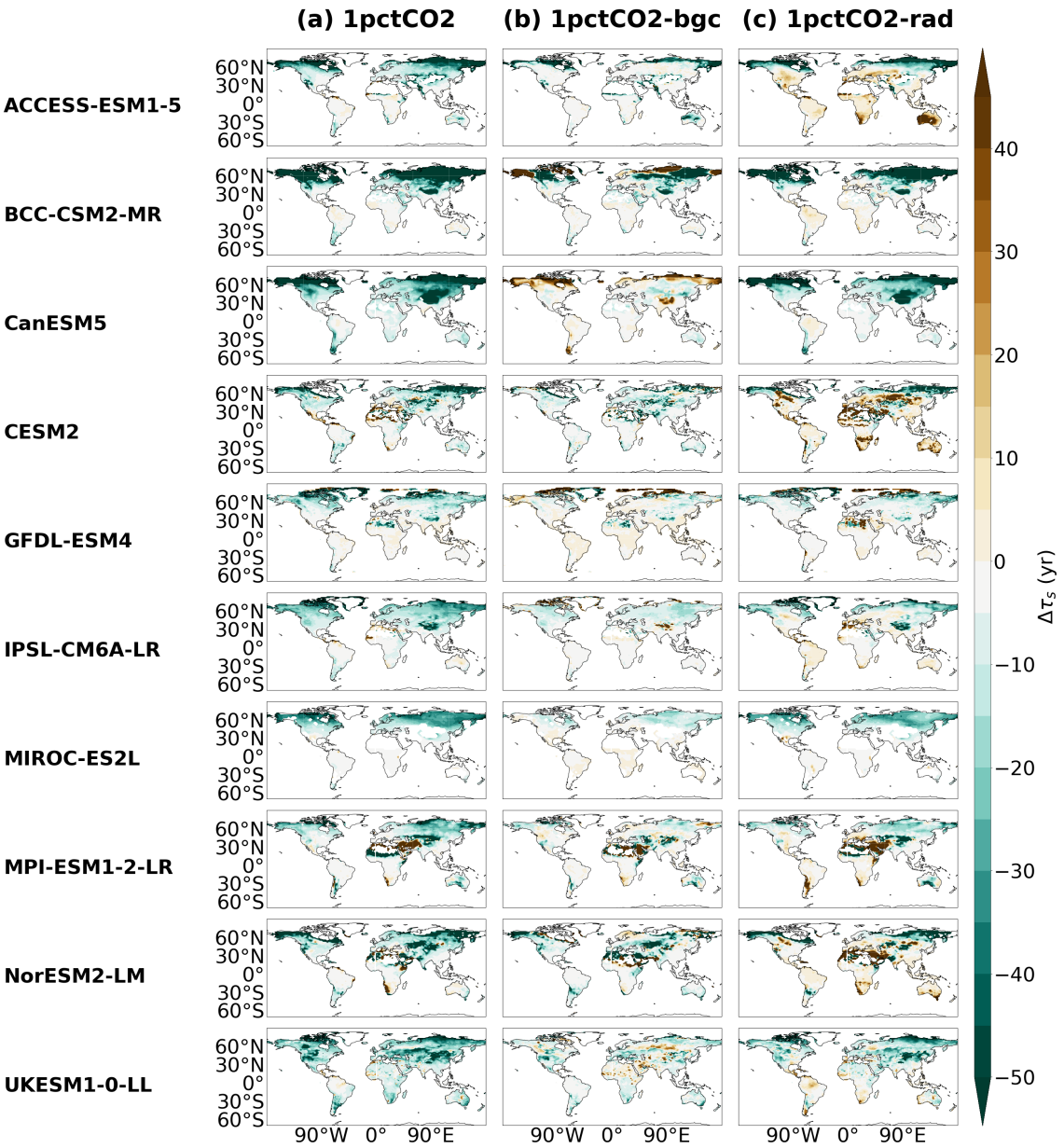

Figure 6.3: Maps of changes in soil carbon turnover time ($\Delta\tau_s$) at 4xCO_2 in CMIP6 ESMs for the idealised simulations 1% CO_2 (left column), biogeochemically coupled 1% CO_2 (BGC, middle column) and radiatively coupled 1% CO_2 (RAD, right column).

In the BGC simulation, a slightly larger range is seen at 2xCO$_2$ for ΔC_s (200 PgC, from 44.2 to 244 PgC) and for $\Delta C_{s,NPP}$ (1336 PgC, from 186 to 1523 PgC), but a slightly reduced range for $\Delta C_{s,\tau}$ (383 PgC, from -97.3 to -481 PgC), when compared to the full 1% CO$_2$ simulation. The non-linear component ($\Delta NPP\Delta\tau_s$) seen in the full 1% CO$_2$ simulation, is also found to be a result of non-linearities in the BGC simulation, where in the majority of models the $\Delta NPP\Delta\tau_s$ term is of similar magnitude in both the full 1% CO$_2$ (393 PgC, from -31.4 to -424 PgC at 2xCO$_2$) and BGC simulations (427 PgC, from -21.3 to -448 PgC at 2xCO$_2$).

The projected contributions in the RAD simulation are generally smaller in magnitude compared with the BGC simulation (Figure 6.4(c)), and the contribution of the $\Delta NPP\Delta\tau_s$ term is less significant. The RAD simulation results in a reduction in ΔC_s, where a changes from -14.3 to -75.3 PgC are found amongst the ESMs at 2xCO$_2$. The projected contribution from $\Delta C_{s,NPP}$ is much smaller in the RAD simulation compared with the full and BGC simulations, where a range of 270 PgC at 2xCO$_2$. There is also disagreement on the sign of this response, with a range from a loss of 190 PgC in ACCESS-ESM1-5 to a gain of 80.1 PgC in CanESM5 at 2xCO$_2$. The greatest uncertainty in the RAD simulation is from the $\Delta C_{s,\tau}$ term, where a range of 187 PgC, predictions from -115 to +72.2 PgC are found at 2xCO$_2$.

6.3.2 Breakdown of the β_s and γ_s feedback parameters

The soil carbon specific carbon-concentration (β_s) and carbon-climate (γ_s) feedback parameters are used to quantify the sensitivity of soil carbon to changes in atmospheric CO$_2$ (BGC simulation) and global temperatures (RAD simulation). In this section, β_s and γ_s are broken down into the individual sensitivities which make up this response. However, as with ΔC_s (Figure 6.4), to obtain the overall soil carbon sensitivities (β_s and γ_s) additional terms must be included (Figure 6.5). As shown in Figure 6.5, the total sensitivities (β_s and γ_s, blue bars) were similarly found to be a result of the linear terms: the sensitivity of NPP (β_{NPP} and γ_{NPP}, green bars) and sensitivity of τ_s (β_τ and γ_τ, red bars), as well as non-negligible contributions due to non-linear sensitivities: $\beta_{\Delta NPP\Delta\tau}$ and $\gamma_{\Delta NPP\Delta\tau}$ (black bars), and additions due to the non-equilibrium terms: β_{NEP} and γ_{NEP} (light green bars), $\beta_{\tau_{NEP}}$ and $\gamma_{\tau_{NEP}}$ (pink bars), and $\beta_{\Delta NEP\Delta\tau}$ and $\gamma_{\Delta NEP\Delta\tau}$ (grey bars), although these final two terms are generally very small.

The calculation of the individual sensitivities of NPP and τ_s to CO$_2$, β_{NPP} and β_τ, and the individual sensitivities to T, γ_{NPP} and γ_τ, for each CMIP6 ESM to 2xCO$_2$, are additionally shown in Figures 6.6 and 6.7. NPP increases with increasing CO$_2$, and therefore β_{NPP} is found to be positive amongst CMIP6 ESMs (Figure

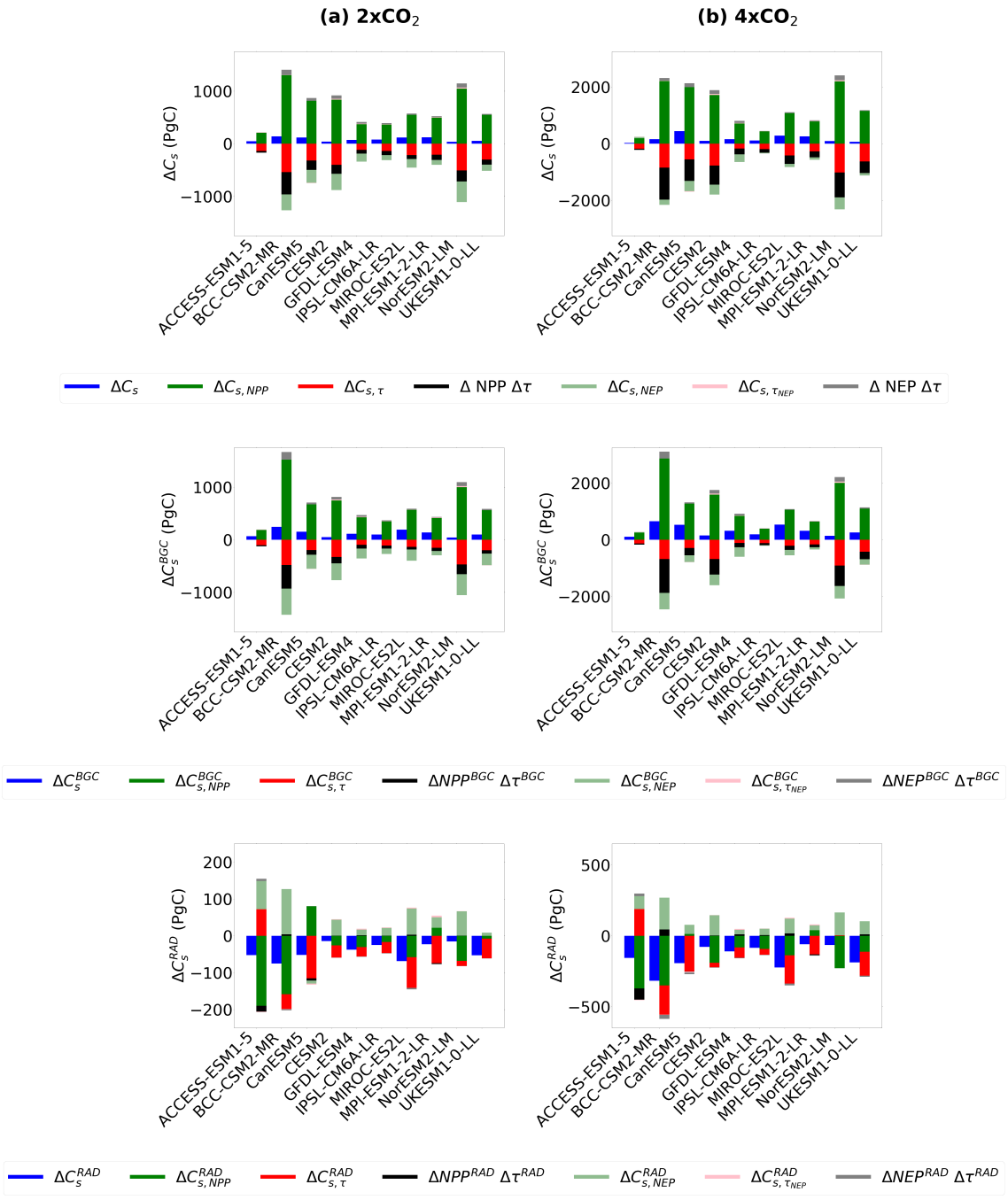

Figure 6.4: Bar charts showing the contributions of NPP and τ_s to changes in soil carbon (ΔC_s) in CMIP6 ESMs for the idealised simulations full 1% CO_2 (top row), biogeochemically coupled 1% CO_2 (BGC, middle row) and radiatively coupled 1% CO_2 (RAD, bottom row), for (a) 2xCO_2 and (b) 4xCO_2. The included terms are: the linear term representing changes in soil carbon due to the changes in NPP ($\Delta C_{s,NPP}$), the linear term representing changes in soil carbon due to the changes in τ_s ($\Delta C_{s,\tau}$), the non-linear term ($\Delta NPP \Delta \tau_s$), and then additional terms to account for the non-equilibrium climate ($\Delta C_{s,NEP}$, $\Delta C_{s,\tau_{NEP}}$, and ΔNEP$\Delta \tau_s$).

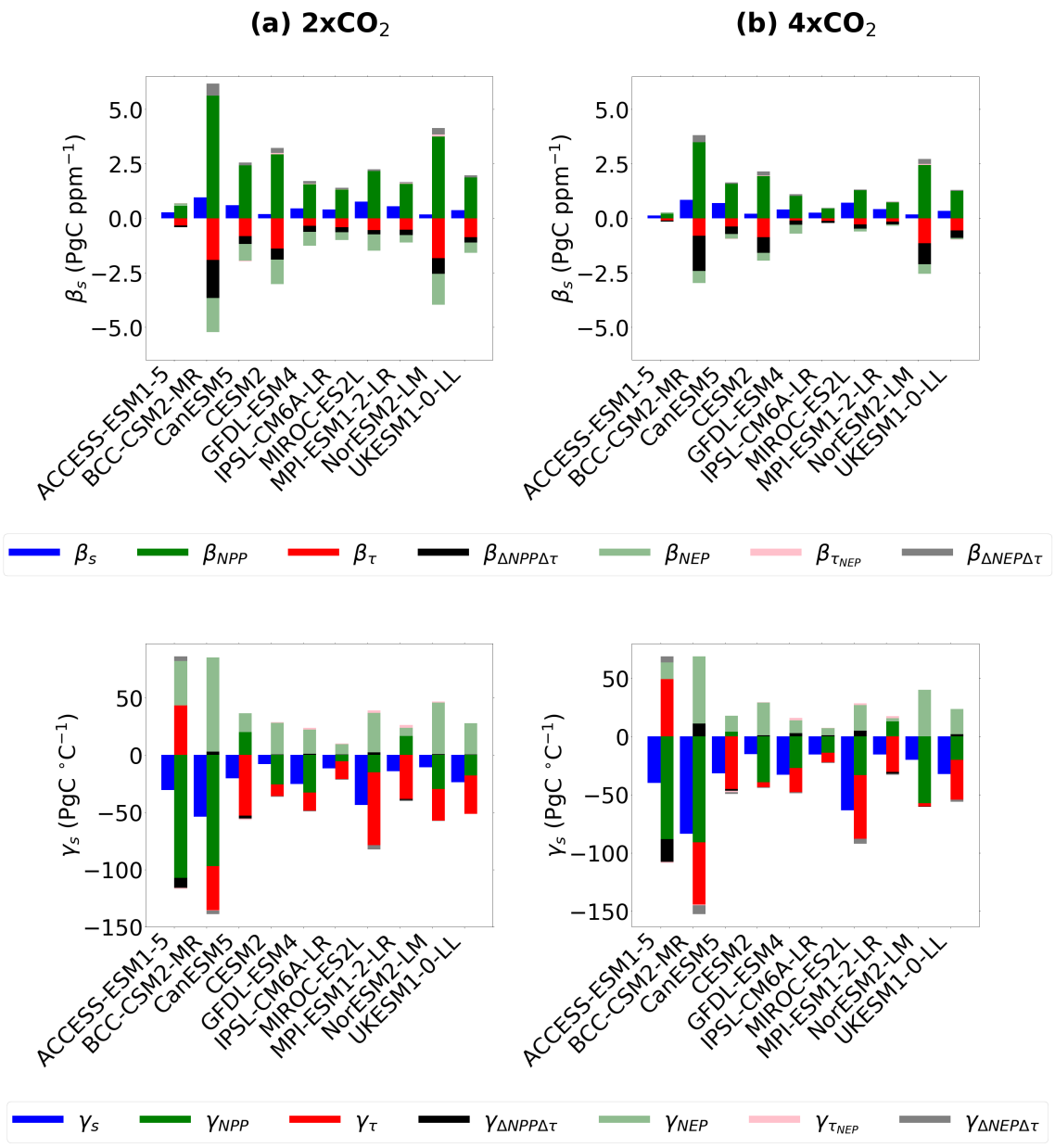

Figure 6.5: Bar charts showing the contribution of individual terms that make up the soil carbon-concentration (β_s, top row) and carbon-climate (γ_s, bottom row) feedback parameters, for each CMIP6 ESM, for (a) 2xCO$_2$ and (b) 4xCO$_2$. The soil carbon feedback parameters were found to be made up of a contribution from NPP (β_{NPP} and γ_{NPP}), τ_s (β_τ and γ_τ), the non-linearity in NPP and τ_s ($\beta_{\Delta NPP\Delta\tau}$ and $\gamma_{\Delta NPP\Delta\tau}$), and the effect from the non-equilibrium term NEP (β_{NEP}, $\beta_{\tau_{NEP}}$, $\beta_{\Delta NEP\Delta\tau}$ and γ_{NEP}, $\gamma_{\tau_{NEP}}$, $\gamma_{\Delta NEP\Delta\tau}$).

6.6(a)). At 2xCO$_2$, β_{NPP} ranges from 0.567 PgC ppm^{-1} (ACCESS-ESM1-5) to 5.62 PgC ppm^{-1} (BCC-CSM2-MR), with an ensemble mean of 2.37 $\pm$ 1.37 PgC ppm^{-1} (Figure 6.5). There is some evidence of a saturation of global NPP at higher CO$_2$, with the sensitivity of NPP to CO$_2$ decreasing by 4xCO$_2$ to an ensemble mean of 1.44 $\pm$ 0.933 PgC ppm^{-1} is seen (Figure 6.5).

The sensitivity of NPP to global temperature changes (γ_{NPP}) is found to be more variable amongst the ensemble (Figure 6.6(b)). The majority of models find γ_{NPP} to be negative, however it is found to be positive in two ESMs (CanESM5 and MPI-ESM1-2-LR). The sensitivity of NPP to temperature (γ_{NPP}) is found to be more consistently linear with climate change than the sensitivity to CO$_2$ (β_{NPP}), where the γ_{NPP} ensemble mean changes from -29.4 $\pm$ 40.1 PgC °C at 2xCO$_2$ to -35.3 $\pm$ 33.1 PgC °C at 4xCO$_2$ (Figure 6.5). At 4xCO$_2$, the lowest sensitivity of NPP to temperature is seen in CanESM5 (+3.95 PgC °C), and the greatest sensitivity in BCC-CSM2-MR (-90.8 PgC °C).

τ_s has been shown to decrease with both increasing CO$_2$ and global temperatures, where negative β_τ and γ_τ values are found amongst the CMIP6 models (Figure 6.7). An anomaly is found where τ_s is found to increase with temperature in the ACCESS-ESM1-5 model, where the reason for this is unclear (Figure 6.7(b)). The sensitivity of τ_s to T (γ_τ) is also found to be more linear with increasing climate change than the sensitivity to CO$_2$, where an ensemble mean of -25.2 $\pm$ 27.9 PgC °C at 2xCO$_2$ and -20.5 $\pm$ 29.5 PgC °C at 4xCO$_2$ is seen. At 4xCO$_2$, the greatest sensitivity of τ_s to temperature is seen in the MIROC-ES2L model (-54.6 PgC °C) and the lowest sensitivity is seen in the NorESM2-LM model (-2.80 PgC °C). τ_s is found to decrease non-linearly with increasing CO$_2$ (β_τ), but with varying sensitivity curves seen amongst the models (Figure 6.7(a)). At 2xCO$_2$, β_τ ranges from -0.329 PgC ppm^{-1} (ACCESS-ESM1-5) to -1.90 PgC ppm^{-1} (BCC-CSM2-MR), with an ensemble mean of -0.900 $\pm$ 0.574 PgC ppm^{-1}. Due to the non-linearity, a reduced ensemble mean of -0.450 $\pm$ 0.359 PgC ppm^{-1} is found at 4xCO$_2$ compared with 2xCO$_2$ (Figure 6.5).

It is apparent in Figure 6.5 that the sensitivities of NPP and τ_s to both CO$_2$ and T must be accounted for to obtain the overall sensitivities of soil carbon. The magnitude of β_τ is found to be approximately a third of the magnitude of β_{NPP} at both 2xCO$_2$ and 4xCO$_2$, but with counteracting signs of change. Models with the lowest β_{NPP} sensitivities also see the lowest β_τ sensitivities (e.g. ACCESS-ESM1-5), and via versa. The magnitude of γ_{NPP} is generally found to be greater across the ensemble compared with γ_τ, however with a greater range of sensitivities. Additionally, similarly to the results found when

investigating the absolute change in soil carbon (Figure 6.4), the apparent sensitivity of soil carbon to CO_2 is less then the individual sensitivities of NPP and τ_s, due to a cancellation affect from opposing signs, leading to a lower apparent β_s. The magnitudes of β_{NPP} and β_τ are lower at 4xCO_2 than 2xCO_2, which means a reduced sensitivity of NPP and τ_s to CO_2 at greater levels of climate change, However, due to this cancellation affect the same reduced sensitivity is not seen in β_s. Conversely, a reduced sensitivity of NPP and τ_s to temperature is not suggested under increasing climate forcing. No clear relationship between γ_{NPP} and γ_τ is seen amongst the CMIP6 ESMs (Figure 6.5).

The contribution of the non-linearity between NPP and τ_s to the net soil carbon sensitivity is also investigated ($\beta_{\Delta NPP\Delta\tau}$ and $\gamma_{\Delta NPP\Delta\tau}$). Figure 6.5 suggests that the non-linearity between NPP and τ_s is more robustly projected to a result from increasing CO_2 (β), however non-linearities in γ are seen in the models which the greatest temperature sensitivities. The ensemble mean predicted $\beta_{\Delta NPP\Delta\tau}$ is found to be -0.462 $\pm$ 0.462 at 2xCO_2, and -0.463 $\pm$ 0.468 PgC ppm^{-1} at 4xCO_2 (the black bars). As expected from Figure 6.5, predicted $\gamma_{\Delta NPP\Delta\tau}$ is found to have a low sensitivity, where the ensemble means of -0.374 $\pm$ 3.12 at 2xCO_2 and -0.0478 $\pm$ 7.42 PgC °C at 4xCO_2 are found (the black bars). Additionally, the NEP terms (β_{NEP} and γ_{NEP}) are shown to contribute to both CO_2 and T sensitivities (Figure 6.5), due to the disequilibrium of land carbon changes under 1% increasing CO_2.

6.3.3 Investigating the relationship between NPP and τ_s

For each CMIP6 ESM, NPP and τ_s are found to be strongly inversely correlated in the full 1% CO_2 simulation (Figure 6.8). The r^2 values between NPP/NPP_0 and $\tau_{s,0}/\tau_s$ are found to be greater than 0.95 in all models, expect for ACCESS-ESM1-5 where an r^2 value of 0.65 is found. In the BGC simulation, a similar relationship between NPP/NPP_0 and $\tau_{s,0}/\tau_s$ is seen up until approximately 2xCO_2 in all ESMs. The relationship between 2xCO_2 and 4xCO_2 varies between models in the BGC simulation, where a greater rate of NPP/NPP_0 increase compared to $\tau_{s,0}/\tau_s$ is seen at greater levels of climate forcing, where the τ_s changes appear to saturate and a limit to increases is seen. However, the correlation remains and the r^2 values between NPP/NPP_0 and $\tau_{s,0}/\tau_s$ is greater than 0.9 in all models, expect for GFDL-ESM4 where an r^2 value of 0.78 is found. In the CESM2 and NorESM2-LM models, a consistent relationship is seen in both the full and BGC simulations, suggesting the changes in NPP and τ_s are solely due to changes in CO_2 concentrations. In the remaining CMIP6 ESMs, the changes seen in the full and BGC simulations differ due to a climate effect which appears to negate the apparent limit or saturation seen in $\tau_{s,0}/\tau_s$ in the BGC simulation.

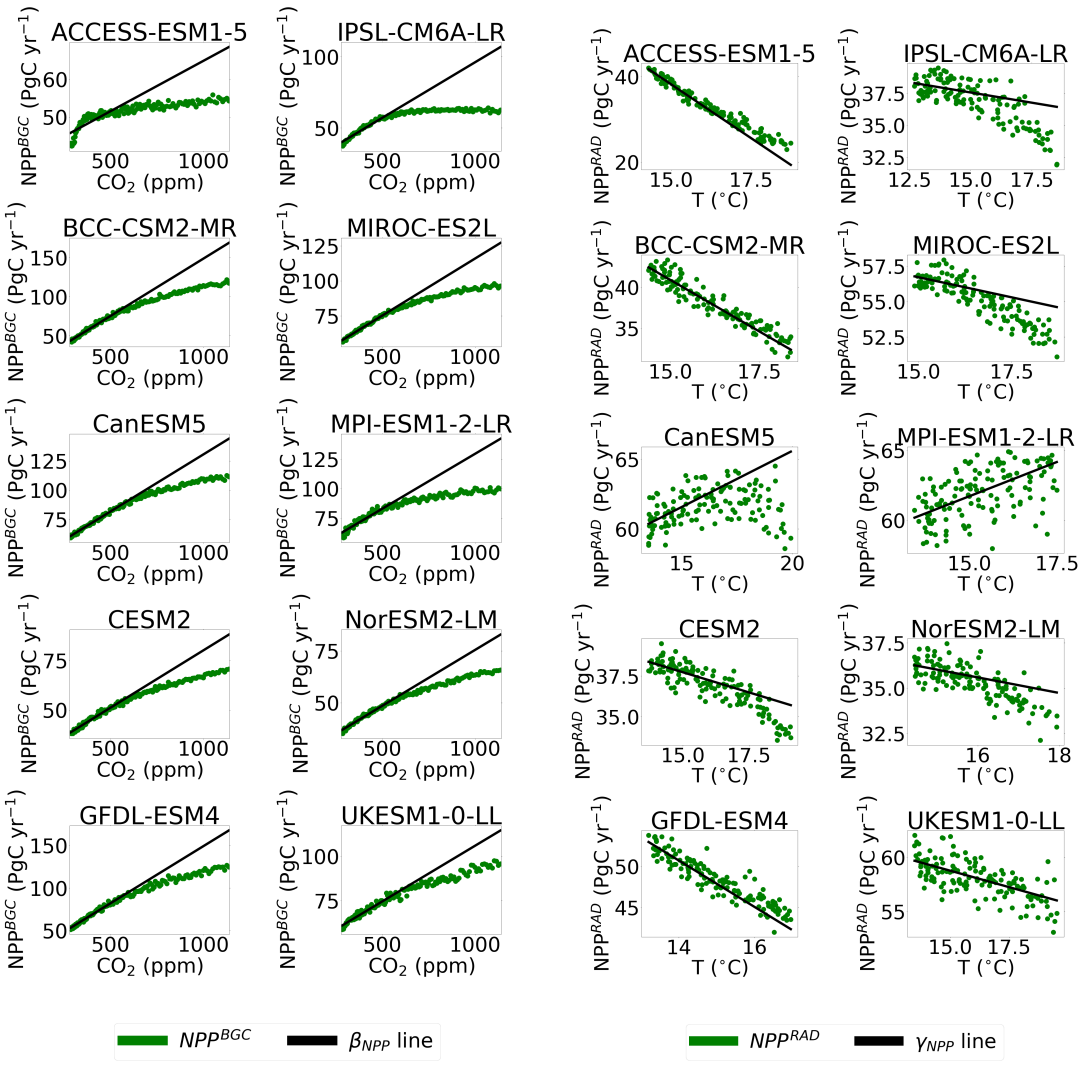

(a) β_{NPP} (b) γ_{NPP}

Figure 6.6: Timeseries plots showing the calculation of the NPP contribution to the soil carbon-concentration feedback parameters (a) β_{NPP}, and NPP contribution to the soil carbon-climate feedback parameters (b) γ_{NPP}, to 2xCO_2 for each CMIP6 ESM.

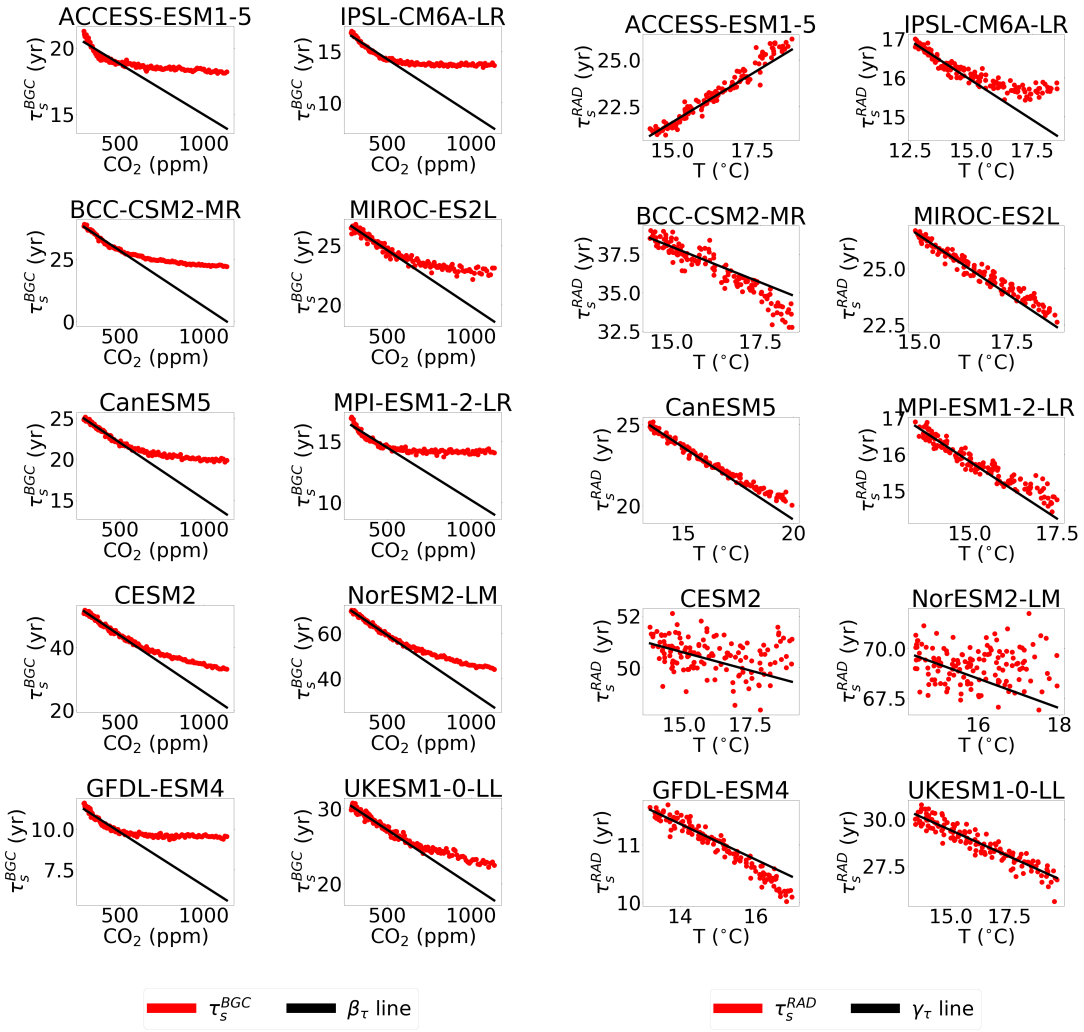

(a) β_τ (b) γ_τ

Figure 6.7: Timeseries plots showing the calculation of the τ_s contribution to the soil carbon-concentration feedback parameters (a) β_τ, and NPP contribution to the soil carbon-climate feedback parameters (b) γ_τ, to 2xCO_2 for each CMIP6 ESM.

The relationship between $\Delta C_{s,NPP}$ and $\Delta C_{s,\tau}$ for each CMIP6 ESMs, is shown for the 1% CO_2 simulation, BGC and RAD simulations in Figure 6.9 (as in Figure 8, Chapter 3). $\Delta C_{s,NPP}$ and $\Delta C_{s,\tau}$ are found to be strongly correlated in the full 1% CO_2 simulation, at both 2xCO_2 (r^2 value of 0.925) and 4xCO_2 (r^2 value of 0.839). The correlation in the full 1% CO_2 simulation is found to be a result of a strong correlation in the BGC simulation, where r^2 values in the BGC simulation are found to be 0.838 and 0.708 for 2xCO_2 and 4xCO_2, respectively. The slightly reduced correlation in the BGC simulation at 4xCO_2 suggests a potential limit to the effect at high levels of atmospheric CO_2. A correlation is seen in the RAD simulation at 2xCO_2 (r^2 value of 0.601), however this correlation is less significant than the correlation seen in the BGC simulation. Additionally, the correlation in the RAD simulation does not hold at 4xCO_2, where the r^2 value reduces to 0.265. The reduced correlation in the RAD simulation at 4xCO_2 suggests no interaction between NPP and τ_s due to temperature changes at high levels of atmospheric CO_2.

6.3.4 The role of 'false priming'

Koven et al. (2015) presents the concept of 'false priming', which produces a reduction in effective carbon turnover due to increases in productivity. In this subsection, false priming is explored as a possible explanation for the correlations seen between NPP changes and τ_s changes, which are seen even in the BGC runs where the climate does not change significantly (second row of Figure 6.9). Koven et al. (2015) demonstrates false priming with a simple three-box soil carbon model, which has been adapted here to use notation consistent with the rest of this thesis:

$$\frac{dC_1}{dt} = NPP - \frac{C_1}{\tau_{s,1}} \tag{6.21}$$

$$\frac{dC_2}{dt} = \frac{e_1 C_1}{\tau_{s,1}} - \frac{C_2}{\tau_{s,2}} \tag{6.22}$$

$$\frac{dC_3}{dt} = \frac{e_2 C_2}{\tau_{s,2}} - \frac{C_3}{\tau_{s,3}} \tag{6.23}$$

$$R_h = \frac{(1-e_1)C_1}{\tau_{s,1}} + \frac{(1-e_2)C_2}{\tau_{s,2}} + \frac{(1-e_3)C_3}{\tau_{s,3}} \tag{6.24}$$

$$C_s = C_1 + C_2 + C_3 \tag{6.25}$$

$$\tau_{s,1} = 1, \tau_{s,2} = 10, \tau_{s,3} = 100, e_1 = 0.3, e_2 = 0.3, e_3 = 0. \tag{6.26}$$

where, C_1, C_2, C_3 represent the carbon stored in soil carbon pools 1, 2, and 3, and $\tau_{s,1}$, $\tau_{s,2}$, $\tau_{s,3}$ are the respective soil carbon turnover times. The coefficients e_i

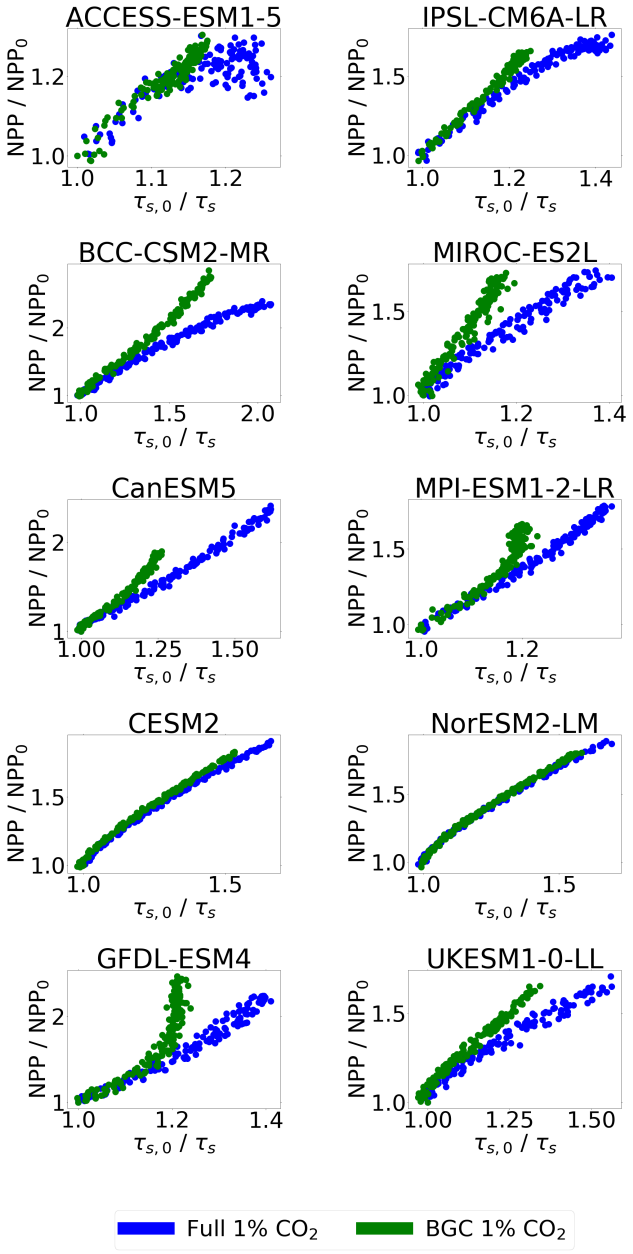

Figure 6.8: Scatter plots showing the correlation between NPP/NPP_0 and $\tau_{s,0}/\tau_s$ for each CMIP6 ESM, in the full 1% CO_2 simulation (blue) and the BGC simulation (green), up to 4xCO_2.

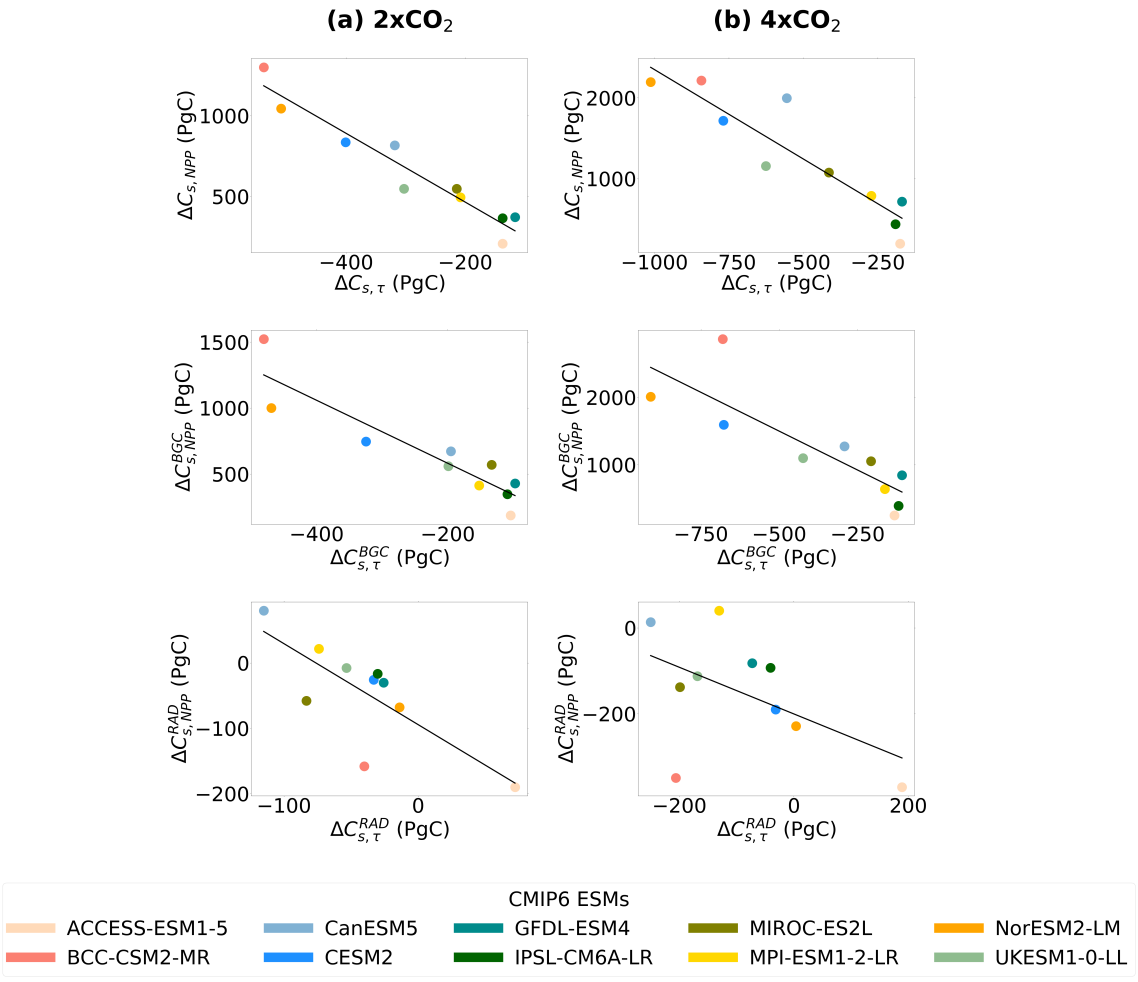

Figure 6.9: Scatter plots showing the relationship between $\Delta C_{s,NPP}$ and $\Delta C_{s,\tau}$ for each CMIP6 ESM, in the full 1% CO_2 simulation (top row), BGC simulation (middle row) and RAD simulation (bottom row), for (a) 2xCO_2 and (b) 4xCO_2.

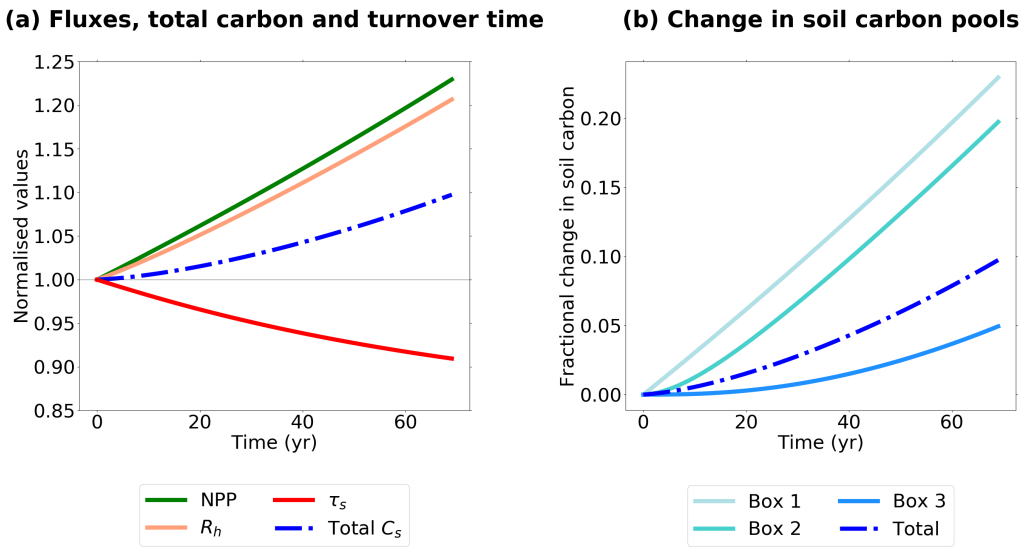

Figure 6.10: Timeseries plot showing the results from the simple three-box model: (a) normalised changes in NPP, R_h, τ_s and C_s (recreation of Figure 12 in Koven et al. (2015)); (b) fractional change in each of the three soil carbon boxes and in the total soil carbon.

represents the fraction of carbon that is passed to the next pool rather than lost as heterotrophic respiration.

Figure 6.10 reproduces a simulation of the response of this three-box model to an NPP flux that increases at 0.3% per year (see Figure 12 in Koven et al. (2015)). The false priming decline in τ_s with increasing NPP is clear, and for this set of parameters, offsets about 40% of the increase in soil carbon that would arise from the NPP increase alone. Figure 6.11 demonstrates that false priming is a transient effect associated with a disequilibrium in the distribution of soil carbon amongst the three pools. It shows results from the same model, but for a step increase in global NPP from 50 PgC yr^{-1} to 70 PgC yr^{-1} at year 100. The instantaneous decline in τ_s of about 10% eventually reduces to return the soil to the original τ_s, but this occurs on the timescale of the slowest carbon pool, and so may take many centuries.

The same three-box model can also be used to investigate the relationship between the contributions of changes in NPP ($\Delta C_{s,NPP} = \tau_s\ \Delta NPP$) and τ_s ($\Delta C_{s,\tau} = NPP_0\ \Delta \tau_s$), that was noted in Chapter 3 and is also seen in Figure 6.9 of this chapter. Figure 6.12 plots $\Delta C_{s,NPP}$ against $\Delta C_{s,\tau}$ from the three-box model, after 70 years of runs that assume different rates of increase of NPP (0% to 0.8% per year in increments of 0.05%). A clear relationship between $\Delta C_{s,NPP}$ and $\Delta C_{s,\tau}$ is seen, with greater false priming (more negative $\Delta C_{s,\tau}$) when the NPP increase is larger (larger $\Delta C_{s,NPP}$). The similarity of Figure 6.12 to both Figure 6.9 in this chapter and Figure 3.8 in Chapter 3 is clear, suggesting that

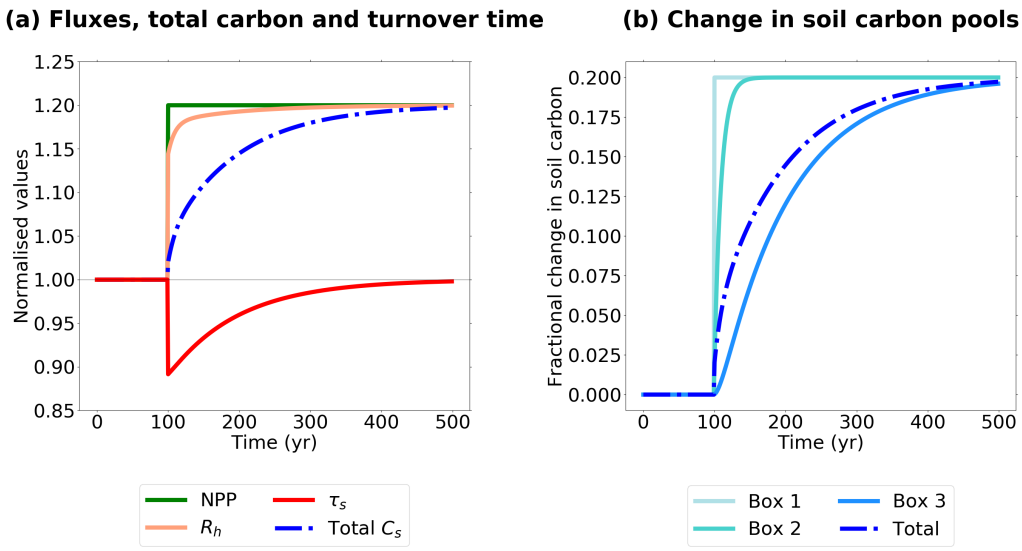

Figure 6.11: As Figure 6.10 but for an abrupt change in global NPP, from 50 PgC yr^{-1} to 70 PgC yr^{-1} at year 100.

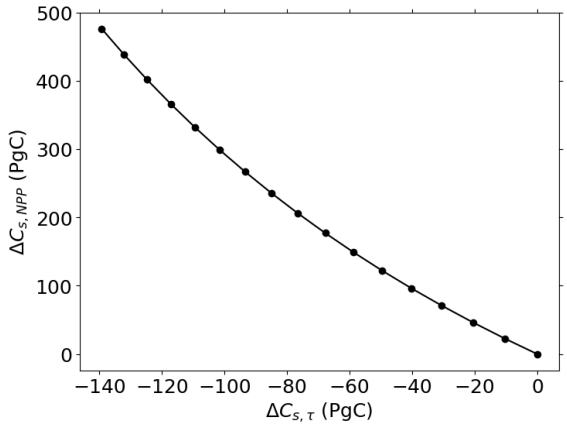

Figure 6.12: Relationship between $\Delta C_{s,NPP} = \tau_s \, \Delta NPP$ and $\Delta C_{s,\tau} = NPP_0 \, \Delta \tau_s$ from the three-box model. Each dot represents the results at the end of a 70 year run with a different assumed rate of increase of NPP ($\sim$ 0.0% to 0.8% per year in increments of 0.05%).

these correlations in CMIP6 (and to a lesser extent in CMIP5) are predominantly due to false priming.

6.4 Discussion

Soil carbon storage in the future will be determined by the net response to increases in both atmospheric CO_2 concentrations and the resultant changes in the Earth's climate system. However, this response will be determined by the net sensitivity of soil carbon controls to changes in atmospheric CO_2 and associated climate changes, which drive soil carbon feedbacks under climate change. Soil carbon controls are often considered to be Net Primary Productivity (NPP, Π_N) and soil carbon turnover time (τ_s), which control the input and output fluxes of

carbon between the soil and the atmosphere (Todd-Brown et al., 2014, 2013). Previously, it was assumed that on a global scale, a first-order approximation could be made for the future changes in soil carbon stocks, where changes in NPP could be approximated as the response to CO_2, and changes to τ_s could be approximated as the response to temperature (T), which would be equivalent to assuming β_s is mostly due to the term $\tau_{s,0}\ \partial\Pi_N/\partial CO_2$ and γ_s is mostly due to the term $\Pi_{N,0}\partial\tau_s/\partial T$ (see Equations 6.5 and 6.6).

Chapter 3 found an apparent non-linearity between NPP and τ_s in CMIP6 ESM projections of soil carbon change in Shared Socioeconomic Pathways (SSP) climate scenarios (see Figure 3.6 in Chapter 3). This chapter makes use of the C4MIP idealised simulations, which exclude additional processes such as land-use change, allowing for a more focused investigation into this non-linearity. The non-linearity between NPP and τ_s was shown here to exist in the C4MIP simulations across all ESMs (Figure 6.4), specifically in the full 1% CO_2 and BGC simulations. Conversely, a robust non-linearity was not found across the CMIP6 ESMs between soil carbon sensitivities to CO_2 and T, especially at lower levels of CO_2 forcing (see Figure 5.4 in Chapter 5). By breaking down the $\{\beta, \gamma\}$ formulation into sensitivity components which make up the soil carbon sensitivities (Figure 6.5), non-negligible contributions from NPP and τ_s were found as a result of both CO_2 and T changes (Figures 6.6 and 6.7). This result implies interactions between NPP and τ_s, opposed to interactions between CO_2 and T. It was further shown that NPP and τ_s are sensitive to both CO_2 and T changes in ESMs (Figure 6.1).

The sensitivity of NPP to climatic changes was expected on the regional scale (Figure 6.2), but the net global effects were expected to be small compared to CO_2 induced changes. ESM predictions for the global sensitivity are shown to vary amongst the ensemble (Figure 6.1), with both positive and negative global responses. A negative sensitivity to increased warming (-γ_{NPP}, Figure 6.6(b)) implies a reduction in NPP with climate change, for example due to detrimental effects of warming and drying in the tropics (Green et al., 2019; Phillips et al., 2009; Betts et al., 2004). A positive sensitivity of NPP to increased warming (+γ_{NPP}, Figure 6.6(b)) implies NPP increases with warming, for example due to increased growing season length in mid and high latitudes (Forkel et al., 2016; Graven et al., 2013; Reichstein et al., 2013). However, the non-negligible sensitivity of τ_s to changes in CO_2 predicted by ESMs is less widely understood.

The sensitivity of τ_s to CO_2 changes has been found to be associated with a strong correlation between NPP and τ_s across the CMIP6 ESMs (Figure 6.8).

This result suggests that changes in NPP may induce changes in τ_s, and the β_τ value is a result of NPP changes and not direct changes from CO_2. This was found to be consistent with 'false priming', which has previously been found in CMIP5 ESMs (Koven et al., 2015). The false priming reduction in effective τ_s is a transient phenomenon that arises in soil models that represent multiple carbon pools with different turnover times (Figure 6.11). Under continually increasing NPP, proportionally more of the additional litter is put into the faster pools, which brings down the overall effective τ_s value of the soil (Figure 6.10). The resultant τ_s reduction due to changes in NPP results in a clear relationship between soil carbon increments due to changes in NPP ($\Delta C_{s,NPP}$) and changes in τ_s ($\Delta C_{s,\tau}$), which was seen both in Chapter 3 (Figure 3.8) and here (Figure 6.9). The effect was found to be more prominent amongst the CMIP6 ESMs compared with the previous generation of CMIP5 ESMs, with the inverse correlation between NPP and τ_s stronger across the CMIP6 ESMs (r^2 range from 0.65 to 0.99) than what was found by Koven et al. (2015) across the CMIP5 ESMs (r^2 range from 0.25 to 0.89, see Figure 9 in Koven et al. (2015)), which suggests an increased false priming effect in CMIP6. This result is consistent with an increase in the simulation of multiple soil carbon pools within ESMs in CMIP6 (see Tables 2.1 and 2.2 in Chapter 2 for CMIP6 and CMIP5 ESMs, respectively).

6.5 Conclusions

Understanding the response of soil carbon under anthropogenic emissions of CO_2 is required to quantify future carbon cycle feedbacks. To investigate future changes to soil carbon stocks, different approaches can be used. One method is to analyse the input and output fluxes which control the magnitude of carbon stored in the soil (which we called the $\{NPP, \tau_s\}$ formulation), which allows for understanding of the individual processes involved (Koven et al., 2015; Todd-Brown et al., 2014). Another method is to investigate the individual sensitivities of soil carbon to changes in CO_2 and the resultant climate impacts, known as the $\{\beta, \gamma\}$ formulation (Arora et al., 2020; Friedlingstein et al., 2006), which allows for a quantification of soil carbon sensitivities to CO_2 and temperature changes. The aim of this chapter was to break-down defined soil carbon sensitivities using the $\{\beta, \gamma\}$ formulation, to further investigate the non-linearities in the future soil carbon response to climate change. This was done using the idealised Coupled Climate-Carbon Cycle Model Intercomparison Project (C4MIP) experiments with CMIP6 ESMs.

It was found that the sensitivity of soil carbon to CO_2 (β_s) and T (γ_s) are made up of sensitivities of both the above and below ground controls of carbon

within the soil. This is a result of climate effects on NPP, but mostly due to apparent CO_2 affects on τ_s. The sensitivity of τ_s to CO_2 was found to be a result of increased productivity, which shifts the effective turnover in models to give more weighting to the faster turnover pools, a process previously called false priming (Koven et al., 2015). The non-linearity between NPP and τ_s is therefore found to be a result of subsequent turnover reductions from NPP increases, where this non-linearity is found to be distinct from non-linearities between CO_2 and T. An apparent cancellation of the NPP-τ_s non-linearity is present in the majority of CMIP6 ESMs, which results in the Friedlingstein et al. (2006) $\{\beta, \gamma\}$ formulation providing a better approximation than expected given the complex, interacting processes involved.

Chapter 7

Conclusions

Abstract

This thesis has focused on the role of soil carbon in understanding and quantifying future changes in the Earth's climate system under increased atmospheric CO_2 concentrations. This research has included: model evaluation and analysis of future projections, the method of emergent constraints, and quantifying the soil carbon feedback to climate change using metrics which link the thesis analysis with the wider context of carbon cycle feedback research. The aim of this thesis was to improve understanding and reduce uncertainty in the response of soil carbon to climate change. In this chapter, the key conclusions from each of the thesis chapters are identified and promising areas for future research are highlighted.

7.1 Overview

Chapter 1 was a broad overview of the role of the carbon cycle in future changes to the Earth system. Soil carbon was introduced as the largest terrestrial store of carbon and a vital component in understanding future land carbon storage (Canadell et al., 2021). Therefore, quantifying the net soil carbon feedback to climate change was identified as an important area of research for understanding the overall climate change response. Uncertainty was shown to exist in both modelling and empirical studies investigating soil carbon change, which was shown to be due to uncertain sensitivities of the competing fluxes which control the magnitude of carbon stored. Earth System Models (ESMs) were introduced as a vital tool for predicting future soil carbon, where improvements are made through model development between each generation. Within ESMs, biogeochemical models for soil carbon are used to simulate soil carbon processes, where an overview of the mathematical representation of decomposition was given and a link to the complexity of processes which control soil carbon decomposition was

discussed. After reviewing literature for the 5$^{\text{th}}$ generation of the Coupled-Model Intercomparison Project (CMIP5) (Taylor et al., 2012), it was identified that the newest ESM ensemble, CMIP6 (Eyring et al., 2016; Meehl et al., 2014), is yet to be fully evaluated, especially with regard to soil carbon. Therefore, evaluation and analysis of soil carbon in CMIP6 ESMs was identified as an aim of this thesis to help quantify future soil carbon changes. On top of model development, emergent constraints were introduced as a method to reduce uncertainty in projections of climate change. Therefore, an additional aim of the thesis was identified: to reduce uncertainty in future soil carbon projections using emergent constraints.

In Chapter 2, the aim was to investigate how consistently ESMs simulate 'present day' soil carbon compared with what is seen in the real world. To do this, soil carbon and related controls, defined as Net Primary Productivity (NPP) and soil carbon turnover time (τ_s), were evaluated in CMIP6 ESMs against empirical datasets. Additionally, to evaluate the differences between CMIP6 with the previous generation of ESMs, comparisons were made with ESMs from CMIP5. Comparing CMIP6 with CMIP5, a lack of consistency in modelled soil carbon was shown to remain, particularly the underestimation of northern high-latitude soil carbon stocks where the greatest discrepancies were seen. It was shown that improvements have been made in the simulation of spatial patterns of contemporary NPP in CMIP6 compared with CMIP5, when compared to satellite-derived estimates. However, no significant improvements were seen in the spatial patterns of τ_s in CMIP6 models, when compared to estimates derived from observational datasets of soil carbon (C_s) and heterotrophic respiration (R_h). The poor representation of τ_s in CMIP6 ESMs, together with C_s simulations in both the CMIP5 and CMIP6 ESM generations being found to be spuriously highly-correlated with NPP, suggests soil carbon in these models may be over responsive to future projected changes in NPP, and not responsive enough to changes in turnover. This pointed to a need for a much greater emphasis on improving the representation of below-ground soil processes in next generation (CMIP7) of ESMs and suggests the potential for an overestimation of the long-term terrestrial carbon sink in CMIP6 projections (Varney et al., 2022).

In Chapter 3, the aim was to evaluate projections of soil carbon during the 21$^{\text{st}}$ century, to quantify future soil carbon changes (ΔC_s) in CMIP6 ESMs. The response of ΔC_s was broken down into changes due to increases in NPP ($\Delta C_{s,NPP}$) and reductions in τ_s ($\Delta C_{s,\tau}$), with the aim of isolating the differing responses which influence changes in future soil carbon storage. The evaluation was completed using three Shared Socioeconomic Pathways (SSP126, SSP245, and SSP585) scenarios, and comparisons were made with ΔC_s projections

from CMIP5 ESMs using equivalent future climate scenarios (RCP2.6, RCP4.5, and RCP8.5). The chapter identified a reduction in the CMIP6 ΔC_s model spread compared to CMIP5. However, similar reductions were not seen in the components due respectively to changes in NPP ($\Delta C_{s,NPP}$) and τ_s ($\Delta C_{s,\tau}$). The first point taken from this chapter was the need for constraints on both these terms (see Chapter 4). Additionally, the chapter reported a strong correlation between the linear soil carbon contributions, $\Delta C_{s,NPP}$ and $\Delta C_{s,\tau}$ within CMIP6 ESMs, which seemed to be the cause of the reduction in the CMIP6 ΔC_s spread. This correlation was further investigated in Chapter 6.

Chapter 4 presented a spatial emergent constraint on the sensitivity of soil carbon turnover to global warming (Varney et al., 2020). The response of soil carbon was found in Chapter 3 to be due to large counteracting contributions from feedbacks due to changes in NPP and changes in soil carbon turnover time (τ_s). The change in soil carbon due to reductions in τ_s ($\Delta C_{s,\tau}$) was found to vary amongst CMIP5 and CMIP6 ESMs, and the uncertainty in τ_s has been highlighted within literature as an important process to constrain (Ito et al., 2020; Todd-Brown et al., 2014). This chapter used the 'Emergent Constraint' technique to reduce the uncertainty in model projections of this response (Hall and Qu, 2006). This has been termed as a 'spatial emergent constraint', as the method makes use of a spatial temperature sensitivity to infer the sensitivity of $\Delta C_{s,\tau}$ to global warming. Therefore, this chapter successfully constrained a component of uncertainty in the overall soil carbon climate change response, and provides the potential of new emergent constraints using spatial variability.

In Chapter 5, the Coupled Climate-Carbon Cycle Model Intercomparison Project (C4MIP) simulations were introduced, which allows for the isolation of effects on soil carbon due to changes in atmospheric CO_2 and changes in global temperatures. These simulations were used together with the most commonly used approach to quantify changes in land carbon storage, with the aim of quantifying future changes in soil carbon storage. This approach was referred to as the $\{\beta, \gamma\}$ formulation, which enabled the break-down of the changes in soil carbon storage into two distinct linear feedback terms: soil carbon-concentration (β_s) and soil carbon-climate (γ_s) feedbacks (Friedlingstein et al., 2006). The adapted Friedlingstein et al. (2006) methodology was found to suggest that a linear approximation into β_s and γ_s sensitivities was a valid assumption for projected soil carbon changes in CMIP6 ESMs up until a doubling of CO_2. Additionally, the contribution of soil carbon to the overall land carbon sensitivity to climate change was investigated, where soil carbon was found to have a greater sensitivity to global temperature changes compared with carbon stored within

vegetation. This result suggested that soil carbon is particularly important in the long-term response of land carbon storage under extreme levels of global warming, and highlighted the need for further understanding and quantification of the sensitivity of global soils to changes in climate.

Chapter 6 connected the research presented in both Chapters 3 and 5, where the individual sensitivities of soil carbon controls (NPP and τ_s) to changes in both atmospheric CO_2 and global temperatures were investigated in CMIP6 ESMs using the C4MIP simulations. The soil carbon-concentration (β_s) and soil carbon-climate (γ_s) feedbacks were found to be made up of terms representing the sensitivities of both the above and below ground controls to CO_2 and temperature. A very significant change in the effective turnover time for global soil carbon (τ_s) was seen even in the C4MIP BGC simulations, that only included direct CO_2 effects on plants. This effect was identified as being due to 'false priming' (Koven et al., 2015). False priming occurs when an increase in NPP leads to the additional carbon input preferentially stored in fast turnover carbon pools, which reduces the effective turnover time of the soil as a whole. In Chapter 6, the three-box model of Koven et al. (2015) was used to show how false priming is a transient effect that arises from a disequilibrium in the distribution of soil carbon across pools of different turnover times. This was most clearly demonstrated under an idealised step change in NPP. The timescale of the 'transient' is set by the slowest soil carbon pool, and so can be over many centuries. False priming in the same three-box model was also shown to explain the negative correlation between $\Delta C_{s,NPP}$ and $\Delta C_{s,\tau}$, which was noted in both Chapters 3 and 6. The negative correlation was found to be much stronger across the CMIP6 ensemble than the CMIP5 ensemble, which contributes to the reduced model spread in projections of changes in global soil carbon in CMIP6, as reported in Chapter 3.

7.2 Future research

The work presented in this thesis can be built upon to further improve the quantification and understanding of soil carbon under climate change. A thorough evaluation of CMIP6 ESMs has helped to identify key areas for future development for the next generation CMIP7, and to identify relationships within the climate system which present the potential for new emergent constraints. In this section, specific areas for future research are highlighted.

7.2.1 Model development of below-ground processes

This thesis has highlighted the progress in the simulation of above-ground processes in CMIP6 ESMs compared to the previous generation of CMIP5 ESMs. This was first shown by the evaluation of contemporary Net Primary Productivity (NPP) in ESMs compared with empirical datasets (Chapter 2), where an improved consistency was found in CMIP6 compared with CMIP5. Additionally, Chapter 3 showed an improvement in the agreement amongst models in CMIP6 on projections of future NPP, and this was shown to result from the inclusion of an interactive nitrogen cycle which was a key highlighted model development in ESMs since CMIP5. In contrast, another common theme throughout this thesis has been the persistent uncertainty surrounding the soil carbon turnover time (τ_s) within ESMs, where the same advances in below-ground processes are less clear.

One way to reduce this uncertainty in τ_s is to focus efforts into improving the representation of below-ground soil processes in the next generation (CMIP7) of ESMs. In Chapter 1, biogeochemical models were discussed and the common assumptions that have been made with regards to the modelling of soil carbon cycling were presented. New insights into the way soil carbon exists in the real world suggests this differs from the way soil carbon has been historically modelled in these first-order biogeochemical models, which are used within ESMs to simulate microbial decomposition. Specifically, soil carbon models have been commonly based on the molecular structure of SOC controlling the long-term stability within the soil, however it is now understood that this affect is also controlled by environmental and biological influences (Schmidt et al., 2011). The coupling of these insights into new generations of ESMs is required for future model development, which will allow for known processes which influence future soil carbon to be simulated within ESMs (Canadell et al., 2021).

Previoulsy, the rate of decomposition in biogeochemical models has been dependent on the chemical composition of organic carbon within the soil; however, it is now thought that the biological influence on soil carbon decomposition is important in the long-term stabilisation of carbon within soils (Wieder et al., 2015a; Schmidt et al., 2011). This has lead to an aim of more explicitly representing microbial dynamics within ESMs (Chadburn et al., 2020; Walker et al., 2018; Koven et al., 2015), including the effects of microbial priming on decomposition (Todd-Brown et al., 2014; Wieder et al., 2013). In current ESMs, microbial activity is often implicitly represented, where the respired CO_2 is assumed to be proportional to the carbon stored within the soil (see Equation 1.3 in Chapter 1). However, soil microbial dynamics are expected to shift in

response to temperature, by a change in microbial physiology and community composition (Wieder et al., 2015a), as seen in long-term experimental warming studies (Melillo et al., 2017), which implies a complex long-term response of microbial decomposition (Canadell et al., 2021). In order to capture this long-term response, significant effort should be made to increase the explicit representation of microbial dynamics in ESMs.

Chapter 1 also discussed how biogeochemical models include soil carbon pools to represent differing turnover times of carbon within the soil. However, the representation of specific carbon pools, such as permafrost or peatland carbon, within ESMs is limited (Todd-Brown et al., 2013). The CMIP6 ensemble included the first ESMs to represent vertically resolved soil carbon, which was discussed in this thesis and found to be especially important in the northern latitudes due to deeper levels of soil carbon stocks. Vertically resolved soil carbon allows for differing turnover rates at depth, opposed to diagnosing the turnover rate of carbon in the whole soil column using temperature near the soil surface, and is necessary for improving the simulation of both permafrost and peatland carbon (Lawrence et al., 2019). Therefore, a continued attempt to include this representation within more ESMs is required. The representation of permafrost dynamics is not routinely included in CMIP6 ESMs, and has been suggested as an area for model development (Burke et al., 2020; Koven et al., 2011). Similarly, peatland soils present a potential source of carbon to the atmosphere and are not routinely included in the majority of CMIP6 ESMs (Canadell et al., 2021). The simulation of associated processes, such as peat accumulation, should be an additional focus for future model development (Chadburn et al., 2022). Additionally, the development of models with continuous 'age' variables (Shi et al., 2020), opposed to the soil carbon pool 'box model' approach (Parton et al., 1988; Jenkinson et al., 1991), suggest potential for more 'realistically' representing global soil carbon stocks (Schmidt et al., 2011; Aber et al., 1997).

Finally, there is a clear need for an improved evaluation and calibration of soil carbon within ESMs. As described above the inclusion of an interactive nitrogen cycle has resulted in improved consistency amongst CMIP6 models in terms of their predictions of above-ground fluxes. The nitrogen cycle also has a large impact on below-ground processes and yet similar improvements to below-ground carbon decomposition have not been seen. A greater focus on how model developments affect processes within the soil is needed. For example, this could be done by introducing a 'SoilCarbonMIP', to be completed as part of new CMIP generations. This would allow for a more structured benchmarking of model parameterisation and understanding of the processes included

within models, and focuses for model development in the future. The results in Chapter 5 confirmed that global soils dominated the response of land carbon to changes in climate, especially at more extreme levels of climate change, which emphasises the importance of reliably simulating below-ground process in ESMs.

7.2.2 Implication of false priming on the spatial emergent constraint on soil carbon turnover to global warming

The spatial emergent constraint on soil carbon turnover to global warming presented in Chapter 4 and published in Varney et al. (2020), is based on the sensitivity of soil carbon turnover time (τ_s) to climate change being 'reconstructed' using the present day spatial variations in τ_s and near surface air temperature. It was implicitly assumed that temperature would be the dominant control of future changes in τ_s, consistent with previous literature (Jenkinson et al., 1991). However, it was later found in Chapter 6 that the future response of τ_s under climate change is due both to the sensitivity to changing temperatures, as well as an effective sensitivity to CO_2, due to an interaction between increasing productivity and turnover (false priming).

Despite this, the emergent constraint was successful, and the use of the spatial temperature sensitivity of τ_s was able to reproduce the subsequent changes in soil carbon ($\Delta C_{s,\tau}$) predicted by both CMIP5 and CMIP6 ESMs (see Figure 4.7(b) in Chapter 4). This suggests that the derived spatial relationships between τ_s and temperature in the models, includes an effective sensitivity of τ_s to changes in NPP. This demands further investigation to relate present day spatial patterns in τ_s and temperature, with future spatial patterns of changes in NPP. The success of the constraint without the inclusion of this effect suggests that either: (1) there is an emergent relationship between τ_s in the present day and how NPP changes in the future, or (2) the transient nature of both the historical and future simulations used in deriving the constraint includes an influence from faster equilibration of fast-turnover compared to slow-turnover carbon pools (Koven et al., 2015). To fully understand the robustness of this constraint on $\Delta C_{s,\tau}$, a better understanding of the false priming effect on this process is required.

7.2.3 Additional potential spatial emergent constraints on the climate system

In more recent years, emergent constraints have become increasingly common, and have been used to successfully constrain terrestrial carbon cycle processes (Barkhordarian et al., 2021; Xu et al., 2020; Winkler et al., 2019; Cox, 2019; Wenzel et al., 2016; Cox et al., 2013). However, these emergent constraints almost exclusively use temporal variation (trends or variability). This thesis introduced the term 'spatial emergent constraint', which instead uses spatial variability to constrain future changes. This section presents some ideas for potential spatial emergent constraints which can be investigated.

7.2.3.1 Constraint on carbon input to the soil

A natural progression from the spatial emergent constraint on soil carbon turnover to global warming (Chapter 4, Varney et al. (2020)), is to attempt to constrain the global input of carbon into soils. If each individual component which makes up the total soil carbon response to climate change is successfully constrained, the constraints can be combined to obtain an overall uncertainty reduction. Throughout this thesis, the input of carbon into the soil has been approximated as Net Primary Productivity (NPP). Previously, Wenzel et al. (2016) constrained the projected land photosynthesis by relating to changes in the seasonal cycle of atmospheric CO_2 in CMIP3 and CMIP5 ESMs, where land photosynthesis was approximated by Gross Primary Productivity (GPP). More recently, Winkler et al. (2019) constrain increased GPP in the northern high latitudes in CMIP5 ESMs by constraining leaf area sensitivity to ambient CO_2 from the past 36 years of satellite measurements. A spatial constraint due to CO_2 fertilization is not possible from a direct spatial sensitivity to CO_2, however a spatial pattern of NPP related to temperature and precipitation patterns globally is known. The possibility of constraining future NPP changes due to future climate changes using the spatial climate sensitivities is therefore suggested for future research.

7.2.3.2 Emergent constraint on $\Delta C_{s,NPP}$ using $\Delta C_{s,\tau}$

An additional potential emergent constraint could be based on the existing spatial emergent constraint on $\Delta C_{s,\tau}$, together with the deduced emergent relationship between $\Delta C_{s,NPP}$ and $\Delta C_{s,\tau}$ in CMIP6 ESMs found in this thesis. In Chapter 3 (see Figure 3.8), a strong correlation was found between soil carbon changes due to increased NPP ($\Delta C_{s,NPP}$) and changes due to reductions in soil carbon turnover time ($\Delta C_{s,\tau}$), which was present across CMIP6 ESMs in three future

climate scenarios (SSP126, SSP245, SSP585). In Chapter 6 (see Figure 6.9), the strong correlation was also found to hold using the full 1% CO_2 C4MIP simulation, where a 1% increase in CO_2 is seen each year. These results suggest an apparent emergent relationship between $\Delta C_{s,NPP}$ and $\Delta C_{s,\tau}$ that is robust across the CMIP6 model ensemble.

The apparent strong anti-correlation between changes in productivity and turnover has the potential to simplify the future soil carbon response to climate change, at least at a global scale, as a constraint on both $\Delta C_{s,\tau}$ and $\Delta C_{s,NPP}$ could be deduced from the spatial variability of τ_s inferred from observations. In theory, the emergent constraint technique could be followed; the idea would be to use the spatial emergent constraint on $\Delta C_{s,\tau}$ (Chapter 4, Varney et al. (2020)) as the required observational trend or variation (x-axis), which could be used together with the uncertainty surrounding the emergent relationship, to obtain an emergent constraint on $\Delta C_{s,NPP}$ projections in CMIP6 (y-axis). However, the fundamental mechanisms behind this emergent relationship, and the role of false priming on the spatial emergent constraint would need to be investigated and fully understood.

Additionally, it has been presented in this thesis that the future soil carbon response to climate change (ΔC_s) is made up of multiple terms, including additional terms to the $\Delta C_{s,NPP}$ and $\Delta C_{s,\tau}$ responses. Specifically, the most significant are the non-linear ($\Delta NPP \Delta \tau_s$) and transient ($\Delta C_{s,NEP}$) terms, which contribute to future changes in soil carbon. To obtain a constraint on the full ΔC_s response, additional constraints would also be required on these terms. For the implication of the emergent constraint technique, further understanding of the $\Delta NPP \Delta \tau_s$ and $\Delta C_{s,NEP}$ terms would be needed, as well as a more thorough understanding of their implication of future soil carbon changes.

7.2.3.3 Constraint on the C_s sensitivity to T

In Chapter 5, it was found that a linear approximation of future changes in soil carbon (ΔC_s) into CO_2 and temperature (T) changes, was a good approximation up until a doubling of atmospheric CO_2 (Friedlingstein et al., 2006). Therefore, a constraint on the sensitivity of soil carbon to CO_2 (β_s) and a constraint on the sensitivity of soil carbon to T (γ_s), could be combined to obtain a constraint on the overall change in soil carbon (where, $\Delta C_s = \beta_s \Delta CO_2 + \gamma_s \Delta T$).

Previously, the sensitivity of tropical land carbon to temperature (named γ_{LT}) has been successfully constrained for ESMs up until the CMIP5 generation

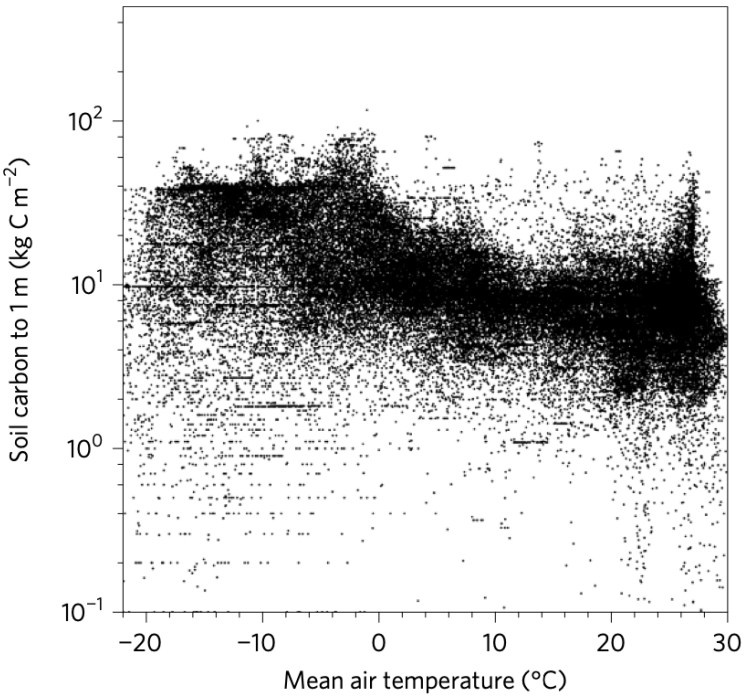

Figure 7.1: A scatter plot showing observation soil carbon (C_s) for each latitude and longitude point against observational temperature (T), as presented in Koven et al. (2017).

(Cox et al., 2013; Wenzel et al., 2014). Here the possibility of a spatial constraint on γ_s is suggested, which can be investigated with CMIP5 and CMIP6 ESMs. Koven et al. (2017) present a figure (Figure 7.1), which shows the spatial temperature sensitivity of C_s, as shown by empirical data. A suggestion as a future possible constrain is to investigate whether the spatial temperature sensitivity of C_s could provide a spatial emergent constraint on future soil carbon change. This could be tested specifically using the RAD simulation from the C4MIP project (see Chapter 5), and would allow for a constraint on model predicted γ_s.

7.2.3.4 Spatial emergent constraint on the sensitivity of ecosystem carbon turnover to global warming

The constraint on soil carbon turnover to global warming (Chapter 4, Varney et al. (2020)) using the spatial variability of τ_s inferred by observations, suggests the possibility of constraining ecosystem turnover time (τ_e) using a similar concept. Carvalhais et al. (2014) defines τ_e as the total ecosystem carbon ($C_L = C_v + C_s$) divided by the total input or output flux, which in this case the total input flux (GPP) is used. However, total ecosystem respiration ($R_e = R_a + R_h$, where R_a is autotrophic respiration by plants) could be used to represent the output flux of carbon, as in Varney et al. (2020). Carvalhais et al. (2014) describe ecosystem turnover as 'an ecosystem property that emerges from the interplay between

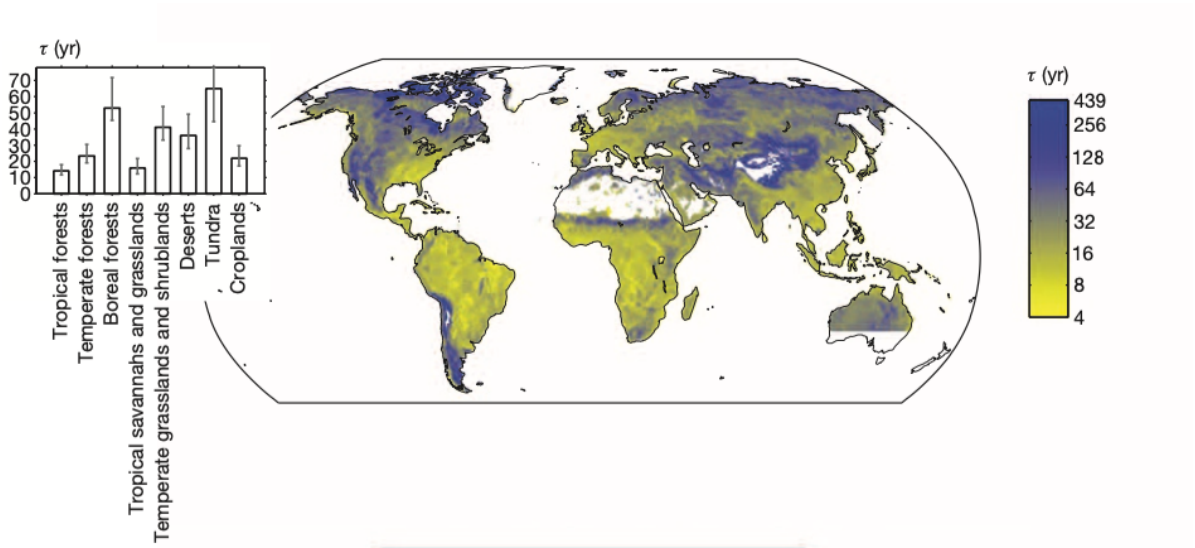

Figure 7.2: A map plot showing the spatial pattern of ecosystem carbon turnover time (τ_e), and including a break down of τ_e within different climate biomes, as presented in Carvalhais et al. (2014).

climate, soil and vegetation type', and the study finds a strong dependence τ_e to both temperature and precipitation patterns using observational data (see Figure 7.2). It is shown that ESMs in CMIP5 to do match these dependencies, particularly the relationship of τ_e to precipitation.

Therefore, the possibility of constraining future projections of τ_e, or the subsequent change in ecosystem carbon from changes in τ_e (defined $\Delta C_{e,\tau}$, where $\Delta C_{e,\tau} = (R_{a,0} + R_{h,0})\Delta\tau_e$ following the method of Varney et al. (2020)), should be investigated as future research. The findings of Carvalhais et al. (2014) suggest the potential of constraining this response using real world measurements of spatial ecosystem respiration, together with the spatial variability of τ_e to both temperature and precipitation inferred from observations.

Bibliography

Aber, J. D., Ollinger, S. V., and Driscoll, C. T. (1997). Modeling nitrogen saturation in forest ecosystems in response to land use and atmospheric deposition. *Ecological Modelling*, 101(1):61–78.

Amthor, J. S. (1995). Terrestrial higher-plant response to increasing atmospheric [co2] in relation to the global carbon cycle. *Global Change Biology*, 1(4):243–274.

Amundson, R. and Biardeau, L. (2018). Opinion: Soil carbon sequestration is an elusive climate mitigation tool. *Proceedings of the National Academy of Sciences*, 115(46):11652–11656.

Anav, A., Friedlingstein, P., Kidston, M., Bopp, L., Ciais, P., Cox, P., Jones, C., Jung, M., Myneni, R., and Zhu, Z. (2013). Evaluating the land and ocean components of the global carbon cycle in the cmip5 earth system models. *Journal of Climate*, 26(18):6801–6843.

Arias, P., Bellouin, N., Coppola, E., Jones, R., Krinner, G., Marotzke, J., Naik, V., Palmer, M., Plattner, G.-K., Rogelj, J., Rojas, M., Sillmann, J., Storelvmo, T., Thorne, P., Trewin, B., Achuta Rao, K., Adhikary, B., Allan, R., Armour, K., Bala, G., Barimalala, R., Berger, S., Canadell, J., Cassou, C., Cherchi, A., Collins, W., Collins, W., Connors, S., Corti, S., Cruz, F., Dentener, F., Dereczynski, C., Di Luca, A., Diongue Niang, A., Doblas-Reyes, F., Dosio, A., Douville, H., Engelbrecht, F., Eyring, V., Fischer, E., Forster, P., Fox-Kemper, B., Fuglestvedt, J., Fyfe, J., Gillett, N., Goldfarb, L., Gorodetskaya, I., Gutierrez, J., Hamdi, R., Hawkins, E., Hewitt, H., Hope, P., Islam, A., Jones, C., Kaufman, D., Kopp, R., Kosaka, Y., Kossin, J., Krakovska, S., Lee, J.-Y., Li, J., Mauritsen, T., Maycock, T., Meinshausen, M., Min, S.-K., Monteiro, P., Ngo-Duc, T., Otto, F., Pinto, I., Pirani, A., Raghavan, K., Ranasinghe, R., Ruane, A., Ruiz, L., Sallée, J.-B., Samset, B., Sathyendranath, S., Seneviratne, S., Sörensson, A., Szopa, S., Takayabu, I., Tréguier, A.-M., van den Hurk, B., Vautard, R., von Schuckmann, K., Zaehle, S., Zhang, X., and Zickfeld, K. (2021). *Technical Summary*. Cambridge University Press, Cambridge, United Kingdom and New York, NY, USA.

Arora, V. and Boer, G. (2010). Uncertainties in the 20th century carbon budget associated with land use change. *Global Change Biology*, 16(12):3327–3348.

Arora, V., Boer, G., Christian, J., Curry, C., Denman, K., Zahariev, K., Flato, G., Scinocca, J., Merryfield, W., and Lee, W. (2009). The effect of terrestrial photosynthesis down regulation on the twentieth-century carbon budget simulated with the cccma earth system model. *Journal of Climate*, 22(22):6066–6088.

Arora, V. K., Boer, G. J., Friedlingstein, P., Eby, M., Jones, C. D., Christian, J. R., Bonan, G., Bopp, L., Brovkin, V., Cadule, P., et al. (2013). Carbon–concentration and carbon–climate feedbacks in cmip5 earth system models. *Journal of Climate*, 26(15):5289–5314.

Arora, V. K., Katavouta, A., Williams, R. G., Jones, C. D., Brovkin, V., Friedlingstein, P., Schwinger, J., Bopp, L., Boucher, O., Cadule, P., et al. (2020). Carbon–concentration and carbon–climate feedbacks in cmip6 models and their comparison to cmip5 models. *Biogeosciences*, 17(16):4173–4222.

Bader, M. K.-F., Leuzinger, S., Keel, S. G., Siegwolf, R. T., Hagedorn, F., Schleppi, P., and Körner, C. (2013). Central e uropean hardwood trees in a high-co 2 future: synthesis of an 8-year forest canopy co 2 enrichment project. *Journal of Ecology*, 101(6):1509–1519.

Bai, E., Li, S., Xu, W., Li, W., Dai, W., and Jiang, P. (2013). A meta-analysis of experimental warming effects on terrestrial nitrogen pools and dynamics. *New Phytologist*, 199(2):441–451.

Ballantyne, A., Andres, R., Houghton, R., Stocker, B., Wanninkhof, R., Anderegg, W., Cooper, L., DeGrandpre, M., Tans, P., Miller, J., et al. (2015). Audit of the global carbon budget: estimate errors and their impact on uptake uncertainty. *Biogeosciences*, 12(8):2565–2584.

Barkhordarian, A., Bowman, K. W., Cressie, N., Jewell, J., and Liu, J. (2021). Emergent constraints on tropical atmospheric aridity—carbon feedbacks and the future of carbon sequestration. *Environmental Research Letters*, 16(11):114008.

Batjes, N. H. (2016). Harmonized soil property values for broad-scale modelling (wise30sec) with estimates of global soil carbon stocks. *Geoderma*, 269:61–68.

Beer, C. (2016). Permafrost sub-grid heterogeneity of soil properties key for 3-d soil processes and future climate projections. *Frontiers in Earth Science*, 4:81.

Bentsen, M., Bethke, I., Debernard, J. B., Iversen, T., Kirkevåg, A., Seland, Ø., Drange, H., Roelandt, C., Seierstad, I. A., Hoose, C., et al. (2013). The norwegian earth system model, noresm1-m–part 1: description and basic evaluation of the physical climate. *Geoscientific Model Development*, 6(3):687–720.

Best, M., Pryor, M., Clark, D., Rooney, G., Essery, R., Ménard, C., Edwards, J., Hendry, M., Porson, A., Gedney, N., et al. (2011). The joint uk land environment simulator (jules), model description–part 1: energy and water fluxes. *Geoscientific Model Development*, 4(3):677–699.

Betts, R., Cox, P., Collins, M., Harris, P., Huntingford, C., and Jones, C. (2004). The role of ecosystem-atmosphere interactions in simulated amazonian precipitation decrease and forest dieback under global climate warming. *Theoretical and applied climatology*, 78(1-3):157–175.

Bloom, A., Williams, M., et al. (2015). Cardamom 2001-2010 global carbon model-data fusion (mdf) analysis.

Blyth, E. M., Arora, V. K., Clark, D. B., Dadson, S. J., De Kauwe, M. G., Lawrence, D. M., Melton, J. R., Pongratz, J., Turton, R. H., Yoshimura, K., et al. (2021). Advances in land surface modelling. *Current Climate Change Reports*, 7(2):45–71.

Boer, G. and Arora, V. (2009). Temperature and concentration feedbacks in the carbon cycle. *Geophysical Research Letters*, 36(2).

Boer, G. and Arora, V. (2013). Feedbacks in emission-driven and concentration-driven global carbon budgets. *Journal of climate*, 26(10):3326–3341.

Bonan, G. B. (2008). Forests and climate change: forcings, feedbacks, and the climate benefits of forests. *science*, 320(5882):1444–1449.

Bossio, D., Cook-Patton, S., Ellis, P., Fargione, J., Sanderman, J., Smith, P., Wood, S., Zomer, R., Von Unger, M., Emmer, I., et al. (2020). The role of soil carbon in natural climate solutions. *Nature Sustainability*, 3(5):391–398.

Boucher, O., Servonnat, J., Albright, A. L., Aumont, O., Balkanski, Y., Bastrikov, V., Bekki, S., Bonnet, R., Bony, S., Bopp, L., et al. (2020). Presentation and evaluation of the ipsl-cm6a-lr climate model. *Journal of Advances in Modeling Earth Systems*, 12(7):e2019MS002010.

Bradford, M. A., Wieder, W. R., Bonan, G. B., Fierer, N., Raymond, P. A., and Crowther, T. W. (2016). Managing uncertainty in soil carbon feedbacks to climate change. *Nature Climate Change*, 6(8):751.

Brovkin, V., Boysen, L., Arora, V. K., Boisier, J., Cadule, P., Chini, L., Claussen, M., Friedlingstein, P., Gayler, V., Van Den Hurk, B., et al. (2013). Effect of anthropogenic land-use and land-cover changes on climate and land carbon storage in cmip5 projections for the twenty-first century. *Journal of Climate*, 26(18):6859–6881.

Burke, E. J., Ekici, A., Huang, Y., Chadburn, S. E., Huntingford, C., Ciais, P., Friedlingstein, P., Peng, S., and Krinner, G. (2017). Quantifying uncertainties of permafrost carbon–climate feedbacks. *Biogeosciences*, 14(12):3051–3066.

Burke, E. J., Zhang, Y., and Krinner, G. (2020). Evaluating permafrost physics in the coupled model intercomparison project 6 (cmip6) models and their sensitivity to climate change. *The Cryosphere*, 14(9):3155–3174.

Caldwell, P. M., Bretherton, C. S., Zelinka, M. D., Klein, S. A., Santer, B. D., and Sanderson, B. M. (2014). Statistical significance of climate sensitivity predictors obtained by data mining. *Geophysical Research Letters*, 41(5):1803–1808.

Canadell, J., Monteiro, P., Costa, M., Cotrim da Cunha, L., Cox, P., Eliseev, A., Henson, S., Ishii, M., Jaccard, S., Koven, C., Lohila, A., Patra, P., Piao, S., Rogelj, J., Syampungani, S., Zaehle, S., and Zickfeld, K. (2021). *Global Carbon and other Biogeochemical Cycles and Feedbacks*. Cambridge University Press, Cambridge, United Kingdom and New York, NY, USA.

Cao, M. and Woodward, F. I. (1998). Dynamic responses of terrestrial ecosystem carbon cycling to global climate change. *Nature*, 393(6682):249–252.

Carvalhais, N., Forkel, M., Khomik, M., Bellarby, J., Jung, M., Migliavacca, M., Mu, M., Saatchi, S., Santoro, M., Thurner, M., et al. (2014). Global covariation of carbon turnover times with climate in terrestrial ecosystems. *Nature*, 514(7521):213.

Chadburn, S., Burke, E., Cox, P., Friedlingstein, P., Hugelius, G., and Westermann, S. (2017). An observation-based constraint on permafrost loss as a function of global warming. *Nature Climate Change*, 7(5):340.

Chadburn, S. E., Aalto, T., Aurela, M., Baldocchi, D., Biasi, C., Boike, J., Burke, E. J., Comyn-Platt, E., Dolman, A. J., Duran-Rojas, C., et al. (2020). Modeled microbial dynamics explain the apparent temperature sensitivity of wetland methane emissions. *Global Biogeochemical Cycles*, 34(11):e2020GB006678.

Chadburn, S. E., Burke, E. J., Gallego-Sala, A. V., Smith, N. D., Bret-Harte, M. S., Charman, D. J., Drewer, J., Edgar, C. W., Euskirchen, E. S., Fortuniak, K., et al.

(2022). A new approach to simulate peat accumulation, degradation and stability in a global land surface scheme (jules vn5. 8_accumulate_soil) for northern and temperate peatlands. *Geoscientific Model Development*, 15(4):1633–1657.

Cheruy, F., Ducharne, A., Hourdin, F., Musat, I., Vignon, É., Gastineau, G., Bastrikov, V., Vuichard, N., Diallo, B., Dufresne, J.-L., et al. (2020). Improved near-surface continental climate in ipsl-cm6a-lr by combined evolutions of atmospheric and land surface physics. *Journal of Advances in Modeling Earth Systems*, 12(10):e2019MS002005.

Ciais, P., Sabine, C., Bala, G., Bopp, L., Brovkin, V., Canadell, J., Chhabra, A., DeFries, R., Galloway, J., Heimann, M., Jones, C., Le Quéré, C., Myneni, R., Piao, S., and Thornton, P. (2013). Carbon and other biogeochemical cycles. In Stocker, T., Qin, D., Plattner, G.-K., Tignor, M., Allen, S., Boschung, J., Nauels, A., Xia, Y., Bex, V., and Midgley, P., editors, *Climate Change 2013: The Physical Science Basis. Contribution of Working Group I to the Fifth Assessment Report of the Intergovernmental Panel on Climate Change*, book section 6, pages 465–570. Cambridge University Press, Cambridge, United Kingdom and New York, NY, USA.

Clark, D., Mercado, L., Sitch, S., Jones, C., Gedney, N., Best, M., Pryor, M., Rooney, G., Essery, R., Blyth, E., et al. (2011). The joint uk land environment simulator (jules), model description–part 2: carbon fluxes and vegetation dynamics. *Geoscientific Model Development*, 4(3):701–722.

Conant, R. T., Ryan, M. G., Ågren, G. I., Birge, H. E., Davidson, E. A., Eliasson, P. E., Evans, S. E., Frey, S. D., Giardina, C. P., Hopkins, F. M., et al. (2011). Temperature and soil organic matter decomposition rates–synthesis of current knowledge and a way forward. *Global Change Biology*, 17(11):3392–3404.

Cook, F. J. and Orchard, V. A. (2008). Relationships between soil respiration and soil moisture. *Soil Biology and Biochemistry*, 40(5):1013–1018.

Copernicus Climate Change Service, E. K. (2021). Copernicus climate change service, product user guide and specification.

Cox, P. M. (2001). Description of the" triffid" dynamic global vegetation model. *Hadley Centre for Climate Prediction and Research*.

Cox, P. M. (2019). Emergent constraints on climate-carbon cycle feedbacks. *Current climate change reports*, 5(4):275–281.

Cox, P. M., Betts, R., Collins, M., Harris, P. P., Huntingford, C., and Jones, C. (2004). Amazonian forest dieback under climate-carbon cycle projections for the 21st century. *Theoretical and applied climatology*, 78(1):137–156.

Cox, P. M., Betts, R. A., Jones, C. D., Spall, S. A., and Totterdell, I. J. (2000). Acceleration of global warming due to carbon-cycle feedbacks in a coupled climate model. *Nature*, 408(6809):184.

Cox, P. M., Huntingford, C., and Williamson, M. S. (2018). Emergent constraint on equilibrium climate sensitivity from global temperature variability. *Nature*, 553(7688):319.

Cox, P. M., Pearson, D., Booth, B. B., Friedlingstein, P., Huntingford, C., Jones, C. D., and Luke, C. M. (2013). Sensitivity of tropical carbon to climate change constrained by carbon dioxide variability. *Nature*, 494(7437):341.

Cramer, W., Bondeau, A., Woodward, F. I., Prentice, I. C., Betts, R. A., Brovkin, V., Cox, P. M., Fisher, V., Foley, J. A., Friend, A. D., et al. (2001). Global response of terrestrial ecosystem structure and function to co2 and climate change: results from six dynamic global vegetation models. *Global change biology*, 7(4):357–373.

Crowther, T. W., Todd-Brown, K. E., Rowe, C. W., Wieder, W. R., Carey, J. C., Machmuller, M. B., Snoek, B., Fang, S., Zhou, G., Allison, S. D., et al. (2016). Quantifying global soil carbon losses in response to warming. *Nature*, 540(7631):104.

Crowther, T. W., Van den Hoogen, J., Wan, J., Mayes, M. A., Keiser, A., Mo, L., Averill, C., and Maynard, D. S. (2019). The global soil community and its influence on biogeochemistry. *Science*, 365(6455):eaav0550.

Dai, Y., Zeng, X., Dickinson, R. E., Baker, I., Bonan, G. B., Bosilovich, M. G., Denning, A. S., Dirmeyer, P. A., Houser, P. R., Niu, G., et al. (2003). The common land model. *Bulletin of the American Meteorological Society*, 84(8):1013–1024.

Dalias, P., Anderson, J., Bottner, P., and Coûteaux, M.-M. (2001). Long-term effects of temperature on carbon mineralisation processes. *Soil biology and Biochemistry*, 33(7-8):1049–1057.

Danabasoglu, G., Lamarque, J.-F., Bacmeister, J., Bailey, D., DuVivier, A., Edwards, J., Emmons, L., Fasullo, J., Garcia, R., Gettelman, A., et al. (2020). The community earth system model version 2 (cesm2). *Journal of Advances in Modeling Earth Systems*, 12(2).

Davidson, E. A. and Janssens, I. A. (2006). Temperature sensitivity of soil carbon decomposition and feedbacks to climate change. *Nature*, 440(7081):165.

Davidson, E. A., Trumbore, S. E., and Amundson, R. (2000). Soil warming and organic carbon content. *Nature*, 408(6814):789–790.

Davies-Barnard, T., Meyerholt, J., Zaehle, S., Friedlingstein, P., Brovkin, V., Fan, Y., Fisher, R. A., Jones, C. D., Lee, H., Peano, D., et al. (2020). Nitrogen cycling in cmip6 land surface models: progress and limitations. *Biogeosciences*, 17(20):5129–5148.

De Kauwe, M. G., Keenan, T. F., Medlyn, B. E., Prentice, I. C., and Terrer, C. (2016). Satellite based estimates underestimate the effect of co 2 fertilization on net primary productivity. *Nature Climate Change*, 6(10):892–893.

Del Grosso, S., Parton, W., Mosier, A., Holland, E., Pendall, E., Schimel, D., and Ojima, D. (2005). Modeling soil co 2 emissions from ecosystems. *Biogeochemistry*, 73(1):71–91.

Delire, C., Séférian, R., Decharme, B., Alkama, R., Calvet, J.-C., Carrer, D., Gibelin, A.-L., Joetzjer, E., Morel, X., Rocher, M., et al. (2020). The global land carbon cycle simulated with isba-ctrip: Improvements over the last decade. *Journal of Advances in Modeling Earth Systems*, 12(9):e2019MS001886.

Dorigo, W., Wagner, W., Albergel, C., Albrecht, F., Balsamo, G., Brocca, L., Chung, D., Ertl, M., Forkel, M., Gruber, A., et al. (2017). Esa cci soil moisture for improved earth system understanding: State-of-the art and future directions. *Remote Sensing of Environment*, 203:185–215.

Dufresne, J.-L., Foujols, M.-A., Denvil, S., Caubel, A., Marti, O., Aumont, O., Balkanski, Y., Bekki, S., Bellenger, H., Benshila, R., et al. (2013). Climate change projections using the ipsl-cm5 earth system model: from cmip3 to cmip5. *Climate dynamics*, 40(9):2123–2165.

Dunne, J., Horowitz, L., Adcroft, A., Ginoux, P., Held, I., John, J., Krasting, J., Malyshev, S., Naik, V., Paulot, F., et al. (2020). The gfdl earth system model version 4.1 (gfdl-esm 4.1): Overall coupled model description and simulation characteristics. *Journal of Advances in Modeling Earth Systems*, 12(11):e2019MS002015.

Dunne, J. P., John, J. G., Adcroft, A. J., Griffies, S. M., Hallberg, R. W., Shevliakova, E., Stouffer, R. J., Cooke, W., Dunne, K. A., Harrison, M. J., et al. (2012). Gfdl's esm2 global coupled climate–carbon earth system models. part i: Physical formulation and baseline simulation characteristics. *Journal of climate*, 25(19):6646–6665.

Dunne, J. P., John, J. G., Shevliakova, E., Stouffer, R. J., Krasting, J. P., Malyshev, S. L., Milly, P., Sentman, L. T., Adcroft, A. J., Cooke, W., et al. (2013). Gfdl's esm2 global coupled climate–carbon earth system models. part ii: carbon system formulation and baseline simulation characteristics. *Journal of Climate*, 26(7):2247–2267.

Eswaran, H., Van Den Berg, E., and Reich, P. (1993). Organic carbon in soils of the world. *Soil science society of America journal*, 57(1):192–194.

Evans, C., Peacock, M., Baird, A., Artz, R., Burden, A., Callaghan, N., Chapman, P., Cooper, H., Coyle, M., Craig, E., et al. (2021). Overriding water table control on managed peatland greenhouse gas emissions. *Nature*, 593(7860):548–552.

Exbrayat, J.-F., Pitman, A., Zhang, Q., Abramowitz, G., and Wang, Y.-P. (2013a). Examining soil carbon uncertainty in a global model: response of microbial decomposition to temperature, moisture and nutrient limitation. *Biogeosciences*, 10(11):7095–7108.

Exbrayat, J.-F., Pitman, A. J., Zhang, Q., Abramowitz, G., and Wang, Y.-P. (2013b). Examining soil carbon uncertainty in a global model: response of microbial decomposition to temperature, moisture and nutrient limitation. *Biogeosciences*, 10(11):7095–7108.

Eyring, V., Bony, S., Meehl, G. A., Senior, C. A., Stevens, B., Stouffer, R. J., and Taylor, K. E. (2016). Overview of the coupled model intercomparison project phase 6 (cmip6) experimental design and organization. *Geoscientific Model Development (Online)*, 9(LLNL-JRNL-736881).

Eyring, V., Cox, P. M., Flato, G. M., Gleckler, P. J., Abramowitz, G., Caldwell, P., Collins, W. D., Gier, B. K., Hall, A. D., Hoffman, F. M., et al. (2019). Taking climate model evaluation to the next level. *Nature Climate Change*, 9(2):102–110.

Falloon, P., Jones, C. D., Ades, M., and Paul, K. (2011). Direct soil moisture controls of future global soil carbon changes: An important source of uncertainty. *Global Biogeochemical Cycles*, 25(3).

FAO, I. and ISRIC, I. (2012). Jrc: Harmonized world soil database (version 1.2). *FAO, Rome, Italy and IIASA, Laxenburg, Austria*.

Forkel, M., Carvalhais, N., Rödenbeck, C., Keeling, R., Heimann, M., Thonicke, K., Zaehle, S., and Reichstein, M. (2016). Enhanced seasonal co2 exchange caused by amplified plant productivity in northern ecosystems. *Science*, 351(6274):696–699.

Friedlingstein, P., Cox, P., Betts, R., Bopp, L., von Bloh, W., Brovkin, V., Cadule, P., Doney, S., Eby, M., Fung, I., et al. (2006). Climate–carbon cycle feedback analysis: results from the c4mip model intercomparison. *Journal of climate*, 19(14):3337–3353.

Friedlingstein, P., Dufresne, J.-L., Cox, P., and Rayner, P. (2003). How positive is the feedback between climate change and the carbon cycle? *Tellus B: Chemical and Physical Meteorology*, 55(2):692–700.

Friedlingstein, P., Fung, I., Holland, E., John, J., Brasseur, G., Erickson, D., and Schimel, D. (1995). On the contribution of co2 fertilization to the missing biospheric sink. *Global Biogeochemical Cycles*, 9(4):541–556.

Friedlingstein, P., Jones, M. W., O'Sullivan, M., Andrew, R. M., Bakker, D. C., Hauck, J., Le Quéré, C., Peters, G. P., Peters, W., Pongratz, J., et al. (2022). Global carbon budget 2021. *Earth System Science Data*, 14(4):1917–2005.

Friedlingstein, P., Jones, M. W., O'sullivan, M., Andrew, R. M., Hauck, J., Peters, G. P., Peters, W., Pongratz, J., Sitch, S., Le Quéré, C., et al. (2019). Global carbon budget 2019. *Earth System Science Data*, 11(4):1783–1838.

Friedlingstein, P., Meinshausen, M., Arora, V. K., Jones, C. D., Anav, A., Liddicoat, S. K., and Knutti, R. (2014). Uncertainties in cmip5 climate projections due to carbon cycle feedbacks. *Journal of Climate*, 27(2):511–526.

Friedlingstein, P., O'sullivan, M., Jones, M. W., Andrew, R. M., Hauck, J., Olsen, A., Peters, G. P., Peters, W., Pongratz, J., Sitch, S., et al. (2020). Global carbon budget 2020. *Earth System Science Data*, 12(4):3269–3340.

Gent, P. R., Danabasoglu, G., Donner, L. J., Holland, M. M., Hunke, E. C., Jayne, S. R., Lawrence, D. M., Neale, R. B., Rasch, P. J., Vertenstein, M., et al. (2011). The community climate system model version 4. *Journal of climate*, 24(19):4973–4991.

Georgiou, K., Koven, C. D., Riley, W. J., and Torn, M. S. (2015). Toward improved model structures for analyzing priming: potential pitfalls of using bulk turnover time. *Global Change Biology*, 21(12):4298–4302.

Georgiou, K., Malhotra, A., Wieder, W. R., Ennis, J. H., Hartman, M. D., Sulman, B. N., Berhe, A. A., Grandy, A. S., Kyker-Snowman, E., Lajtha, K., et al. (2021). Divergent controls of soil organic carbon between observations and process-based models. *Biogeochemistry*, 156(1):5–17.

Giardina, C. P. and Ryan, M. G. (2000). Evidence that decomposition rates of organic carbon in mineral soil do not vary with temperature. *Nature*, 404(6780):858–861.

Goll, D. S., Brovkin, V., Liski, J., Raddatz, T., Thum, T., and Todd-Brown, K. E. (2015). Strong dependence of co2 emissions from anthropogenic land cover change on initial land cover and soil carbon parametrization. *Global Biogeochemical Cycles*, 29(9):1511–1523.

Goll, D. S., Winkler, A. J., Raddatz, T., Dong, N., Prentice, I. C., Ciais, P., and Brovkin, V. (2017). Carbon–nitrogen interactions in idealized simulations with jsbach (version 3.10). *Geoscientific Model Development*, 10(5):2009–2030.

Graven, H., Keeling, R., Piper, S., Patra, P., Stephens, B., Wofsy, S., Welp, L., Sweeney, C., Tans, P., Kelley, J., et al. (2013). Enhanced seasonal exchange of co2 by northern ecosystems since 1960. *Science*, 341(6150):1085–1089.

Green, J., Seneviratne, S., Berg, A., Findell, K., Hagemann, S., Lawrence, D., and Gentine, P. (2019). Large influence of soil moisture on long-term terrestrial carbon uptake. *Nature*, 565(7740):476–479.

Gregory, J. M., Jones, C., Cadule, P., and Friedlingstein, P. (2009). Quantifying carbon cycle feedbacks. *Journal of Climate*, 22(19):5232–5250.

Gruber, A., Dorigo, W. A., Crow, W., and Wagner, W. (2017). Triple collocation-based merging of satellite soil moisture retrievals. *IEEE Transactions on Geoscience and Remote Sensing*, 55(12):6780–6792.

Guimberteau, M., Zhu, D., Maignan, F., Huang, Y., Yue, C., Dantec-Nédélec, S., Ottlé, C., Jornet-Puig, A., Bastos, A., Laurent, P., et al. (2018). Orchidee-mict (v8. 4.1), a land surface model for the high latitudes: model description and validation. *Geoscientific Model Development*, 11(1):121–163.

Hajima, T., Watanabe, M., Yamamoto, A., Tatebe, H., Noguchi, M. A., Abe, M., Ohgaito, R., Ito, A., Yamazaki, D., Okajima, H., et al. (2020). Development of the miroc-es2l earth system model and the evaluation of biogeochemical processes and feedbacks. *Geoscientific Model Development*, 13(5):2197–2244.

Hall, A., Cox, P., Huntingford, C., and Klein, S. (2019). Progressing emergent constraints on future climate change. *Nature Climate Change*, 9(4):269–278.

Hall, A. and Qu, X. (2006). Using the current seasonal cycle to constrain snow albedo feedback in future climate change. *Geophysical Research Letters*, 33(3).

Hansen, J. E. and Takahashi, T. (1984). Climate processes and climate sensitivity. *Washington DC American Geophysical Union Geophysical Monograph Series*, 29.

Harper, A. B., Wiltshire, A. J., Cox, P. M., Friedlingstein, P., Jones, C. D., Mercado, L. M., Sitch, S., Williams, K., and Duran-Rojas, C. (2018). Vegetation distribution and terrestrial carbon cycle in a carbon cycle configuration of jules4. 6 with new plant functional types. *Geoscientific Model Development*, 11(7):2857–2873.

Hartley, I. P. and Ineson, P. (2008). Substrate quality and the temperature sensitivity of soil organic matter decomposition. *Soil Biology and Biochemistry*, 40(7):1567–1574.

Hashimoto, S., Carvalhais, N., Ito, A., Migliavacca, M., Nishina, K., and Reichstein, M. (2015). Global spatiotemporal distribution of soil respiration modeled using a global database. *Biogeosciences*, 12:4121–4132.

Haverd, V., Smith, B., Nieradzik, L., Briggs, P. R., Woodgate, W., Trudinger, C. M., Canadell, J. G., and Cuntz, M. (2018). A new version of the cable land surface model (subversion revision r4601) incorporating land use and land cover change, woody vegetation demography, and a novel optimisation-based approach to plant coordination of photosynthesis. *Geoscientific Model Development*, 11(7):2995–3026.

Holland, E. A., Neff, J. C., Townsend, A. R., and McKeown, B. (2000). Uncertainties in the temperature sensitivity of decomposition in tropical and subtropical ecosystems: implications for models. *Global Biogeochemical Cycles*, 14(4):1137–1151.

Hugelius, G., Loisel, J., Chadburn, S., Jackson, R. B., Jones, M., MacDonald, G., Marushchak, M., Olefeldt, D., Packalen, M., Siewert, M. B., et al. (2020). Large stocks of peatland carbon and nitrogen are vulnerable to permafrost thaw. *Proceedings of the National Academy of Sciences*, 117(34):20438–20446.

Hugelius, G., Tarnocai, C., Broll, G., Canadell, J., Kuhry, P., and Swanson, D. (2013). The northern circumpolar soil carbon database: spatially distributed datasets of soil coverage and soil carbon storage in the northern permafrost regions. *Earth System Science Data*, 5(1):3–13.

IGBP (2000). Global gridded surfaces of selected soil characteristics (igbp-dis).[global gridded surfaces of selected soil characteristics (international geosphere-biosphere programme-data and information system)].

IPCC (2013). Summary for policymakers. In Stocker, T., Qin, D., Plattner, G.-K., Tignor, M., Allen, S., Boschung, J., Nauels, A., Xia, Y., Bex, V., and Midgley, P., editors, *Climate Change 2013: The Physical Science Basis. Contribution of Working Group I to the Fifth Assessment Report of the Intergovernmental Panel on Climate Change*, book section SPM, page 1–30. Cambridge University Press, Cambridge, United Kingdom and New York, NY, USA.

IPCC (2021a). *Climate Change 2021: The Physical Science Basis. Contribution of Working Group I to the Sixth Assessment Report of the Intergovernmental Panel on Climate Change*, volume In Press. Cambridge University Press, Cambridge, United Kingdom and New York, NY, USA.

IPCC (2021b). *Summary for Policymakers*. Cambridge University Press, Cambridge, United Kingdom and New York, NY, USA.

Ito, A. (2011). A historical meta-analysis of global terrestrial net primary productivity: are estimates converging? *Global Change Biology*, 17(10):3161–3175.

Ito, A., Hajima, T., Lawrence, D. M., Brovkin, V., Delire, C., Guenet, B., Jones, C. D., Malyshev, S., Materia, S., McDermid, S. P., et al. (2020). Soil carbon sequestration simulated in cmip6-lumip models: implications for climatic mitigation. *Environmental Research Letters*, 15(12):124061.

Ito, A. and Oikawa, T. (2002). A simulation model of the carbon cycle in land ecosystems (sim-cycle): a description based on dry-matter production theory and plot-scale validation. *Ecological modelling*, 151(2-3):143–176.

Iversen, T., Bentsen, M., Bethke, I., Debernard, J., Kirkevåg, A., Seland, Ø., Drange, H., Kristjansson, J., Medhaug, I., Sand, M., et al. (2013). The norwegian earth system model, noresm1-m–part 2: climate response and scenario projections. *Geoscientific Model Development*, 6(2):389–415.

Jackson, R. B., Lajtha, K., Crow, S. E., Hugelius, G., Kramer, M. G., and Piñeiro, G. (2017). The ecology of soil carbon: pools, vulnerabilities, and biotic and abiotic controls. *Annual Review of Ecology, Evolution, and Systematics*, 48:419–445.

Jansson, P.-E. and Berg, B. (1985). Temporal variation of litter decomposition in relation to simulated soil climate. long-term decomposition in a scots pine forest. v. *Canadian Journal of Botany*, 63(6):1008–1016.

Jastrow, J. D., Michael Miller, R., Matamala, R., Norby, R. J., Boutton, T. W., Rice, C. W., and Owensby, C. E. (2005). Elevated atmospheric carbon dioxide increases soil carbon. *Global Change Biology*, 11(12):2057–2064.

Jenkinson, D. and Ayanaba, A. (1977). Decomposition of carbon-14 labeled plant material under tropical conditions. *Soil Science Society of America Journal*, 41(5):912–915.

Jenkinson, D. S., Adams, D., and Wild, A. (1991). Model estimates of co2 emissions from soil in response to global warming. *Nature*, 351(6324):304.

Ji, D., Wang, L., Feng, J., Wu, Q., Cheng, H., Zhang, Q., Yang, J., Dong, W., Dai, Y., Gong, D., et al. (2014). Description and basic evaluation of beijing normal university earth system model (bnu-esm) version 1. *Geoscientific Model Development*, 7(5):2039–2064.

Ji, J., Huang, M., and Li, K. (2008). Prediction of carbon exchanges between china terrestrial ecosystem and atmosphere in 21st century. *Science in China Series D: Earth Sciences*, 51(6):885–898.

Jobbágy, E. G. and Jackson, R. B. (2000). The vertical distribution of soil organic carbon and its relation to climate and vegetation. *Ecological applications*, 10(2):423–436.

Jones, C., Hughes, J., Bellouin, N., Hardiman, S., Jones, G., Knight, J., Liddicoat, S., O'connor, F., Andres, R. J., Bell, C., et al. (2011). The hadgem2-es implementation of cmip5 centennial simulations. *Geoscientific Model Development*, 4(3):543–570.

Jones, C., McConnell, C., Coleman, K., Cox, P., Falloon, P., Jenkinson, D., and Powlson, D. (2005). Global climate change and soil carbon stocks; predictions from two contrasting models for the turnover of organic carbon in soil. *Global Change Biology*, 11(1):154–166.

Jones, C., Robertson, E., Arora, V., Friedlingstein, P., Shevliakova, E., Bopp, L., Brovkin, V., Hajima, T., Kato, E., Kawamiya, M., et al. (2013). Twenty-first-century compatible co2 emissions and airborne fraction simulated by cmip5 earth system models under four representative concentration pathways. *Journal of Climate*, 26(13):4398–4413.

Jones, C. D., Arora, V., Friedlingstein, P., Bopp, L., Brovkin, V., Dunne, J., Graven, H., Hoffman, F., Ilyina, T., John, J. G., et al. (2016). C4mip–the coupled climate–carbon cycle model intercomparison project: Experimental protocol for cmip6. *Geoscientific Model Development*, 9(8):2853–2880.

Kätterer, T., Reichstein, M., Andrén, O., and Lomander, A. (1998). Temperature dependence of organic matter decomposition: a critical review using literature data analyzed with different models. *Biology and fertility of soils*, 27(3):258–262.

Kimball, B., Mauney, J., Nakayama, F., and Idso, S. (1993). Effects of increasing atmospheric co 2 on vegetation. *Vegetatio*, 104(1):65–75.

Kirschbaum, M. U. (1995). The temperature dependence of soil organic matter decomposition, and the effect of global warming on soil organic c storage. *Soil Biology and biochemistry*, 27(6):753–760.

Klein, S. A. and Hall, A. (2015). Emergent constraints for cloud feedbacks. *Current climate change reports*, 1(4):276–287.

Knorr, W. (2000). Annual and interannual co2 exchanges of the terrestrial biosphere: Process-based simulations and uncertainties. *Global Ecology and Biogeography*, 9(3):225–252.

Knorr, W., Prentice, I. C., House, J., and Holland, E. (2005). Long-term sensitivity of soil carbon turnover to warming. *Nature*, 433(7023):298.

Knutti, R. and Sedláček, J. (2013). Robustness and uncertainties in the new cmip5 climate model projections. *Nature climate change*, 3(4):369–373.

Koster, R. D., Guo, Z., Yang, R., Dirmeyer, P. A., Mitchell, K., and Puma, M. J. (2009). On the nature of soil moisture in land surface models. *Journal of Climate*, 22(16):4322–4335.

Koven, C., Riley, W., Subin, Z., Tang, J., Torn, M., Collins, W., Bonan, G., Lawrence, D., and Swenson, S. (2013). The effect of vertically resolved soil biogeochemistry and alternate soil c and n models on c dynamics of clm4. *Biogeosciences*, 10(11):7109–7131.

Koven, C. D., Chambers, J. Q., Georgiou, K., Knox, R., Negron-Juarez, R., Riley, W. J., Arora, V. K., Brovkin, V., Friedlingstein, P., and Jones, C. D. (2015). Controls on terrestrial carbon feedbacks by productivity versus turnover in the cmip5 earth system models. *Biogeosciences*, 12(17):5211–5228.

Koven, C. D., Hugelius, G., Lawrence, D. M., and Wieder, W. R. (2017). Higher climatological temperature sensitivity of soil carbon in cold than warm climates. *Nature Climate Change*, 7(11):817.

Koven, C. D., Ringeval, B., Friedlingstein, P., Ciais, P., Cadule, P., Khvorostyanov, D., Krinner, G., and Tarnocai, C. (2011). Permafrost carbon-climate feedbacks accelerate global warming. *Proceedings of the National Academy of Sciences*, 108(36):14769–14774.

Krankina, O., Dixon, R., Kirilenko, A., and Kobak, K. (1997). Global climate change adaptation: examples from russian boreal forests. *Climatic Change*, 36(1):197–215.

Krinner, G., Viovy, N., de Noblet-Ducoudré, N., Ogée, J., Polcher, J., Friedlingstein, P., Ciais, P., Sitch, S., and Prentice, I. C. (2005). A dynamic global vegetation model for studies of the coupled atmosphere-biosphere system. *Global Biogeochemical Cycles*, 19(1).

Lawrence, D. M., Fisher, R. A., Koven, C. D., Oleson, K. W., Swenson, S. C., Bonan, G., Collier, N., Ghimire, B., Van Kampenhout, L., Kennedy, D., et al. (2019). The community land model version 5: Description of new features,

benchmarking, and impact of forcing uncertainty. *Journal of Advances in Modeling Earth Systems*, 11(12):4245–4287.

Lawrence, D. M., Oleson, K. W., Flanner, M. G., Thornton, P. E., Swenson, S. C., Lawrence, P. J., Zeng, X., Yang, Z.-L., Levis, S., Sakaguchi, K., et al. (2011). Parameterization improvements and functional and structural advances in version 4 of the community land model. *Journal of Advances in Modeling Earth Systems*, 3(1).

Le Quéré, C., Andrew, R. M., Friedlingstein, P., Sitch, S., Hauck, J., Pongratz, J., Pickers, P. A., Korsbakken, J. I., Peters, G. P., Canadell, J. G., et al. (2018). Global carbon budget 2018. *Earth System Science Data*, 10(4):2141–2194.

Lichter, J., Billings, S. A., Ziegler, S. E., Gaindh, D., Ryals, R., Finzi, A. C., Jackson, R. B., Stemmler, E. A., and Schlesinger, W. H. (2008). Soil carbon sequestration in a pine forest after 9 years of atmospheric co2 enrichment. *Global Change Biology*, 14(12):2910–2922.

Liu, Y., Dorigo, W. A., Parinussa, R., de Jeu, R. A., Wagner, W., McCabe, M. F., Evans, J., and Van Dijk, A. (2012). Trend-preserving blending of passive and active microwave soil moisture retrievals. *Remote Sensing of Environment*, 123:280–297.

Liu, Y. Y., Parinussa, R., Dorigo, W. A., De Jeu, R. A., Wagner, W., Van Dijk, A., McCabe, M. F., and Evans, J. (2011). Developing an improved soil moisture dataset by blending passive and active microwave satellite-based retrievals. *Hydrology and Earth System Sciences*, 15(2):425–436.

Lloyd, J. and Taylor, J. (1994). On the temperature dependence of soil respiration. *Functional ecology*, pages 315–323.

Mahecha, M. D., Reichstein, M., Carvalhais, N., Lasslop, G., Lange, H., Seneviratne, S. I., Vargas, R., Ammann, C., Arain, M. A., Cescatti, A., et al. (2010). Global convergence in the temperature sensitivity of respiration at ecosystem level. *Science*, 329(5993):838–840.

Manzoni, S., Katul, G. G., and Porporato, A. (2009). Analysis of soil carbon transit times and age distributions using network theories. *Journal of Geophysical Research: Biogeosciences*, 114(G4).

Matthews, H. D., Eby, M., Weaver, A. J., and Hawkins, B. J. (2005). Primary productivity control of simulated carbon cycle–climate feedbacks. *Geophysical research letters*, 32(14).

Mauritsen, T., Bader, J., Becker, T., Behrens, J., Bittner, M., Brokopf, R., Brovkin, V., Claussen, M., Crueger, T., Esch, M., et al. (2019). Developments in the mpi-m earth system model version 1.2 (mpi-esm1. 2) and its response to increasing co2. *Journal of Advances in Modeling Earth Systems*, 11(4):998–1038.

McDowell, N. G. and Allen, C. D. (2015). Darcy's law predicts widespread forest mortality under climate warming. *Nature Climate Change*, 5(7):669–672.

Medlyn, B. E., McMurtrie, R. E., Dewar, R. C., and Jeffreys, M. P. (2000). Soil processes dominate the long-term response of forest net primary productivity to increased temperature and atmospheric co2 concentration. *Canadian Journal of Forest Research*, 30(6):873–888.

Meehl, G. A., Boer, G. J., Covey, C., Latif, M., and Stouffer, R. J. (2000). The coupled model intercomparison project (cmip). *Bulletin of the American Meteorological Society*, 81(2):313–318.

Meehl, G. A., Covey, C., Delworth, T., Latif, M., McAvaney, B., Mitchell, J. F., Stouffer, R. J., and Taylor, K. E. (2007). The wcrp cmip3 multimodel dataset: A new era in climate change research. *Bulletin of the American meteorological society*, 88(9):1383–1394.

Meehl, G. A., Moss, R., Taylor, K. E., Eyring, V., Stouffer, R. J., Bony, S., and Stevens, B. (2014). Climate model intercomparisons: Preparing for the next phase. *Eos, Transactions American Geophysical Union*, 95(9):77–78.

Meinshausen, M., Smith, S. J., Calvin, K., Daniel, J. S., Kainuma, M., Lamarque, J.-F., Matsumoto, K., Montzka, S., Raper, S., Riahi, K., et al. (2011). The rcp greenhouse gas concentrations and their extensions from 1765 to 2300. *Climatic change*, 109(1-2):213.

Melillo, J. M., Frey, S. D., DeAngelis, K. M., Werner, W. J., Bernard, M. J., Bowles, F. P., Pold, G., Knorr, M. A., and Grandy, A. S. (2017). Long-term pattern and magnitude of soil carbon feedback to the climate system in a warming world. *Science*, 358(6359):101–105.

Melton, J. R., Arora, V. K., Wisernig-Cojoc, E., Seiler, C., Fortier, M., Chan, E., and Teckentrup, L. (2020). Classic v1. 0: the open-source community successor to the canadian land surface scheme (class) and the canadian terrestrial ecosystem model (ctem)–part 1: Model framework and site-level performance. *Geoscientific Model Development*, 13(6):2825–2850.

Met Office (2010 - 2013). *Iris: A Python package for analysing and visualising meteorological and oceanographic data sets*. Exeter, Devon, v1.2 edition.

Mundim, K. C., Baraldi, S., Machado, H. G., and Vieira, F. M. (2020). Temperature coefficient (q10) and its applications in biological systems: Beyond the arrhenius theory. *Ecological Modelling*, 431:109127.

Neill, C. and Gignoux, J. (2006). Soil organic matter decomposition driven by microbial growth: A simple model for a complex network of interactions. *Soil Biology and Biochemistry*, 38(4):803–811.

Nijsse, F. J., Cox, P. M., and Williamson, M. S. (2020). Emergent constraints on transient climate response (tcr) and equilibrium climate sensitivity (ecs) from historical warming in cmip5 and cmip6 models. *Earth System Dynamics*, 11(3):737–750.

Nishina, K., Ito, A., Beerling, D., Cadule, P., Ciais, P., Clark, D., Falloon, P., Friend, A., Kahana, R., Kato, E., et al. (2014). Quantifying uncertainties in soil carbon responses to changes in global mean temperature and precipitation. *Earth System Dynamics*, 5(1):197–209.

Nishina, K., Ito, A., Falloon, P., Friend, A., Beerling, D., Ciais, P., Clark, D., Kahana, R., Kato, E., Lucht, W., et al. (2015). Decomposing uncertainties in the future terrestrial carbon budget associated with emission scenarios, climate projections, and ecosystem simulations using the isi-mip results. *Earth System Dynamics*, 6(2):435–445.

Norby, R. J., Warren, J. M., Iversen, C. M., Medlyn, B. E., and McMurtrie, R. E. (2010). Co2 enhancement of forest productivity constrained by limited nitrogen availability. *Proceedings of the National Academy of Sciences*, 107(45):19368–19373.

Nyawira, S.-S., Nabel, J. E., Brovkin, V., and Pongratz, J. (2017). Input-driven versus turnover-driven controls of simulated changes in soil carbon due to land-use change. *Environmental Research Letters*, 12(8):084015.

O'Neill, B. C., Tebaldi, C., Vuuren, D. P. v., Eyring, V., Friedlingstein, P., Hurtt, G., Knutti, R., Kriegler, E., Lamarque, J.-F., Lowe, J., et al. (2016). The scenario model intercomparison project (scenariomip) for cmip6. *Geoscientific Model Development*, 9(9):3461–3482.

Orchard, V. A. and Cook, F. (1983). Relationship between soil respiration and soil moisture. *Soil Biology and Biochemistry*, 15(4):447–453.

O'Neill, B. C., Kriegler, E., Riahi, K., Ebi, K. L., Hallegatte, S., Carter, T. R., Mathur, R., and van Vuuren, D. P. (2014). A new scenario framework for climate change research: the concept of shared socioeconomic pathways. *Climatic change*, 122(3):387–400.

Parton, W. J., Stewart, J. W., and Cole, C. V. (1988). Dynamics of c, n, p and s in grassland soils: a model. *Biogeochemistry*, 5(1):109–131.

Pendall, E., Bridgham, S., Hanson, P. J., Hungate, B., Kicklighter, D. W., Johnson, D. W., Law, B. E., Luo, Y., Megonigal, J. P., Olsrud, M., et al. (2004). Below-ground process responses to elevated co2 and temperature: a discussion of observations, measurement methods, and models. *New Phytologist*, 162(2):311–322.

Peng, Q., Dong, Y., Qi, Y., Xiao, S., He, Y., and Ma, T. (2011). Effects of nitrogen fertilization on soil respiration in temperate grassland in inner mongolia, china. *Environmental Earth Sciences*, 62(6):1163–1171.

Peñuelas, J. and Filella, I. (2001). Responses to a warming world. *Science*, 294(5543):793–795.

Phillips, O. L., Aragão, L. E., Lewis, S. L., Fisher, J. B., Lloyd, J., López-González, G., Malhi, Y., Monteagudo, A., Peacock, J., Quesada, C. A., et al. (2009). Drought sensitivity of the amazon rainforest. *Science*, 323(5919):1344–1347.

Piao, S., Sitch, S., Ciais, P., Friedlingstein, P., Peylin, P., Wang, X., Ahlström, A., Anav, A., Canadell, J. G., Cong, N., et al. (2013). Evaluation of terrestrial carbon cycle models for their response to climate variability and to co2 trends. *Global change biology*, 19(7):2117–2132.

Post, W. M., Emanuel, W. R., Zinke, P. J., and Stangenberger, A. G. (1982). Soil carbon pools and world life zones. *Nature*, 298(5870):156–159.

Pugh, T., Jones, C., Huntingford, C., Burton, C., Arneth, A., Brovkin, V., Ciais, P., Lomas, M., Robertson, E., Piao, S., et al. (2018). A large committed long-term sink of carbon due to vegetation dynamics. *Earth's Future*, 6(10):1413–1432.

Qu, X. and Hall, A. (2007). What controls the strength of snow-albedo feedback? *Journal of Climate*, 20(15):3971–3981.

Raddatz, T., Reick, C., Knorr, W., Kattge, J., Roeckner, E., Schnur, R., Schnitzler, K.-G., Wetzel, P., and Jungclaus, J. (2007). Will the tropical land biosphere dominate the climate–carbon cycle feedback during the twenty-first century? *Climate dynamics*, 29(6):565–574.

Raich, J. W., Potter, C. S., and Bhagawati, D. (2002). Interannual variability in global soil respiration, 1980–94. *Global Change Biology*, 8(8):800–812.

Raich, J. W. and Schlesinger, W. H. (1992). The global carbon dioxide flux in soil respiration and its relationship to vegetation and climate. *Tellus B*, 44(2):81–99.

Ran, Y., Li, X., Cheng, G., Che, J., Aalto, J., Karjalainen, O., Hjort, J., Luoto, M., Jin, H., Obu, J., et al. (2021). New high-resolution estimates of the permafrost thermal state and hydrothermal conditions over the northern hemisphere. *Earth System Science Data Discussions*, pages 1–27.

Reichstein, M., Bahn, M., Ciais, P., Frank, D., Mahecha, M. D., Seneviratne, S. I., Zscheischler, J., Beer, C., Buchmann, N., Frank, D. C., et al. (2013). Climate extremes and the carbon cycle. *Nature*, 500(7462):287–295.

Rustad, L., Campbell, J., Marion, G., Norby, R., Mitchell, M., Hartley, A., Cornelissen, J., Gurevitch, J., et al. (2001). A meta-analysis of the response of soil respiration, net nitrogen mineralization, and aboveground plant growth to experimental ecosystem warming. *Oecologia*, 126(4):543–562.

Sanderman, J., Amundson, R. G., and Baldocchi, D. D. (2003). Application of eddy covariance measurements to the temperature dependence of soil organic matter mean residence time. *Global Biogeochemical Cycles*, 17(2).

Sanderman, J., Hengl, T., and Fiske, G. J. (2017). Soil carbon debt of 12,000 years of human land use. *Proceedings of the National Academy of Sciences*, 114(36):9575–9580.

Sanderson, B. M., Pendergrass, A., Koven, C. D., Brient, F., Booth, B. B., Fisher, R. A., and Knutti, R. (2021). On structural errors in emergent constraints. *Earth Syst. Dyn. Discuss*.

Sato, H., Itoh, A., and Kohyama, T. (2007). Seib–dgvm: A new dynamic global vegetation model using a spatially explicit individual-based approach. *Ecological Modelling*, 200(3-4):279–307.

Schädel, C., Bader, M. K.-F., Schuur, E. A., Biasi, C., Bracho, R., Čapek, P., De Baets, S., Diáková, K., Ernakovich, J., Estop-Aragones, C., et al. (2016). Potential carbon emissions dominated by carbon dioxide from thawed permafrost soils. *Nature climate change*, 6(10):950–953.

Schimel, D., Stephens, B. B., and Fisher, J. B. (2015). Effect of increasing co2 on the terrestrial carbon cycle. *Proceedings of the National Academy of Sciences*, 112(2):436–441.

Schlund, M., Lauer, A., Gentine, P., Sherwood, S. C., and Eyring, V. (2020). Emergent constraints on equilibrium climate sensitivity in cmip5: do they hold for cmip6? *Earth System Dynamics*, 11(4):1233–1258.

Schmidt, G. A., Kelley, M., Nazarenko, L., Ruedy, R., Russell, G. L., Aleinov, I., Bauer, M., Bauer, S. E., Bhat, M. K., Bleck, R., et al. (2014). Configuration and

assessment of the giss modele2 contributions to the cmip5 archive. *Journal of Advances in Modeling Earth Systems*, 6(1):141–184.

Schmidt, M. W., Torn, M. S., Abiven, S., Dittmar, T., Guggenberger, G., Janssens, I. A., Kleber, M., Kögel-Knabner, I., Lehmann, J., Manning, D. A., et al. (2011). Persistence of soil organic matter as an ecosystem property. *Nature*, 478(7367):49–56.

Schuur, E. A., McGuire, A. D., Schädel, C., Grosse, G., Harden, J. W., Hayes, D. J., Hugelius, G., Koven, C. D., Kuhry, P., Lawrence, D. M., et al. (2015). Climate change and the permafrost carbon feedback. *Nature*, 520(7546):171–179.

Schwinger, J., Tjiputra, J. F., Heinze, C., Bopp, L., Christian, J. R., Gehlen, M., Ilyina, T., Jones, C. D., Salas-Mélia, D., Segschneider, J., et al. (2014). Nonlinearity of ocean carbon cycle feedbacks in cmip5 earth system models. *Journal of Climate*, 27(11):3869–3888.

Séférian, R., Nabat, P., Michou, M., Saint-Martin, D., Voldoire, A., Colin, J., Decharme, B., Delire, C., Berthet, S., Chevallier, M., et al. (2019). Evaluation of cnrm earth system model, cnrm-esm2-1: Role of earth system processes in present-day and future climate. *Journal of Advances in Modeling Earth Systems*, 11(12):4182–4227.

Seiler, C., Melton, J. R., Arora, V. K., and Wang, L. (2021). Classic v1. 0: the open-source community successor to the canadian land surface scheme (class) and the canadian terrestrial ecosystem model (ctem)–part 2: Global benchmarking. *Geoscientific Model Development*, 14(5):2371–2417.

Seland, Ø., Bentsen, M., Olivié, D., Toniazzo, T., Gjermundsen, A., Graff, L. S., Debernard, J. B., Gupta, A. K., He, Y.-C., Kirkevåg, A., et al. (2020). Overview of the norwegian earth system model (noresm2) and key climate response of cmip6 deck, historical, and scenario simulations. *Geoscientific Model Development*, 13(12):6165–6200.

Sellar, A. A., Walton, J., Jones, C. G., Wood, R., Abraham, N. L., Andrejczuk, M., Andrews, M. B., Andrews, T., Archibald, A. T., de Mora, L., et al. (2020). Implementation of uk earth system models for cmip6. *Journal of Advances in Modeling Earth Systems*, 12(4):e2019MS001946.

Serreze, M. C. and Barry, R. G. (2011). Processes and impacts of arctic amplification: A research synthesis. *Global and planetary change*, 77(1-2):85–96.

Shangguan, W., Dai, Y., Duan, Q., Liu, B., and Yuan, H. (2014). A global soil data set for earth system modeling. *Journal of Advances in Modeling Earth Systems*, 6(1):249–263.

Shevliakova, E., Pacala, S. W., Malyshev, S., Hurtt, G. C., Milly, P., Caspersen, J. P., Sentman, L. T., Fisk, J. P., Wirth, C., and Crevoisier, C. (2009). Carbon cycling under 300 years of land use change: Importance of the secondary vegetation sink. *Global Biogeochemical Cycles*, 23(2).

Shi, Z., Allison, S. D., He, Y., Levine, P. A., Hoyt, A. M., Beem-Miller, J., Zhu, Q., Wieder, W. R., Trumbore, S., and Randerson, J. T. (2020). The age distribution of global soil carbon inferred from radiocarbon measurements. *Nature Geoscience*, 13(8):555–559.

Sierra, C. A., Trumbore, S. E., Davidson, E. A., Vicca, S., and Janssens, I. (2015). Sensitivity of decomposition rates of soil organic matter with respect to simultaneous changes in temperature and moisture. *Journal of Advances in Modeling Earth Systems*, 7(1):335–356.

Six, J., Feller, C., Denef, K., Ogle, S., de Moraes Sa, J. C., and Albrecht, A. (2002). Soil organic matter, biota and aggregation in temperate and tropical soils-effects of no-tillage. *Agronomie*, 22(7-8):755–775.

Sombroek, W. G., Nachtergaele, F. O., and Hebel, A. (1993). Amounts, dynamics and sequestering of carbon in tropical and subtropical soils. *Ambio (Journal of the Human Environment, Research and Management);(Sweden)*, 22(7).

Soong, J. L., Phillips, C. L., Ledna, C., Koven, C. D., and Torn, M. S. (2020). Cmip5 models predict rapid and deep soil warming over the 21st century. *Journal of Geophysical Research: Biogeosciences*, 125(2):e2019JG005266.

Stocker, T., Qin, D., Plattner, G.-K., Alexander, L., Allen, S., Bindoff, N., Bréon, F.-M., Church, J., Cubasch, U., Emori, S., Forster, P., Friedlingstein, P., Gillett, N., Gregory, J., Hartmann, D., Jansen, E., Kirtman, B., Knutti, R., Krishna Kumar, K., Lemke, P., Marotzke, J., Masson-Delmotte, V., Meehl, G., Mokhov, I., Piao, S., Ramaswamy, V., Randall, D., Rhein, M., Rojas, M., Sabine, C., Shindell, D., Talley, L., Vaughan, D., and Xie, S.-P. (2013). *Technical Summary*, book section TS, page 33–115. Cambridge University Press, Cambridge, United Kingdom and New York, NY, USA.

Sulman, B. N., Salmon, V. G., Iversen, C. M., Breen, A. L., Yuan, F., and Thornton, P. E. (2021). Integrating arctic plant functional types in a land surface model using above-and belowground field observations. *Journal of Advances in Modeling Earth Systems*, 13(4):e2020MS002396.

Swart, N. C., Cole, J. N., Kharin, V. V., Lazare, M., Scinocca, J. F., Gillett, N. P., Anstey, J., Arora, V., Christian, J. R., Hanna, S., et al. (2019). The canadian earth system model version 5 (canesm5. 0.3). *Geoscientific Model Development*, 12(11):4823–4873.

Tarnocai, C., Canadell, J., Schuur, E. A., Kuhry, P., Mazhitova, G., and Zimov, S. (2009). Soil organic carbon pools in the northern circumpolar permafrost region. *Global biogeochemical cycles*, 23(2).

Taylor, K. E. (2001). Summarizing multiple aspects of model performance in a single diagram. *Journal of Geophysical Research: Atmospheres*, 106(D7):7183–7192.

Taylor, K. E., Stouffer, R. J., and Meehl, G. A. (2012). An overview of cmip5 and the experiment design. *Bulletin of the American Meteorological Society*, 93(4):485–498.

Thackeray, C. W., Hall, A., Zelinka, M. D., and Fletcher, C. G. (2021). Assessing prior emergent constraints on surface albedo feedback in cmip6. *Journal of Climate*, 34(10):3889–3905.

Thornton, P. E., Doney, S. C., Lindsay, K., Moore, J. K., Mahowald, N., Randerson, J. T., Fung, I., Lamarque, J.-F., Feddema, J. J., and Lee, Y.-H. (2009). Carbon-nitrogen interactions regulate climate-carbon cycle feedbacks: results from an atmosphere-ocean general circulation model. *Biogeosciences*, 6(10):2099–2120.

Tian, H., Lu, C., Yang, J., Banger, K., Huntzinger, D. N., Schwalm, C. R., Michalak, A. M., Cook, R., Ciais, P., Hayes, D., et al. (2015). Global patterns and controls of soil organic carbon dynamics as simulated by multiple terrestrial biosphere models: Current status and future directions. *Global biogeochemical cycles*, 29(6):775–792.

Todd-Brown, K., Randerson, J., Hopkins, F., Arora, V., Hajima, T., Jones, C., Shevliakova, E., Tjiputra, J., Volodin, E., Wu, T., et al. (2014). Changes in soil organic carbon storage predicted by earth system models during the 21st century. *Biogeosciences*, 11(8):2341–2356.

Todd-Brown, K., Randerson, J., Post, W., Hoffman, F., Tarnocai, C., Schuur, E., and Allison, S. (2013). Causes of variation in soil carbon simulations from cmip5 earth system models and comparison with observations. *Biogeosciences*, 10(3):1717–1736.

Todd-Brown, K., Zheng, B., and Crowther, T. W. (2018). Field-warmed soil carbon changes imply high 21st-century modeling uncertainty. *Biogeosciences*, 15(12):3659–3671.

Trudinger, C. M., Haverd, V., Briggs, P. R., and Canadell, J. G. (2016). Interannual variability in australia's terrestrial carbon cycle constrained by multiple observation types. *Biogeosciences*, 13(23):6363–6383.

Trumbore, S. E., Chadwick, O. A., and Amundson, R. (1996). Rapid exchange between soil carbon and atmospheric carbon dioxide driven by temperature change. *Science*, 272(5260):393–396.

UNFCCC (2015). Adoption of the paris agreementfccc/cp/2015/l.9/rev.1.

Van Gestel, N., Shi, Z., Van Groenigen, K. J., Osenberg, C. W., Andresen, L. C., Dukes, J. S., Hovenden, M. J., Luo, Y., Michelsen, A., Pendall, E., et al. (2018). Predicting soil carbon loss with warming. *Nature*, 554(7693):E4–E5.

Van Groenigen, K. J., Qi, X., Osenberg, C. W., Luo, Y., and Hungate, B. A. (2014). Faster decomposition under increased atmospheric co2 limits soil carbon storage. *Science*, 344(6183):508–509.

Varney, R. M., Chadburn, S. E., Burke, E. J., and Cox, P. M. (2022). Evaluation of soil carbon simulation in cmip6 earth system models. *Biogeosciences*, 19(19):4671–4704.

Varney, R. M., Chadburn, S. E., Friedlingstein, P., Burke, E. J., Koven, C. D., Hugelius, G., and Cox, P. M. (2020). A spatial emergent constraint on the sensitivity of soil carbon turnover to global warming. *Nature communications*, 11(1):1–8.

Waddington, J., Morris, P., Kettridge, N., Granath, G., Thompson, D., and Moore, P. (2015). Hydrological feedbacks in northern peatlands. *Ecohydrology*, 8(1):113–127.

Wagner, W., Dorigo, W., de Jeu, R., Fernandez, D., Benveniste, J., Haas, E., Ertl, M., et al. (2012). Fusion of active and passive microwave observations to create an essential climate variable data record on soil moisture. *ISPRS Annals of the Photogrammetry, Remote Sensing and Spatial Information Sciences (ISPRS Annals)*, 7:315–321.

Walker, T. W., Kaiser, C., Strasser, F., Herbold, C. W., Leblans, N. I., Woebken, D., Janssens, I. A., Sigurdsson, B. D., and Richter, A. (2018). Microbial temperature sensitivity and biomass change explain soil carbon loss with warming. *Nature climate change*, 8(10):885–889.

Wang, Y., Law, R., and Pak, B. (2010). A global model of carbon, nitrogen and phosphorus cycles for the terrestrial biosphere. *Biogeosciences*, 7(7):2261–2282.

Wang, Y. P., Kowalczyk, E., Leuning, R., Abramowitz, G., Raupach, M. R., Pak, B., van Gorsel, E., and Luhar, A. (2011). Diagnosing errors in a land surface model (cable) in the time and frequency domains. *Journal of Geophysical Research: Biogeosciences*, 116(G1).

Watanabe, S., Hajima, T., Sudo, K., Nagashima, T., Takemura, T., Okajima, H., Nozawa, T., Kawase, H., Abe, M., Yokohata, T., et al. (2011). Miroc-esm 2010: Model description and basic results of cmip5-20c3m experiments. *Geoscientific Model Development*, 4(4):845–872.

Weedon, G. P., Balsamo, G., Bellouin, N., Gomes, S., Best, M. J., and Viterbo, P. (2014). The wfdei meteorological forcing data set: Watch forcing data methodology applied to era-interim reanalysis data. *Water Resources Research*, 50(9):7505–7514.

Wei, H., Guenet, B., Vicca, S., Nunan, N., Asard, H., AbdElgawad, H., Shen, W., and Janssens, I. A. (2014). High clay content accelerates the decomposition of fresh organic matter in artificial soils. *Soil Biology and Biochemistry*, 77:100–108.

Wenzel, S., Cox, P. M., Eyring, V., and Friedlingstein, P. (2014). Emergent constraints on climate-carbon cycle feedbacks in the cmip5 earth system models. *Journal of Geophysical Research: Biogeosciences*, 119(5):794–807.

Wenzel, S., Cox, P. M., Eyring, V., and Friedlingstein, P. (2016). Projected land photosynthesis constrained by changes in the seasonal cycle of atmospheric co 2. *Nature*, 538(7626):499.

Wieder, W. R., Allison, S. D., Davidson, E. A., Georgiou, K., Hararuk, O., He, Y., Hopkins, F., Luo, Y., Smith, M. J., Sulman, B., et al. (2015a). Explicitly representing soil microbial processes in earth system models. *Global Biogeochemical Cycles*, 29(10):1782–1800.

Wieder, W. R., Bonan, G. B., and Allison, S. D. (2013). Global soil carbon projections are improved by modelling microbial processes. *Nature Climate Change*, 3(10):909.

Wieder, W. R., Cleveland, C. C., Smith, W. K., and Todd-Brown, K. (2015b). Future productivity and carbon storage limited by terrestrial nutrient availability. *Nature Geoscience*, 8(6):441–444.

Williamson, D. B. and Sansom, P. G. (2019). How are emergent constraints quantifying uncertainty and what do they leave behind? *Bulletin of the American Meteorological Society*, 100(12):2571–2588.

Wiltshire, A. J., Burke, E. J., Chadburn, S. E., Jones, C. D., Cox, P. M., Davies-Barnard, T., Friedlingstein, P., Harper, A. B., Liddicoat, S., Sitch, S., et al. (2021). Jules-cn: a coupled terrestrial carbon–nitrogen scheme (jules vn5. 1). *Geoscientific Model Development*, 14(4):2161–2186.

Winkler, A. J., Myneni, R. B., Alexandrov, G. A., and Brovkin, V. (2019). Earth system models underestimate carbon fixation by plants in the high latitudes. *Nature Communications*, 10(1):1–8.

Witzgall, K., Vidal, A., Schubert, D. I., Höschen, C., Schweizer, S. A., Buegger, F., Pouteau, V., Chenu, C., and Mueller, C. W. (2021). Particulate organic matter as a functional soil component for persistent soil organic carbon. *Nature communications*, 12(1):1–10.

Woodward, F., Lomas, M. R., and Betts, R. A. (1998). Vegetation-climate feedbacks in a greenhouse world. *Philosophical Transactions of the Royal Society of London. Series B: Biological Sciences*, 353(1365):29–39.

Wu, D., Piao, S., Liu, Y., Ciais, P., and Yao, Y. (2018). Evaluation of cmip5 earth system models for the spatial patterns of biomass and soil carbon turnover times and their linkage with climate. *Journal of Climate*, 31(15):5947–5960.

Wu, T., Lu, Y., Fang, Y., Xin, X., Li, L., Li, W., Jie, W., Zhang, J., Liu, Y., Zhang, L., et al. (2019). The beijing climate center climate system model (bcc-csm): The main progress from cmip5 to cmip6. *Geoscientific Model Development*, 12(4):1573–1600.

Xenakis, G. and Williams, M. (2014). Comparing microbial and chemical kinetics for modelling soil organic carbon decomposition using the decochem v1. 0 and decobio v1. 0 models. *Geoscientific Model Development*, 7(4):1519–1533.

Xu, W., Chang, J., Ciais, P., Guenet, B., Viovy, N., Ito, A., Reyer, C. P., Tian, H., Shi, H., Frieler, K., et al. (2020). Reducing uncertainties of future global soil carbon responses to climate and land use change with emergent constraints. *Global Biogeochemical Cycles*, 34(10):e2020GB006589.

Yue, X. and Unger, N. (2015). The yale interactive terrestrial biosphere model version 1.0: description, evaluation and implementation into nasa giss modele2. *Geoscientific Model Development*, 8(8):2399–2417.

Zaehle, S., Friedlingstein, P., and Friend, A. D. (2010). Terrestrial nitrogen feedbacks may accelerate future climate change. *Geophysical Research Letters*, 37(1).

Zhang, Q., Wang, Y.-P., Matear, R., Pitman, A., and Dai, Y. (2014). Nitrogen and phosphorous limitations significantly reduce future allowable co2 emissions. *Geophysical Research Letters*, 41(2):632–637.

Zhao, M., Golaz, J.-C., Held, I., Guo, H., Balaji, V., Benson, R., Chen, J.-H., Chen, X., Donner, L., Dunne, J., et al. (2018). The gfdl global atmosphere and land model am4. 0/lm4. 0: 2. model description, sensitivity studies, and tuning strategies. *Journal of Advances in Modeling Earth Systems*, 10(3):735–769.

Zhao, M., Heinsch, F. A., Nemani, R. R., and Running, S. W. (2005). Improvements of the modis terrestrial gross and net primary production global data set. *Remote sensing of Environment*, 95(2):164–176.

Zhu, D., Peng, S., Ciais, P., Zech, R., Krinner, G., Zimov, S., and Grosse, G. (2016). Simulating soil organic carbon in yedoma deposits during the last glacial maximum in a land surface model. *Geophysical Research Letters*, 43(10):5133–5142.

Zickfeld, K., Eby, M., Matthews, H. D., Schmittner, A., and Weaver, A. J. (2011). Nonlinearity of carbon cycle feedbacks. *Journal of Climate*, 24(16):4255–4275.

Ziehn, T., Chamberlain, M. A., Law, R. M., Lenton, A., Bodman, R. W., Dix, M., Stevens, L., Wang, Y.-P., and Srbinovsky, J. (2020). The australian earth system model: Access-esm1. 5. *Journal of Southern Hemisphere Earth Systems Science*, 70(1):193–214.

Zimov, S. A., Schuur, E. A., and Chapin III, F. S. (2006). Permafrost and the global carbon budget. *Science(Washington)*, 312(5780):1612–1613.